DOE/ER-0313/21
Distribution
Categories
UC-423, -424

FUSION MATERIALS
SEMIANNUAL PROGRESS REPORT
FOR THE PERIOD ENDING
DECEMBER 31, 1996

Prepared for
DOE Office of Fusion Energy Sciences
(AT 60 20 00 0)

DATE PUBLISHED: APRIL 1997

Prepared for
OAK RIDGE NATIONAL LABORATORY
Oak Ridge, Tennessee 37831
Managed by
Lockheed Martin Energy Research Corp.
for the
U.S. DEPARTMENT OF ENERGY
under Contract DE-AC05-96OR22464

FOREWORD

This is the tweny-first in a series of semiannual technical progress reports on fusion materials. This report combines the full spectrum of research and development activities on both metallic and non-metallic materials with primary emphasis on the effects of the neutronic and chemical environment on the properties and performance of materials for in-vessel components. This effort forms one element of the materials program being conducted in support of the Fusion Energy Sciences Program of the U.S. Department of Energy. The other major element of the program is concerned with the interactions between reactor materials and the plasma and is reported separately.

The Fusion Materials Program is a national effort involving several national laboratories, universities, and industries. A large fraction of this work, particularly in relation to fission reactor experiments, is carried out collaboratively with our partners in Japan, Russia, and the European Union. The purpose of this series of reports is to provide a working technical record for the use of the program participants, and to provide a means of communicating the efforts of materials scientists to the rest of the fusion community, both nationally and worldwide.

This report has been compiled and edited under the guidance of A. F. Rowcliffe by Gabrielle Burn, Oak Ridge National Laboratory. Their efforts, and the efforts of the many persons who made technical contributions, are gratefully acknowledged.

F. W. Wiffen
International and Technology Division

Reports previously listed in this series are as follows:

DOE/ER-0313/1	Period ending September 30, 1986
DOE/ER-0313/2	Period ending March 31, 1987
DOE/ER-0313/3	Period ending September 30, 1987
DOE/ER-0313/4	Period ending March 31, 1988
DOE/ER-0313/5	Period ending September 30, 1988
DOE/ER-0313/6	Period ending March 31, 1989
DOE/ER-0313/7	Period ending September 30, 1989
DOE/ER-0313/8	Period ending March 31, 1990
DOE/ER-0313/9	Period ending September 30, 1990
DOE/ER-0313/10	Period ending March 31, 1991
DOE/ER-0313/11	Period ending September 30, 1991
DOE/ER-0313/12	Period ending March 31, 1992
DOE/ER-0313/13	Period ending September 30, 1992
DOE/ER-0313/14	Period ending March 31, 1993
DOE/ER-0313/15	Period ending September 30, 1993
DOE/ER-0313/16	Period ending March 31, 1994
DOE/ER-0313/17	Period ending September 30, 1994
DOE/ER-0313/18	Period ending March 31, 1995
DOE/ER-0313/19	Period ending December 31, 1995
DOE/ER-0313/20	Period ending June 30, 1996
DOE/ER-0313/100	Technical Evaluation of the Technology of Vanadium Alloys for Use as Blanket Structural Materials in Fusion Power Systems

CONTENTS

1.0 VANADIUM ALLOYS

PRODUCTION AND FABRICATION OF VANADIUM ALLOYS FOR THE RADIATIVE DIVERTOR PROGRAM OF DIII–D — W. R. Johnson, J. P. Smith, and P. W. Trester (General Atomics)

SUMMARY

V-4Cr-4Ti alloy has been selected for use in the manufacture of a portion of the DIII–D Radiative Divertor upgrade. The production of a 1200-kg ingot of V-4Cr-4Ti alloy, and processing into final sheet and rod product forms suitable for components of the DIII–D Radiative Divertor structure, has been completed at Wah Chang (formerly Teledyne Wah Chang) of Albany, Oregon (WCA). Joining of V-4Cr-4Ti alloy has been identified as the most critical fabrication issue for its use in the RD Program, and research into several joining methods for fabrication of the RD components, including resistance seam, friction, and electron beam welding, is continuing. Preliminary trials have been successful in the joining of V-alloy to itself by electron beam, resistance, and friction welding processes, and to Inconel 625 by friction welding. An effort to investigate the explosive bonding of V-4Cr-4Ti alloy to Inconel 625 has also been initiated, and results have been encouraging. In addition, preliminary tests have been completed to evaluate the susceptibility of V-4Cr-4Ti alloy to stress corrosion cracking in DIII–D cooling water, and the effects of exposure to DIII–D bakeout conditions on the tensile and fracture behavior of V-4Cr-4Ti alloy.

PROGRESS AND STATUS

1. Introduction

General Atomics (GA) has developed a plan for the utilization of vanadium alloys in the DIII–D tokamak. The plan is being implemented with the assistance of the Argonne, Oak Ridge, and Pacific Northwest National Laboratories (ANL, ORNL and PNNL), and will culminate in the operation of a water-cooled vanadium alloy structure in the DIII–D Radiative Divertor (RD) upgrade.[1,2] The use of a vanadium alloy will provide a meaningful step towards developing advanced materials for fusion power applications by 1) demonstrating the in-service behavior of a vanadium alloy (V-4Cr-4Ti) in a typical tokamak environment, and 2) developing knowledge and experience on the design, processing, and fabrication of full-scale vanadium alloy components.

The program currently consists of three phases: first, small vanadium alloy specimens and coupons are being exposed inside the DIII–D vacuum vessel to evaluate the effects of the DIII–D vacuum environment; second, a small vanadium alloy component will be designed, manufactured, and operated in conjunction with the existing DIII–D divertor; and third, the upper private flux baffle of the new double-null, slotted divertor will be designed, fabricated from vanadium alloy product forms, and installed in DIII–D. A major portion of the program is research and development to support fabrication and resolve key issues related to environmental effects. The plan is being carried out by GA as part of the DIII-D Program, and with the support of ANL, ORNL, and PNNL, participants in the Materials Program of the Department of Energy's Office of Fusion Energy (DOE/OFE).

2. PHASE 1: Specimen and Coupon Exposures and Analysis

Minature Charpy V-notch (CVN) impact and tensile specimens of V-4Cr-4Ti alloy (ANL 500 Kg heat)[3] were exposed/monitored in DIII–D in a position on the vessel wall behind the divertor baffle for ~9 months.[4] The maximum temperature experienced by the specimens during vacuum bakeouts was ~350°C. GA has collated the environmental data, and ANL has developed and is now implementing an analysis plan for the evaluation of the specimens.[5] CVN tests conducted at temperatures over the range of –196 to +150°C indicated ductile behavior for all test temperatures. Tensile tests conducted at ambient and elevated

temperatures indicated values similar to unexposed material. A new set of V-4Cr-4Ti alloy samples, installed during the January 1996 vent, is currently undergoing exposure to provide more data for confirmation and statistical verification.

In parallel to these exposures, additional V-4Cr-4Ti alloy samples underwent short-term exposures utilizing the DIII–D Divertor Material Exposure System (DiMES). A V-4Cr-4Ti alloy disc, and subsequently CVN specimens, were exposed/monitored during bakeout of the DIII–D vacuum vessel.[4] The maximum temperature experienced by the specimens during vacuum bakeouts was also ~350°C . GA has collated the environmental data, and ANL has developed and is now implementing an analysis plan to determine the pickup of any impurities in these specimens.[5] CVN tests conducted at temperatures over the range of –196 to +150°C have indicated ductile behavior for all temperatures. A surface analysis of the V-4Cr-4Ti alloy disc specimen has been completed at Sandia National Laboratory in Albuquerque, NM, and evaluation of that data is being performed at ANL. Other DiMES exposures of V-4Cr-4Ti alloy are being considered to evaluate the effects of other DIII–D environmental conditions (e.g., discharge cleaning, boronization, etc.).

3. PHASE 2: Small Component Exposure

A second step in the DIII–D Vanadium Plan is to install a small V-4Cr-4Ti alloy component in DIII–D. This component will be manufactured utilizing many of the methods proposed for the Phase 3 water-cooled private flux baffle. The component will be installed, exposed for some period of tokamak operations, and then removed. Samples from the component will be excised, and metallurgical analyses and property measurements will be made on the excised materials. Specific plans have not yet been defined.

4. PHASE 3: Radiative Divertor Program

The design, manufacture, and installation of a V-4Cr-4Ti alloy private flux baffle structure for the upper divertor of the RDP will be performed as the third phase of the vanadium alloy program. Details of the structural design of the toroidally-continuous, water-cooled and radiatively-cooled structural panels which make up the V-4Cr-4Ti alloy PFB were presented in a previous report.[6]

The water-cooled panels for the V-4Cr-4Ti alloy baffle will be fabricated of sandwich construction from two 4.8 mm sheets, each containing a wide 1.5 mm deep slot milled into its face to provide an internal coolant channel. Resistance seam welding is the primary candidate process being considered for structurally joining the panel edges, with electron beam welding proposed for making a leak-tight perimeter seal. Other methods of joining are proposed for different areas of the design such as the graphite armor tile attachment studs and cooling water inlet and outlet manifolds. To facilitate installation, V-4Cr-4Ti alloy/Inconel 625 joints are planned to provide a bi-metallic tube nipple. This component will be used to transition V-alloy water-cooled panels to Inconel 625 tubes which provide a cooling water supply.

A. Fabrication of Product Forms For The Radiative Divertor

Processing of the V-4Cr-4Ti alloy by WCA was initiated in September 1995. Prior to this reporting period, the alloy had been processed into a 1200 kg ingot, extruded into two (2) billets (A and B1), and machined/ground into sheet bar material. Details of these stages of the processing were presented in previous reports.[4,6]

During July 1996, full chemical analyses of the sheet bar materials, A and B1 (samples from both ends), were completed. The analyses for both materials were within specification limits except for Nb (87–92 ppm measured; <20 ppm specified), Ag (<1–3 ppm measured; <1 ppm specified), and Ca, Na, K, and Mg (<5 ppm, 1–3 ppm, 3–4 ppm, and <10 ppm, respectively, measured; <1 ppm specified for each), and were

accepted. The two pieces of sheet bar (10.4 cm × 23.4 cm × 245.1 cm and 107.4 cm, respectively) were heated to 400°C and longitudinally rolled into 4.7 cm thick × 23.4 cm wide plate (~540 cm and ~240 cm long, respectively). Plate from sheet bar A (Plate A) was cut into seven (7) 60.3 cm long sections, one (1) 67.3 cm long section, and one (1) 39.7 cm long section. Plate from sheet bar B1 (Plate B1) was cut into three (3) 60.3 cm long sections and one (1) 44.4 cm long section.

The ten (10) 60.3 cm long sections from both plates (designated A1, A2, A3, A5, A6, A7, A8, B1A, B1C, and B1D via their relative locations in the two plates) were cross-rolled after heating to 400°C, and succesively reduced to 4.8 mm thick × ~65 cm wide by ~185 cm long sheets. Several 400°C rolling cycles, with intermediate vacuum anneals of 2 hours at ~1050°C, were used. The sheets were then trimmed to ~59 cm wide × ~178 cm long, roller leveled after heating to 315°C, cleaned and pickled, and final vacuum annealed for 2 hours at 1000°C. The final annealing treatment was selected based on an annealing study performed at GA on edge trim material taken from one of the as-rolled sheets (sheet B1C). The GA study indicated that recrystallization of the material was complete after 1 to 2 hours at 1000°C, with a final grain size of ~ASTM 6–8. A metallographic analysis (at WCA) of samples taken from both ends of a full-length piece of edge trim material (from sheet A2), which was production annealed along with the ten sheets, indicated 98% recrystallization of the material, with a final average grain size of ASTM 8. Chemical analyses (for H, O, N, and C only) were performed on samples taken from each of the finished sheets. The values obtained were within specification limits except for O values for two sheets, B1C and B1D (400–410 ppm measured; <400 ppm specified), and were accepted. The values were close to the in-specification values obtained previously for extruded billet material, and were also within the accuracy of the analysis method relative to the specification limit for O.

The 67.3 m long section from Plate A (A4), taken from the middle of the sheet bar, was cut into several 4.7 cm × 4.7 cm x 67.3 cm long sections, and machined to a diameter of ~4 cm. This material was swaged after heating to 400°C and successively reduced to 11 mm diameter rod in several 400°C swageing cycles. Intermediate vacuum anneals of 2 hours at ~1050°C were used between swageing cycles. The rods were then cut into fifteen (15) 180 cm lengths, straightened, centerless ground to 10.1 mm diameter, cleaned and pickled, and final vacuum annealed for 2 hours at 1000°C. The final annealing treatment was again selected based on an annealing study performed at GA on a sample of as-swaged rod. The GA study indicated that complete recrystallization of the material, with a final grain size of ~ASTM 5–7, occurred at 1000°C after 1 to 2 hours. Metallographic analysis (at WCA) of samples taken from the ends of one representative production-annealed rod length indicated 95%–98% recrystallization of the material, with a final average grain size of ASTM 6. Chemical analyses (for H, O, N, and C only) were performed on samples taken from three (3) representative finished rod lengths. The values obtained were within specification limits except for O values for one rod sample (420 ppm measured; <400 ppm specified), and were accepted. Like those out-of specification values for sheet material, this value was also close to the in-specification values obtained previously for extruded billet material, and was also within the accuracy of the analysis method relative to the specification limit for O.

The finished sheet and rod product forms were received by GA from WCA in October 1996. Support will be provided by ANL and ORNL in the development of basic engineering design properties for these product forms.

B. Manufacturing Technology Development

As manufacturing development is a major focus of this project a significant amount of research and development is being performed in this area. The RD structure will require many metal/metal joints, and joining development is therefore a key area of study. GA is using private IR&D funds to complement welding efforts at ANL and ORNL, investigating several different joining processes which are attractive for

fabrication of RD components including resistance seam, friction, electron beam welding, and most recently, explosive bonding. The scope of the GA joining development efforts has been limited by the availability of material, some of which has been purchased from WCA (V-5Cr-5Ti; Heat ID #932394) and some of which has been supplied by ANL (V-5Cr-5Ti alloy; Heat ID #832394 and V-4Cr-4Ti alloy; Heat ID #832665[3]).

Resistance Welding Studies

Resistance seam welding studies in air are continuing to develop the method for structurally joining sheets of vanadium alloy together to make the water-cooled panels for the RDP.

As reported previously,[6] spot weld trials were performed on 4.8 mm thick V-5Cr-5Ti alloy sheet material producing diffusion bonds at the lowest power levels utilized and weld nuggets at higher power levels. Representative weld trial samples demonstrated considerable strength (~685 MPa based on weld nugget diameter only, and ~380 Mpa based on total bonded diameter, i.e., diffusion bond + weld nugget) in simple spot weld lap shear tests even though they typically contained single, small, centrally-located pores. The lower strength values reported (380 MPa) were still greater that that specified by American Welding Society standards for material of this strength level. Additional spot weld trials were performed on this material using increased electrode (forge) pressures at the end of the weld cycle in an attempt to minimize the previously-observed porosity. Although the porosity was not completely eliminated, it was substantially reduced.

Additional confirmatory spot weld trials have recently been performed on 4.8 mm thick V-4Cr-4Ti alloy sheet procured by GA for the DIII–D Radiative Divertor program. Using power settings similar to those utilized for the previous trials on V-5Cr-5Ti alloy, successful joints were also produced, again ranging from diffusion bonds to fully-melted weld nuggets. Single spot lap shear tests on welded joints demonstrated strengths which were similar to those developed previously for V-5Cr-5Ti alloy (~380 Mpa). In addition, room-temperature strengths obtained for diffusion-bonded samples, i.e., samples with no detectable melting at the faying surfaces, were observed to be substantially the same as for those which developed fully-melted nuggets, thus demonstrating that successful high strength spot weld joints in V-alloy could be obtained in air, and over a wide range of power levels (from diffusion bonds to welds).

Resistance seam (overlapping spots) welds were then performed on similar 4.8 mm V-4Cr-4Ti alloy sheet using copper alloy wheel electrodes and a variety of power settings, and electrode (wheel) pressures, wheel diameters, and wheel radii. Although full melting (i.e., nugget formation) was not achieved at the faying surfaces of the coupon samples, seam diffusion bonds (~5 to 10 mm in width) were obtained which exhibited room-temperature lap shear test strengths comparable to that achieved for similar spot-welded (and spot-bonded) material. A vacuum leak test of a sectioned ~75 mm (~30 overlapping spot welds) long seam-bonded sample indicated a helium leak rate of $<1 \times 10^{-11}$ std. cc/s, well below that required for DIII–D components. Attempts at producing fully-melted nuggets, i.e., welds, at the faying surfaces, by utilizing very high power inputs, resulted in some melting of the copper electrodes, infiltration of copper into the alloy, and surface cracking.

In addition to the resistance welding studies, preliminary tests have been completed to study the potential for stress corrosion cracking of vanadium alloy resistance welds in DIII–D cooling water. A potential for slow crack growth under static and dynamic loading conditions was identified for the crevice created between RD water-cooled panel plates via the structural resistance seam weld to be utilized during component fabrication. PNNL has performed several crack growth tests in DIII–D cooling water on specimens of V-4Cr-4Ti alloy (ANL 500 kg heat[3]) to investigate this potential issue.[7]

Typical operating conditions expected for the V-alloy RD component, including stress and temperature cycles, were provided to PNNL in order to select the type of test and test conditions to be imposed. Two room-temperature crack growth tests were performed on compact tension specimens exposed under a static load condition to DIII–D water. GA computer analyses/calculations indicated a very small stress intensity factor (~3 ksi-$\sqrt{in.}$) could be operable in the vicinity of a seam weld crevice, resulting from possible crevice-opening loads in this area (water pressure in the panel). Since very little extension of this crevice (flaw) was expected at this value based on the known behavior of similar materials, crack growth tests were performed at a stress intensity of 30 Ksi-$\sqrt{in.}$, a factor of ten times the calculated value. Two tests were conducted, one for 32 days and another for 60 days. No measurable crack growth was observed during either test. This result was confirmed by SEM analysis of fracture surfaces obtained after the specimens were rapidly broken in tension.

Friction Welding Studies

Two types of friction welding trials are in progress. Inertia (shop) and portable friction welding have been selected as candidate processes for joining vanadium alloy to itself, and inertia welding has been selected for creating a bi-metallic joint between vanadium alloy and Inconel 625. Initial rod-to-rod inertia weld trials of vanadium alloy (V-5Cr-5Ti alloy) bonded to itself, and to Inconel 625, were successful in air, without any protective environment. Metallography showed complete bonding with no indications of porosity or cracking, and mechanical tests at room temperature resulted in failures in material well away from the joint and HAZs.

As reported previously,[6] inertia weld trials were performed to fabricate bi-metallic V-5Cr-5Ti alloy/Inconel 625 joints in a butt joint configuration which could be machined into a bi-metallic tube nipple, a component which could be joined to a V-alloy water-cooled panel (via a controlled shop weld, e.g., electron beam welding) and subsequently to an Inconel 625 cooling water tube (via a field tungsten-inert gas weld). These trials, although encouraging, were not completely successful, producing joints which were not vacuum leak tight during helium leak checking and with variable strengths in room-temperature tensile tests (~70 to 380 MPa). Metallography of a typical sample revealed that bonding could be substantially enhanced by a modified joint configuration/design.

Additional trials were performed using the new joint configuration, and were successful. Metallography of a representative sample indicated complete bonding with no porosity. A number of representative trial samples were then machined for checking the vacuum leak tightness of the joints and their strengths. All samples were observed to be vacuum leak tight to DIII–D standards (down to 4.4×10^{-8} Torr) and exhibited strengths >~720 MPa in room-temperature tensile pull tests, with failures occurring in a ductile (tearing) mode in the V-alloy away from the joint. This strength level is considerably higher than the ultimate tensile strength of the V-alloy (~520 MPa), and is believed to result from a combination of increases in the strength of the V-alloy near the joint due to the heavily hot-worked structure (fine grain size) developed in this vicinity by the welding process, and the presence of the notch from the transition of the smaller diameter joint area to the larger diameter threaded region for the specimen grips.

As previously reported,[6] preliminary portable friction welding trials of vanadium alloy rod to plate were performed to develop methods of *in-situ* replacement of studs on water-cooled panels. Initial trials achieved substantial bonding, but the hardness of the weld interface increased significantly, signaling the development of a brittle joint. In addition, a large amount of grain growth occurred at the interface and substantial heat-affected zones (HAZs) were developed. It was also noted during the trials that the temperature of the weld interface was significantly higher than that observed in the inertia weld process, and the time to create the weld was considerably longer.

Additional friction welding trials were performed using parameters [higher ram (rod) pressures and ram rotational speeds] which were expected to minimze the excessive heat input observed in previous samples. As a starting point, welding (ram) pressures were selected to be similar to those previous used in successful rod-to-plate inertia (in-shop friction) welds of V-alloy,[4] and welding times were reduced to decrease the heat input to the joint and minimize the development of HAZs near the joint interface. Metallographic evaluation of selected samples from these trials indicated porosity-free bonding over ~100% of the contacting areas and thinner HAZs compared to previous trial samples. The HAZ thickness generally decreased with increased ram pressure for a given ram speed. A single room-temperature tensile pull test performed on a sample processed using an intermediate ram speed failed at or near the joint at a stress value of ~345 MPa, approximately equivalent to the tensile yield strength of the base V-alloy.

Electron Beam Welding Studies

Preliminary electron beam welding trials on 6.35 mm V-5Cr-5Ti alloy sheet have been completed, and were reported previously.[6]

Explosive Bonding Studies

Explosive bonding have been investigated as an alternate method for producing a dissimilar metal joint between V-alloy and Inconel 625 for application as a tube nipple/connector. This connector would be used to transition a V-alloy water-cooled RD panel to an Inconel 625 water supply tube. A lap joint for this tube-to-tube configuration may be more preferable for this application compared to the butt joint configuration developed by inertia welding because of its enhanced mechanical strength and potential for a longer (up to ~10 times) leak path between the cooling water inside the tube and the external vacuum environment of DIII–D.

A preliminary explosive bonding trial of a V-4Cr-4Ti alloy tube to an Inconel 625 round bar was performed. Dye penetrant inspection of specimens sectioned along the length of the ~150 mm long (22.1 mm o.d. × 2 mm wall tube) processed trial sample indicated good bonding and no interface porosity at the end opposite the explosive charge detonation end of the sample, and minimal bonding at the detonation end. Metallography of the sample confirmed that bonding (with no porosity) had been achieved over about 1/2 of the length of the sample, the interface between the V-4Cr-4Ti alloy and Inconel 625 along the length of the sample exhibiting the serrated structure typical of explosively-bonded metals. The joint was also leak tight, a helium leak check of a ~12 mm length section of the sample indicating a helium leak rate of $\sim 6 \times 10^{-10}$ std. cc/s, well below required DIII–D standards. Strength tests of the joint and additional bonding trials are planned. Complete bonding over the entire length of a trial sample is expected to be achievable by the addition of more explosive material on the outer surface of the V-4Cr-4Ti alloy tube.

CONCLUSIONS

A program for utilizing vanadium alloys in DIII–D has been developed to progress the deployment of low activation alloys for fusion applications, and production of material for this program has been completed. A 1200 kg V-4Cr-4Ti alloy ingot of acceptable chemical composition has been melted, extruded into rectangular billets, and processed into sheet and rod product forms. Preliminary successes have been achieved in developing similar and dissimilar metal welds in vanadium alloy by resistance, inertia, portable friction, and electron beam welding, and explosive bonding methods.

ACKNOWLEDGEMENTS

This is a report of work supported by the U.S. Department of Energy under Contract No. DE-AC03-89ER51114, and General Atomics under internal R&D funding.

REFERENCES

[1]J. P. Smith, W. R. Johnson, R. D. Stambaugh, P. W. Trester, D. Smith, and E. Bloom, "Vanadium Alloys For The Radiative Divertor Program of DIII–D," to be published in *Proc. of the 16th IEEE/NPSS Symposium on Fusion* Engineering, Champlain, Illinois, September 30 through October 5, 1995.

[2]J. P. Smith, W. R. Johnson, R. D. Stambaugh, P. W. Trester, D. Smith, and E. Bloom, "Utilization of Vanadium Alloys In The DIII–D Radiative Divertor Program," to be published in *Proc. of the 7th International Conf. on Fusion Reactor Materials* (ICFRM-7), Obninsk, Russia, September 25–29, 1995.

[3]H. M. Chung, H.--C. Tsai, D. L. Smith, R. Peterson, C. Curtis, C. Wojcik, and R. Kinney, "Fabrication of 500-kg Heat of V-4Cr-4Ti," in *Fusion Reactor Materials Semiannual Progress Report*, DOE/ER-0313/17, Oak Ridge National Laboratory, Oak Ridge, Tennessee (1994), p. 178–187.

[4]W. R. Johnson, J. P. Smith, and R. D. Stambaugh, "Production and Fabrication of Vanadium Alloys for the Radiative Divertor Program of DIII–D", in *Fusion Reactor Materials Semiannual Progress Report*, DOE/ER-0313/19, Oak Ridge National Laboratory, Oak Ridge, Tennessee (1995), p. 5–11.

[5]H. Tsai, D. L. Smith, W. R. Johnson, and J. P. Smith, "Performance of V-4Cr-4Ti Material Exposed to the DIII–D Tokamak Environment", to be published in *Fusion Reactor Materials Semiannual Progress Report*, DOE/ER-0313/21, Oak Ridge National Laboratory, Oak Ridge Tennessee (1997).

[6]R. J. Kurtz and W. R., "An Evaluation of the Susceptibility of V-4Cr-4Ti to Stress Corrosion Cracking in DIII–D Cooling Water", to be published in *Fusion Reactor Materials Semiannual Progress Report*, DOE/ER-0313/21, Oak Ridge National Laboratory, Oak Ridge Tennessee (1997).

[7]W. R. Johnson, J. P. Smith, and R. D. Stambaugh, "Production and Fabrication of Vanadium Alloys for the Radiative Divertor Program of DIII–D", in *Fusion Reactor Materials Semiannual Progress Report*, DOE/ER-0313/20, Oak Ridge National Laboratory, Oak Ridge, Tennessee (1996), p. 3–10.

PERFORMANCE OF V-4Cr-4Ti MATERIAL EXPOSED TO DIII-D TOKAMAK ENVIRONMENT -- H. Tsai, H. M. Chung, and D. L. Smith (Argonne National Laboratory), W. R. Johnson and J. P. Smith (General Atomics)

SUMMARY

Test specimens made with the 832665 heat of V-4Cr-4Ti alloy were exposed in the DIII-D tokamak environment to support the installation of components made of a V-4Cr-4Ti alloy in the radiative divertor of the DIII-D. Some of the tests were conducted with the Divertor Materials Evaluation System (DiMES) to study the short-term effects of postvent bakeout, when concentrations of gaseous impurities in the DIII-D chamber are the highest. Other specimens were mounted next to the chamber wall behind the divertor baffle plate, to study the effects of longer-term exposures. By design, none of the specimens directly interacted with the plasma. Preliminary results from testing the exposed specimens indicate only minor degradation of mechanical properties. Additional testing and microstructural characterization are in progress.

OBJECTIVE

In service, V-4Cr-4Ti divertor components in the DIII-D vessel will be exposed to a range of temperature and impurity conditions and to alternating vacuum/low-pressure hydrogen plasma operation, thermal cycles, periodic bakeout, glow-discharge cleaning with helium, periodic boron coating, and occasional re-exposure to air during vents for maintenance. The objective of this task is to determine the effects of these environmental exposures on the performance of the vanadium alloy material. It is particularly important to determine whether interstitial impurities are absorbed sufficiently to lead to material embrittlement.

TEST RESULTS

To date, three experiments (D1, D2, and W1) have been completed. Another experiment, W2, is still ongoing. The D1 and D2 experiments were conducted with the DiMES,[1] a device located below the vessel floor that, when extended, allows the specimen mounted on it to be inserted into the plasma chamber without disturbing the system vacuum. The specimens for experiments W1 and W2, on the other hand, were mounted on a bracket next to the vessel wall behind the divertor baffle plate (i.e., nonplasma-facing). Because loading and unloading the specimens require a manned entry, which is possible only during an air vent, their exposures encompass full DIII-D operating cycles.

D1 Experiment

The specimen for the D1 experiment, a polished disk 33.0 mm in diam. and 3.8 mm thick, was exposed to the vessel atmosphere during bakeouts on April 1, 9, 15, and 16, 1995, following air (dirty) vents on March 28 and April 5, 1995 and a nitrogen (clean) vent on April 11, 1995. The exposure conditions, as determined by infrared camera and residual gas analyzer (RGA), are summarized in Table 1. In each of the four bakeouts, the duration at temperature was ≈5-10 h. Temperatures measured by the infrared camera tracked with the average vessel temperature (the mean of the inner vessel and outer vessel wall temperatures). During the experiment, the sample surface was recessed ≈3.8 mm below the DIII-D graphite tile floor.

The exposed area of the disk exhibited a slight loss of luster (dulling). Surface hydrogen analyses were conducted by following an elastic recoil diffraction technique with a 2.6-

MeV ^{4}He beam for both the front (i.e., exposed) and back sides of the disk. The measurements showed pronounced surface peaks of hydrogen: ≈25,000 appm for the front and ≈65,000 appm for the back. The concentration profiles for both sides, however, decreased rapidly with depth within the first ≈0.1μm. At a depth of ≈0.45 μm, the approximate limit of beam penetration, the concentration profiles appear to have reached an asymptote of ≈7,000 appm for both sides. The fact that hydrogen concentration is greater on the back side suggests that the high surface readings may be a storage or handling artifact unrelated to the actual DIII-D exposure. Additional analyses, including bulk hydrogen analysis (by outgassing) and microhardness measurements, are planned to evaluate the extent and effect of bulk hydrogen uptake. Also to be conducted are Auger microprobe analyses for oxygen, carbon, and boron impurities to a depth of ≈5 μm for comparison with nonexposed sibling data.

Table 1. Partial pressure of gaseous impurities during the bakeouts in the D1 experiment. All values are peak readings.

			Partial Pressure (10^{-9} atm)			
Bakeout Date	Temp. (°C)	Pressure (torr)	H_2O	N_2	CO	O_2
4/1/95	250	4.6×10^{-4}	490	0.016	80	3.1
4/9/95	150	1.1×10^{-3}	1400	0.018	30	3.5
4/15/95	325	2.6×10^{-4}	240	0.013	64	2.6
4/16/95	325	6.2×10^{-5}	67	0.003	11	0.63

D2 Experiment

In the D2 experiment, five miniature Charpy impact specimens were exposed to the DIII-D tokamak environment with the DiMES during a single bakeout that followed a clean vent on June 6, 1995. The vent, for diagnostics repairs, lasted 35 days. The exposure conditions, as determined from measured inner and outer vessel wall temperatures and RGA measurements, are summarized in Table 2. The specimens were 1/3-size (3.3 x 3.3 x 25.4 mm) and contained a 0.6 mm-deep, 30° blunt notch with a root radius of 0.08 mm. The crack plane direction was perpendicular to the rolling direction and through the thickness of the plate from which the specimens were prepared. After machining, the specimens were vacuum-annealed at 1000°C for 1.0 h in a pure Ti foil wrap, which acted as an impurity getter. The vacuum, produced by a diffusion pump with a cold trap, was ≈10^{-6} torr during the annealing.

Table 2. Partial pressure of gaseous impurities during the bakeout in the D2 experiment. All values are peak readings.

			Partial Pressurse (10^{-9} atm)			
Bakeout Date	Temp. (°C)	Pressure (torr)	H_2O	N_2	CO	O_2
7/13/95	250	5.5 x 10-5	31	0.33	2.4	0.08

Four of the specimens were impact-tested, one each at -190, -150, 23 and 150°C. Preliminary results, shown in Fig. 1, reveal that the exposed specimens were ductile over

the entire test temperature range and that the ductile-brittle transition temperature (DBTT) was below the lowest test temperature, which was -190°C. In the lower temperature range, the measured upper-shelf energies agree closely with available nonexposed sibling data, also shown Fig. 1. (The sibling data were obtained with specimens prepared and annealed under conditions that were identical as to those used for the test specimens.) In the above-room-temperature range, however, there appears to be a decrease in the upper-shelf energy of the test specimens. The cause of this decrease is currently not known, although data scatter cannot be ruled out. To better define the upper-shelf energy curves, additional tests with sibling specimens and with the remaining exposed specimen are planned during the next reporting period. Also to be completed are bulk hydrogen analysis and microstructural/chemical characterization of both the exposed and fracture surfaces.

W1 Experiment

In the W1 experiment, five Charpy and five tensile specimens were exposed to the DIII-D environment for an entire DIII-D operation cycle, from February through December 1995. The configuration of the Charpy specimens was the same as the configuration of the specimens in the D2 test. The tensile specimens were 25.4 mm long and had a gauge section of 7.62 mm(length) x 1.52 mm(width) x 0.76 mm(thickness). The long direction of the gauge section was parallel to the final rolling direction of the plate from which the tensile specimens were machined. All specimens were annealed in an ion-pumped vacuum at 1000°C for 1.0 h prior to the test. For the exposure, the specimens were held in a frame mounted on the vessel wall behind the divertor baffle plate. The temperatures of the specimens were measured with four thermocouples attached to the ends of the specimens.

The specimens were installed in DIII-D after a dirty vent which was initiated on February 14, 1995, and were removed after a dirty vent on December 15, 1995. During this time period the specimens were exposed for a total of 265 days to a complete range of DIII-D operating conditions including dirty and clean vessel vents, elevated-temperature bakeouts, helium glow discharge cleanings, boronizations of the first wall (graphite tiles), and plasma operations. In their positions behind the DIII-D divertor, the specimens would be expected to have been most affected only by those DIII-D operations for which the specimens would have been heated to elevated temperatures and at which the greatest interactions with gaseous impurities in the DIII-D environment might be expected. These operations include the elevated-temperature bakeouts and boronizations. Based on the specimen thermocouple data, the temperatures of the specimens tracked with the measured outside vessel wall temperature, and reached values in the range of ~150 to 330°C during bakeouts and ~250 to 280°C during boronizations. Analysis of the RGA monitoring data obtained during the exposure period indicated that the specimens were exposed to impurities in the DIII-D environment which generally ranged, depending on the type of vent, between those indicated in Tables 1 and 2. A summary of the various vents and bakeouts experienced by the specimens is presented in Table 3.

Table 3. DIII-D environment history for the W1 experiment - February 14 to December 15, 1995.

Air Vents	N_2 Vents	150°C Bakeouts	200-250°C Bakeouts	280-350°C Bakeouts	280°C Boronizations
		4-6 h	2-7 h	5-20 h	5.5 h
5	5	2	3	20	2

Tensile tests have been conducted on two of the five specimens: one at room temperature in air and the other at 350°C in argon. Strain rate for both tests was 1.1 x 10^{-3}/s. The results, summarized in Table 4 along with the nonexposed sibling data, indicate that DIII-D exposure produced no appreciable changes in either strength or ductility.

Four of the five Charpy specimens have been tested, one each at -190, -150, 23, and 150°C. The results are shown in Fig. 2, along with sibling data obtained from specimens prepared and annealed under identical conditions.[2] All specimens were ductile over the entire temperature range. But again, their upper-shelf energies seem to be lower than those of the nonexposed siblingse

Table 4. Tensile properties of specimens exposed in the W1 experiment in DIII-D (YS:0.2% offset yield stress; UTS: engineering ultimate tensile stress; US: uniform elongation; TE: total elongation.)

	25°		350°	
Test Temp. (°C)	DIII-D	Control	DIII-D	Control
YS (Mpa)	334	357	421	205
UTS (Mpa)	449	428	377	359
UE (%)	19.0	19.1	14.8	17.6
TE (%)	27.0	29.2	22.0	25.4

FUTURE ACTIVITIES

Additional testing and examination of the discharged specimens from the D1, D2, and W1 experiments will be completed to elucidate the possible effects of impurity uptake, particularly the effects of hydrogen. Testing will commence for the W2 specimens once the exposure is completed.

ACKNOWLEDGMENTS

The authors thank the DIII-D staff at General Atomics for conducting the experiments, W. R. Wampler and D. Walsh (Sandia National Laboratory) for conducting the hydrogen analysis of the D1 sample, and L. Nowicki and H. Chung (Argonne National Laboratory) for mechanical testing of the D2 and W1 specimens.

REFERENCES

1. Wang, C. P. C., et al., "Divertor Materials Evaluation System at DIII-D," Journal of Nuclear Materials, 196-198 (1992), pp-871-875.

2. H. M. Chung, L. Nowicki, and D. L. Smith, "Effect of Annealing on Impact Properties of Production-Scale Heat of V-4Cr-4Ti," Fusion Reactor Materials Semiannual Progress Report for Period Ending March 31, 1995, DOE/ER-0313/18, pp.273-278.

Fig. 1. Charpy impact data for D2 experiment specimens exposed in DIII-D, showing ductile behavior even at ≈-190°C. Triangles denote nonexposed sibling data.

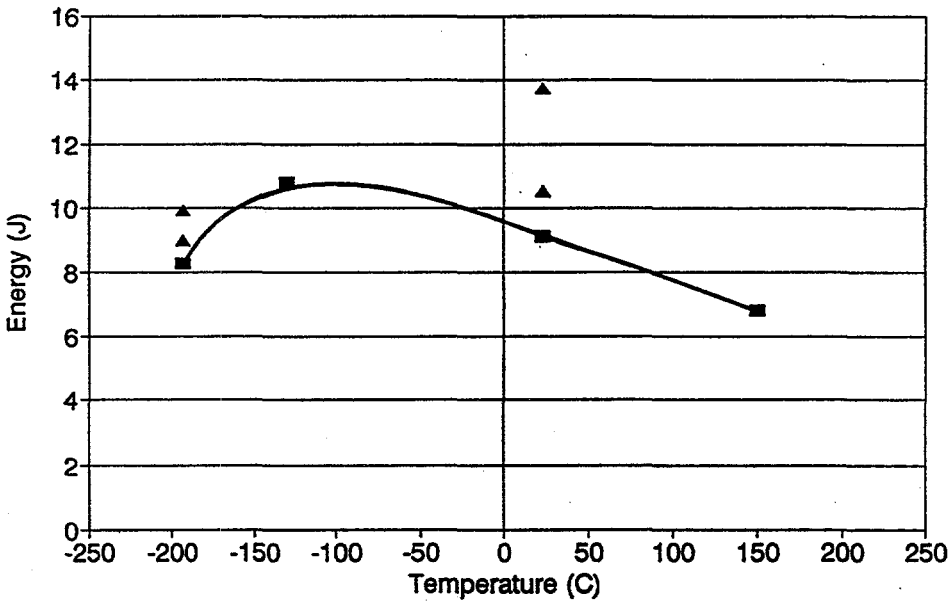

Fig. 2. Charpy impact data for W1 experiment specimens exposed in the DIII-D, showing ductile behavior even at ≈-190°C. Shelf energies, however, are not as high as those of nonexposed siblings (triangles).

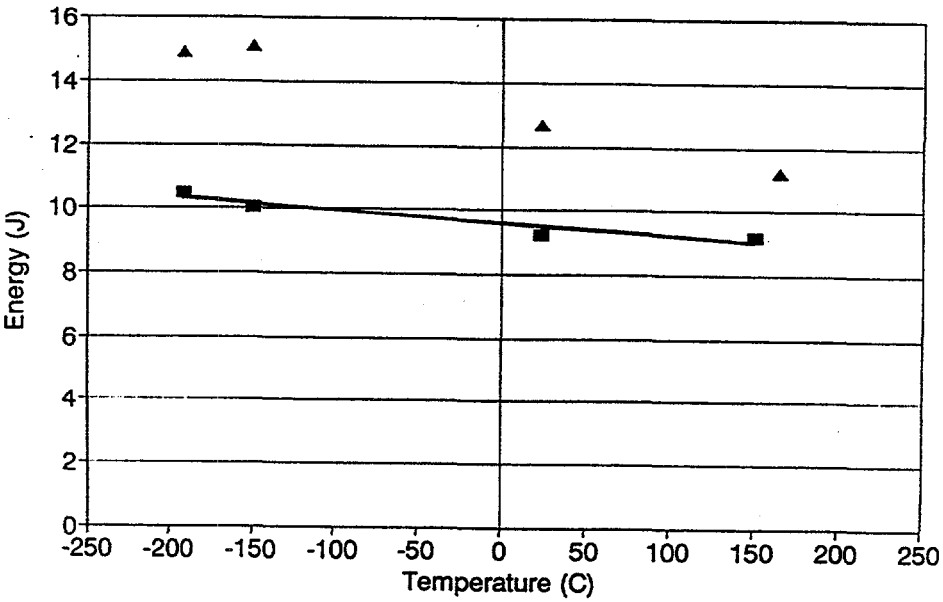

ELECTRICAL RESISTIVITY OF V-Cr-Ti ALLOYS — S. J. Zinkle, A. N. Gubbi, and W. S. Eatherly (Oak Ridge National Laboratory)

OBJECTIVE

The objective of this report is to summarize electrical resistivity measurements on vanadium alloys containing 3-6% Cr and 3-6% Ti.

SUMMARY

Room temperature electrical resistivity measurements have been performed on vanadium alloys containing 3-6%Cr and 3-6%Ti in order to evaluate the microstructural stability of these alloys. A nonlinear dependence on Cr and Ti concentration was observed, which suggests that either short range ordering or solute precipitation (perhaps in concert with interstitial solute clustering) has occurred in V-6Cr-6Ti.

PROGRESS AND STATUS

Introduction

Vanadium alloys with solute contents near 4% Cr and 4% Ti are being considered for fusion energy structural applications. The microstructure of these alloys has been characterized as a solid solution bcc phase, with a moderate density of Ti-rich precipitates that are associated with O,C,N interstitial impurities [1-3]. Phase stability studies on V-Ti alloys have reported conflicting results regarding the possible existence of a miscibility gap [4-6]. If such a miscibility gap was present, then precipitation of alpha-titanium would be energetically favorable in alloys containing more than ~5-10%Ti at temperatures below ~500°C, although the kinetics of the precipitation would be very slow. Recent ultrasonic acoustic measurements suggest that there may be periodic compositional fluctuations in V-(4-10%)Cr-(4-10%)Ti alloys [7]. It would be anticipated that radiation enhanced diffusion would accelerate phase decomposition during neutron irradiation, which might cause a degradation in the ductility of the alloy. In the present study, we have employed electrical resistivity measurements to investigate the phase stability of V-(3-6%)Cr-(3-6%)Ti alloys following various thermomechanical treatments.

Experimental Procedure

The electrical resistivity measurements were performed on type SS-3 sheet tensile specimens with nominal gage dimensions of 0.76x1.52x7.6 mm and an overall length of 25.4 mm. Sheet tensile specimens of V-3%Cr-3%Ti (heat T91), V-6%Cr-3%Ti (heat T92), V-5%Cr-5%Ti (heat T87), and V-6%Cr-6%Ti (heat T90) were punched or electro-discharge machined from 0.76 mm thick sheets from several 15 kg vanadium alloy heats fabricated by Teledyne Wah Chang, Albany, Oregon (TWCA). The V-4%Cr-4%Ti tensile specimens were either punched from 0.76 mm sheet which was cold rolled at ORNL from 1.0 mm thick sheet received as part of a 500 kg heat from TWCA (heat #832665), or else electro-discharge machined from the 1.0 mm sheet. Several specimens were annealed for 2 h at temperatures ranging from 900 to 1100°C (furnace cool) in a vacuum better than $1x10^{-6}$ torr ($<10^{-4}$ Pa). The chemical composition of the alloys (for solute contents >20 wt. ppm) is summarized in Table 1 [8].

Four-point probe electrical resistivity measurements were performed on the SS-3 tensile specimens following the general recommendations summarized in ASTM Standard Method of Test for Resistivity of Electrical Conductor Materials, ASTM B193-87 (reapproved 1992). The distance between the

Table 1. Chemical composition (at. ppm unless indicated otherwise) of the solutes and major impurities in the vanadium alloys examined in this study [8].

Element	V-3Cr-3Ti (T91)	V-6Cr-3Ti (T92)	V-4Cr-4Ti (832665)	V-5Cr-5Ti (T87)	V-6Cr-6Ti (T90)
Cr	2.86 at.%	5.92 at.%	3.68 at.%	4.70 at.%	5.62 at.%
Ti	3.25 at.%	3.18 at.%	4.15 at.%	5.3 at.%	6.35 at.%
C	510	440	340	470	440
N	220	340	310	320	310
O	730	890	990	1210	800
Al	380	480	300	300	440
Si	1710	1730	1420	990	1740
Fe	120	150	200	150	180
Cu	66	110	—	62	44
Mo	200	200	—	270	180

spring-loaded voltage contacts was 7.10 mm. The temperature was recorded for each measurement and the resistivity data were corrected to a reference temperature of 20°C using the V-Cr-Ti temperature coefficient for resistivity of $d\rho/dT = 0.75$ nΩ-m/K [9-13]. A Keithley 237 Source Measure Unit was used to supply a constant current of 100 mA, and the voltage drop was measured with a Keithley 182 Sensitive Digital Voltmeter equipped with a low thermal connector cable. Thermal emf offset potentials were subtracted using the "relative reading" offset function on the Keithley 182. The specimen thickness and width were measured to a nominal accuracy of ±1 μm in two different gage locations with a Mitotoyo precision digital micrometer in order to convert the resistance measurements to resistivity values. Nonuniformities in the width and thickness in the specimen gage region caused the typical experimental uncertainty of individual resistivity measurements to be ±0.5%. A minimum of two different unirradiated specimens were tested for each thermomechanical condition.

Results and Discussion

Table 2 summarizes the results of the electrical resistivity measurements. A moderate scatter in the resistivity data (±5 nΩ-m) was obtained from different lots of specimens machined from a given heat that were given nominally identical heat treatments, which suggests that there may be some slight inhomogeneities in the chemical composition at different positions within each alloy heat. The resistivity data did not exhibit any systematic dependence on heat treatment (900-1100°C) or cold-work level (0-24%), partly because of the aforementioned variability of resistivity data obtained from different specimen lots in the same alloy heat. A previous study reported that a cold work level of 16% produced a resistivity increase of ~3.5 nΩ-m in vanadium [14]. Therefore, a significantly higher resistivity would have been expected for the 24% cold-worked specimens compared to the annealed specimens in this study.

Table 2. Summary of electrical resistivity measurements, including standard error of the mean.

V-3Cr-3Ti	V-4Cr-4Ti	V-6Cr-3Ti	V-5Cr-5Ti	V-6Cr-6Ti
276.8 ±1.5 nΩ-m (11 specimens)	285.4 ±0.5 nΩ-m (66 specimens)	281.1 ±1.3 nΩ-m (8 specimens)	304.4 ±0.8 nΩ-m (10 specimens)	302.0 ±1.1 nΩ-m (11 specimens)

Table 3. Summary of vanadium electrical resistivity literature.

	Resistivity	Reference
Pure Vanadium		
base resistivity	ρ_V=196 nΩ-m	[9-12]
temperature coefficient	$d\rho_V/dT$=0.75 nΩ-m/K	[9-12]
dislocation resistivity	$\Delta\rho_d$=3.5 nΩ-m for 16%CW	[14]
Solutes		
Ti	$\rho_{Ti}\geq$15.5 nΩ-m/at.%Ti	[10]
Cr	ρ_{Cr}=4.0 nΩ-m/at.%Cr	[13]
H	ρ_H~10 nΩ-m/at.%H	[15,16]
O	ρ_O=52 nΩ-m/at.%O	[17,18]
N	ρ_N=50 nΩ-m/at.%N	[17]
C	ρ_C~90 nΩ-m/at.%C	[19]
Mo	ρ_{Mo}~5 nΩ-m/at.%Mo	[20]
W	ρ_W~3 nΩ-m/at.%W	[20,21]
Ta	ρ_{Ta}=13 nΩ-m/at.%Ta	[22]
Re	$\rho_{Re}\geq$10 nΩ-m/at.%Re	[23]
Nb	ρ_{Nb}~8 nΩ-m/at.%Nb	[21]

Table 4. Calculated resistivity contributions (nΩ-m) from solute atoms in the vanadium alloys.

Element	V-3Cr-3Ti	V-6Cr-3Ti	V-4Cr-4Ti	V-5Cr-5Ti	V-6Cr-6Ti
V	196	196	196	196	196
Cr	11.4	23.7	14.7	18.8	22.5
Ti	52.0	50.9	66.4	84.8	101.6
O,C,N	9.5	10.3	9.8	12.1	9.7
Al,Si,Fe,Cu,Mo	2.4	2.6	2.4	1.6	2.5
Total	271.3	283.5	289.3	313.3	332.3

The resistivity increased with increasing Cr and Ti solute content, with Ti exerting a stronger influence than Cr on an atom percent basis. The measured resistivity values were compared with the resistivities calculated from Matthiessen's rule

$$\rho=\rho_V + \rho_{Cr}\bullet X_{Cr} + \rho_{Ti}\bullet X_{Ti} + \rho_C\bullet X_C + \rho_N\bullet X_N + \ldots \quad (1)$$

where ρ_V is the resistivity of pure vanadium (196 nΩ-m) [9-12] and ρ_i and X_i are the specific resistivity (nΩ-m/at.%) and atomic concentration of the *ith* solute species. The calculations used experimental specific resistivities that have been measured for various solute atoms in vanadium, as summarized in Table 3. The resistivities of the Al,Si,Fe,Cu, and Mo solutes were assumed to be ~10 nΩ-m/at.%, based on data for W, Ta, Re and Nb solutes in vanadium [20-23]. The results of the calculation are shown in Table 4. In all of the alloys, Ti had the largest solute contribution to the calculated resistivity.

Figure 1 compares the measured and calculated electrical resistivities of the five alloys. The experimental and calculated values are in good agreement (<2% difference) for V-3%Cr-3%Ti, V-6%Cr-3%Ti and V-4%Cr-4%Ti. On the other hand, the measured resistivities for the V-5%Cr-5%Ti and V-6%Cr-6%Ti alloys were significantly lower than the calculated values. The data for all of the alloys except for V-6%Cr-6%Ti could be equally well fitted by a Matthiessen equation consisting of an effective base vanadium resistivity of 215 nΩ-m and lower specific resistivities for Cr and Ti solutes compared to the literature values. This

suggests that a resistivity component associated with a moderate amount of chemical ordering or precipitation (e.g., Ti(O,C,N) precipitates) may be present in all of the alloys. The large discrepancy for the V-6%Cr-6%Ti alloy, where the measured resistivity was 10% less than the calculated value, suggests that a more pronounced chemical ordering or precipitation process may be occurring for the alloys containing 5-6% Ti. It should be noted that the measured resistivity in the V-6%Cr-6%Ti alloy was less than that for the V-5%Cr-5%Ti alloy.

As noted in the introduction, a previous study has reported the existence of a miscibility gap in binary V-Ti alloys [5]. Conversely, another study refuted the existence of the miscibility gap [6]. The nonlinear dependence of the resistivity in the present study (particularly for V-5-6%Cr-5-6%Ti alloys) is evidence for some type of phase instability, but further microstructural work is needed to investigate this issue. X-ray diffraction studies on these alloys are currently in progress, and the results will be summarized in the next reporting period.

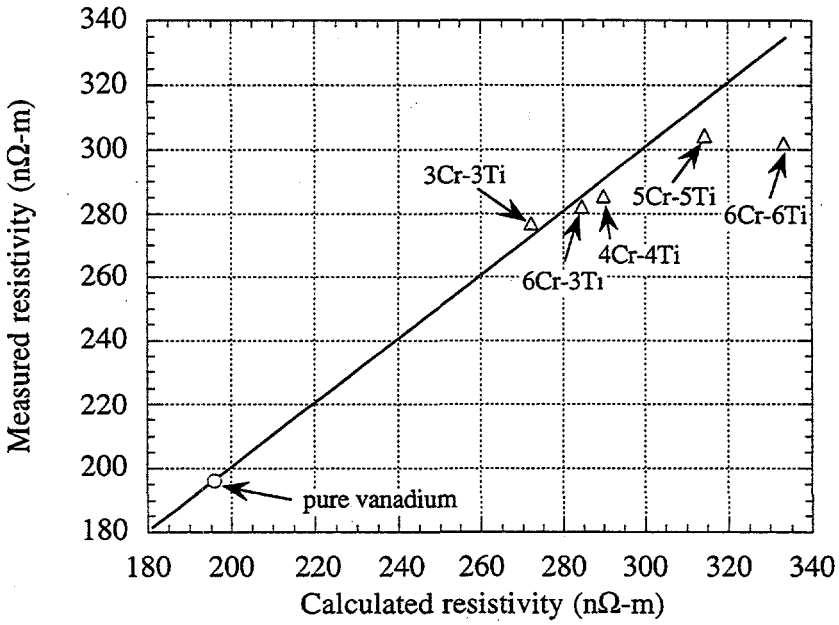

Fig. 1. Comparison of measured and calculated electrical resistivity for the 5 vanadium alloys.

References

[1] T. Schober and D.N. Braski, Metall. Trans. A 20 (1989) 1927.
[2] H.M. Chung, L.J. Nowicki, and D.L. Smith, in Fusion Reactor Materials Semiannual Progress Report for Period ending September 30, 1991, DOE/ER-0313/11 (Oak Ridge National Lab, 1991) p. 215.
[3] M. Satou and H.M. Chung, in Fusion Reactor Materials Semiannual Progress Report for Period ending September 30, 1992, DOE/ER-0313/13 (Oak Ridge National Lab, 1992) p. 227.
[4] M. Enomoto, Journal of Phase Equilibria 13 (1992) 195.
[5] O. Nakano, H. Sasano, T. Suzuki and H. Kimura, in Titanium '80 (Proc. 4th Int. Conf. on Titanium) vol. 2, eds. H. Kimura and O. Izumi , 1980) p. 2889.
[6] F. Wei and H.M. Flower, Mater. Sci. Technol. 5 (1989) 1172.

[7] V.M. Chernov, personal communication.
[8] A.N. Gubbi, A.F. Rowcliffe, and W.S. Eatherly, in Fusion Materials Semiannual Progress Report for Period ending March 31, 1995, DOE/ER-0313/18 (Oak Ridge National Lab, 1995) p. 187.
[9] G.T. Meadon, Electrical resistance of metals (Plenum, New York, 1965).
[10] E.W. Collings, Phys. Rev. B 9 (1970) 3989.
[11] B.N. Aleksandrov et al., Sov. J. Low Temperature Phys. 1 (1975) 1904.
[12] V.E. Peletskii, High Temperature 16 (1978) 57.
[13] A. Giannuzzi, H. Tomaschke, and K. Schroeder, Philos. Mag. 21 (1970) 479.
[14] M. Eto and M. Narutani, J. Mater. Sci. Lett. 9 (1974) 1902.
[15] E. Lang and J. Bressers, Z. Metallkde. 67 (1976) 66.
[16] H.P. Bleichert, Kernforschungsanlage Jülich, Jülich, Germany Report Jül-2005 (1985).
[17] G. Hörz, Z. Metallkde. 61 (1970) 371.
[18] E. Lang and J. Bressers, Z. Metallkde. 66 (1975) 619.
[19] J.T. Stanley, J.M. Williams, W.E. Brundage, and M.S. Wechsler, Acta Metall. 20 (1972) 191.
[20] I.P. Druzhinina, A.A. Fraktovnikova, and T.M. Vladimirskaya, High Temperature 14 (1976) 200.
[21] M.V. Vedernikov, V.G. Dvunitkin, and A. Zhumagulov, Sov. Phys. Solid State 20 (1978) 1904.
[22] N.A. Chernoplekov et al., Phys. Met. Metallogr. 36 (1973) 72.
[23] I.P. Druzhinina, A.A. Fraktovnikova, and T.M. Vladimirskaya, High Temperature 14 (1976) 579.

DYNAMIC FINITE ELEMENT ANALYSIS OF THIRD SIZE CHARPY SPECIMENS OF V-4Cr-4Ti - M. R. Lansberry (University of Missouri-Rolla), R. J. Kurtz (Pacific Northwest National Laboratory), A. S. Kumar (University of Missouri-Rolla), and G. E. Mueller (University of Missouri-Rolla)

OBJECTIVE

The objective of this analysis is to accurately model the behavior of one third size Charpy V-notched (CVN) and fatigue precracked specimens of V-4Cr-4Ti alloys using the dynamic finite element analysis code, ABAQUS / Explicit v5.4 [1].

SUMMARY

A 2-D finite element analysis was performed on precracked, one third scale CVN specimens to investigate the sensitivity of model results to key material parameters such as yield strength, failure strain and work hardening characteristics. Calculations were carried out at temperatures of -196°C and 50°C. The dynamic finite element analyses were conducted using ABAQUS / Explicit v5.4. The finite element results were compared to experimental results [2] for the production-scale heat of V-4Cr-4Ti (ANL Heat #832665) as a benchmark. Agreement between the finite element model and experimental data was very good at -196°C, whereas at 50°C the model predicted a slightly lower absorbed energy than actually measured.

INTRODUCTION

Recent work on A533B pressure vessel steel has indicated that finite element analysis (FEA) can be used to predict the upper shelf energy of precracked, full size CVN specimens using data obtained from subsize specimens to calibrate the model [3]. Furthermore, FEA may also be used to validate empirical correlations for size effects between CVN specimens of various sizes (fracture volume--$(Bb)^{3/2}$, etc.) [3]. A similar analysis will be performed for V-4Cr-4Ti, a possible fusion power system first wall structural material. A first step in predicting size effects for V-4Cr-Ti is the establishment of a reliable and accurate material model for use in the FEA.

ANALYSIS PROCEDURE

Tensile test data was obtained from the University of California at Santa Barbara [4] on the production-scale heat of V-4Cr-4Ti (ANL Heat #832665). Initially in load-displacement format, data at -196°C and 50°C were converted to true stress-true strain format. A plot of these data is shown in Figure 1. Note the usual yield drop exhibited by bcc metals has been suppressed in this plot.

Since the reduction of area was not measured throughout the tensile test, the curves are only valid up to the ultimate tensile strength of the material. In order to better simulate material behavior during a Charpy impact test, load-displacement data collected at the highest possible strain rate were selected for the FEA. For the 50°C case, the strain rate was 2 s^{-1} while at -196°C, a lower strain rate of 0.02 s^{-1} was used due to high scatter in the 2 s^{-1} strain rate data.

In the ABAQUS / Explicit dynamic fracture mechanics code, material properties play a key role. In Charpy impact studies, for example, the energy absorbed by the material is directly related to the area under the true stress-true strain curve. To achieve an accurate model of such a test, one could simply use point-to-point data as input. Although ABAQUS / Explicit allows this approach, limitations in the material failure criteria require the use of a user defined failure model. In this case, the true stress-

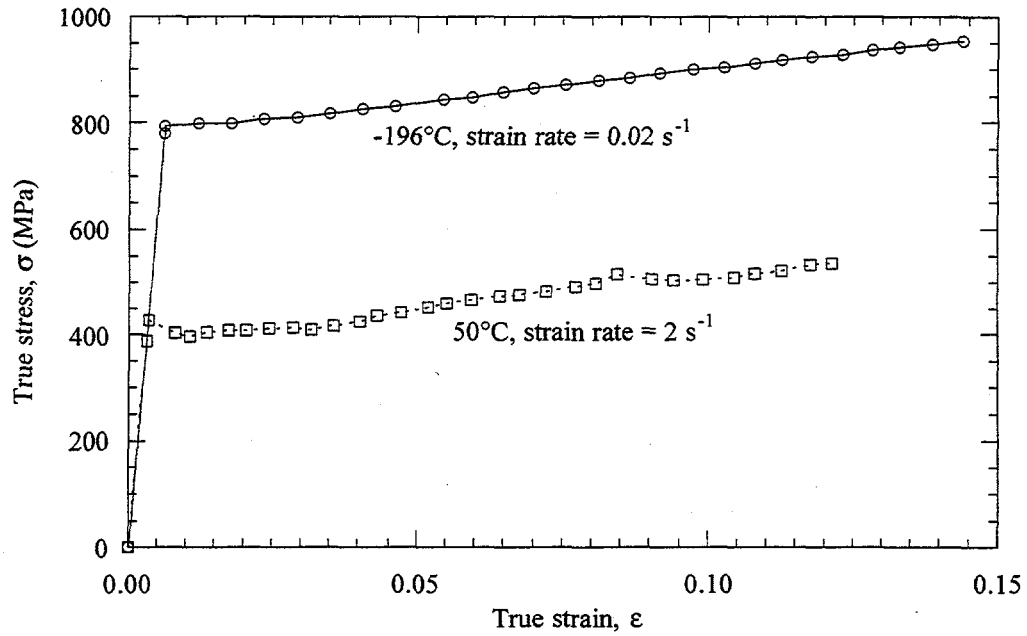

Figure 1 True stress - true strain curves for V-4Cr-4Ti derived from UC Santa Barbara tensile dat

true strain data is approximated by a bilinear curve. The general approach is highlighted in Figure 2. As noted in Figure 2, several material properties are required for the bilinear approximation. These include the following Young's modulus, tensile yield strength, Poisson's ratio, hardening modulus (a linear approximation of the work hardening rate), offset failure strain, and the true failure strain.

The Young's modulus and 0.2% yield strength are used to fully describe the elastic region of the true stress-strain curve. In the model, the onset of plastic deformation begins when the elastic limit is exceeded. As plastic deformation of the specimen increases, the metal strain hardens so that the load required to extend the specimen increases with further straining. In order to describe this behavior, the true stress-true strain curve in the plastic region may be approximated by a straight line with a slope denoted as the hardening modulus. This linear behavior continues up to the offset failure strain (ε_{ofs}) of the material. The offset failure strain represents the point at which the material **begins** to fail and is slightly less than the true failure strain. The material then unloads gradually to zero until the true failure strain (ε_{fs}) is reached. This gradual decline is necessary since an instantaneous drop produces unstable solutions within ABAQUS / Explicit [3]. In general, stable solutions were found to occur when the offset failure strain was approximately 5-10% below the true failure strain. A summary of the material properties used in the FEA for both the -196°C and 50°C cases is given in Table 1.

As noted in Table 1, both the hardening modulus and true failure strain of V-4Cr-4Ti were allowed to vary in a number of cases. Using this approach, the effect of both the hardening modulus and the true failure strain on the Charpy impact absorbed energy could be investigated at different temperatures.

ABAQUS / Explicit was used to analyze a 2-D finite element model of a precracked third size CVN specimen (3.33 mm x 3.33 mm x 25.4 mm). For all cases, the Charpy specimen was precracked to half width (1.665 mm). The finite element model consisted of a very fine mesh with a total of 4,000

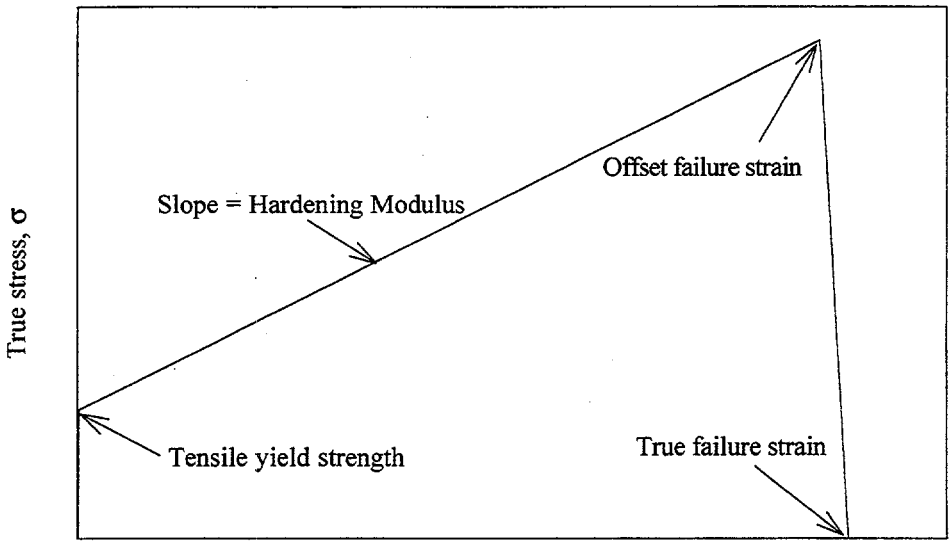

Figure 2 Model true stress - true strain curve for V-4Cr-4Ti

elements making up the Charpy specimen. The striker and anvil were ideally modeled as rigid bodies (i.e., no deformation). As a result, the total energy absorbed by the system was concentrated in the Charpy specimen.

Table 1: V-4Cr-4Ti material properties used in finite element modeling.

Temperature (°C)	Young's Modulus (GPa)	0.2% Yield Strength[4] (MPa)	Poisson's Ratio[5]*	Hardening Modulus (GPa)	Offset Failure Strain	True Failure Strain
-196	127.3	779.3	0.321	variable	ε_{fs} - 0.10	variable
50	124.9	387.4	0.355	variable	ε_{fs} - 0.10	variable

* Values were calculated based on the Young's modulus and shear modulus

RESULTS AND DISCUSSION

Argonne National Laboratory (ANL) conducted several Charpy impact tests on both blunt notch and precracked CVN specimens over a wide temperature range [2]. Table 2 summarizes the results of the precracked CVN cases for the production-scale heat of V-4Cr-4Ti. These values were used to benchmark the finite element results.

Normalized energy was calculated based on a fracture volume of $(Bb)^{3/2}$ where B is the thickness of the Charpy specimen and b is the ligament size (= 3.33 mm - Average Crack Length). This method of reporting absorbed energies is recommended per ASTM E23-94b (Standard Test Methods for Notched Bar Impact Testing of Metallic Materials) [6]. Since the finite element model was precracked to half

width in all cases, results from the finite element analyses were normalized to the average crack length values given above to correct for the difference in precrack length. Only the absorbed energies of the finite element model and the ANL experimental data were compared. Finally, results quoted for 50°C stand as is since experimental Charpy data were not available.

Table 2: Summary of combined notch and precracking depths and absorbed energies for ANL production-scale heat #832665 [2].

Impact Temperature (°C)	Crack Length Left (mm)	Crack Length Center (mm)	Crack Length Right (mm)	Crack Length Average (mm)	Absorbed Energy (J)	Normalized Absorbed Energy (J)
-196	1.65	1.66	1.65	1.65	4.34	8.60
-150	1.61	1.63	1.62	1.62	5.59	10.89
-100	1.58	1.60	1.56	1.58	4.86	9.25
21	1.67	1.69	1.70	1.69	3.68	7.47
175	1.64	1.64	1.62	1.64	3.62	7.13

For the first case, the hardening modulus was allowed to vary over a wide spectrum in order to gauge its effect on absorbed energy. During the analysis, the true failure strain was estimated from reduction of area data on the same heat of material [7]. Due to the similar nature of the true stress-true strain curves for the -196°C and 50°C cases, a constant true failure strain of 2.659 was used for both temperatures based on a $\approx$ 93% reduction of area. The results are shown in Figure 3.

From Figure 3, it is clearly seen that the hardening modulus has only a slight effect on the total absorbed energy even when the hardening modulus values differ by an order of magnitude. There is approximately a 2 J difference between the upper and lower bounds of both curves. In addition, it is a highly linear relationship. Table 3 summarizes the values plotted in Figure 3.

Table 3: Calculated absorbed energy as a function of hardening modulus.

Hardening Modulus (GPa)	Absorbed Energy (J)	
	-196°C	50°C
0.10	2.90	1.79
0.40	3.34	2.18
0.80	3.85	2.61
1.20	4.29	3.03
1.60	4.71	3.43
2.00	5.11	3.83

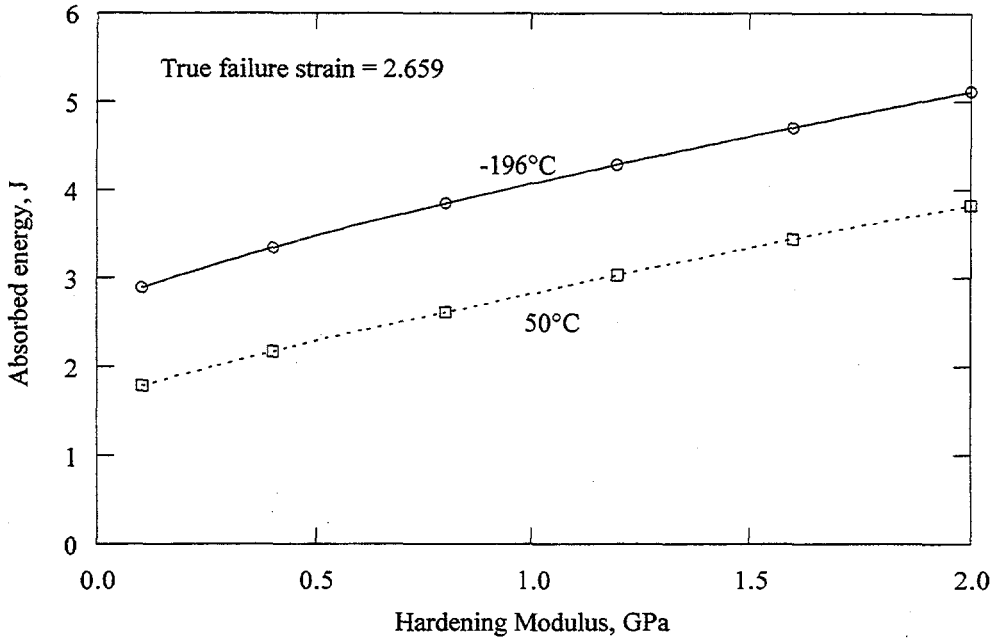

Figure 3 Calculated absorbed energy versus hardening modulus.

The experimentally measured absorbed energies at -196°C and 50°C are 4.34 J and 3.67 J, respectively. The 50°C value was interpolated from the ANL data given in Table 2. From Figure 3, a hardening modulus of about 1.23 GPa at -196°C and 1.80 GPa at 50°C are required for reasonable agreement with the ANL experimental data.

In a similar approach, the true failure strain of the material model was also varied to determine its effect on absorbed energy. For this case, the hardening modulus of the material was calculated from the slope of the plastic strain portion of each true stress-true strain curve. The effect of true failure strain is displayed in Figure 4.

The plot in Figure 4 is very similar in appearance to a DBTT curve. In fact, for a given true failure strain, the model predicts whether ductile or brittle failure will occur. Table 4 summarizes the data points shown in the graph and the fracture behavior predicted by the finite element model.

Table 4: Calculated absorbed energy as a function of true failure strain.

True Failure Strain	Failure Mode*	Absorbed Energy (J)	
		-196°C	50°C
0.30	Complete fracture	0.58	0.45
0.60	Complete fracture	1.58	1.30
1.20	Partial fracture	3.68	2.82
2.40	Pure bending	4.36	3.13

* Both cases exhibited the same failure behavior for the given data points

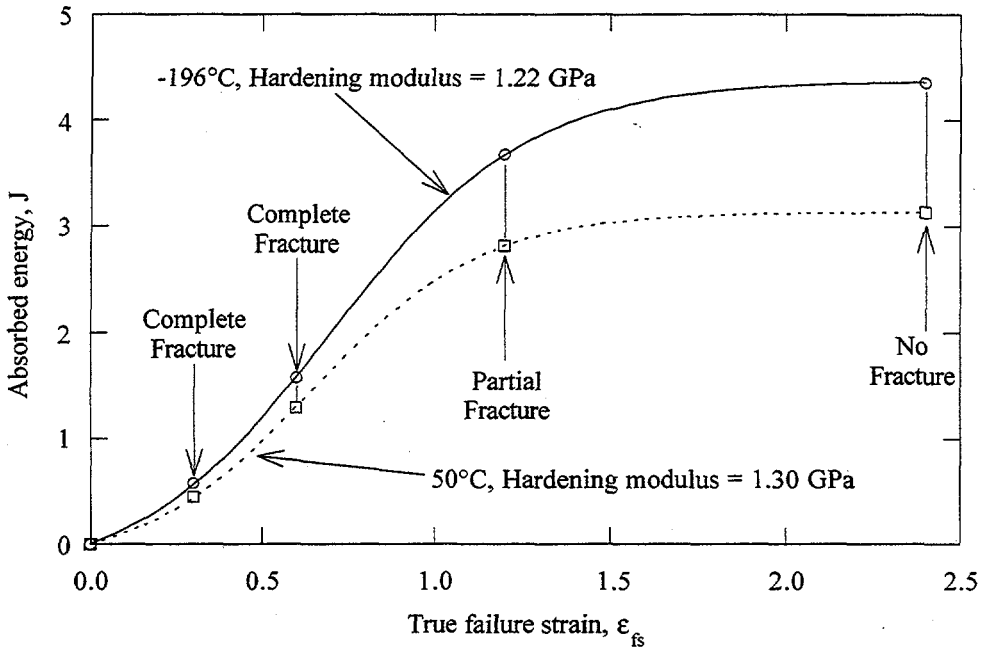

Figure 4 Calculated absorbed energy versus true failure strain.

Agreement between the finite element model and ANL experimental data is very good at -196°C (4.34 J vs.≈ 4.36 J). At 50°C, the finite element model predicts slightly less absorbed energy than the interpolated experimental value (3.67 J vs. ≈ 3.12 J). As seen above, the true failure strain plays a significant role in modeling the impact properties of V-4Cr-4Ti.

CONCLUSIONS

- The importance of accurate tensile data in determining a true stress- true strain curve cannot be overstated. It may prove necessary to actually perform a series of tensile tests and specifically measure important quantities such as reduction of area to obtain an accurate measurement of the true failure strain.

- Due to the limited detail present in the bilinear approximation, a better material model could be developed. It may be possible to generate a more accurate approximation of the true stress-true strain curve by defining the curve in a piecewise linear manner.

- Varying the hardening modulus from 0.1 GPa to 2.0 GPa at a true failure strain of 2.659 had a relatively small effect on absorbed energy. Over this range the absorbed energy increased by a factor of 1.8 at -196°C and a factor of 2.1 at 50°C. In contrast, the true failure strain played a more significant role in determining both the absorbed energy and the fracture behavior of the material. Varying the true failure strain from 0.30 to 2.40 changed the absorbed energy by a factor of 7.5 at -196°C and 7.0 at 50°C.

ACKNOWLEDGMENTS

We would like to thank Eric Donahue from the University of California at Santa Barbara for providing

the V-4Cr-4Ti tensile test data.

REFERENCES

1. Hibbit, Karlsson, & Sorensen, Inc., *ABAQUS Explicit Users Manual v5.4*, HKS, 1995.

2. H. M. Chung, L. Nowicki, and D. L. Smith, "Impact Properties of Precracked V-4Cr-4Ti Charpy Specimens," in Fusion Reactor Materials, Semiannual Progress Report, DOE/ER-0313/18, March 31, 1995, Oak Ridge National Laboratory, Oak Ridge, TN, pp. 253-258.

3. S. E. Sidener, *Dynamic Finite Element Analysis of Charpy Impact Tests for use in Nuclear Power Plant Life Extension*, M.S. Thesis, University of Missouri-Rolla, December 1995.

4. R. Odette, E. Donahue and G. Lucas, "Characterization of Fracture Properties of a V-4Cr-4Ti Alloy," presented at the Second IEA Workshop on Vanadium Alloys, Petten, Netherlands, May 20-22, 1996.

5. W. A. Simpson, "Room Temperature Elastic Properties of V-5Cr-5Ti," in Fusion Reactor Materials, Semiannual Progress Report, DOE/ER-0313/16, March 31, 1994, Oak Ridge National Laboratory, Oak Ridge, TN, pp. 258-259.

6. ASTM E23-94b, Standard Test Methods for Notched Bar Impact Testing of Metallic Materials, American Society for Testing and Materials, Philadelphia, PA, 1994, pp. 137-153.

7. H. M. Chung, L. Nowicki, D. Busch, and D. L. Smith, "Tensile Properties of V-(4-5)Cr-(4-5)-Ti Alloys," in Fusion Reactor Materials, Semiannual Progress Report, DOE/ER-0313/19, December 31, 1995, Oak Ridge National Laboratory, Oak Ridge, TN, pp. 17-21.

MODE I AND MIXED MODE I/III CRACK INITIATION AND PROPAGATION BEHAVIOR OF V-4Cr-4Ti ALLOY AT 25°C

H-X (Huaxin) Li, R. J. Kurtz, R. H. Jones (Pacific Northwest National Laboratory)[1]

OBJECTIVE

To investigate mode I and mixed-mode I/III crack initiation and propagation behavior of the production-scale heat (#832665) of V-4Cr-4Ti using compact tension specimens and modified compact tension specimens.

SUMMARY

The mode I and mixed-mode I/III fracture behavior of the production-scale heat (#832665) of V-4Cr-4Ti has been investigated at 25°C using compact tension (CT) specimens for a mode I crack and modified CT specimens for a mixed-mode I/III crack. The mode III to mode I load ratio was 0.47. Test specimens were vacuum annealed at 1000°C for 1 h after final machining. Both mode I and mixed-mode I/III specimens were fatigue cracked prior to J-integral testing. It was noticed that the mixed-mode I/III crack angle decreased from an initial 25 degrees to approximately 23 degrees due to crack plane rotation during fatigue cracking. No crack plane rotation occurred in the mode I specimen. The crack initiation and propagation behavior was evaluated by generating J-R curves. Due to the high ductility of this alloy and the limited specimen thickness (6.35 mm), plane strain requirements were not be met so valid critical J-integral values were not obtained. However, it was found that the crack initiation and propagation behavior was significantly different between the mode I and the mixed-mode I/III specimens. In the mode I specimen crack initiation did not occur, only extensive crack tip blunting due to plastic deformation. During J-integral testing the mixed-mode crack rotated to an increased crack angle (in contrast to fatigue precracking) by crack blunting. When the crack initiated, the crack angle was about 30 degrees. After crack initiation the crack plane remained at 30 degrees until the test was completed. Mixed-mode crack initiation was difficult, but propagation was easy. The fracture surface of the mixed-mode specimen was characterized by microvoid coalescence.

PROGRESS AND STATUS

1. Material and Experimental Method

The production-scale heat (#832665) of V-4Cr-4Ti was used for this study. CT specimens were machined from 6.35 mm thick plates. The plate was received in the warm-rolled condition and was heat treated at 1000°C for 1 hour in a vacuum of 10^{-7} torr (HT1) at PNNL following machining of specimens. CT specimens were used to evaluate mode I fracture and modified CT specimens were used for mixed-mode I/III fracture. The modified CT specimen geometry has been reported previously [1]. The crack angle used in this work was 25 degrees. With 25 degree crack angle the ratio of resolved mode III to mode I load component is 0.47. All specimens had the T-L orientation and all testing was performed at room temperature. J-integral tests were performed according to the J-integral test procedure given in ASTM E 813. Fracture surfaces were examined in a scanning electron microscope (SEM) to determine the failure mode.

[1] Operated for the U.S. Department of Energy by Battelle Memorial Institute under Contract DE-AC06-76RLO 1830.

2. Results And Discussion

J-integral values versus crack growth increments (Δa) for both mode I and mixed-mode I/III specimens are plotted in Figure 1. From Figure 1, it can be seen that V-4Cr-4Ti is very tough in the unirradiated condition at room temperature. No crack initiation took place in the mode I specimen. The crack extension resulted from severe crack tip blunting and necking. Most of the J-Δa data fall outside the lower exclusion line (see Figure 1) because of the severe crack blunting. The exclusion line is defined by Eq. 1

$$J = \frac{(\sigma_y + \sigma_u)}{2}(\Delta a - 0.0015) \qquad (1)$$

Where σ_y is the yield strength (387 MPa) and σ_u is the ultimate tensile strength (454 MPa). Δa is the crack growth increment (m).

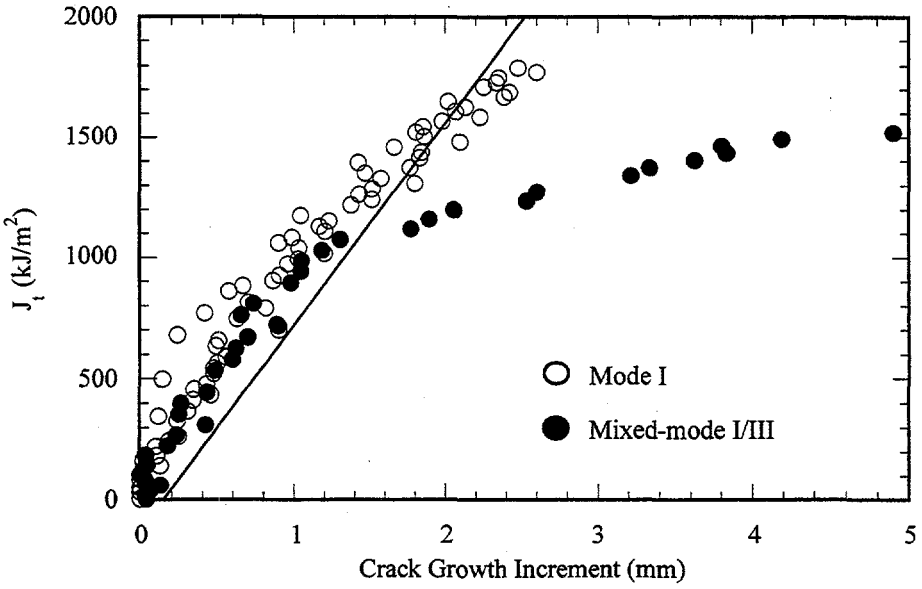

Figure 1. Effect of loading mode on J-R curves of a production scale heat of V-4Cr-4Ti.

A valid fracture toughness for the mode I specimen could not be determined because the alloy was extremely ductile and no crack initiation occurred, as shown in Figure 1. All of the crack "growth" indicated in Figure 1 for the mode I specimen was due to plastic deformation at the crack tip.

The mixed-mode specimen behaved differently from the mode I specimen. During fatigue precracking the crack plane rotated from 25 degrees to 23 degrees. However, during J testing, the crack plane angle increased from 23 degrees to about 30 degrees when the crack started to grow. After crack initiation, the crack plane angle remained at 30 degrees until the end of the test. Total crack growth was up to 5.2 mm. The mixed-mode specimen also experienced extensive plastic deformation similar to the mode I specimen. The estimated J_{Mq} value for crack initiation (not valid per ASTM criteria) was 1100 kJ/m2, indicating that crack initiation was difficult. The reasons for the high J_{Mq} have not been determined. Crack plane rotation before crack initiation was one of the factors which contributed

to the high J_{Mq} value. While the mixed-mode crack was difficult to initiate, it propagated easily. The slope of the mixed-mode I/III J-R curve beyond the exclusion line was only 140 kJ/m^2/mm.

Because no crack initiation occurred in the mode I specimen, SEM examination was only done on the mixed-mode I/III specimen. The mixed-mode specimen failed by microvoid coalescence, as depicted in Figure 2a and 2b. Microvoids were distorted along the shear loading component (see Figure 2).

FUTURE WORK

Mixed-mode I/III fracture toughness under a higher mode III component (45 degree crack angle specimens) will be tested for the V-4Cr-4Ti alloy and mode I fracture toughness will be measured using 1 in. thick plate (GA Heat #832864).

REFERENCE

1. H. Li, R. H. Jones, and J. P. Hirth, Fusion Materials Semiannual Progress Report, DOE/ER-0313/16, Oak Ridge National Laboratory , Oak Ridge, TN, March 1994.

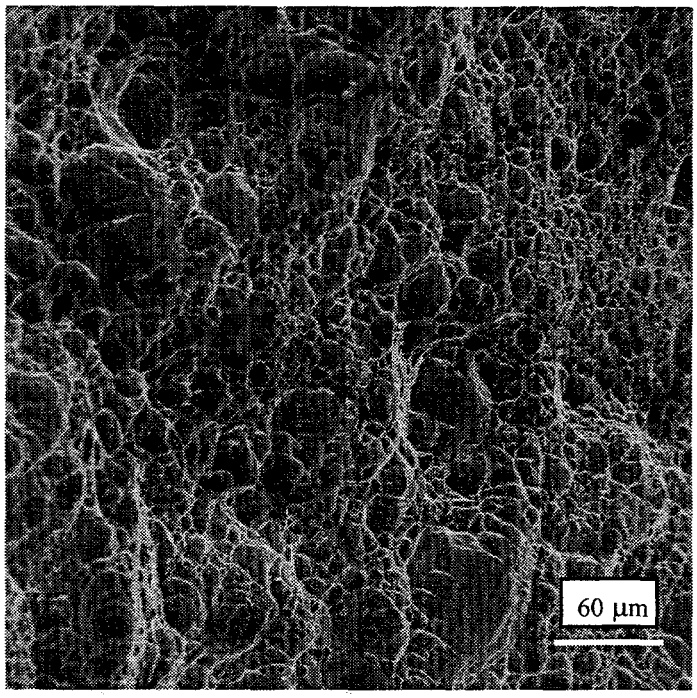

(a)

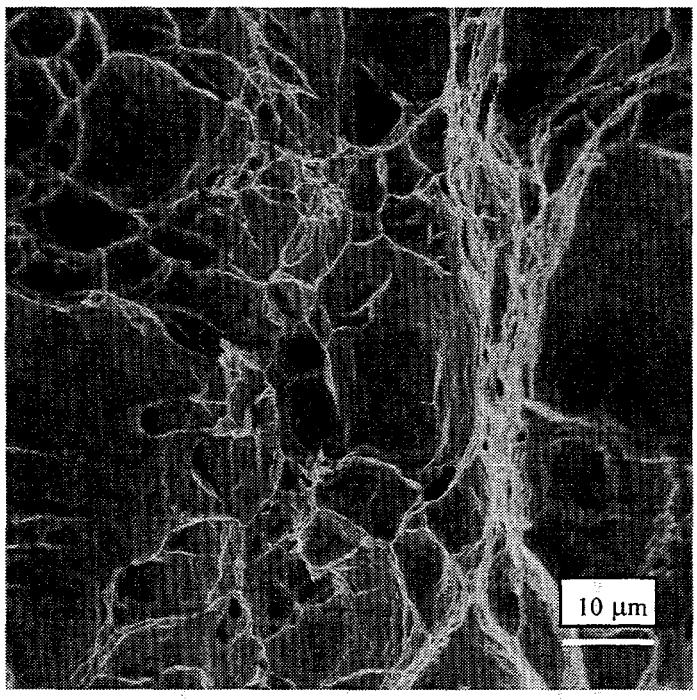

(b)

Figure 2. SEM photograph of mixed-mode fracture surface in V-4Cr-4Ti specimen tested at 25°C.

AN EVALUATION OF THE SUSCEPTIBILITY OF V-4Cr-4Ti TO STRESS CORROSION CRACKING IN ROOM TEMPERATURE DIII-D WATER - R. J. Kurtz (Pacific Northwest National Laboratory), W. R. Johnson (General Atomics Company), and R. H. Jones (Pacific Northwest National Laboratory)

OBJECTIVE

The objective of this research was to evaluate the susceptibility of V-4Cr-4Ti to stress corrosion cracking (SCC) in the DIII-D tokamak water environment.

SUMMARY

Two fatigue precracked compact tension (CT) specimens of V-4Cr-4Ti were statically loaded to a stress intensity factor of about 30 MPa$\sqrt{m}$ in room temperature DIII-D water. The first specimen was tested for a period of about 30 days and the second specimen for about 54 days. At the conclusion of each test the specimens were fractured, and the fracture surfaces examined with a scanning electron microscope (SEM) to determine if SCC had occurred. No SCC was found in either test specimen.

INTRODUCTION

For the past several years the DIII-D Program has been progressing toward installation of a sizeable structural component in DIII-D fabricated from a vanadium alloy. The goals of the DIII-D effort are 1) to provide a meaningful deployment of a low activation material in an operating fusion system, 2) to demonstrate the in-service behavior of a vanadium alloy in a typical tokamak environment, and 3) to gain knowledge and experience in the design, processing, and fabrication of a vanadium alloy. The current plan calls for use of a V-4Cr-4Ti component in the Radiative Divertor of DIII-D known as a private flux baffle, Figures 1 and 2. The private flux baffle is a toroidally continuous, water cooled structure.

During DIII-D plasma operations the private flux baffle will, most of the time, experience very low applied stresses. The main sources of stress include internal water pressure (0.4 MPa) and thermal stresses caused by temperature differences between the private flux baffle and the vessel to which it is mounted. The temperature of the private flux baffle during operation shall be about 30°C with occasional periods when the temperature will rise by about 30 to 40°C as the heat from each plasma shot is radiated to the graphite tiles attached to the water cooling panels. Stress transients will be induced in the private flux baffle due to plasma disruptions. The highest disruption stresses calculated are about 138 MPa [1]. The disruption stresses are mostly normal to the plates and last for only a few milliseconds.

The potential for SCC in the private flux baffle arises from its design. Two vanadium alloy plates will be joined by spot welding, Figure 2. The size of the spot weld will encompass about half the mating surface of the plates. Thus, an artificial crevice exists which, along with the residual stresses from welding and the presence of the water environment, creates the potential for SCC. Fortunately, the stresses during normal operation are low, and the plasma disruption stresses do not appear to act in a manner which would exacerbate the crevice tip stress field. Estimates of the maximum applied stress intensity factor are about 3 MPa$\sqrt{m}$. In order to assess the potential for SCC of V-4Cr-4Ti in the private flux baffle, two experiments were performed using CT specimens statically loaded to a stress intensity factor approximately an order of magnitude greater than that expected during service.

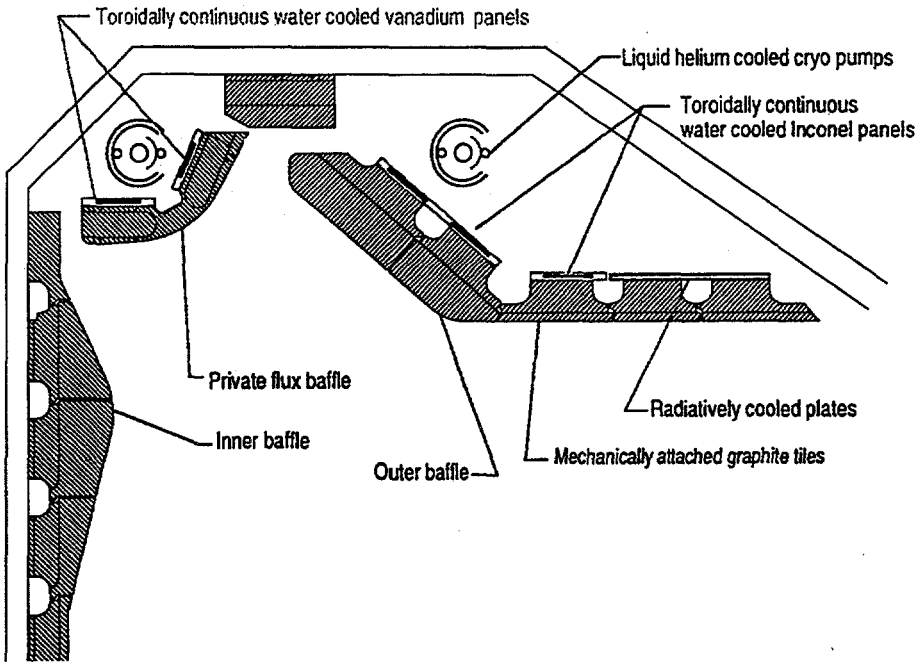

Figure 1: Vanadium Components of the DIII-D Radiative Divertor

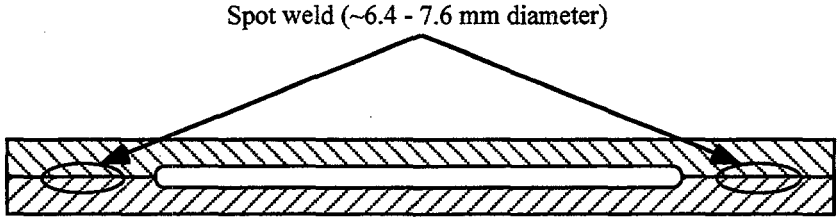

Figure 2: Cross-Sectional View of Vanadium Private Flux Baffle

PROCEDURE

Two CT specimens were machined from 3.81 mm thick V-4Cr-4Ti plate in the as-rolled condition supplied by Argonne National Laboratory (Heat 832665). The specimens were machined in the T-L orientation and were side-grooved 10% on each face. Following machining the specimens were heat treated for one hour at 1000°C in a high vacuum furnace. Fatigue precracking was performed after heat treatment in room temperature air at a maximum load of 1.8 kN and minimum load of 0.18 kN. Specimens were dead-weight loaded to 2.8 kN in a sealed polyethylene container of DIII-D water. Loading pins fabricated from V-4Cr-4Ti were used to connect the test specimens to the load train. Vanadium loading pins were used to remove the potential for galvanic corrosion. Table 1 lists specimen dimensions together with initial crack lengths and applied stress intensity factors. Table 2 gives results of chemical analyses performed on DIII-D water samples.

Specimen C44-15 was exposed to DIII-D water for about 15 days, and then removed to determine if crack growth had occurred. The specimen was loaded in a servo-hydraulic test frame to 2.7 kN and the crack length measured optically with a traveling stage microscope. Initial measurements indicated some crack extension might have occurred so C44-15 was exposed for another 15 days. At the end of the second exposure the specimen was removed and an additional ~2.5 mm of fatigue crack growth introduced at high R-ratio. High R-ratio was used so as to not disturb the existing fracture surface. The specimen was then broken open and examined in the SEM. A similar procedure was followed for specimen C44-14, but instead of two exposure periods only one exposure lasting about 54 days was utilized.

Table 1: Specimen Dimensions, Initial Crack Lengths, and Applied Stress Intensity Factors

ID No.	Width, mm	Height, mm	Net Thickness, mm	Initial Crack Length, mm	Initial Stress Intensity Factor, MPa$\sqrt{m}$
C44-14	30.5	36.6	3.05	16.93	30.5
C44-15	30.5	36.6	3.05	17.60	33.0

Table 1: Chemistry of DIII-D water.

Anion	mg/L	Element	mg/L	Element	mg/L
Cl^{-1}	0.62	Sn	<0.10	Mg	<0.05
NO_3^{-1}	<0.025	Mo	0.07	Cu	<0.05
SO_4^{-1}	1.6	Cr	<0.05	Ca	<0.10
		Zn	<0.02	Al	<0.10
pH	6.22	Pb	<0.10	Fe	<0.05
Cond.(μS/cm)	10.9	Ni	<0.10		

RESULTS

SEM examination of fracture surfaces from both C44-14 and C44-15 revealed no environmentally induced crack growth. Figure 3 shows the fracture surface of C44-14 at three key locations. Figure 3a

shows fracture features associated with the fatigue precrack region. Figure 3b presents a view of the fracture surface at the tip of the fatigue precrack. Figure 3c displays the fracture surface just beyond the tip of the fatigue precrack. No evidence was found for SCC by examination of the fracture surfaces. The fracture surface features seen in Figure 3c are the same as those found in Figure 3a. Fatigue striations are observed in both cases indicating all crack growth is due to fatigue and not to intergranular or transgranular SCC.

CONCLUSION

- V-4Cr-4Ti was not susceptible to SCC in room temperature DIII-D water at a stress intensity factor of about 30 MPa$\sqrt{m}$ for up to 54 days. The results of this work suggest that SCC of the private flux baffle will not be a concern for DIII-D under normal operating conditions.

REFERENCES

1. Hollerbach, M. A., J. P. Smith, C. B. Baxi, A. S. Bozek, E. Chin, R. D. Phelps, K. M. Redler, and E. E. Reis (1995). "Design and Analysis of the DIII-D Radiative Divertor Water-Cooled Structures," in Proceedings of the 16th Symposium on Fusion Engineering, Vol. 1, pp. 817-820.

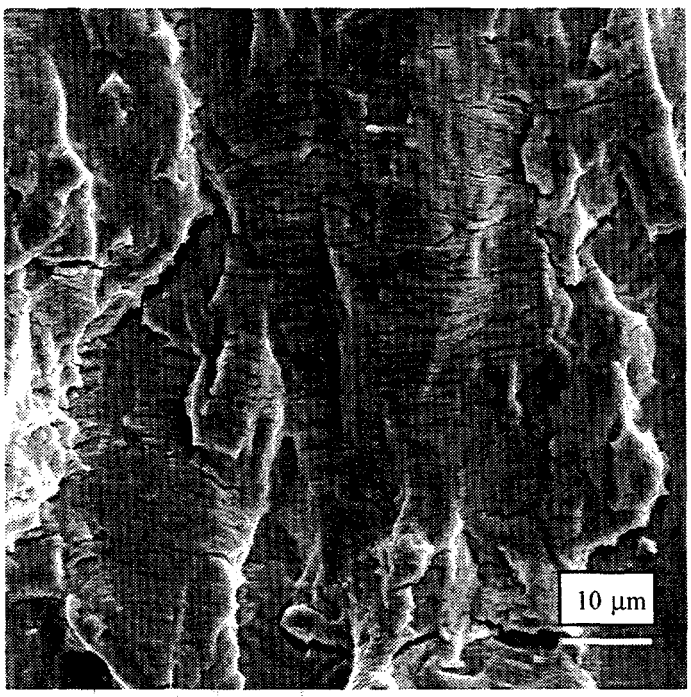

Figure 3a: Fracture Surface of C44-14 - Precrack Region

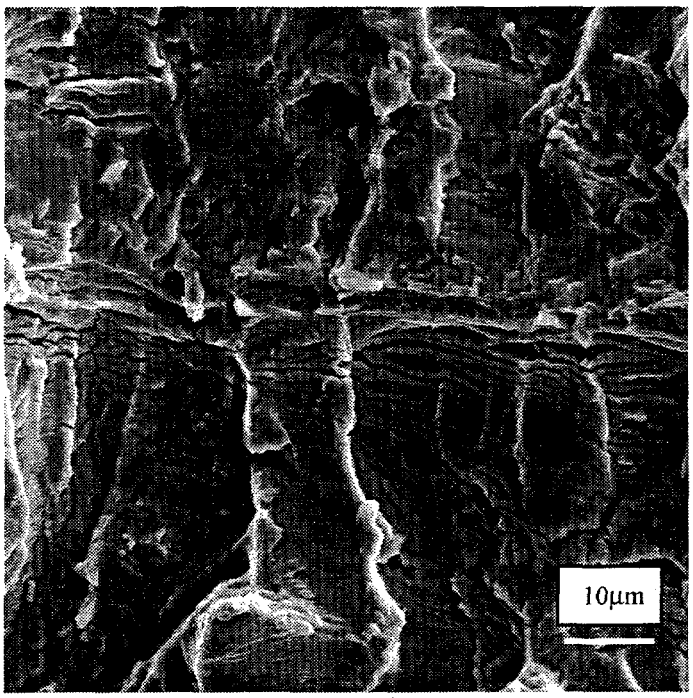

Figure 3b: Fracture Surface of C44-14 - Precrack Tip Region

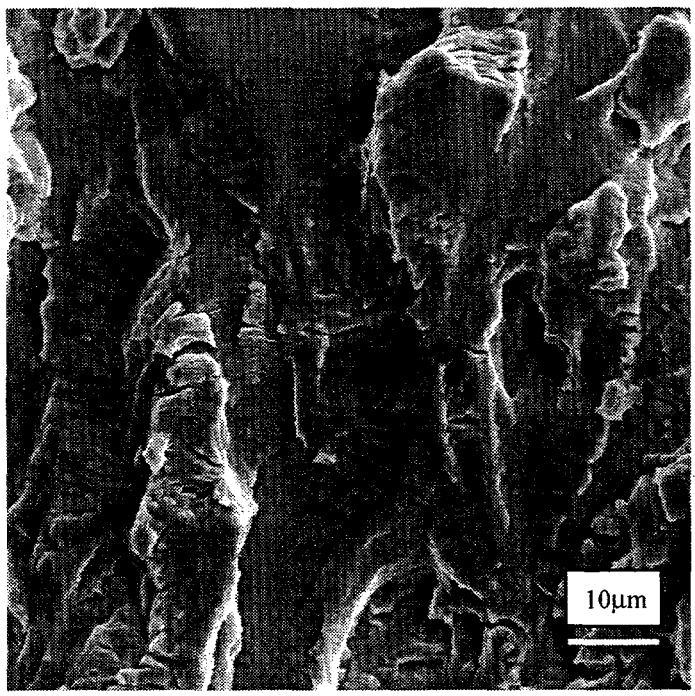

Figure 3c: Fracture Surface of C44-14 - Just Beyond Precrack Tip Region

TENSILE PROPERTIES OF V-5Cr-5Ti ALLOY AFTER EXPOSURE IN AIR ENVIRONMENT*

K. Natesan and W. K. Soppet (Argonne National Laboratory)

OBJECTIVE

The objectives of this task are to (a) evaluate the oxygen uptake of V-Cr-Ti alloys as a function of temperature and oxygen partial pressure in the exposure environment, (b) examine the microstructural characteristics of oxide scales and oxygen entrapped at the grain boundaries of the substrate alloys, (c) evaluate the influence of oxygen uptake on the tensile properties of the alloys at room and elevated temperatures, and (d) determine the effect of oxygen uptake on the tensile behavior of the alloys.

SUMMARY

Oxidation studies were conducted on V-5Cr-5Ti alloy specimens in an air environment to evaluate the oxygen uptake behavior of the alloy as a function of temperature and exposure time. The oxidation rates, calculated from parabolic kinetic measurements of thermogravimetric testing and confirmed by microscopic analyses of cross sections of exposed specimens, were 5, 17, and 27 μm per year after exposure at 300, 400, and 500°C, respectively. Uniaxial tensile tests were conducted at room temperature and at 500°C on preoxidized specimens of the alloy to examine the effects of oxidation and oxygen migration on tensile strength and ductility. Correlations were developed between tensile strength and ductility of the oxidized alloy and microstructural characteristics such as oxide thickness, depth of hardened layer, depth of intergranular fracture zone, and transverse crack length.

EXPERIMENTAL PROGRAM

The heat of vanadium alloy selected for the study had a nominal composition of V-5 wt.%Cr -5 wt.%Ti and was designated BL-63. A sheet of the alloy was annealed for 1 h at 1050°C prior to oxidation and tensile testing. Coupon specimens that measured ≈15 x 7.5 x 1 mm were used for the oxidation studies. Oxidation experiments were conducted in air in a thermogravimetric test apparatus at temperatures between 300 and 650°C.

Tensile specimens were fabricated according to ASTM Standard E8-69 specifications and had a gauge length of ≈19 mm and a gauge width of ≈4.5 mm. The grain size of the specimens was ≈32 μm. The specimens were preoxidized in air at 500°C for 24, 250, 600, 1000, and 2060 h prior to tensile testing in air at 500°C. Similar specimens, preoxidized up to 1000 h at 500°C in air, were also subjected to tensile testing at room temperature. As-annealed (control) specimens were tensile tested on an Instron machine at constant crosshead speeds between 0.0005 and 0.2 cm/min, which correspond to initial strain rates in the range of 4.4×10^{-6} to 1.8×10^{-3} s^{-1}. The preoxidized specimens were tested at a strain rate of 1.8×10^{-4} s^{-1}. The test temperature was maintained within 2°C in all tests performed in air at 500°C. The specimens were loaded by means of pins that pass through holes in the grips and enlarged end sections of the specimen, thus minimizing misalignment. Total elongation was measured with a vernier caliper and by using load/elongation chart records. The fracture surfaces and longitudinal and axial cross sections of tested specimens were examined by scanning electron microscopy (SEM). In addition, Vickers hardness of several tested specimens. Coupon specimens of the alloy that were oxidized with the tensile specimens were analyzed for bulk oxygen content by a vacuum-fusion technique.

RESULTS AND DISCUSSION

Oxidation Behavior

Oxidation of the alloy followed parabolic kinetics with respect to time. Detailed SEM analysis (with both energy-dispersive and wavelength-dispersive analysis) of the oxidized samples showed that the outer layer was predominantly vanadium-rich oxide and the inner layer was (V,Ti) oxide. Furthermore, X-ray diffraction of the oxides showed the outer oxide to be V_2O_5; no nitrogen or nitride phases were detected.

---

*This work has been supported by the U.S. Department of Energy, Office of Fusion Energy Research, under Contract W-31-109-Eng-38.

The thickness of the oxide scale of the specimens, calculated from a parabolic rate equation, was in good agreement with the values determined by microscopy. The results were discussed in earlier reports (1, 2). Secondary-ion mass spectrometry was used to obtain depth profiles for oxygen in the tested specimens.

Effect of Oxidation on Tensile Properties

To evaluate the effect of oxide scale formation and oxygen penetration into the substrate alloy, tensile behavior of the alloy was examined as a function of oxygen ingress and oxide scale formation. Specimens were exposed to air for 24-2060 h at 500°C and then tensile tested in air at either room temperature or 500°C at a strain rate of 1.8×10^{-4} s^{-1}. Figure 1 shows the engineering stress/engineering strain curves at 500°C for specimens after oxidation for several exposure times up to 2060 h. Stress/strain behavior of the alloy is virtually unaffected by 24 h of exposure in air at 500°C. As exposure time increases to 250 h, alloy strength increases, with some loss in tensile ductility. In the exposure range of 250-1000 h, the alloy essentially has the same ultimate tensile strength but showed substantial reduction in tensile ductility. Further exposure of the alloy to air at 500°C causes loss of strength and tensile ductility, as evidenced by the stress/strain curve for the specimen that was preoxidized for 2060 h.

Figure 2 shows engineering stress/engineering strain curves obtained at room temperature for specimens after oxidation for several exposure times up to 1000 h. A significant increase in tensile strength and a moderate decrease in tensile ductility of the alloy occurs after 24 h of oxidation. However, the effect of oxidation on ductility was more severe as oxidation time increased to 260 h and beyond.

The load-displacement curves were reanalyzed by drawing lines parallel to the initial portion of the loading curve at the points of maximum load and rupture load. The intersects of these lines with the displacement axis are used to calculate the uniform and total elongation for the specimens subjected to various oxidation treatments. The present approach accounts for the stiffness, or lack of it, in the loading fixture of the tensile machine and, as a result, yields elongation values that are more representative of the gauge section of the tensile specimen; the values are generally lower than those in the last report (3).

Figures 3 and 4 show the variations in maximum engineering stress and uniform and total eleongation as a function of preoxidation time in air at 500°C for tests conducted at room temperature and 500°C.

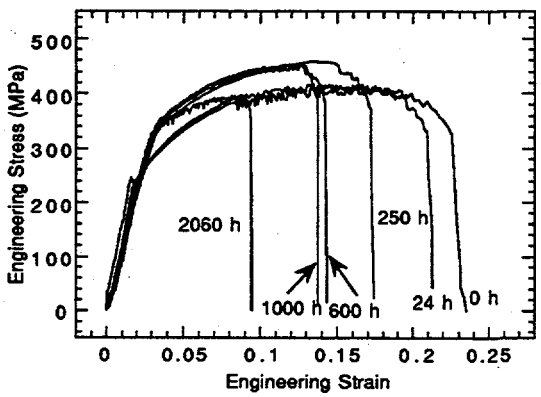

Figure 1. Effect of preoxidation at 500°C on stress/strain behavior of V-5Cr-5Ti alloy tested at 500°C in air at a strain rate of 1.75×10^{-4} s^{-1}.

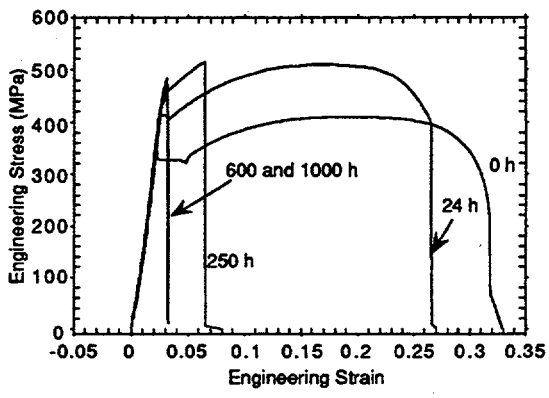

Figure 2. Effect of preoxidation at 500°C on stress/strain behavior of V-5Cr-5Ti alloy tested at room temperature in air at a strain rate of 1.75×10^{-4} s^{-1}.

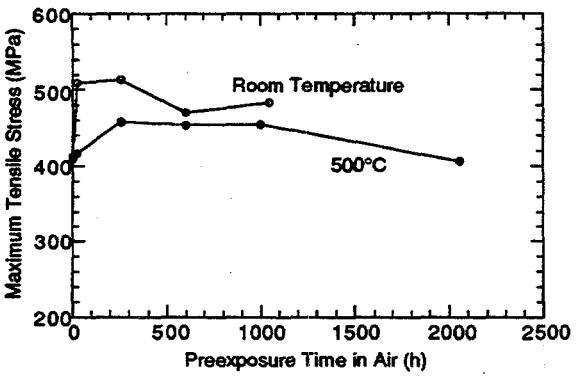

Figure 3. Maximum tensile stress as a function of preexposure time in air for specimens of V-5Cr-5Ti alloy tested in air.

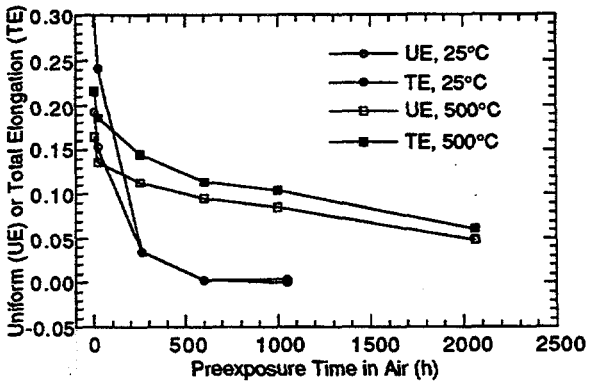

Figure 4. Rupture strain as a function of preexposure time in air for specimens of V-5Cr-5Ti alloy tested in air.

Table 1 lists the calculated and measured thickness of oxide layers, depth of hardened layers (from Vickers hardness measurements), thickness of intergranular fracture zones, and transverse crack length for specimens as-annealed, preoxidized, and tensile-tested at room temperature and 500°C. The results indicate that the specimens that were oxidized for 600 and 1000 h at 500°C registered only 0.003 and 0 uniform elongation at room temperature.

Additional exposures as a function of oxygen partial pressure in the exposure environment, as well as tensile tests at other temperatures on oxidized specimens, are underway to establish alloy performance in an oxygen-containing environment.

Table 1. Oxidation, hardness, and fracture data for V-5Cr-5Ti alloy

Exposure time (h)	Calculated oxide thickness[a] (μm)	Measured oxide thickness (μm)	Depth of hardened layer after exposure at 500°C (μm)	Intergranular-fracture zone (μm)		Measured crack length (μm)		Uniform elongation[c]		Total elongation[c]	
				RT[b]	500°C	RT[b]	500°C	RT[b]	500°C	RT[b]	500°C
0	0	0	0	0	0	0	10	0.193	0.164	0.301	0.216
24	1.4	1.2	<25	d	25	24	22	0.153	0.136	0.241	0.186
250[e]	4.6	5.0	45	>500	65	f	50	0.035	0.113	0.035	0.145
600	7.1	7.1	68	>500	100	f	90	0.003	0.095	0.003	0.114
1000[e]	9.1	9.0	80	>500	120	f	110	0	0.085	0.004	0.104
2060	13.1	14.0	120	NT[g]	165	NT[g]	160	NT[g]	0.048	NT[g]	0.061

[a]Values were calculated with an equation developed from a parabolic fit of all the oxidation data .

[b]RT = room temperature.

[c]Values that were recalculated by following the revised procedure discussed above.

[d]Fracture is partially ductile and no transition is noted from ductile to brittle fracture.

[e]Exposure times were 260 and 1050 h for the samples tested at room temperature.

[f]Specimen fully embrittled.

[g]NT=not tested.

REFERENCES

1. K. Natesan and W. K. Soppet, "Effect of Oxidation on Tensile Behavior of V-Cr-Ti Alloys," Fusion Reactor Materials Progress Report for the Period Ending March 31, 1995, Argonne National Laboratory, DOE/ER-0313/18, p. 247, July 1995.

2. K. Natesan and W. K. Soppet, "Effect of Oxidation on Tensile Behavior of a V-Cr-Ti Alloy," Proc. 2nd Intl. Conf. on Heat Resistant Materials, ASM International, Materials Park, OH, p. 375 (1995).

3. K. Natesan and W. K. Soppet, "Effect of Oxygen and Oxidation on Tensile Behavior of V-5Cr-5Ti," Fusion Reactor Materials Progress Report for the Period Ending December 31, 1995, Argonne National Laboratory, DOE/ER-0313/19, p. 50, April 1996.

TENSILE PROPERTIES OF V-Cr-Ti ALLOYS AFTER EXPOSURE IN HELIUM AND LOW-PARTIAL-PRESSURE OXYGEN ENVIRONMENTS*

K. Natesan and W. K. Soppet (Argonne National Laboratory)

OBJECTIVE

The objectives of this task are to (a) quantify the oxygen partial pressure (pO_2) in argon and helium environments of different purity, (b) determine the oxygen uptake of V-Cr-Ti alloys as a function of temperature and pO_2 in the exposure environment, (b) examine the microstructural characteristics of oxide scales and oxygen trapped at the grain boundaries in the substrate alloys, (c) evaluate the influence of oxygen uptake in low-pO_2 environments (which include oxygen and helium of various purities) on the tensile properties and cracking propensity of the alloys at room and elevated temperatures.

SUMMARY

A test program is in progress to evaluate the effect of oxygen at low pO_2 on the tensile properties of V-(4-5)wt.% Cr-(4-5)wt.% Ti alloys. Some of the tensile specimens were precharged with oxygen at low pO_2 at 500°C and reannealed in vacuum at 500°C prior to tensile testing. In another series of tests, specimens were exposed for 250-275 h at 500°C in environments with various pO_2 levels and subsequently tensile tested at room temperature. The preliminary results indicate that both approaches are appropriate for evaluating the effect of oxygen uptake on the tensile properties of the alloys. The data showed that in the relatively short-time tests conducted thus far, the maximum engineering stress slightly increased after oxygen exposure but the uniform and total elongation values exhibited significant decrease after exposure in oxygen-containing environments. The data for a specimen exposed to a helium environment were similar to those obtained in low pO_2 environments.

EXPERIMENTAL PROGRAM

The heats of vanadium alloy selected for the study had nominal compositions of V-5 wt.%Cr-5 wt.%Ti (designated BL-63) and V-4 wt.%Cr-4 wt.%Ti (designated BL-71). Sheets of the alloys were annealed for 1 h at 1050°C prior to oxidation and tensile testing. Coupon specimens that measured ≈15 x 7.5 x 1 mm were used for the oxidation studies. Oxidation experiments were conducted in air in a thermogravimetric test apparatus at temperatures of 300 to 650°C; results were discussed in an earlier report (1).

Tensile specimens were fabricated according to ASTM Standard E8-69 specifications and had a gauge length of ≈19 mm and a gauge width of ≈4.5 mm. Grain sizes of the V-4Cr-4Ti and V-5Cr-5Ti specimens were ≈18 and 32 μm, respectively. Three types of exposures were used to evaluate the oxygen effect on the properties. In the first approach, specimens were exposed to a low-pO_2 environment for 4 to 24 h at 500°C, and subsequently the surface-charged specimens were annealed under vacuum at 500°C for 100 h to diffuse the surface oxygen into the interior of the specimens. In the second approach, specimens were exposed at 500-700°C to high-purity oxygen gas at low partial pressures, maintained by a feed/bleed system. In the third approach, specimens were exposed to helium environments of various purity grades at temperatures of 500 to 700°C.

Pretreated specimens from the above-described approaches were tensile-tested in air at room and elevated temperatures. The crosshead speed in an Instron machine was set to yield a strain rate of 1.8×10^{-4} s^{-1} for all the tests. The specimens were loaded by means of pins that pass through holes in the grips and enlarged end sections of the specimen, thus minimizing misalignment. Total elongation was measured with a vernier caliper and by using load/elongation chart records. The fracture surfaces and longitudinal and axial cross sections of tested specimens were examined by scanning electron microscopy (SEM). In addition, Vickers hardness of several tested specimens was determined. Coupon specimens of the alloy that were oxidized with the tensile specimens were analyzed for bulk oxygen content by a vacuum-fusion technique.

RESULTS AND DISCUSSION

Measurement of Oxygen in Environment

The pO_2 in the exposure environment was characterized by using a solid electrolyte oxygen sensor. The electrolyte was a stabilized zirconia tube containing 8 wt.% yttria. Based on conduction domains reported in the literature for solid electrolytes (2), the yttria-stabilized zirconia electrolyte should exhibit fully ionic conductivity at temperatures above 500°C in the low-pO_2 environments of interest in the present study. The sensor used in the present investigation had the following approximate dimensions: ID, 6.3 mm, OD, 9.5 mm, and length 610 mm. A porous platinum coating ≈40 mm long was applied at the closed end of the electrolyte tube and used for the electrode leads. Air was used as the reference gas mixture and continuously flowed inside the zirconia tube. The outside electrode was exposed to the low pO_2 environment of the desired pressure. Pure gases such as argon and helium, and premixed gases such as CO-CO_2 and O_2-N_2 were used in the study.

The equilibrium voltage E of the cell with respect to an air reference electrode is given by the Nernst equation:

$$E \text{ (in volts)} = 2.15 \times 10^{-5} \times T \times \ln(-0.21/pO_2),$$

where pO_2 is the oxygen partial pressure in the low-pressure side of the cell, 0.21 is the partial pressure of oxygen in air at the reference electrode, and T is the absolute temperature.

Figure 1 shows the response of the cell, after conversion into oxygen partial pressure for the calibration gases CO-CO_2 and O_2-N_2 gases and for 99.999% pure argon and helium. The cell response for the calibration gases was in agreement with values calculated on the basis of thermodynamic equilibrium and gas composition. Figure 2 shows an expanded version of the data on the pO_2, in torr, for the argon and helium gases. In addition, the argon gas was further purified to eliminate moisture, which resulted in substantial reduction in pO_2 relative to that of unpurified gas. The data indicate that the pO_2 in 99.999% He is ≈0.1-0.3 torr over the temperature range 400-700°C.

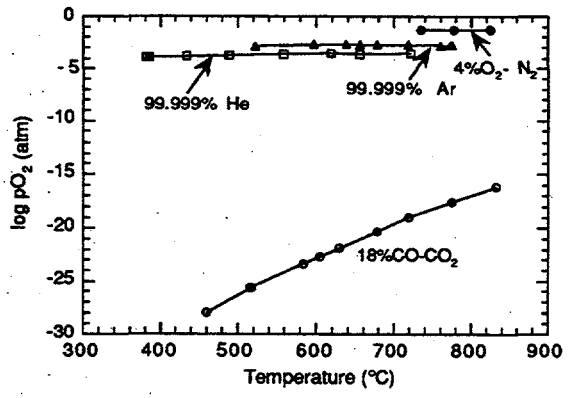

Figure 1. Variation in oxygen partial pressure as a function of temperature for calibration gases O_2-N_2 and CO-CO_2 and for argon and helium.

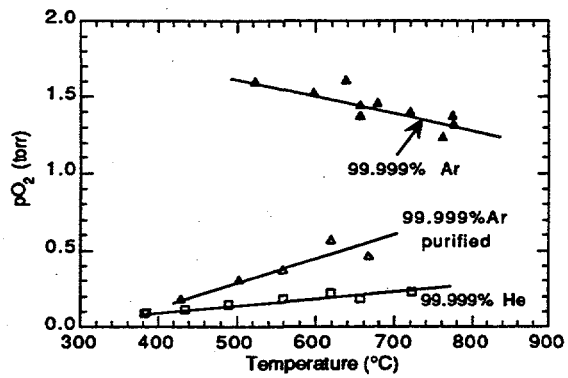

Figure 2. Expanded plot of variation in oxygen partial pressure as a function of temperature for argon and helium.

Effect of Oxygen Exposure on Tensile Properties

Figure 3 shows the engineering stress/engineering strain curves at room temperature for specimens of V-5Cr-5Ti alloy in as-rolled condition, after annealing for 1 h at 1050°C, after a second annealing for 100 h at 500°C, and after oxygen charging for 4, 8, and 24 h at 500°C in an environment with $pO_2 = 1.0 \times 10^{-6}$ torr followed by a 100 h annealing at 500°C in vacuum. The purpose of a 100-h annealing at 500°C is to diffuse the oxygen at the surface of the specimens obtained by charging for 4, 8, and 24 h in a low-pO_2 environment.

The load-displacement curves were analyzed by drawing lines parallel to the initial portion of the loading curve at the points of maximum load and rupture load. The intersects of these lines with the displacement axis are used to calculate the uniform and total elongation for the specimens subjected to various oxidation treatments. Table 1 lists the maximum engineering stress and uniform and total elongation for the specimens with various pretreatments tensile-tested at room temperature. Maximum engineering stress is ≈505-537 MPa after oxygen charging and annealing at 500°C. The uniform elongation values are ≈0.131-0.155 and are slightly less than the 0.165 observed for the specimen with only an initial annealing treatment of 1 h at 1050°C. Total elongation for the specimens annealed for 100 h at 500°C decreased

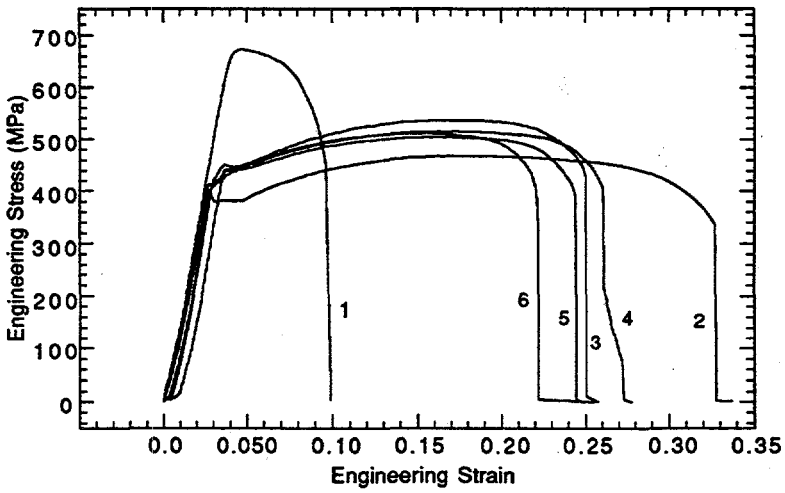

1: as-rolled; 2: annealed 1 h at 1050°C in vacuum
3: 2 plus 100 h anneal at 500°C in vacuum
4: 2 plus 4 h O charge at 500°C in 10^{-6} torr O plus 100 h annealing in vacuum
5: same as 4 except 8 h O charge
6: same as 4 except 24 h O charge

Figure 3. Engineering stress/engineering strain curves for V-5Cr-5Ti alloy with several pretreatments tested at room temperature.

Table 1. Tensile test data at room temperature for V-5Cr-5Ti alloy after several pretreatments

Specimen pretreatment	Maximum engineering stress (MPa)	Uniform elongation	Total elongation
As-rolled	673.7	0.011	0.074
Vacuum annealing, 1 h at 1050°C (a)	468.7	0.165	0.303
(a) + vacuum annealing, 100 h at 500°C (b)	537.3	0.148	0.214
(a) + 4 h O charge + (b)	515.1	0.155	0.232
(a) + 8 h O charge + (b)	505.0	0.146	0.221
(a) + 24 h O charge + (b)	511.4	0.131	0.198

substantially from an initial value of 0.303 to values of ≈0.198-0.232. Examination of the surfaces and cross sections of the specimens exposed to different oxygenated treatments showed significant surface cracks spaced uniformly but appearing to become blunted after a certain depth indicating that the extent of oxygen diffusion and the local concentration of oxygen in the surface regions of the specimens will determine the cracking depth. Figure 4 shows the engineering stress/engineering strain curves at room temperature for specimens of V-4Cr-4Ti alloy in as-rolled condition, after annealing for 1 h at 1050°C, after exposure in environments with different pO_2 at 500°C, and in 99.999% He environment. Table 2 lists the maximum engineering stress and uniform and total elongation for the specimens with various treatments tensile-tested at room temperature. The maximum engineering stress for this alloy in as-rolled condition is similar to that of V-5Cr-5Ti alloy. However, upon annealing for 1 h at 1050°C, the strength falls to 423.7 MPa, which is somewhat lower than that for V-5Cr-5Ti alloy. Correspondingly, the uniform and total elongation values were slightly higher for the V-4Cr-4Ti alloy than for the V-5Cr-5Ti alloy. The effect of 250 h exposure in oxygen at three different levels is to slightly increase the maximum stress, especially at higher

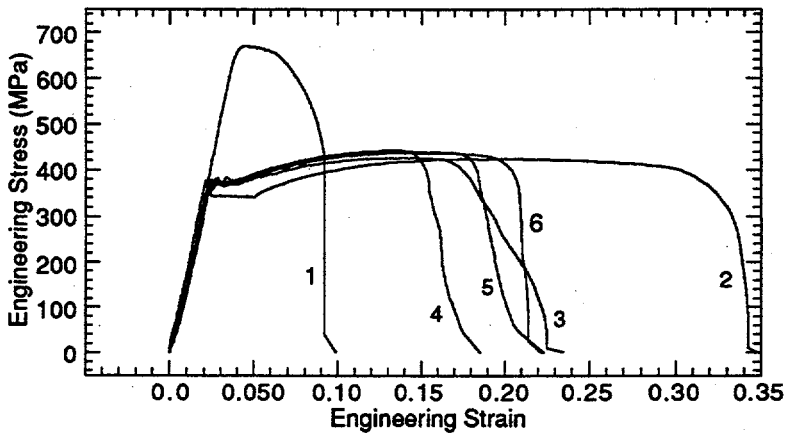

1: as-rolled; 2: annealed 1 h at 1050°C in vacuum
3: 250 h exposure at $pO_2=10^{-6}$ torr at 500°C
4: same as 3 except $pO_2=7.6\times10^{-4}$ torr at 500°C
5: same as 3 except $pO_2=0.1$ torr at 500°C
6: 275 h exposure in 99.999% He environment at 500°C

Figure 4. Engineering stress/engineering strain curves for V-4Cr-4Ti alloy exposed to several pO_2 environments and tested at room temperature.

Table 2. Tensile test data at room temperature for V-4Cr-4Ti alloy exposed to low-pO_2 environments

Specimen pretreatment	Maximum engineering stress (MPa)	Uniform elongation	Total elongation
As-rolled	670.1	0.010	0.067
Vacuum annealing, 1 h at 1050°C (a)	423.7	0.186	0.322
(a) + 250 h in $pO_2 = 1 \times 10^{-6}$ torr at 500°C	426.3	0.127	0.217
(a) + 250 h in $pO_2 = 7.6 \times 10^{-4}$ torr at 500°C	443.0	0.110	0.145
(a) + 250 h in $pO_2 = 0.1$ torr at 500°C	440.6	0.133	0.202
(a) + 275 h in 99.999% He at 500°C	437.8	0.140	0.191

pO_2 levels; however, the uniform and total elongation values decreased substantially, even though exposure time was only 250 h and exposure temperature was relatively modest at 500°C. The specimen tested in 99.999% He gas at 500°C exhibited properties similar to those tested in oxygen environments. Microstructural characteristics of the tested specimens are presently being examined by several electro-optical techniques.

REFERENCES

1. K. Natesan and M. Uz, "Oxidation Kinetics and Microstructure of V-(4-5)wt.% Cr-(4-5)wt.% Ti Alloys Exposed to Air at 300-650°C," Fusion Reactor Materials Progress Report for the Period Ending June 30, 1996, Argonne National Laboratory, DOE/ER-0313/20, p. 105, Oct. 1996.

2. J. W. Patterson, "Conduction Domains for Solid Electrolytes," J. Electrochem. Soc. 118, p. 1033-1039, 1971.

MEASUREMENT OF HYDROGEN SOLUBILITY AND DESORPTION RATE IN V-4Cr-4Ti AND LIQUID LITHIUM-CALCIUM ALLOYS* J.-H. Park, R. Erck, E.-T. Park, S. Crossley, and F. Deleglise (Argonne National Laboratory)

OBJECTIVE

The objective of this study is to develop an in-situ experimental method to determine the solubility and desorption rate of hydrogen in V-4Cr-4Ti and liquid lithium-calcium alloys at temperatures and hydrogen partial pressures in a magnetic fusion reactor.

SUMMARY

Hydrogen solubility in V-4Cr-4Ti and liquid lithium-calcium was measured at a hydrogen pressure of 9.09 x 10^{-4} torr at temperatures between 250 and 700°C. Hydrogen solubility in V-4Cr-4Ti and liquid lithium decreased with temperature. The measured desorption rate of hydrogen in V-4Cr-4Ti is a thermally activated process; the activation energy is 0.067 eV. Oxygen-charged V-4Cr-4Ti specimens were also investigated to determine the effect of oxygen impurity on hydrogen solubility and desorption in the alloy. Oxygen in V-4Cr-4Ti increases hydrogen solubility and desorption kinetics. To determine the effect of a calcium oxide insulator coating on V-4Cr-4Ti, hydrogen solubility in lithium-calcium alloys that contained 0-8.0 percent calcium was also measured. The distribution ratio R of hydrogen between liquid lithium or lithium-calcium and V-4Cr-4Ti increased as temperature decreased (R ≈ 10 and 100 at 700 and 250°C, respectively). However at <267°C, solubility data could not be obtained by this method because of the slow kinetics of hydrogen permeation through the vanadium alloy.

INTRODUCTION

The hydrogen ion density for fusion reactor designs is 1.2 x $10^{20}/m^3$, which corresponds to a pressure of 10^{-5} torr at room temperature. Interaction between hydrogen and first-wall components may not be a significant concern for hydrogen embrittlement of structural materials because of the low density of hydrogen. However, for the design of a liquid-metal cooling system for fusion-reactor blanket applications, it is important to determine the solubility and transport kinetics of hydrogen in the structure and coolant. This study focused on developing methods for in-situ measurement of the solubility of hydrogen in vanadium-base alloys and liquid lithium. Initial results were presented in a previous report [1]. To investigate the effect of oxygen impurity in the vanadium alloy, oxygen-charged samples were tested in addition to those that were used previously [2]. The rate of hydrogen penetration into vanadium and its alloys is among the highest for metals [3-7]. Currently, we are proposing a calcium oxide insulator coating for magnetic-fusion-reactor (MFR) applications because of its a high thermodynamic stability and electrical resistivity [8]. Therefore this study has been extended to include liquid lithium with calcium and calcium oxide.

EXPERIMENTAL PROCEDURES

Sample Preparation

V-4Cr-4Ti. Small tabular-shaped samples of V-4Cr-4Ti (Table 1) were used in the investigation. To determine the oxygen impurity effect, several samples were charged with oxygen by exposure to high-purity argon (99.999%) at 625-650°C for 17 h [2]. Samples were weighed before and after oxygen charging. Typical depth of the oxygen enriched layer was 25 μm, which was determined from back-scattered-electron images obtained in a scanning electron microscope and from microhardness profiles of specimen cross sections.

---

* Work supported by Office of Fusion Energy, U.S. Department of Energy, under Contract W–31–109–Eng–38.

Li and Li-Ca alloys. Approximately 1.3 g of liquid lithium was loaded (Table 2) into a V-7.5Cr-15Ti tube (7.5-mm diameter, 0.4-mm wall thickness, 128.5-mm long, and 6.8289 g) with V-20Ti end plugs (7–mm long, 2.313 g). Small amounts of calcium were added in some experiments. After loading the lithium and lithium-calcium, the tube was sealed by tungsten inert gas (TIG) welding in a helium gas environment. To check for leakage, individual sealed cells were heated in a vacuum chamber at 700°C for 24 h. None of the cells leaked. The cells were cleaned by heating during the leak testing procedure, and after cooling, the outside of the cells was sputter-coated with palladium to avoid surface contamination during hydrogen desorption measurements.

Table 1. Description of samples and experimental procedures

Item Code	Sample wt. (g)	Sample Area (mm^2)	Data No. Code	Materials and Shape	Obtainable Parameters and Calculation	Notes
A			1-6 12-16	Ta tube furnace (178 mm long x 12.7 mm dia. x 0.5 mm thick)	Background for desorption and solubility	
B	21.89	28.68	7-11 17-21 28 41-43	A + V-4Cr-4Ti bar (101.3 x 10.15 x 3.64 mm)	Desorption rate and solubility (B-A)	Solubility and desorption rate in V-4Cr-4Ti
C	10.0	35.4	47-50	A + V-4Cr-4Ti (128.3 x 12.7 x 1 mm)	Desorption rate and solubility (C-A)	Solubility and desorption rate in V-4Cr-4Ti
D	23.5	90.57	44-46 51	A + C+ V-4Cr-4Ti: (128.3 x 6.65 x 1 mm) and (128.3 x 12.7 x 1 mm)	Desorption rate and solubility (D-C) or (D-A)	Solubility and desorption rate in V-4Cr-4Ti
E	–	–	22-25 27	A + V-7.5Cr-15Ti (two plugs)	Background for Liquid-Li (+Ca) solubility	Base for solubility
F	–	31.16	29-32 37-40	A + Cell 2 (Li)	Solubility (F-E)	Solubility in Li
G	–	31.16	33-36	A + Cell 4 (Li+Ca)	Solubility in Li-Ca (G-E), (G-F)	Solubility effect of Ca in Li
H	–	31.16	88-91	A + Cell 1 (Li+Ca)	Solubility (H-E), (H-F), (H-G)	Effect of CaO layer

Table 2. Amount of lithium and calcium loaded in V-7.5Cr-15Ti tubes

V-7.5Cr-15Ti Tube	Li (g)	Ca (g)	wt.% Ca in Ca-Li	Mole fraction Ca in Ca-Li
Cell 1[a]	1.23	0.07	5.4	9.78×10^{-3}
Cell 2	1.34	none	0.0	0.0
Cell 3[b]	1.27	0.01	0.78	1.36×10^{-3}
Cell 4	1.29	0.11	7.86	1.46×10^{-2}

[a]Cell 1 was oxygen-charged in 99.999% argon and had a CaO coating on the inside wall (Ref. 2).

[b]Cell 3 was not tested.

Instrumentation and Method

Hydrogen charging and the desorption procedures and parameters (e.g., volume of the vacuum chamber, steady-state flow rate vs. residual pressure) were described in a previous report [1]. Figure 1 is a schematic drawing of the apparatus.

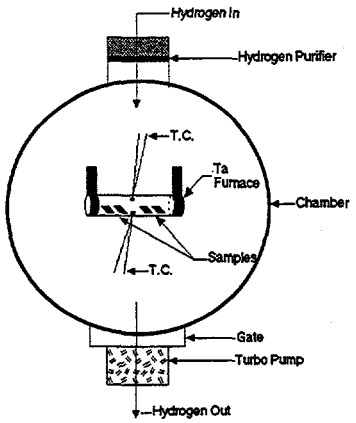

Figure 1.
Schematic drawing of the apparatus

RESULTS AND DISCUSSION

V-4Cr-4Ti

Desorption experiment. Figure 2 (a) shows the integral amount of hydrogen evolved at 518°C during degassing of an oxygen-charged V-4Cr-4Ti specimen after exposure to hydrogen for 1, 5, and 18 h and for an as-received V-4Cr-4Ti specimen after a 30 h exposure to hydrogen; Fig. 2 (b) shows hydrogen desorption rates during degassing of the specimens at these times. During degassing experiments at higher temperature, the specimen was held at 518°C for 2 min before heating to a higher temperature (850°C), at which the amount of degassed hydrogen was monitored by hydrogen pressure and the calculated flow rate, which was integrated with time to obtain solubility data as described previously [1].

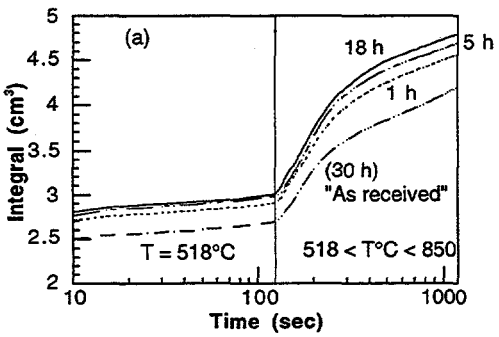

Figure 2(a).
Integral amount of hydrogen evolved during degassing of oxygen-charged V-4Cr-4Ti at 518°C after exposure to hydrogen for 1, 5, and 18 h and of as-received V-4Cr-4Ti after hydrogen charging for 30 h

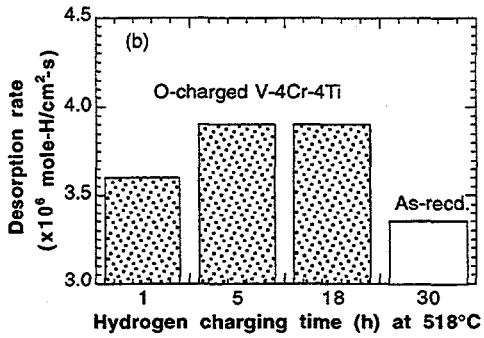

Figure 2(b).
Desorption rates of hydrogen from oxygen-charged V-4Cr-4Ti at 518°C after hydrogen-charging for 1, 5, and 18 h, and for as-received V-4Cr-4Ti after 30 h

Oxygen in V-4Cr-4Ti increases both the hydrogen solubility and desorption kinetics, as shown in Fig. 2. When we examine the degassing data at 518°C in Fig. 2 (b), initially (0 - 2 min), the integrated hydrogen desorption is higher for the oxygen-charged sample. The degassing process at 518°C showed a slight difference in the amount of hydrogen evolved from the specimen at 5 and 18 h. This means that a 1-mm-thick oxygen-charged V-4Cr-4Ti specimen is not equilibrated in 5 h. Therefore, the diffusivity of hydrogen (D_H) in oxygen-charged V-4Cr-4Ti at 518°C should be $D_H \leq 5.56 \times 10^{-7}$ mm^2/s, a value that is similar to the value for the as-received samples and much lower than literature values [5,6]. To resolve this difference, more effort will be required to analyze the degassing of components in the apparatus by mass spectroscopy with a residual-gas analyzer. Figure 4 shows the temperature dependence of the hydrogen desorption rate obtained from the difference of curves C and D in Fig. 3. Figure 5 shows the Vickers hardness-versus-depth profile for as-received, oxygen-charged, and an oxygen-charged sample equilibrated with hydrogen at 518°C. The decrease in hardness near the surface of the hydrogen-equilibrated sample indicates that, during the degassing process, oxygen was also removed to a depth of ≈8 μm, as shown in Fig. 5. The measured desorption rate of hydrogen in V-4Cr-4Ti is a thermally activated process and the activation energy is 0.067 eV. However, more work is needed to determine the dependence of D_H on microstructure, as shown for nickel in Ref. 9.

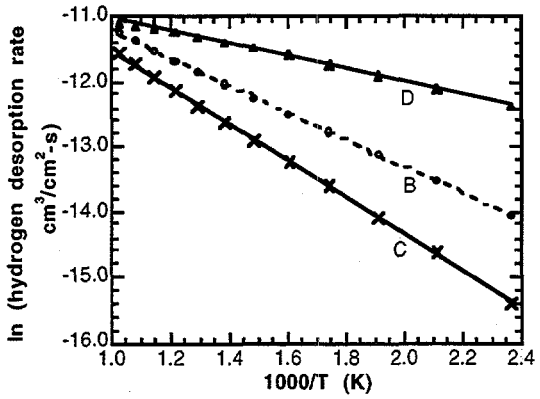

Figure 3.
Hydrogen desorption rate vs. reciprocal temperature for V-4Cr-4Ti. B, C, and D denote the Item Code in Table 1.

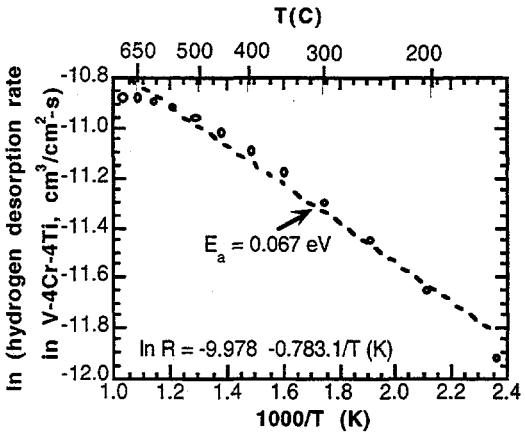

Figure 4.
Hydrogen desorption rate vs. reciprocal temperature for V-4Cr-4Ti. Data obtained by taking the difference between C and D in Fig. 3.

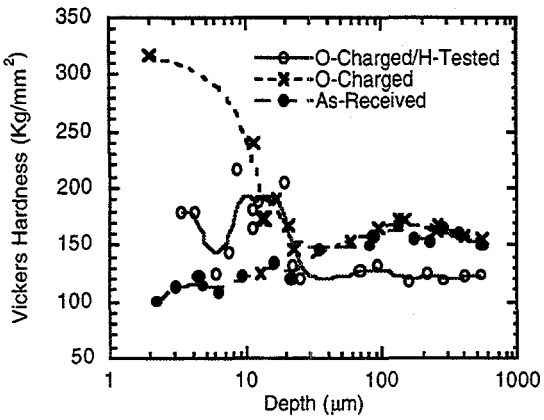

Figure 5.
Vickers hardness-vs.-depth profiles for as-received and oxygen-charged samples, and oxygen-charged samples after hydrogen charging

Li or Li-Ca

Solubility measurement. Solubility was determined according to item codes F-H in Table 1. Figure 6 indicates typical hydrogen desorption behavior for liquid-metal cells (e.g., Cell 4 in Table 2) that contained a mixture of lithium (1.29 g) and calcium (0.11 g), i.e., 7.86 wt.% of calcium at four temperatures (267-674°C). The difference in the integrated amount of hydrogen at the various temperatures indicates the temperature dependence of hydrogen solubility. However, the result at the lowest temperature (267°C) does not show the expected profile (Fig. 6). We assume that this behavior is caused by slow hydrogen penetration through the vanadium capsules at low temperatures. Even after 756 h at 267°C, the specimen had not reached the equilibrium partial pressure of hydrogen.

Hydrogen degassing from the tantalum furnace for 900 s at temperatures between 260 and 600°C was almost constant, 3200-3300 mm^3. Figure 7 shows results for liquid lithium and two lithium-calcium alloys and the temperature dependence of the solubility of hydrogen in lithium from the literature [10]. Figure 8 shows the combined results for lithium, lithium-calcium, and V-4Cr-4Ti obtained from this study. When we compare the solubility of hydrogen in liquid metals with that in V-4Cr-4Ti (Fig. 8), we can obtain the hydrogen distribution ratio between liquid lithium or Li-Ca alloys and V-4Cr-4Ti. The hydrogen distribution between a liquid-metal coolant and the structural material is an essential factor in the design of fusion reactors. Figure 9 indicates that the hydrogen distribution ratio R between liquid lithium or lithium-calcium alloys and V-4Cr-4Ti decreases with temperature; R ≈10 and 100 at 700 and 250°C, respectively.

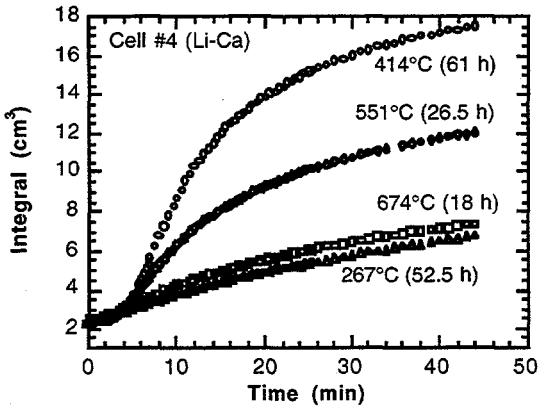

Figure 6.
Typical integrated amount of hydrogen degassed versus time for Li-7.86 wt.% Ca at temperatures between 267 and 674°C

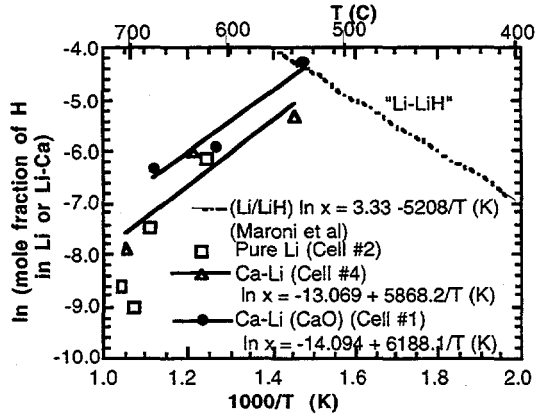

Figure 7.
ln mole fraction of H in Li, Li-Ca and Li-LiH [10] versus reciprocal temperature

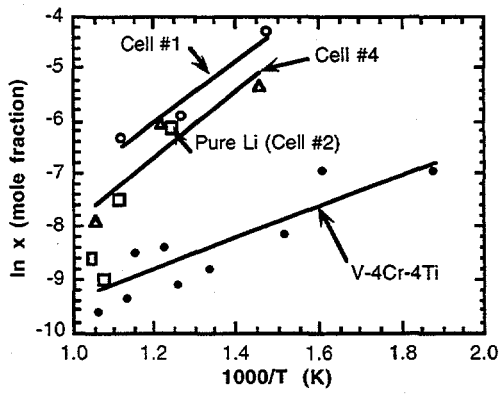

Figure 8.
ln mole fraction of H in Li, Li-Ca, and V-4Cr-4Ti versus reciprocal temperature

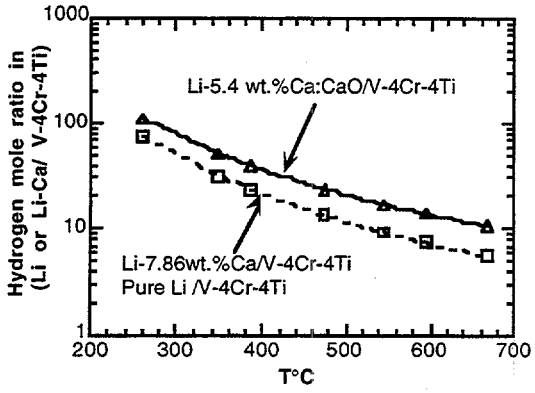

Figure 9.
Hydrogen molar distribution ratio between in Li and Li-Ca and in V-4Cr-4Ti versus temperature

CONCLUSIONS

An in-situ experimental method was developed to determine hydrogen solubility and hydrogen desorption rate in a vanadium-base alloy and liquid lithium-calcium alloys at MFR temperatures and hydrogen partial pressures. The solubility of hydrogen in V-4Cr-4Ti and liquid lithium-calcium has been measured at a hydrogen pressure of 9.09×10^{-4} torr at temperatures between 250 and 700°C.

To determine the effect of oxygen impurity in a vanadium-base alloy on hydrogen solubility and desorption, oxygen-charged V-4Cr-4Ti was also investigated. Hydrogen solubility in V-4Cr-4Ti and liquid lithium decreased with temperature. Oxygen in V-4Cr-4Ti increases hydrogen solubility and desorption kinetics. Hydrogen solubility in a Li-8 wt.% Ca alloy was also measured.

The ratio R for the distribution of hydrogen between liquid lithium or lithium-calcium alloys and V-4Cr-4Ti increases as temperature decreases (R ≈10 and 100 at 700 and 250°C, respectively). However, at temperatures <267°C, solubility data could not be obtained by this method because of the slow kinetics of hydrogen permeation through the vanadium alloy. The measured desorption rate of hydrogen in V-4Cr-4Ti is a thermally activated process; the activation energy is 0.067 eV.

ACKNOWLEDGMENTS

C. Konicek sealed the liquid-metal cells by TIG welding. S. Crossley participated as a student in the summer research program, and F. Deleglise participated as a U.S./France foreign exchange student.

REFERENCES

[1] J.-H. Park, G. Dragel, R. Erck, and D. L. Smith, *Solubility and Desorption of Hydrogen in V-4Cr-4Ti and Lithium*, in Fusion Materials, pp. 240-243, DOE/ER-0313/19 (1995).

[2] J.-H. Park, D. Kupperman, and E.-T. Park, *Mechanical Properties of and Phase Transformation in V-Cr-Ti-O Solid Solutions, in* Elevated Temperature Coatings: Science and Technology II, N. B. Dahotre and J. N. Hampikian, eds., p. 323, The Minerals, Metals, and Materials Society (1996).

[3] J. Volkl and G. Alefeld, in Topics in Applied Physics: Vol. 28, *Hydrogen in Metals I, Basic Properties*, G. Alefeld and J. Volkl, eds., Chap 12, p. 321, Springer-Verlag, Berlin, Heidelberg, New York (1978).

[4] J. Volkl and G. Alefeld, in *Diffusion in Solids, Recent Developments*, A. S. Nowick and J. J. Burton, eds, p. 231, Academic Press, New York (1975).

[5] R. Cantelli, F. M. Mazzolai, and M. Nuovo, J. Phys. Chem. Solids **31**, 1811 (1970).

[6] N. Bose and H. Zuchner, Z. Naturforsch **31a**, 760 (1976).

[7] B. Y. Liaw, G. Deublein, and R. A. Huggins, J. Electrochem. Soc., **142**(7) 2196 (1995).

[8] J.-H. Park, *Intermetallic and Electrical Insulator Coatings on High-Temperature Alloys in Liquid-Lithium Environments,* Elevated Temperature Coatings: Science and Technology I, N. B. Dahotre, J. N. Hampikian, and J. J. Stiglich, eds., p. 227, The Minerals, Metals, and Materials Society (1995).

[9] A. M. Brass and A. Chanfreau, Acta Metal. **44**(9) 3823 (1996).

[10] N. Rumbaut, F. Casteels, M. Brabers, *Thermodynamic Potential of Nitrogen, Carbon, Oxygen, and Hydrogen in Liquid Lithium and Sodium,* in Material Behavior and Physical Chemistry in Liquid Metal Systems, H. U. Borgstedt, ed., p. 437, Plenum Press, New York and London (1981).

EVALUATING ELECTRICALLY INSULATING FILMS DEPOSITED ON V–4%Cr–4%Ti BY REACTIVE CVD*

J.–H. Park and W. D. Cho (Argonne National Laboratory)

OBJECTIVE

Corrosion resistance of structural materials and magnetohydrodynamic forces and their influence on thermal hydraulics and corrosion are major concerns in the design of liquid–metal blankets for magnetic fusion reactors. The objective of this study is to evaluate electrically insulating films that were deposited on V–4%Cr–4%Ti by a reactive chemical vapor deposition (CVD) method.

SUMMARY

Previous CaO coatings on V–4%Cr–4%Ti exhibited high–ohmic insulator behavior even though a small amount of vanadium from the alloy was incorporated in the coating. However, when the vanadium concentration in the coating is > 15 wt.%, the coating becomes conductive. When the vanadium concentration is high in localized areas, a calcium vanadate phase that exhibits semiconductor behavior can form. To explore this situation, CaO and Ca–V–O coatings were produced on vanadium alloys by chemical vapor deposition (CVD) and by a metallic-vapor process to investigate the electrical resistance of the coatings. Initially, the vanadium alloy specimens were either charged with oxygen in argon that contained trace levels of oxygen, or oxidized for 1.5–3 h in a 1% CO-CO_2 gas mixture or in air to form vanadium oxide at 625–650°C. Most of the specimens were exposed to calcium vapor at 800–850°C. Initial and final weights were obtained to monitor each step, and surveillance samples were removed for examination by optical and scanning electron microscopy and electron–energy–dispersive and X–ray diffraction analysis; the electrical resistivity was also measured. We found that Ca–V–O films exhibited insulator behavior when the ratio of calcium concentration to vanadium concentration R in the film was > 0.9, and semiconductor or conductor behavior for R < 0.8. However, in some cases, semiconductor behavior was observed when CaO-coated samples with R > 0.98 were exposed in liquid lithium. Based on these studies, we conclude that semiconductor behavior occurs if a conductive calcium vanadate phase is present in localized regions in the CaO coating.

INTRODUCTION

Corrosion resistance of structural materials and magnetohydrodynamic (MHD) forces and their influence on thermal hydraulics are major concerns in the design of a liquid–metal cooling system for a first–wall/blanket in a magnetic fusion reactor (MFR).[1,2] Vanadium–base alloys (V–Ti or V–Ti–Cr) are leading candidate materials for structural applications in fusion reactors.[3] The objective of this study is to develop stable, corrosion–resistant coatings, as well as insulator coatings, at the liquid–metal/structural–material interface. Previous studies focused on in–situ formation of AlN on as–received and prealuminided vanadium alloys in liquid–lithium environments.[4,5] Subsequent work addressed in–situ formation of CaO in a liquid–lithium environment because the electrical resistivity of CaO is 10,000 times greater than that of AlN, and because, among the available insulator candidates (i.e., CaO, Y_2O_3, BeO, MgO, $MgAl_2O_4$, $Y_3Al_2O_{12}$, etc.), CaO exhibits high thermodynamic stability in liquid lithium. [5,6]

The coatings should be formable on various shapes, such as the inside of tubes or irregular shapes, to prevent adverse currents generated by MHD forces from passing through the structural walls. The coatings could also improve general corrosion resistance and act as a diffusion barrier for hydrogen isotopes, i.e., deuterium and tritium. Based on our previous work, CaO coatings on V–4%Cr–4%Ti exhibited high–ohmic-insulator characteristics even when a small amount of vanadium was incorporated in the CaO. However, the coating becomes conductive when the vanadium concentration is >15 wt.%.

---

* Work supported by Office of Fusion Energy, U.S. Department of Energy, under Contract W–31–109–Eng–38.

We hypothesize that, despite the highly resistive nature of CaO, when vanadium is incorporated in the material a calcium vanadate phase that exhibits semiconductor behavior forms in local regions. To explore this hypothesis, CaO and Ca–V–O coatings were produced on vanadium–base alloys by chemical vapor deposition (CVD) and metallic-vapor processes to investigate their electrical behavior. In some cases, when CaO–coated samples were exposed in liquid lithium, semiconductor behavior was observed and we sought the reason for this phenomenon.

Synthesis of Ca-Vanadates by Self-Ignition Reaction

To examine the electrical behavior of CaO–V_xO_y specimens, several calcium vanadates were synthesized by a self-reactive method. Calcium and vanadium pentoxide (V_2O_5) were mixed in various proportions (5-90 wt.% of calcium) and allowed to react in vacuo by self-ignition in sealed quartz capsules in response to heating with a hydrogen–flame torch, and in a Type 304 stainless steel (SS) tube in response to heating in a furnace. An exothermic reaction occurred in only ≈2 s. The synthesized samples were examined by scanning electron microscopy/electron dispersive spectroscopy (SEM/EDS), and electrical resistance was determined. All samples fabricated by these methods were conductive and the results were similar to those of F. Iga and Y. Nishihara,[7] except for single–phase CaO, which showed high resistance.[5] The results indicate that calcium vanadates do not provide sufficient electrical resistance for insulator coatings in MFR applications.

High–Temperature Metallic Vapor Deposition of CaO and Calcium Vanadate Coatings

Solid–state interactions between calcium vapor and oxygen–charged V–4%Cr–4%Ti were investigated. An as–received V–4%Cr–4%Ti sheet was cut into 12.7 x 12.7 x 1.0-mm and 9.4 x 9.4 x 1.0-mm specimens and then ultrasonically cleaned in isopropyl alcohol; the specimens were used for electrical resistance and weight–gain measurements, respectively. The near–surface region of the specimens was charged with oxygen by heating the specimens for 2–3 h in argon (99.999% pure with 5–10 ppm oxygen), or in a 1% CO-CO_2 gas mixture or air to form vanadium oxide at 625 to 650°C. The specimens were placed above a calcium vapor source in a Knudsen sublimation cell that was contained in a Type 304 SS chamber surrounded by a furnace (Fig. 1). A detailed description of the apparatus and method of preparation of oxygen–charged vanadium alloys was described in Ref. 8.

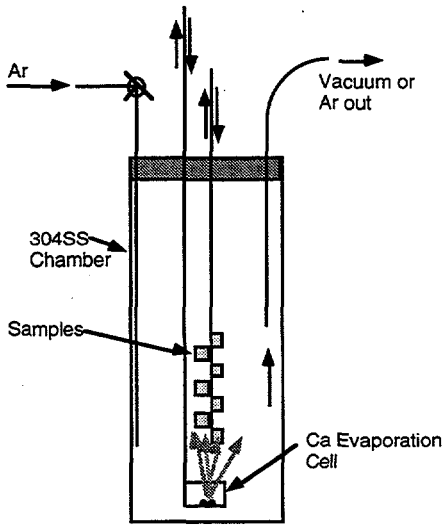

Figure 1.
Schematic diagram of CVD apparatus

In another apparatus, a Type 304 SS chamber was heated from 25 to 850°C within ≈1 h while purging with 99.999% argon; it was then cooled. Vanadium–alloy samples and a calcium source vessel were then placed

near the bottom and top of the chamber, respectively. The calcium source at the top of the furnace remained at room temperature when the furnace was heated. The vanadium alloy specimens in these experiments were either charged with oxygen for 2–3 h in argon that contained 5–10 ppm oxygen or oxidized in air to form vanadium oxide. Several specimens were retained to quantify oxygen uptake by the specimens during the oxygen-charging step. Subsequently, the stainless steel chamber was evacuated with a vacuum pump and the calcium reservoir was lowered into the hot zone of the furnace to evaporate calcium, which deposited on and reacted with the oxygen–charged and oxidized vanadium alloy surfaces at 800-850°C for 1.5–4 h. The formation of several vanadates ($Ca–V_xO_y$) can be predicted from the CaO–vanadium oxide phase diagram.[9] These phase relationships are the basis for the formation of vanadate coatings on vanadium and its alloys. Calcium reacts with the oxygen–precharged surface and diffuses through the CaO or $Ca–V_xO_y$ layer, as shown in Fig. 2. Reactions for the formation of the coatings are

$$Ca\ (vapor) + \underline{O}\ (alloy) = CaO, \tag{1}$$

$$Ca\ (vapor) + V_xO_y\ (alloy\ surface) = CaV_xO_y, \tag{2}$$

where $\underline{O}$ represents the oxygen activity at the interface between CaO and oxygen–charged vanadium alloy. These reactions occur spontaneously, and the rate–determining step most likely is ionic diffusion (Ca^{+2}) through the CaO layer.

EDS analysis of the surface of a CaO coating formed on V-4%Cr-4%Ti at 850°C indicated >97 at.% calcium, and the calcium vanadate coatings contained 15-80 at.% calcium. SEM of CVD coatings on V-4%Cr-4%Ti at 850°C revealed uniform surfaces with grain sizes of 0.7-3 μm for CaO and 3-8 μm for the calcium vanadate coatings. The X-ray diffraction spectrum of the CaO coating on V-4%Cr-4%Ti clearly showed the two sets of peaks for CaO and V-4%Cr-4%Ti and indicated no other phases. The X-ray beam can penetrate ≈40 μm into CaO, and into a film thickness of ≈3 μm; the spectrum of the V-4%Cr-4%Ti substrate is also present.

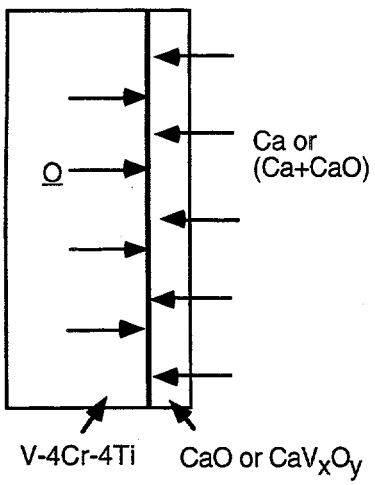

Figure 2.
Schematic diagram of solid–state reaction steps at V–4Cr–4Ti/CaO interface: Ca + O = CaO: initial reaction

Sublimation of calcium in a relatively low vacuum of 10^{-4}–10^{-5} torr, in which oxygen was present as an impurity, enabled the formation of CaO clusters by oxidation of calcium vapor inside the chamber. After coating the V–4%Cr–4%Ti specimens at 800 or 850°C for electrical resistance measurements, the system was cooled to room temperature while purging with 99.999% argon. In one experiment, the calcium reservoir was raised to the top of the furnace (cool region) and the specimens remained at temperature for 3–5 h to determine if any additional oxidation occurred. No appreciable weight gain or loss was detected after CaO had been deposited. The weight gain for CaO coatings on V–4%Cr–4%Ti specimens at 230 min (≈4 h) was determined over the range of 309–883°C and is given by

$$\log (\text{Wt. gain, g/cm}^2) = -0.983 - 2444/T\ (\text{K}), \quad (3)$$

which corresponds to coating thicknesses between ≈0.02 and 2.4 μm at 309–883°C for a CaO density of 3.346 gm/cm^2.

To determine the electrical resistance of the coatings and also facilitate SEM/EDS analysis, the samples were coated with gold by sputter-deposition of an array of ≈1–mm-diameter discs on the surface of the coatings (Fig. 3). The discs, when placed in contact with a gold foil, provided a good electrical connection over a large area of the specimen. Ohmic resistance was measured at 25–500°C in air (Fig. 4). Only the specimen charged with oxygen in 99.999% argon and coated with calcium by CVD exhibited insulator behavior. The specimens oxidized in air and in a 1% CO-CO_2 gas mixture and coated by CVD showed semiconductor behavior.

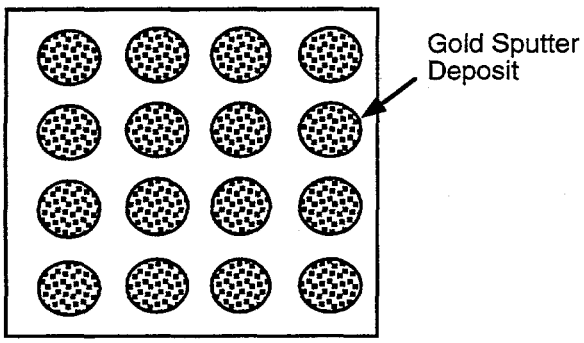

Figure 3.
Schematic diagram of gold sputter coating on CaO coating for electrical resisitivity measurements

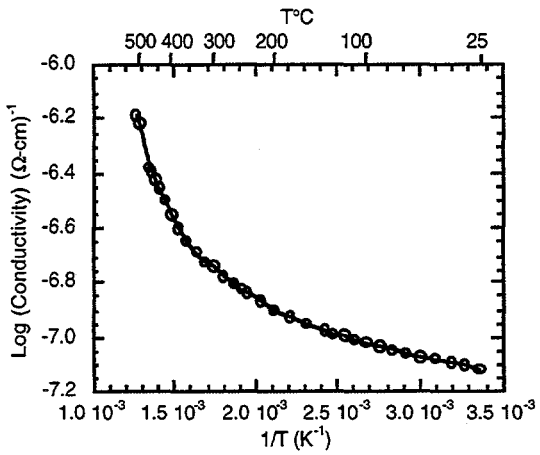

Figure 4.
Log (conductivity) vs. 1/T for the CaO coating in air

CONCLUSIONS

CaO and calcium vanadate films were prepared on vanadium alloys and Types 304 and 316 SS by chemical vapor deposition (CVD) and high–temperature metallic-vapor deposition at 800–850°C. The films were examined by optical and scanning electron microscopy and by electron–energy–dispersive and X–ray diffraction analysis. We found that when the ratio of calcium to vanadium in the oxide coating was >0.9, the film was a good insulator, whereas when the ratio was < 0.8, the coating layer exhibited semiconductor or metallic-conduction behavior. However, in some cases, when a CaO-coated sample was immersed in liquid lithium, semiconductor behavior was observed even though the calcium/vanadium ratio was >0.98 for

a wide surface area. We attribute semiconductor behavior to local regions that contained a conductive calcium vanadate phase in the CaO coating.

The formation of either vanadate or titanate phases in thin (1–5 μm) coatings may not provide sufficient electrical resistance for magnetic fusion reactor (MFR) applications and could present potential problems regarding liquid–metal compatibility.

We believe that the oxygen charging and reactive CVD technique can be extended to other oxides, e.g., MgO, BeO, $MgAl_2O_4$, $Y_3Al_2O_{12}$, etc., to determine whether they are suitable for insulator coatings in MFR applications.

SUGGESTED FUTURE WORK

Several other ternary oxide systems (e.g., spinel, $MgAl_2O_4$; and/or garnet, $Y_3Al_2O_{12}$) could be fabricated by the reactive CVD method and their insulator characteristics could be evaluated before and after exposure to liquid lithium.

CaO films on vanadium–base alloys could be fabricated by oxygen charging with nitrogen–argon gas mixtures to minimize the formation of calcium vanadates. These environments may suppress outward diffusion of vanadium during CaO film formation because of the presence VN or TiN phases. In–situ electrical resistivity should be measured to assess the potential of this approach.

REFERENCES

1. C. C. Baker et al., *Tokamak Power System Studies FY 1985*, Argonne National Laboratory Report ANL/FPP–85–2 (1985).
2. T. Kammash, *Fusion Reactor Physics*, Chapter 15, Ann Arbor Science Pub. Inc., Ann Arbor, MI (1975), pp. 405–439.
3. R. F. Mattas, B. A. Loomis, and D. L. Smith, *Vanadium Alloys for Fusion Reactor Applications*, JOM, **44**(8), 26 (1992).
4. J.–H. Park, T. Domenico, G. Dragel, and R. W. Clark, *Development of Electrical Insulator Coatings for Fusion Power Applications,* Proc. 3rd Intl. Symp. on Fusion Nuclear Technology (ISFNT), June 27–July 1, 1994, Los Angeles.
5. J.–H. Park and G. Dragel, *Development of Aluminide Coatings on Vanadium–Base Alloys in Liquid Lithium*, Fusion Reactor Materials Semiannual Progress Report for the Period Ending March 31, 1993, DOE/ER–0313/14, pp. 405–410 (1993).
6. J.–H. Park and W. D. Cho, *Fabrication of Intermetallic Coatings for Electrical Insulation and Corrosion Resistance on High Temperature Alloys*, Surface Modification Technologies IX, eds. T. S. Sudarshan, W. Reitz, and J. J. Stiglich, The Minerals, Metals & Materials Society (1996), pp. 151–166.
7. F. Iga and Y. Nishihara, *Metal-Insulator Transition with Oxygen Content in* $CaVO_{3-y}$, J. Phy. Soc., Jpn, **61** (6), 1867-1870 (1992).
8. J.-H. Park, D. Kupperman, and E. T. Park, *Mechanical Properties of V-Cr-Ti-(O and N) Solid Solutions,* Submitted to Acta Materialia (1997).
9. A. N. Morozov, Metallurg., **13**(12), 24 (1938).

RECENT PROGRESS ON GAS TUNGSTEN ARC WELDING OF VANADIUM ALLOYS

— J. F. King, M. L. Grossbeck, G. M. Goodwin, and D. J. Alexander (Oak Ridge National Laboratory)

SUMMARY

This is a progress report on a continuing research project to acquire a fundamental understanding of the metallurgical processes in the welding of vanadium alloys. It also has the goal of developing techniques for welding structural vanadium alloys. The alloy V-4Cr-4Ti is used as a representative alloy of the group; it is also the prime candidate vanadium alloy for the U.S. Fusion Program at the present time. However, other alloys of this class were used in the research as necessary. The present work focuses on recent findings of hydrogen embrittlement found in vanadium alloy welds. It was concluded that the atmosphere in the inert gas glove box was insufficient for welding 6mm thick vanadium alloy plates.

PROGRESS AND STATUS

Introduction

The vanadium alloy welding program at ORNL focuses on both gas tungsten arc (GTA) and electron beam (EB) welding methods. The alloy V-4Cr-4Ti of Teledyne Wah Chang heat 832665 was used for the welding research. However, some welds were made on V-45Cr-5Ti from Teledyne Wah Chang heat 832394. Thin plate, usually 0.76 or 1.0 mm in thickness is used for welds that will be studied by microanalytical techniques or by tensile testing. Plate 6mm in thickness is used for welds to be studied by charpy testing as well as microanalytical techniques. The 6mm plate proved to be more challenging since multiple passes are required and the larger heat sink results in slower cooling of the weld zone with consequent contamination by higher levels of impurities.

Experimental Methods and Results

GTA welds in the 6mm plate were made in an argon filled glove box previously evacuated to a pressure of the order of 10-4 Pa. Moisture levels typically below 40 ppm as measured by a CEC moisture monitor were achieved. A 75° included angle V-groove with a 2.4 mm root opening joint geometry was used for the weldments. The filler wire was of matching composition of the same V-4Cr-4Ti heat as the base metal. Multi-pass welds were made using direct current, electrode negative, at a current range of 100 to 140 amperes and 12 volts.

Earlier research on this alloy and the similar V-5Cr-5Ti alloy using similar welding methods has shown that a post-weld heat treatment (PWHT) is necessary [1]. Charpy V-notch testing demonstrated shifts in the ductile to brittle transition temperature (DBTT) of greater than 200°C following welding. Post weld heat treatments resulted in some cases, depending upon the alloy, initial heat treatment of the base metal, and the temperature of the PWHT, in a return of the DBTT to a lower temperature than that of the base metal. This phenomenon was previously explained in terms of precipitation of oxygen, primarily with titanium. As has been observed in refractory metals, precipitates dissolve upon melting of the alloy [2]. The rapid cooling during welding quenches large concentrations of oxygen into the matrix leading to severe hardening and embrittlement. The PWHT allows sufficient time for the oxygen and titanium to form TiO and similar titanium oxycarbonitrides which getter the oxygen and produce a ductile matrix.

Data from Charpy testing is shown in Fig. 1 for as-welded specimens as well as specimens given post-weld heat treatments at various temperatures for a fixed time of two hours. All data were obtained from a single weld, designated GTA10. More consistent curves were usually obtained with other welds; however, occasionally a datum point would fall on the lower shelf with adjacent points at both higher and lower temperatures on the upper shelf. In these cases, the fracture surfaces of the lower-shelf samples revealed almost entirely cleavage fracture. This report will address the problems encountered with consistency of the data and the possible sources of the observed embrittlement. In Fig. 1, the trends are discernable, but the scatter caused by erratic lower shelf values is so high that it is difficult to draw conclusions from the plot. As with previous specimens, the outlying lower shelf specimens failed by cleavage. They did not fail due to an existing flaw in the weld resulting in a reduced load support area. The cleavage fracture resulted from a serious embrittlement mechanism.

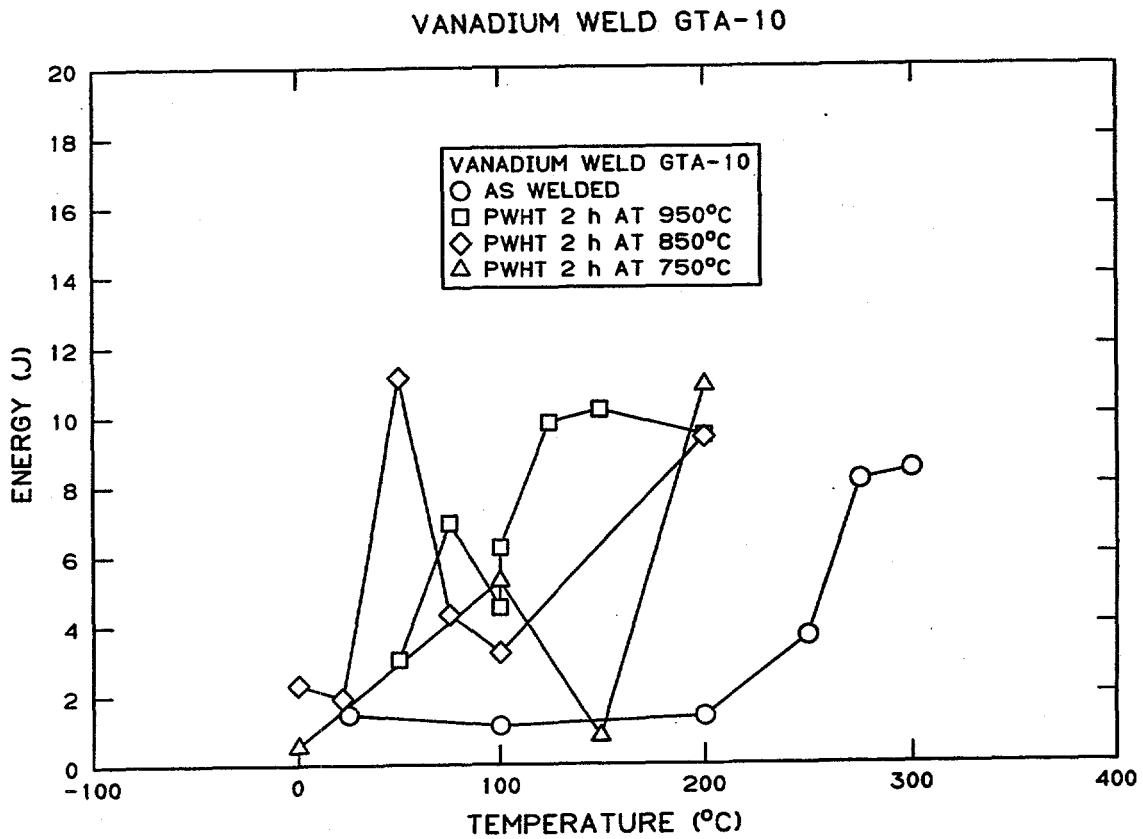

Fig. 1. Charpy impact data from gas-tungsten-arc weld GTA-10 in V-4Cr-4Ti. Samples were given three different post-weld heat treatments (PWHT) as indicated.

The problem was more emphatically brought to light with the subsequent GTA weld (Designated GTA11). GTA11 was prepared using the same procedure as for the previous weld, GTA10. When a sample was cut from one end of the weld for metallography, the plate cracked. As can be seen in Fig. 2, brittle transgranular cracks appear. There are also intergranular cracks connecting with transgranular cracks, but it is not apparent which initiated the failure. The series of non-linking parallel cleavage cracks is very similar to those observed in niobium embrittled by hydrogen [3].

DISCUSSION

Because of the similarity with hydrogen embrittlement in this group of metals, analyses were made for hydrogen and other interstitials. The analyses were done by inert gas fusion analysis by the Leco Corporation, St. Joseph, MI. Samples of as received alloy as well as acid -etched material was analyzed with the results shown in Table 1. Analyses from earlier welds are included in the table to aid in locating the source of the embrittlement. The hydrogen concentration in the etched V-4Cr-4Ti sample shows that the acid etch does not appear to add hydrogen to the alloy. In general, EB welding does not suffer from the hydrogen contamination problem except for one weld, EBW11. It is believed that a leak in the system or a

nother failure in the vacuum system is responsible for the elevated hydrogen concentration in EBW11; the hydrogen concentration is four to ten times that observed in two earlier EB welds. The GTA welds appear to have higher hydrogen concentrations than the EB weld samples. The weld of present interest is GTA11 which had hydrogen concentrations between 50 and 60 wt. ppm in both the fusion zone and the base metal. Considering the high diffusivity of hydrogen in vanadium, the similarity of hydrogen concentrations in the fusion zone and base metal is not unexpected.

Table 1. Concentration of Interstitial Elements, wt. ppm

Base Metal	Weld Metal	H	O	N	C
	GTA11	58.5	446	288	—
GTA11		53.5	364	96	—
V-4Cr-4Ti (as received)		316	114	—	—
V-4Cr-4Ti (acid etched)		1.2	—	—	—
Weld Wire V-4Cr-4Ti		—	360	109	155
	EBW11	36.4	327	99	—
EBW11		23.1	323	97	—
	GTA2 (VQ11 ductile)	11.2	—	—	—
	GTA2 (VQ09 brittle)	10.1	—	—	—
	GTA3	20.5			
	GTA8		410	98	—
GTA8			332	96	—
	EB2	2.8	—	—	—
	EBW12	7.9			

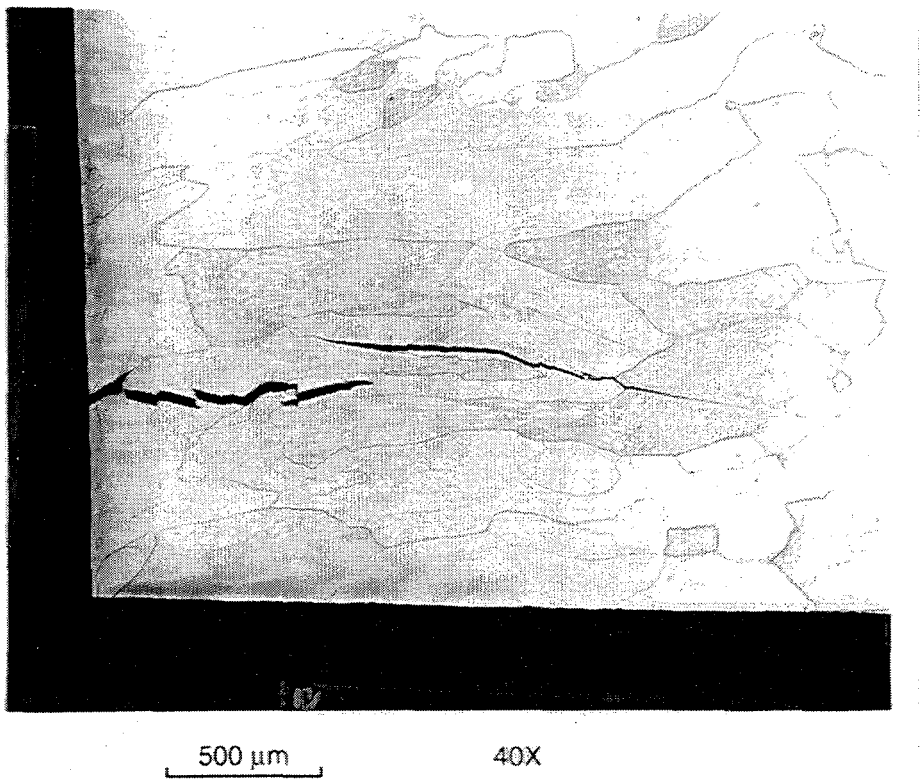

Fig. 2. View of fusion zone of weld GTA-10 in V-4Cr-4Ti showing brittle cracking following cutting of metallography sample (sample 96-0218).

Eustice and Carlson have observed only a mild drop in ductility at room temperature upon the addition of 50 wt. ppm hydrogen [4]. However, in their research, the onset of embrittlement occurs at slightly lower temperatures. Westlake has determined the hydride solvus temperature to be -68°C at 50 wt. ppm hydrogen in vanadium [5]. These observations do not support embrittlement and cracking at such a level of hydrogen. However, hydrogen embrittlement has been shown to occur at slightly higher temperatures in refractory metals because of stress-induced hydride at the crack tip [3]. Such a shift is only expected to be on the order of 10-20°C; however, although 50 wt. ppm does not appear to be an embrittling concentration, the stronger an alloy becomes, the larger the shift in the formation of hydride. As shown in Table 1 the oxygen and nitrigen concentrations in GTA 11 were also high. Such a high impurity concentrations, which might have resulted from a leak in the welding chamber (although none were found), could harden the alloy thus increasing the shift in the hydride solvus beyond the expected 10 or 20 degrees. The chromium and titanium alloying elements could also shift the phase diagram sufficiently to make the embrittlement occur at a slightly higher temperature. Experimental evidence exits on the V-4Cr-4Ti alloy itself. Roehrig et. al observed that 500 wt. ppm hydrogen was necessary to induce room temperature embrittlement as measured by tensile testing but that, in the presence of 850 wt. ppm oxygen, a factor of four reduction in ductility was observed with only 90 wt. ppm hydrogen [6]. Another synergistic mechanism might exist in addition to lattice hardening. In any case, it would be expected to be operational in the welded sample as well. Detailed x-ray phase analysis would have to be done to confirm this mechanism.

At the present time, a better approach is to reduce moisture and oxygen contamination in the welding glove box atmosphere to achieve lower levels of interstitials in the welds. An inert gas purification system as shown in Fig. 3 has been added to the welding glove box. The purification system consists of a gettering furnace which contains a high purity titanium charge that removes oxygen, nitrogen, carbon, and water to extremely low levels. A molecular sieve trap will also be added at the gettering furnace inlet to reduce moisture levels still further. This system is undergoing testing and adjustments at the present time.

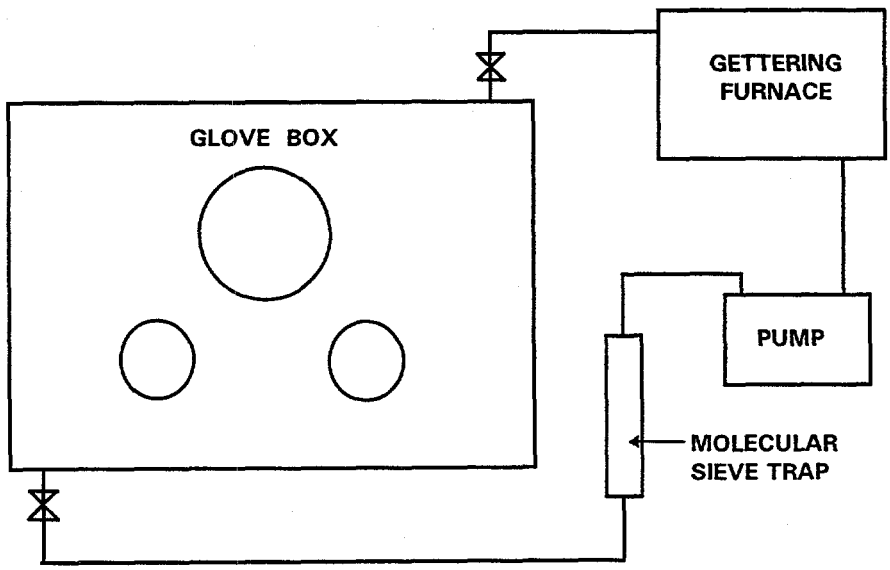

Fig. 3. Diagram of purification system to remove oxygen and water from welding chamber.

Conclusions

1. A post-weld heat treatment is required for welding V-Cr-Ti alloys.
2. Special precautions must be taken to avoid hydrogen embrittlement in GTA welding of V-Cr-Ti alloys.

Future Work

This is a continuing research project. The gettering system is expected to be put into operation during the next reporting period. This will enable uncontaminated welds to be made thus permitting detailed studies of the effects of post-weld heat treatments. It will also permit studies of the effects of impurities in welds.

REFERENCES

1. J. F. King, G. M. Goodwin, and D. J. Alexander, "Welding Development for V-Cr-Ti Alloys," *Fusion Materials Semiannual Progress Report for Period Ending September 30, 1994*, DOE/ER-0313/17 (1995), p. 152.

2. J. R. DiStefano, *Review of Oxidation of Nb-1Zr*, Oak Ridge National Laboratory, ORNL/TM-10907 (1989).

3. M. L. Grossbeck and H. K. Birnbaum, "Low Temperature Hydrogen Embrittlement of Niobium II--Microscopic Observations," *Acta Met. 25* (1977), p. 135.

4. A. L. Eustice and O. N. Carlson, "Effect of Hydrogen on the Tensile Properties of Iodide Vanadium," *Trans. AIME 221* (1961), 238.

5. D. G. Westlake, "A Resistometric Study of Phase Equilibria at Low Temperatures in the Vanadium-Hydrogen System," *Trans AIME 239* (1967), p. 1341.

6. H. D. Roehrig, private communication, Oak Ridge National Laboratory, 1996.

STUDIES ON THE EFFECTS OF HELIUM ON THE MICROSTRUCTURAL EVOLUTION OF V-3.8Cr-3.9Ti

N. Doraiswamy, B. Kestel and D. E. Alexander
Materials Science Division, Argonne National Laboratories, Argonne, IL 60439.

To be published in the proceedings of the symposium on Microstructural Evolution During Irradiation, Symposium B of the Materials Research Society Fall Meeting held in December, 1996.

EXTENDED ABSTRACT

The favorable physical and mechanical properties of V-3.8Cr-3.9Ti (wt.%), when subjected to neutron irradiation, has lead to considerable attention being focused on it for use in fusion reactor structural applications. However, there is limited data on the effects of helium on physical and mechanical properties of this alloy. Understanding these effects are important since helium will be generated by direct α-injection or transmutation reactions in the fusion environment, typically at a rate of $\approx$5 appm He/dpa. Helium has been shown to cause substantial embrittlement, even at room temperature in vanadium and its alloys. Recent simulations of the fusion environment using the Dynamic Helium Charging Experiments (DHCE) have also indicated that the mechanical properties of vanadium alloys are altered by the presence of helium in post-irradiation tests performed at room temperature. While the strengths were lower, room temperature ductilities of the DHCE specimens were higher than those of non-DHCE specimens. These changes have been attributed to the formation of different types of hardening centers in these alloys due to He trapping. Independent thermal desorption experiments suggest that these hardening centers may be associated with helium-vacancy-X (where X= O, N, and C) complexes. These complexes are stable below 290°C and persist at room temperature. However, there has been no direct microstructural evidence correlating the complexes with irradiation effects. An examination of the irradiation induced microstructure in samples preimplanted with He to different levels would enable such a correlation.

In this study the role of helium on the microstructural evolution of V-3.8Cr-3.9Ti has been investigated by in-situ transmission electron microscopy observations of as-prepared and He implanted (<10 appm) samples subjected to 200keV He irradiation at room temperature. Quantitative analysis of the defects showed an increase in the defect density and size with irradiation in both types of samples. The unimplanted sample showed a defect density consistent with previously reported electron irradiation experiments. In comparison, the He preimplanted sample had slightly larger defects and a substantially greater number density of defects.

The large increase in the defect number density caused by He preimplantation as observed in this work is consistent with the formation of He-vacancy-X (X=C,N,O) complexes whose presence alter the interstitial-vacancy populations during irradiation and thus alter the final microstructure. However, consideration of the role of S contaminants, as well as surface C film detected by EDS, may be necessary to completely understand the microstructural differences. In addition, a comparison of the microstructure for higher levels of He implantation would aid in elucidating the behavior of the He-vacancy-X (X=C,N,O) complexes. These activities are in progress.

ASSESSMENT OF THE RADIATION-INDUCED LOSS OF DUCTILITY IN V-Cr-Ti ALLOYS — A. F. Rowcliffe and S. J. Zinkle (Oak Ridge National Laboratory)

OBJECTIVE

To assess the effects of neutron irradiation on the tensile and Charpy impact behavior of alloys in the V-Cr-Ti system.

SUMMARY

The current status of the irradiation data base on V-(4-5%Cr)-(4-5%Ti) alloys for tensile and Charpy impact properties is reviewed. Possible factors contributing to major inconsistencies in the data are examined.

INTRODUCTION

Alloys based on the V-Cr-Ti system are attractive candidates for structural applications in fusion systems because of their low activation properties, high thermal stress factor (high thermal conductivity, moderate strength, and low coefficient of thermal expansion), and their good compatibility with liquid lithium. The U.S. program has defined a V-4Cr-4Ti (wt %) alloy as a leading candidate alloy based upon evidence from laboratory-scale (30 kg) heats covering the approximate composition range 0-8 wt % Ti and 5 to 15 wt % Cr. A review of the effects of neutron displacement damage, helium, and hydrogen generation on mechanical behavior, and of compatibility with lithium, water, and helium environments was presented at the ICFRM-5 conference at Clearwater in 1991 [1]. The results of subsequent optimization studies, focusing on the effects of fast reactor irradiation on tensile and impact properties of a range of alloys, were presented at the ICFRM-6 conference at Stresa in 1993 [2,3]. The primary conclusion of this work was that the V-4Cr-4Ti alloy composition possessed a near-optimal combination of physical and mechanical properties for fusion structural applications. Subsequently, a production-scale (500 kg) heat of V-4Cr-4Ti (Heat No. 832665) was procured from Teledyne Wah-Chang [4], together with several 15 kg heats of alloys with small variations in Cr and Ti.

Further measurements of the effects of neutron irradiation on the swelling and mechanical properties of a range of alloy compositions were carried out in the Dynamic Helium Charging Experiment (DHCE) in FFTF. Neutron doses reached 31 dpa at 425°C and 18 dpa at 525 and 600°C; helium was generated at rates between 0.1 to 4.2 appm/dpa. It was reported that for a laboratory heat of V-4Cr-4Ti (designation BL 47) and several other alloys, uniform elongation values remained in excess of 8% for testing temperatures over the range 25 to 600°C. These data were presented in papers at the ICFRM-7 conference at Obninsk [5,6]. Additional tensile data from the DHCE experiment were presented recently from which it was concluded that the tensile ductilities of V-8Cr-6Ti and V-9Cr-6Ti also remained in excess of 7% uniform and 11% total elongation for test temperatures in the range 25 to 600°C [7].

The favorable mechanical properties data and promising irradiation performance of the V-4Cr-4Ti composition encouraged the ITER project in 1993 to consider this alloy for the first wall/shield structure and other high heat flux applications. To establish an irradiation performance data base relevant to ITER conditions, a series of reactor experiments were initiated by the U.S. program to explore the effects of neutron irradiation at temperatures below the lowest temperature (430°C) attained in the FFTF experiments. These experiments included HFBR V1-V4 (0.1, 0.4 dpa; 110 to 500°C), BOR-60 Fusion 1 (12 dpa, 315-340°C), ATR (5 dpa; 200, 300°C), EBR-II X530 (4 dpa, 370-410°C), and HFIR 400 J (8 dpa, 400°C). The primary focus of these experiments was on the 500 kg production heat of V-4Cr-4Ti. Initial tensile results from the experiments in HFBR and EBR-II indicate that neutron irradiation at temperatures up to 400°C induces large increases in yield stress with a concomitant major reduction in strain hardening capacity and uniform elongation [8, 9]. These changes in deformation behavior are coupled with large increases in the ductile-to-brittle transition temperature measured in 1/3-size Charpy impact tests. The tensile and impact property data reported for the irradiation experiments carried out at temperatures up to 400°C are not consistent with the earlier data reported for irradiation at 430°C to 600°C; possible sources of these inconsistencies are explored in the following.

Measurement of Uniform Elongation

The uniform elongation is a measure of the permanent plastic strain that accumulates prior to necking and failure in a uniaxial tensile test. The ability of a material to strain-harden and the extent of the uniform elongation are extremely important factors in the ability of a material to accommodate secondary stresses. The uniform elongation is utilized in component design to develop design rules to guard against various types of failure [10]. When ε_u exceeds 5%, a material is considered to be ductile and the ASME Code rules are applicable. For ε_u values in the range 1 to 5%, materials are considered to be semi-brittle and additional design rules are required; for example, bending stresses have to be reduced to guard against the embrittlement of outer fibers. In situations where ε_u is reduced to <1%, a material is considered to exhibit brittle behavior with enhanced sensitivity to the presence of flaws and notches; design rules based upon fracture mechanics principles become more appropriate in this situation.

In a tensile test, the region of uniform plastic strain occurs after yielding when the gage length extends uniformly together with a uniform reduction in cross-sectional area. Eventually, the strain-hardening capacity is exhausted; further localized reductions in area and increase in local stress are no longer balanced by an increase in material strength. Beyond this point of maximum load, further plastic deformation is localized in the necked region. Uniform engineering strain in a tensile test is the plastic elongation at the point of maximum load. Contributions to the overall extension from the elastic extension of the specimen are generally subtracted from the reported elongations, as described in the ASTM Standard Test Method for Tension Testing of Metallic Materials (E345-87, paragraph 7.6.6.1). More importantly, elastic extensions associated with the specimen gripping system must be excluded. This component is automatically excluded when the specimen gage extension is measured with an extensometer, and must be excluded by graphical analysis when specimen elongation is monitored from the cross-head displacement. Fig. 1 compares room temperature engineering stress-displacement curves for V-4Cr-4Ti determined by extensometry and by cross-head displacement measurement on the same specimen. In the extensometry case, the strain that precedes yielding is ~0.3% and consists entirely of elastic deformation of the specimen. However, when the cross-head movement is measured there is an effective displacement of ~3.0% before yielding which consists mainly of elastic strains in the specimen gripping system. For irradiated materials with low strain-hardening rates, inclusion of this system displacement can produce a large over-estimate of uniform strain.

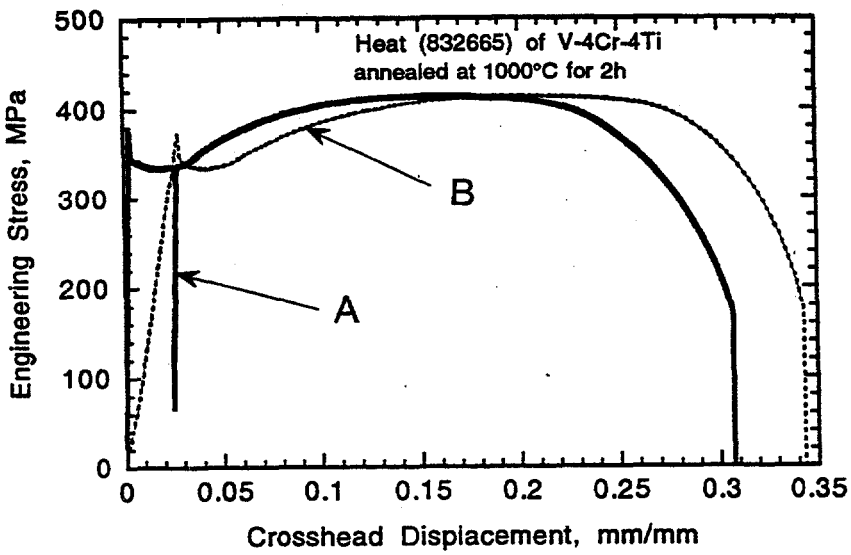

Fig. 1. Comparison of engineering stress-displacement curves for V-4Cr-4Ti determined by extensometry (A) and by crosshead-movement (B).

Tensile Data for Irradiated V-Cr-Ti Alloys

Data that have been reported for V-(4-5)Cr-(4-5)Ti alloys irradiated in various reactors are summarized in Table 1. The earlier data reported for FFTF/MOTA experiments are for small experimental heats; more recently data have been obtained for the production heat (832665) following irradiation to low doses at temperatures ≤420°C. Yield strength at the irradiation temperature is plotted as a function of irradiation temperature in Fig. 2. These data are from a variety of sources; the data for the HFR irradiation are from unpublished work by van Osch et al., Netherlands Energy Research Foundation ECN, Petten. For irradiation temperatures below 400°C, the irradiated yield stress is fairly independent of temperature, reaching values of ~650 MPa at 0.4 dpa and increasing to 900-950 MPa for doses of 4 to 6 dpa. Radiation hardening decreases fairly rapidly with increasing temperatures over the range 400 to 450°C and then decreases more gradually up to 600°C. At 600°C (0.32 Tm), radiation hardening at ~35 dpa is still significant, ($\Delta\sigma_y$, ~130 MPa).

From the limited data shown in Fig. 3, it appears that ε_u begins to increase with increasing irradiation above ~400°C commensurate with the strong decrease in radiation hardening shown in Fig. 2. The ε_u values reported for the FFTF/MOTA experiments at 425-600°C have not been included in Fig. 3. Following extensive discussions within the U.S. program, it now appears that these data have not been reported correctly. ANL researchers are currently re-evaluating the irradiated tensile data for a range of alloys [13], and the corrected values will be published in the near future.

Charpy Impact Data for V-Cr-Ti Alloys

In addition to the discrepancies regarding the effects of neutron irradiation on uniform elongation at temperatures >400°C, there are several conflicting aspects of the reported CVN impact data for the V-4Cr-4Ti alloy. The U.S. vanadium alloy program, following the ferritic-martensitic steels program, has adopted the one-third-size Charpy vee-notch specimen (CVN) as a convenient means of assessing changes in fracture behavior induced by heat-treatment or by irradiation. It has been pointed out by G. R. Odette et. al. that this specimen has some serious shortcomings and that caution must be exercised in interpreting results; not only does the specimen lack the capacity to provide valid intrinsic properties, but it may even fail to detect the propensity for a material to fail by cleavage [16].

Data are available from three separate irradiation experiments designed to assess the effect of neutron irradiation on the impact behavior of V-4Cr-4Ti. Specimens from the experimental heat (BL 47) were irradiated in the FFTF/MOTA (cycles 9-11) experiment at 425, 520, and 600°C to 24 to 36 dpa [3]. Specimens fabricated from heat 832665 were irradiated at lower temperatures in two separate experiments, and data have been reported for specimens irradiated to 0.4 dpa in HFBR at 100, 200, and 230°C [8]. In this current volume of the Semiannual Report, data are also reported on heat 8332665, following irradiation at 380-405°C to ~4 dpa in EBR-II [9].

The CVN data reported for the FFTF/MOTA (cycles 9-11) irradiation experiment at 425°C indicated that the heat BL 47 was highly resistant to cleavage failure following irradiation. However, the other two sets of data for V-4Cr-4Ti from the HFBR and EBR-II experiments are in complete contrast to these data. Large upward shifts in DBTT were observed for specimens irradiated over the range 110 to 400°C; in particular, the specimens of the production heat irradiated in EBR-II at 400°C exhibited brittle cleavage behavior in impact tests carried out at temperatures as high as ~280°C. Using one-half of the upper shelf energy as an index, the radiation-induced increase in DBTT is plotted in Fig. 4 against the corresponding increase in the yield stress at the DBTT (the latter were obtained by interpolation between tensile tests carried out at RT and at the irradiation temperature). Also shown are the FFTF/MOTA data reported for the experimental heats V-3Ti-1Si (BL 45), V-5Ti (BL 46), V-18Ti (BL 15), V-14Cr-5Ti (BL 24), and V-8Cr-6Ti (BL 49). With the striking exception of alloys BL 45, BL 46, and BL 47, the data fit reasonably well to a linear relationship between DBTT shift and radiation hardening with a slope of ~0.7°C/MPa. Similar relationships occur for other irradiated materials exhibiting stress-controlled fracture, such as pressure vessel steels and ferritic-martensitic steels [17]. However, the data for alloys BL 45, 46, and 47 do not follow this relationship. It was reported that CVN specimens for all three alloys bent without fracture at the lowest test temperature, i.e. -196°C; DBTTs of ~-200°C were attributed to each of these alloys.

Table 1. Tensile Properties of V-(4-5)Cr-(4-5)Ti Alloys Irradiated in Various Reactors

Alloy	Irradiation Experiment	Tirr (°C)	Dose (dpa)	σ_y	σ_u	ε_u	ε_t	Ref.
4Cr-4Ti BL47	FFTF/MOTA (cycles 9-11)	420 520 600	~34 ~28 ~27	600 460 365	700 545 460	8 10 13.5	10 14 19	[2]
4Cr-4Ti BL47	FFTF/MOTA 2B (DHCE)	430 500 600	18-31 18-31 18-31	600 410 365	700 570 450	10 9.5 13.5	12.5 14 19	[12]
4Cr-4Ti BL47	HFIR RB* -400 J1	400	8	710	800	4.5	12	[11]
5Cr-5Ti	FFTF/MOTA 2B (DHCE)	430	24	637	714	3.5	8.1	[14]
5Cr-5Ti	BR-2	100	0.7	785	—	—	3	[15]
5Cr-5Ti	FFTF/MOTA (2A)	407	49	535	613	2.0	5.8	[14]
5Cr-5Ti BL63	EBR-II X-530	405	3.6	719	761	1.0	5.7	[9]
4Cr-4Ti 832665	EBR-II X-530	400	4	832	849	0.5	5.0	[9]
4Cr-4Ti 832665	HFBR V1, V2	110 205 240	0.4 0.4 0.4	655 647 637	655 647 637	0.1 0.1 0.1	9.7 9.2 9.0	[8]

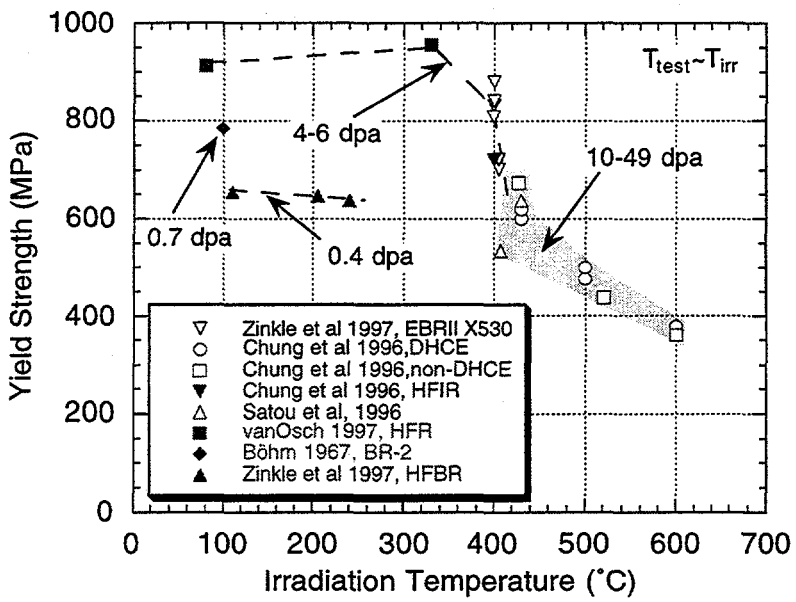

Fig. 2. Temperature dependence of yield strength measured at the irradiation temperature for alloys irradiated in various reactors.

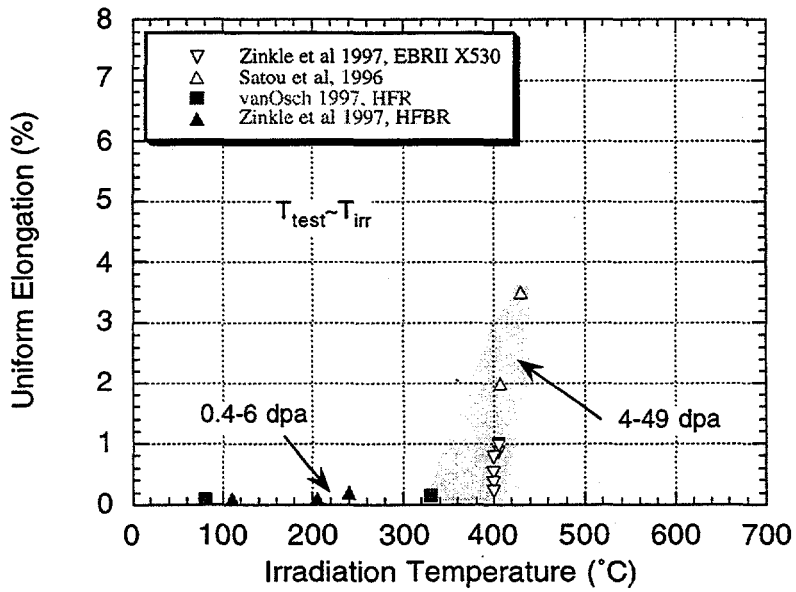

Fig. 3. Temperature dependence of uniform elongation measured at the irradiation temperature for alloys irradiated in various reactors. Data from ANL studies are not presented, pending re-evaluation of published values.

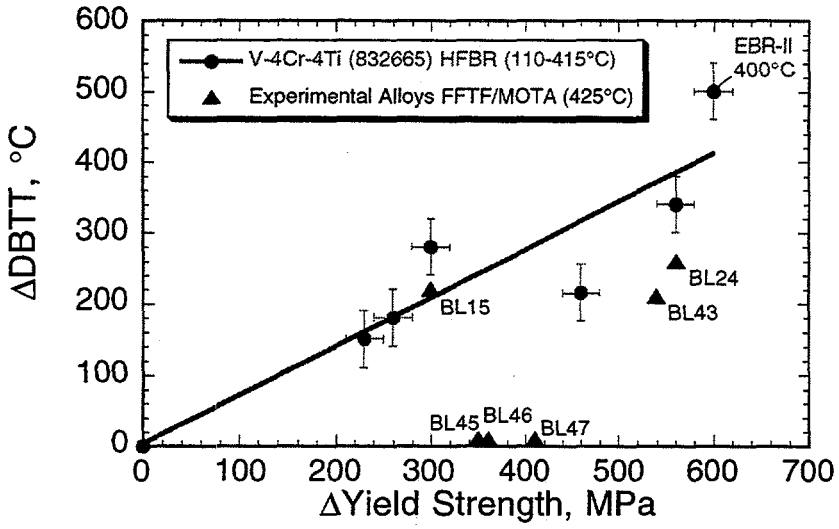

Fig. 4. Increase in DBTT versus increase in room temperature yield stress for heat 832665 irradiated in HFBR (110, 200, 235, 315, and 420°C) and in EBR-II (400°C), and for heat BL 47 irradiated in FFTF/MOTA at 425°C.

The failure to initiate cleavage fracture in these three alloys is surprising in view of the magnitude of the radiation-induced increases in room temperature (RT) yield strength (340-410 MPa). The published absorbed energy vs. test temperature curves for the V-4Cr-4Ti (BL 47) and V-5Ti (BL 46) [3] exhibit unusual behavior in that the absorbed energy initially decreased with decreasing test temperature, reached a minimum at around -120°C and then increased back to upper shelf values at liquid nitrogen temperature. The possibility that this behavior is somehow related to hydrogen diffusion seems implausible since (a) the specimens were vacuum annealed at 400°C prior to testing, and (b) unirradiated specimens charged with hydrogen in the same experiment do not show this behavior.

The three alloys V-5Ti, V-3Cr-1Si, and V-4Cr-4Ti have been reported as being "virtually immune to neutron displacement damage," [18]. Since these alloys are not immune to radiation hardening, their exceptional behavior must derive from an intrinsic resistance to the initiation of cleavage fracture. Considering only the V-4Cr-4Ti composition, there appear to be major differences in the fracture behavior of the two heats BL 47 and 832665. Following irradiation in FFTF/MOTA at 425°C, the BL 47 heat reportedly undergoes plastic collapse rather than cleavage fracture in CVN tests at all temperatures, even though the irradiated RT yield stress was ~800 MPa. On the other hand, following irradiation in HFBR at 275°C, the production heat exhibited brittle cleavage fracture in CVN tests at temperatures <150°C when the irradiated RT yield stress was only ~620 MPa. The production heat (832665) is a scaled-up version of BL 47 and the only significant difference in composition is the lower levels of nitrogen and carbon (~80 wppm vs. ~200 wppm) for the production heat.

Taken at face value, the Charpy test results on unirradiated specimens suggest that the two heats of V-4Cr-4Ti differ in their response to heat treatment. In Fig. 5, data are presented on the effects of recrystallization temperature on the impact properties of the large heat. The ANL data illustrate that in a partially recrystallized condition, produced by annealing 50% CW material at 950°C for 1 hr, the production heat does not exhibit a transition temperature [19]. However, ORNL data show that a fully recrystallized microstructure (1050°C, 2 hrs) exhibits a transition at ~-180°C [20], and this is increased to -140°C when the recrystallization temperature is increased to 1100°C. This type of behavior has been observed in other V alloys. Figure 6 illustrates the effect of recrystallization temperature on a V-5Cr-5Ti alloy (designated BL 63) [21]. The ORNL data, demonstrating an increase in the DBTT with increasing recrystallization temperature for the small heat of V-5Cr-5Ti (BL 63), were obtained using a CVN specimen that was machined in an L-T orientation with a machined notch depth of 0.5 mm, a notch root radius of 0.08 mm,

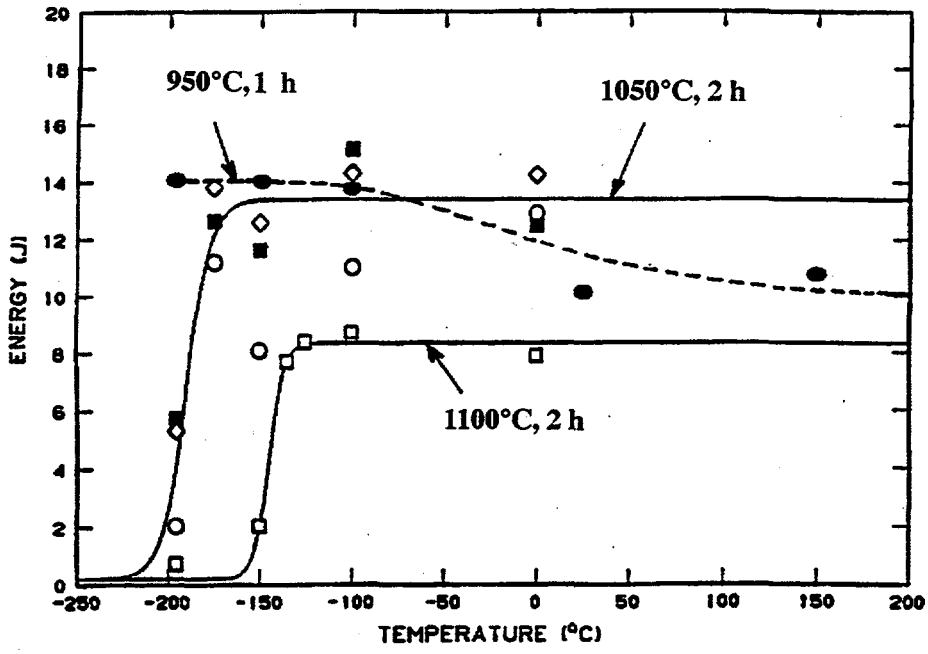

Fig. 5. Unirradiated Charpy impact properties for heat 832665 following recrystallization treatments at 950°C for 1 hr [18], 1050°C for 2 h [19], and 1100°C for 2 h [ORNL data].

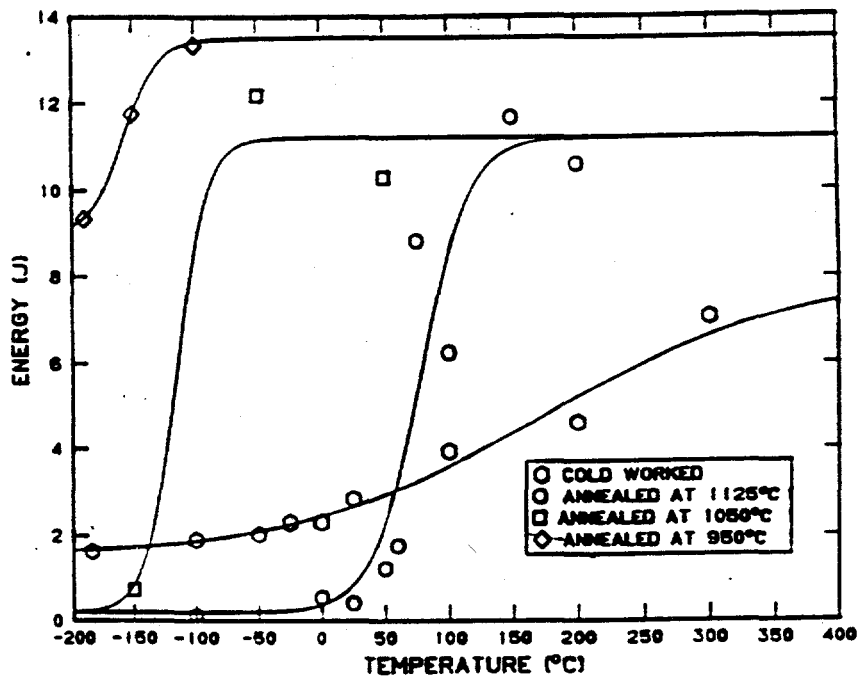

Fig. 6. Effect of recrystallization temperature on the Charpy impact properties of a V-5Cr-5Ti alloy, heat BL 63 [20].

and a notch angle of 30° [21]. For the work on the production heat, the notch depth was increased to 0.67 mm. Other examples of the dependence of DBTT on microstructure have been presented for a V-6Cr-3Ti alloy [19] and a V-4Cr-4Ti-0.1 Si alloy [22]. The BL 47 heat of V-4Cr-4Ti reportedly does not follow the same type of behavior. H. M. Chung et al., [23] reported that heat BL 47 did not a exhibit transition in impact behavior following annealing treatments at 1050 or 1125°C, when the material was presumably in a fully recrystallized condition (Fig. 7). In the same study, both V-5Cr-5Ti and V-5Cr-3Ti exhibited cleavage fracture between -50 and -100°C; the superior behavior of heat BL 47 was ascribed to the absence of various types of precipitation related to impurities of Cl, S, P, Cu, Ne, and K in the other two alloys. While it is possible that the BL 47 heat does indeed possess some undefined combination of impurity and microstructural characteristics that confer superior fracture resistance relative to the production heat, it is equally possible that extrinsic factors relating to the testing methodology are playing a significant role. Although the details of notch geometry for the CVN specimens used in Ref. [23] were not described, ANL workers have reported using an L-S orientation and a machined notch with 0.61 mm depth, 0.25 mm root radius, and a 45° notch angle in other studies on heat BL 47 [24]. The ORNL studies on the large heat of V-4Cr-4Ti used an L-T orientation and a 30° machined notch with 0.67 mm depth and 0.08 mm root radius [8]. Given the marginal capacity of the 1/3-size CVN specimen [16], it is entirely plausible that these differences in notch geometry could account for the appearance of transition behavior in V-4Cr-4Ti in some studies but not in others.

Although arguments based on intrinsic fracture resistance cannot be completely ruled out, explanations for the anomalous irradiation behavior of alloys BL 45, 46, and 47 based upon extrinsic experimental factors would appear to be entirely credible and require further consideration as follows.

(a) It has been shown by Odette et al. [16], that for the production heat of V-4Cr-4Ti, the transition from ductile behavior to cleavage fracture occurs over a fairly narrow temperature range, and that the transition temperature decreases with decreasing strain and with decreasing degree of constraint. They conclude that for the unirradiated alloy, blunt-notched MCVN specimens may not have the capacity to initiate cleavage fracture. These observations raise the possibility that depending upon the selection of notch orientation (L-S, L-T) and notch geometry (depth, angle, radius), the MCVN specimens used for the testing of the BL 45, 46, and 47 alloys did not have the capacity to initiate cleavage even in a radiation-hardened condition. Experimental details regarding notch orientation and geometry for these specimens have not been published.

(b) The CVN impact specimens from the FFTF/MOTA (cycles 9-11) experiments were reportedly given a postirradiation anneal at 400°C for 1 hour in a vacuum to remove hydrogen prior to testing. If the specimen annealing temperatures were actually higher than 400°C, then some of the radiation damage could have annealed out prior to testing. This could conceivably have more of an effect on the alloys in the experiment with the least amount of radiation hardening (BL 45, 46, 47). This could be investigated by verification of the annealing temperature measurement system and by hardness measurements on broken specimens.

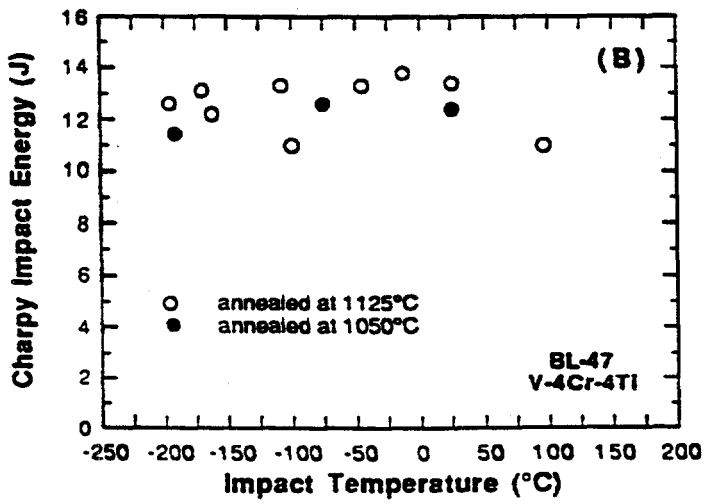

Fig. 7. Effect of annealing temperature on the Charpy impact properties of V-4Cr-4Ti, heat BL 47 [23].

CONCLUSIONS

Severe radiation hardening occurs for V-(4-5%)Cr-(4-5%)Ti alloys for irradiation temperatures up to ~400°C; a sharp decrease in hardening over the range 400-450°C is followed by a more gradual decrease up to 600°C. For irradiation temperatures ≤405°C, hardening is accompanied by a severe reduction in strain-hardening capacity and uniform elongation. The effects of irradiation at higher temperature on tensile ductility must be regarded as uncertain pending a re-evaluation of the ANL data.

There are major inconsistencies in the data reported for the effects of neutron irradiation on CVN impact properties. Earlier ANL data reported for experimental heats of V-5Ti, V-3Ti-1Si, and V-4Cr-4Ti are incompatible with the ΔDBTT versus $\Delta\sigma_y$ relationship determined for the production heat of V-4Cr-4Ti and several other experimental alloys. Explanations of this behavior based upon a combination of extrinsic experimental factors are more credible than arguments based upon an intrinsic resistance to cleavage fracture.

As recommended by Odette et al. [16], the effects of constraint and loading rate must be accounted for in future studies on the effects of compositional and microstructural variants and radiation damage on the fracture behavior of vanadium alloys.

REFERENCES

[1] B. A. Loomis and D. L. Smith, J. Nucl. Mat. 191-194 (1992), pp. 84-91.

[2] B. A. Loomis, L. J. Nowicki, and D. L. Smith, J. Nucl. Mat. 212-215 (1994), pp. 790-793.

[3] B. A. Loomis, H. M. Chung, L. J. Nowicki, and D. L. Smith, J. Nucl. Mat. 212-215 (1994), pp. 799-803.

[4] H. M. Chung, H.-C. Tsai, D. L. Smith R. Peterson, C. Wojcik, and R. Kinney, Fusion Materials Semiannual Progress Report, DOE/ER-0313/17, March 1994, pp. 178-183.

[5] H. M. Chung, B. A. Loomis, and D. L. Smith, J. Nucl. Mat. 233-237 (1996), pp. 466-475.

[6] D. L. Smith, H. M. Chung, B. A. Loomis, and H.-C. Tsai, J. Nucl. Mat 233-237 (1996), pp. 356-363.

[7] H. M. Chung, L. Nowicki, and D. L. Smith, Fusion Materials Semiannual Progress Report, DOE/ER-0313/20, June 1996, pp. 78-84.

[8] D. J. Alexander, L. L. Snead, S. J. Zinkle, A. N. Gubbi, A. F. Rowcliffe, and E. E. Bloom, Fusion Materials Semiannual Progress Report, DOE/ER-0313/20, June 1996, pp. 87-95.

[9] S. J. Zinkle, et al., Effect of Fast Neutron Irradiation to 4 dpa at 400°C on the properties of V-(4-5%)Cr-(4-5%)Ti Alloys, DOE/ER-0313/21 (this report).

[10] B. C. Wei and D. V. Nelson, "Structural Design Criteria for Highly Irradiated Core Components," Pressure Vessels and Piping Design Technology, A Decade of Progress, ASME 1982, Chapter 3.7.

[11] H. M. Chung, L. Nowicki, and D. L. Smith, Fusion Materials Semiannual Progress Report, DOE/ER-0313/20, June 1996, pp. 84-87.

[12] H. M. Chung, B. A. Loomis, L. Nowicki, and D. L. Smith, Fusion Materials Semiannual Progress Report, DOE/ER-0313/17, September 1994, pp. 198-205.

[13] D. L. Smith, private communication.

[14] M. Satou, H. Koide, A. Hasegawa, K. Abe, H. Hayane, and H. Matsui, J. Nucl. Mat., 233-237 (1996), 447-451.

[15] H. Böhm, "Irradiation Effects on the Mechanical Properties of Vanadium-Base Alloys," Effects of Radiation on Structural Materials, ASTM STP 426, 1966, pp. 95-106.

[16] G. R. Odette, E. Donahue, G. E. Lucas, and I. W. Sheckherd, Fusion Materials Semiannual Progress Report, DOE/ER-313/20, June 1996, pp. 11-30.

[17] G. R. Odette, P. Lombrogo, and R. A. Wulluert, "The Relationship Between Irradiation Hardening and Embrittlement," ASTM STP-870, American Society for Testing and Materials, p. 841, 1985.

[18] H. M. Chung, B. A. Loomis, and D. L. Smith, J. Nucl. Mat., 239 (1996), 139-156.

[19] H. M. Chung, L. Nowicki, and D. L. Smith, Fusion Materials Semiannual Progress Report, DOE/ER-0313/18, March 1995, pp. 273-278.

[20] A. N. Gubbi, A. F. Rowcliffe, D. J. Alexander, M. L. Grossbeck, and W. S. Eatherly, Fusion Materials Semiannual Progress Report, DOE/ER-0313/18, pp. 203-213.
[21] M. L. Grossbeck, A. F. Rowcliffe, and D. J. Alexander, Fusion Materials Semiannual Progress Report, DOE/ER-0313/16, March 1994, pp. 244-257.
[22] H. Matsui, K. Fukumoto, M. Satou, and H. Takahashi, "Microstructure and Mechanical Properties of Vanadium Alloys," 2nd IEA Vanadium Workshop, ECN Petten, May 20-22, 1996.
[23] H. M. Chung, J. Gazda, L. J. Nowicki, J. E. Sanecki, and D. L. Smith, Fusion Materials Semiannual Progress Report, DOE/ER-0313/15, September 1993, pp. 207-218.
[24] H. M. Chung, L. Nowicki, and D. L. Smith, Fusion Materials Semiannual Progress Report, DOE/ER-0313/18, March 1995, pp. 253-258.

EFFECT OF FAST NEUTRON IRRADIATION TO 4 DPA AT 400°C ON THE PROPERTIES OF V-(4-5)Cr-(4-5)Ti ALLOYS — S. J. Zinkle, D. J. Alexander, J. P. Robertson, L. L. Snead, A. F. Rowcliffe, L. T. Gibson, W. S. Eatherly (Oak Ridge National Laboratory) and H. Tsai (Argonne National Laboratory)

OBJECTIVE

The objective of this report is to summarize tensile, Charpy impact and electrical resistivity measurements on V-4Cr-4Ti and V-5Cr-5Ti alloys that were irradiated in the EBR-II reactor at ~400°C to a dose of about 4 dpa.

SUMMARY

Tensile, Charpy impact and electrical resistivity measurements have been performed at ORNL on V-4Cr-4Ti and V-5Cr-5Ti specimens that were prepared at ANL and irradiated in the lithium-bonded X530 experiment in the EBR-II fast reactor. All of the specimens were irradiated to a damage level of about 4 dpa at a temperature of ~400°C. A significant amount of radiation hardening was evident in both the tensile and Charpy impact tests. The irradiated V-4Cr-4Ti yield strength measured at ~390°C was >800 MPa, which is more than three times as high as the unirradiated value. The uniform elongations of the irradiated tensile specimens were typically ~1%, with corresponding total elongations of 4-6%. The ductile to brittle transition temperature of the irradiated specimens as determined by dynamic Charpy impact tests was ≥300°C. The electrical resistivity of the irradiated specimens was less than the unirradiated resistivity, which suggests that hardening associated with interstitial solute pickup was minimal.

PROGRESS AND STATUS

Introduction

Vanadium alloys with solute contents of 4-5%Cr and 4-5%Ti have recently been identified as promising candidates for the first wall structure of magnetic fusion energy systems [1,2]. A 500 kg production heat of V-4Cr-4Ti (heat #832665) was recently fabricated in order to perform a comprehensive evaluation of the potential and limitations of this alloy composition. Very favorable mechanical properties were measured for the unirradiated alloy, including ductile to brittle transition temperatures (DBTTs) of about -150°C and -200°C as determined from Charpy vee-notch (CVN) impact tests on precracked and machined notch specimens, respectively [3].

Several fast reactor irradiation experiments have reported that the vanadium alloys containing 4-5% Cr and 4-5% Ti exhibit exceptional resistance to radiation embrittlement at doses of ~18 to 30 dpa at temperatures between 425 and 600°C [1,4-7]. Although radiation hardening increased the yield strength to as high as ~600 MPa at 430°C, the uniform elongations were reported to be >8% for all irradiation conditions and the Charpy impact DBTT in irradiated specimens was reported to remain near -200°C. It was recently discovered that the tensile elongations for these experiments were incorrectly analyzed, and the revised elongations are significantly smaller than previously reported [8]. However, vanadium alloys containing 4-5% Cr and 4-5% Ti still appear to be promising materials for fusion energy structural applications.

A recent low-dose, low-temperature neutron irradiation experiment found that significant radiation hardening and embrittlement occurred in the 500 kg heat of V-4Cr-4Ti following irradiation to a damage level of ~0.4 dpa at 110-275°C [3]. Typical irradiated yield strengths were ~650 MPa, with corresponding uniform elongations of <0.2%. The irradiation caused a dramatic increase in the DBTT, with DBTT values of ~140°C and ~250°C, respectively for machined notch and precracked Charpy specimens irradiated at 235°C. Another study has reported significant radiation hardening and reductions in uniform elongation to 2.0% and 3.5% in a V-5%Cr-5%Ti alloy following FFTF irradiation to 49 dpa at 407°C (non-DHCE) and 24 dpa at 430°C (DHCE), respectively [9]. These two studies [3,9] and the revised tensile data set from other reactor

irradiation experiments [8] suggest that radiation hardening and concomitant reduction in ductility may be pronounced in V-4Cr-4Ti alloys at irradiation temperatures below 430°C.

The X530 experiment in the EBR-II fast reactor was designed to obtain initial irradiation data on the 500 kg heat of V-4Cr-4Ti at a relatively low temperature of ~400°C. Several different preirradiation heat treatments were included in the specimen matrix in order to investigate effects of thermomechanical treatment on the mechanical properties. Specimens from the BL-63 heat of V-5Cr-5Ti with different thermomechanical treatments were also irradiated. Previous work has shown that the BL-63 heat is susceptible to embrittlement following annealing at temperatures above ~1100°C, whereas good mechanical properties were obtained in unirradiated specimens annealed at temperatures ≤1050°C [10].

Experimental procedure

The present study represents a subset of the specimen matrix that was irradiated in the X530 experiment [11,12]. Miniature machined-notch Charpy (MCVN) impact bar specimens (nominal dimensions 3.3 × 3.3 × 25.4 mm) and type SS-3 miniature sheet tensile specimens (nominal gage dimensions 0.76 × 1.52 × 7.6 mm) were fabricated from the V-4Cr-4Ti and V-5Cr-5Ti alloys. As summarized in Table 1, three different preirradiation heat treatments were investigated for each of the two alloys in the present study.

Table 1. Summary of X530 specimen matrix investigated at ORNL in this study

Alloy	Heat treatment	Specimen types
V-4Cr-4Ti (#832665)	TWCA&950 (Wah Chang anneal/1050°C & annealed 950°C/1h)	MCVN*
"	WR/950 (warm rolled at 400°C and annealed at 950°C/1h)	SS3
"	WR/1050 (warm rolled at 400°C and annealed at 1050°C/1h)	SS3
"	WR/1125 (warm rolled at 400°C and annealed at 1125°C/1h)	SS3
V-5Cr-5Ti (#BL-63)	TWCA ann. (Wah Chang mill anneal at 1050°C)	SS3, MCVN
"	CR/950 (cold rolled at 20°C and annealed at 950°C/1h)	SS3, MCVN
"	CR/1050 (cold rolled at 20°C and annealed at 1050°C/1h)	SS3, MCVN

*previously incorrectly reported as warm rolled at 400°C and annealed at 950°C/1h [11,12]

The specimens were irradiated in Li-bonded type 316 stainless steel subcapsules that were contained in two adjacent flow-through (weeper) capsule tubes in the EBR-II core position 2F1. The calculated specimen temperatures ranged from ~371°C for the subcapsules at the bottom on the core to ~410°C for subcapsules near the top of the core [11]. The tensile specimens for the V-4Cr-4Ti (heat 832665) and V-5Cr-5Ti alloys (BL-63) were located slightly above the horizontal midplane of the core in subcapsule positions S9 and S8, with calculated specimen temperatures of ~400°C and ~405°C, respectively [11,12]. The estimated fast neutron (E>0.1 MeV) fluences for these specimens are ~7.3×10^{25} n/m^2 and ~6.6×10^{25} n/m^2, respectively (~4 and ~3.6 dpa). The Charpy impact specimens for these alloys were distributed in 4 different subcapsules (S7,S3,S6,S5) below and above the horizontal midplane of the core, with calculated specimen temperatures of ~380-410°C and damage levels of ~3.5 to 4 dpa. Further irradiation details are given elsewhere [11,12].

Following irradiation, the specimens were removed from the Li-filled subcapsules at ANL-East and shipped to ORNL for testing. The gage dimensions of the irradiated SS-3 tensile specimens were measured prior to testing. Electrical resistivity measurements were performed at room temperature on the tensile specimens using techniques that are summarized elsewhere [3]. For the elevated temperature tensile tests, the specimens were heated in a vacuum furnace to a temperature of ~390°C (typical ramp time of ~15 min.) and held at the test temperature for 30 minutes prior to the start of the tensile test. The pressure during the tensile testing was 1 to 2.5×10^{-6} torr. One of the WR/950 V-4Cr-4Ti specimens was also tested in laboratory air at room temperature. All of the tensile specimens were tested in a servohydraulic machine at a constant crosshead speed of 0.0085 mm/s, which corresponds to an initial strain rate of $1.1 \times 1\ 0^{-3}$ s^{-1}. The data were recorded digitally and also on a chart recorder. The engineering tensile properties were

obtained from analysis of the load vs. crosshead displacement test record. Charpy impact testing was performed in air on a pendulum machine modified for small specimens [3].

Results and discussion

The results of the electrical resistivity measurements are shown in Table 2. The typical experimental standard deviation for the resistivity measurements was ±1 nΩ-m. There was no significant difference in the measured resistivities for the 3 preirradiation heat treatments of the irradiated V-4Cr-4Ti alloy. However, the resistivity measured in the V-5Cr-5Ti alloy was higher for the cold-rolled and annealed specimens compared to the vendor-annealed specimens. Electrical resistivity measurements have not yet been performed on control specimens from this experiment, so the quantitative change in electrical resistivity associated with the neutron irradiation cannot be determined. Comparison with electrical resistivity measurements [13] obtained on specimens from the 500 kg V-4Cr-4Ti heat with nominally identical heat treatments suggests that the resistivity of the neutron-irradiated specimens was ~10 nΩ-m lower than unirradiated specimens. A large increase in the electrical resistivity of ~5 nΩ-m would have occurred if significant amounts (>0.03 at.%) of interstitial solute (H,O,C,N) were picked up and dissolved in the specimen matrix during or following the irradiation.

Table 3 summarizes the results of the tensile testing. The yield strengths of all of the irradiated specimens tested at the irradiation temperature were between 740 and 880 MPa, which is about three times the unirradiated yield strength at this temperature. The high amount of radiation hardening was accompanied by a dramatic reduction in the uniform elongation, with typical values near 1%. Typical unirradiated uniform elongations for these alloys at 400°C are >15%. Figure 1 shows a representative load vs. crosshead displacement curve for irradiated V-4%Cr-4%Ti that was tested at 390°C. Hardening associated with pickup of interstitial solutes (H,O,C,N) does not appear to be a likely explanation for the reduction in ductility, since the electrical resistivity of the irradiated specimens was apparently less than the unirradiated resistivity. The V-4Cr-4Ti specimens that were annealed at 1125°C prior to irradiation exhibited lower ductility and higher strength compared to specimens annealed at 950 or 1050°C. There was no significant difference between the three preirradiation heat treatment conditions for the V-5Cr-5Ti alloy. The tensile elongations and strengths were all higher for a V-4Cr-4Ti specimen tested at room temperature compared to the 390°C test temperature (Table 3). This type of behavior is commonly observed in metals that have been irradiated in the radiation hardening regime (T_{irr}<0.3 T_M).

Table 2. Summary of electrical resistivity measurements on the irradiated specimens

Alloy	Preirradiation heat treatment	Electrical resistivity at 20°C
V-4Cr-4Ti (#832665)	WR/950	276.2 nΩ-m
"	WR/1050	274.2 nΩ-m
"	WR/1125	274.2 nΩ-m
V-5Cr-5Ti (#BL-63)	TWCA ann.	285.2 nΩ-m
"	CR/950	291.5 nΩ-m
"	CR/1050	293.0 nΩ-m

Table 3. Summary of tensile measurements on the irradiated specimens

Alloy	Preirr. heat treatment	T_{irr}	T_{test}	0.2% yield strength (MPa)	Ultimate strength (MPa)	uniform elongation	Total elongation
V-4Cr-4Ti	WR/950	400°C	390°C	819±21*	847±20*	0.8±0.04%*	4.1±0.2%*
"	WR/1050	400°C	390°C	809	818	0.4%	6.0%
"	WR/1125	400°C	390°C	880	883	0.2%	6.0%
V-5Cr-5Ti	TWCA ann.	405°C	390°C	733	774	1.2%	7.3%
"	CR/950	405°C	390°C	701	743	0.8%	2.8%
"	CR/1050	405°C	390°C	723	765	1.0%	7.0%
V-4Cr-4Ti	WR/950	400°C	20°C	880	935	2.2%	8.5%

*average of 2 specimens

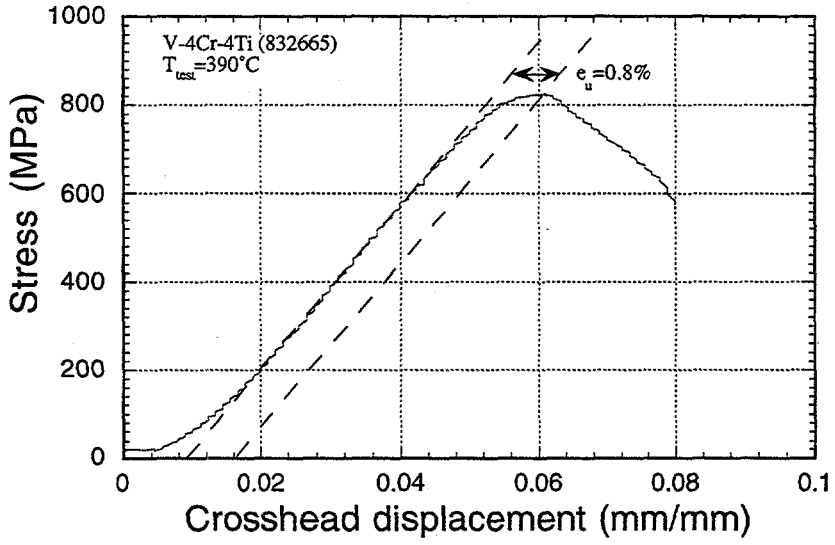

Fig. 1. Load vs. crosshead displacement curve for a warm-worked and 950°C annealed V-4Cr-4Ti specimen (ID# B71/36) that was irradiated to ~4 dpa at ~400°C and tested at 390°C.

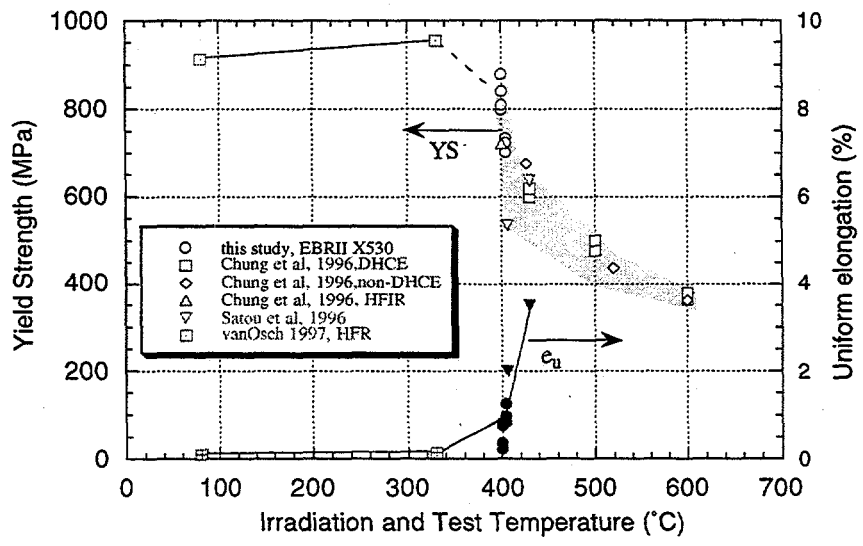

Fig. 2. Yield strength (open symbols) and uniform elongation (filled symbols) of V-(4-5)Cr-(4-5)Ti alloys irradiated and tested at temperatures between 80 and 600°C [7,9,14,15]. The damage levels were 4-6 dpa in ref. [15], 10-31 dpa in refs. [7,14], and 24-49 dpa in ref. [9]. The tensile elongations from refs. [7,14] have not been plotted, pending re-evaluation by ANL [8].

It is interesting to note that the V-5Cr-5Ti alloy had slightly better irradiated tensile elongations than the V-4Cr-4Ti alloy. As shown in Fig. 2, the yield strength and uniform elongation of irradiated V-(4-5)Cr-(4-5)Ti alloys appear to be strongly dependent on irradiation temperature between ~330 and 430°C [7,9,14,15]. The V-4Cr-4Ti and V-5Cr-5Ti tensile specimens were irradiated in different subcapsules in the EBR-II X530 experiment, which produced a slightly higher irradiation temperature (~400 vs. ~405°C) and lower damage level (~3.6 vs. ~4 dpa) in the V-5Cr-%Ti specimens compared to the V-4Cr-4Ti specimens. Further work is needed to determine the effect of damage level, composition and heat-to-heat variations on the radiation hardening behavior of vanadium alloys in this temperature regime.

The initial Charpy impact testing was conducted on specimens in the as-irradiated condition. The results are shown in Table 4. All of the specimens showed very low energies for fracture at all test temperatures (20-300°C), with the exception of the V-5Cr-5Ti (BL63) material, which showed a moderate energy absorption. The low energies measured for all of the specimens indicated that these specimens had become severely embrittled. To verify that this was an irradiation effect and not one caused by pickup of an embrittling impurity such as hydrogen during the irradiation or capsule disassembly, four specimens were annealed for 1 hour at 400°C in vacuum (~2×10^{-6} torr). The Charpy impact results for these specimens are also given in Table 4. The postirradiation-annealed specimens showed similar low levels of energy absorption as the as-irradiated specimens, confirming that the brittle behavior was not caused by the absorption of an interstitial impurity such as hydrogen.

The only specimens which showed some energy absorption were from the V-5Cr-5Ti alloy heat treated at 950°C. The load-displacement traces captured during the fracture process did not show a sudden load drop that would indicate cleavage fracture, despite the low values of energy absorbed. This suggests that the fracture process took place by the relatively slow growth of a crack across the specimen, rather than rapid crack extension by cleavage fracture. Scanning electron microscopy of the fracture surfaces showed transgranular cleavage for the V-4Cr-4Ti specimens and the V-5Cr-5Ti TWCA anneal specimens. The V-5Cr-5Ti specimens that were given a preirradiation anneal at 1050°C showed a mixture of transgranular cleavage and intergranular failure. The CR/950 V-5Cr-5Ti specimens exhibited a mixture of transgranular cleavage and ductile tearing (with intermixed laminated cracking, possibly associated with a precipitate band structure). It should be noted that postirradiation annealing at 400°C of V-5Cr-5Ti CR/950 specimens did not result in any change in the energy absorption (Table 4), again indicating that pickup of hydrogen was not responsible for the observed embrittlement.

Table 4. Summary of Charpy impact tests on EBR-II X530 specimens

Alloy	Preirradiation heat treatment	Spec. No.	Condition	Test Temperature	Absorbed energy (J)
V-4Cr-4Ti	TWCA&950	71-01	as-irradiated	100°C	0.1
"	"	71-02	as-irradiated	200°C	0.0
"	"	71-03	as-irradiated	285°C	0.4
"	"	71-04	vacuum anneal	200°C	0.4
"	"	71-05	vacuum anneal	275°C	0.4
V-5Cr-5Ti	TWCA ann.	63-1	as-irradiated	100°C	0.0
"	"	63-2	as-irradiated	200°C	0.1
"	"	63-3	as-irradiated	285°C	0.4
"	CR/950	63CR9-01	as-irradiated	200°C	2.0
"	"	63CR9-02	as-irradiated	285°C	2.8
"	"	63CR9-03	vacuum anneal	200°C	2.2
"	"	63CR9-04	vacuum anneal	275°C	2.8
"	CR/1050	63CR10-01	as-irradiated	200°C	0.7
"	"	63CR10-02	as-irradiated	285°C	0.4

ACKNOWLEDGEMENTS

The authors thank H. M. Chung and D. L. Smith (ANL) for their assistance with the specimen fabrication and irradiation, and A. M. Williams (ORNL) for providing the SEM analysis.

REFERENCES

1. D.L. Smith, H.M. Chung, B.A. Loomis and H.-C. Tsai, J. Nucl. Mater. 233-237 (1996) 356.
2. H. Matsui et al., J. Nucl. Mater. 233-237 (1996) 92.
3. D.J. Alexander et al., in Fusion Materials Semiannual Progress Report for Period ending June 30, 1996, DOE/ER-0313/20 (Oak Ridge National Lab, 1996) p. 87.
4. B.A. Loomis, L.J. Nowicki and D.L. Smith, J. Nucl. Mater. 212-215 (1994) 790.
5. B.A. Loomis, H.M. Chung, L.J. Nowicki and D.L. Smith, J. Nucl. Mater. 212-215 (1994) 799.
6. H.M. Chung, B.A. Loomis and D.L. Smith, J. Nucl. Mater. 212-215 (1994) 804.
7. H.M. Chung, B.A. Loomis and D.L. Smith, J. Nucl. Mater. 233-237 (1996) 466.
8. M.C. Billone, personal communication
9. M. Satou et al., J. Nucl. Mater. 233-237 (1996) 447.
10. M.L. Grossbeck, A.F. Rowcliffe and D.J. Alexander, in Fusion Materials Semiannual Progress Report for Period ending March 31, 1994, DOE/ER-0313/16 (Oak Ridge National Lab, 1994) p. 244.
11. H. Tsai et al., in Fusion Materials Semiannual Progress Report for Period ending September 30, 1994, DOE/ER-0313/17 (Oak Ridge National Lab, 1994) p. 8.
12. H. Tsai et al., in Fusion Materials Semiannual Progress Report for Period ending March 31, 1995, DOE/ER-0313/18 (Oak Ridge National Lab, 1995) p. 85.
13. S.J. Zinkle, A.N. Gubbi and W.S. Eatherly, in Fusion Materials Semiannual Progress Report for Period ending December 31, 1996, DOE/ER-0313/21 (Oak Ridge National Lab, 1996) in press.
14. H.M. Chung, L. Nowicki and D.L. Smith, in Fusion Materials Semiannual Progress Report for Period ending June 30, 1996, DOE/ER-0313/20 (Oak Ridge National Lab, 1996) p. 84.
15. E. van Osch, personal communication.

MICROSTRUCTURAL EXAMINATION OF IRRADIATED VANADIUM ALLOYS - D. S. Gelles (Pacific Northwest National Laboratory)[a] and H. M. Chung (Argonne National Laboratory)

OBJECTIVE

The objective of this effort is to provide collaborative understanding of microstructural evolution in irradiated vanadium alloys for first wall applications in a fusion power system.

SUMMARY

Microstructural examination results are reported for a V-5Cr-5Ti unirradiated control specimen of heat BL-63 following annealing at 1050°C, and V-4Cr-4Ti heat BL-47 irradiated in three conditions from the DHCE experiment: at 425°C to 31 dpa and 0.39 appm He/dpa, at 600°C to 18 dpa and 0.54 appm He/dpa and at 600°C to 18 dpa and 4.17 appm He/dpa.

PROGRESS AND STATUS

Introduction

Vanadium is being developed for application as a first wall material for fusion power system. It has been shown that an alloy of composition V-4Cr-4Ti has optimum properties[1] and the effort has shifted to demonstration that properties provide an adequate design window. However, degradation of properties has been observed in some heats of V-5Cr-5Ti as a result of high temperature annealing,[2-3] and results from the Dynamic Helium Charging Experiment (DHCE) to determine consequences of helium production during irradiation require further investigation to understand microstructural evolution.[4-5] The present effort was initiated in order to develop interlaboratory collaboration and to investigate two issues: the cause of degraded properties in one heat of V-4Cr-4Ti (Heat BL-63), and the microstructure of a heat of V-4Cr-4Ti (BL-47) following irradiation in the DHCE experiment. The microstructural evolution in the latter heat included both precipitation response as a function of temperature and effects of a different rate of helium production on bubble development.

Experimental Procedure

Four specimens were selected for examination: a control specimen of heat BL-63 following annealing at 1050°C for 1 h in high vacuum, and three irradiated specimens of heat BL-47 from the DHCE experiment: at 425°C to 31 dpa and 0.39 appm He/dpa, at 600°C to 18 dpa and 4.17 appm He/dpa, and at 600°C to 18 dpa and 0.54 appm He/dpa. Heat compositions are provided in Table 1 and irradiation conditions in Table 2. Specimens selected for examination had been examined previously[2,4,5] and had been stored for over a year in a standard laboratory desiccator without any apparent degradation. Examinations were performed on a JEOL 100CX at ANL.

Results

The control specimen of V-5Cr-5Ti heat BL-63 following annealing at 1050°C was examined to determine if unusual microstructures were developing at grain boundaries following heat treatment. A typical grain boundary was examined in a number of dark field imaging conditions, with both grains

---

[a]Operated for the U.S. Department of Energy by Battelle Memorial Institute under Contract DE-AC06-76RLO 1830.

Table 1. Composition of Heats Examined

Heat #	Nominal Composition	Concentration [ppm]			
		O	N	C	Si
BL-63	V-4.6Cr-5.1Ti	440	28	73	310
BL-47	V-4.1Cr-4.3Ti	350	220	200	870

Table 2. Irradiation conditions for DHCE specimens of V-4Cr-4Ti (BL-47) examined.

Packet Code	Irradiation Temperature (°C)	Fluence (n/cm^2)	Dose (dpa)	Helium (appm)	Helium production (appm He/dpa)
4D1	425	$6.4x10^{22}$	31	11.2-13.3	0.39
5C1	600	$3.7x10^{22}$	18	8.4-11.0	0.54
5C2	600	$3.7x10^{22}$	18	74.9-75.3	4.17

diffracting. In each case, the grain boundary region was strongly visible in dark field using non-matrix reflections. The most extreme case, where the strong dark field image was obtained for a very small $\vec{g}$, is shown in Figure 1. Figure 1 provides comparison of a boundary in bright field (a) and in dark field (b) (at a different position of tilt) with the diffraction condition inset showing the aperture position by a double exposure procedure. It was eventually concluded that this imaging condition was a result of double diffraction and therefore misleading. The bright field image shows distortions in the grain boundary thickness fringes probably characteristic of the grain boundary precipitation observed in previous studies.[2,3]

The specimen of V-4Cr-4Ti heat BL-47 irradiated in the DHCE experiment at 425°C to 31 dpa and 0.39 appm He/dpa was examined to provide further understanding of the microstructure and precipitation formed during irradiation. Attempts to produce precipitate dark field images were unsuccessful due to the small size of the precipitate and the resultant weak diffraction spots. Effort was therefore shifted to record microstructural features. A low magnification image of bubbles or voids associated with grain boundaries near a node is provided in Figure 2 (a). Boundaries are not straight, indicating that migration took place during irradiation. The bubbles appear as equiaxed white circular features, most often near but not on the boundary. Figures 2 (b) and (c) provide comparison of another region in $\vec{g} = <0\bar{1}1>$ strain contrast near (011) and in void contrast, respectively, adjacent to a grain boundary. Strain contrast reveals curved dislocation line segments, typical of climbing dislocations, small equiaxed features as large as 5 nm that are probably precipitates, and circular features with dark rings most common near the boundary that can be shown by comparison with Figure 2 (c) to probably be bubbles. Again, bubbles are non-uniformly distributed. Stereoscopic examination showed that several bubbles were on the boundary, but many were not. Figure 2 (c) also reveals precipitation on the order of 4 nm in diameter. The precipitate is only imaged at surfaces and appears typical of a phase formed by solute segregation. It is anticipated that this phase is rich in titanium, silicon and phosphorus.[6,7]

The specimens of V-4Cr-4Ti heat BL-47 irradiated in the DHCE experiment at 600°C to 18 dpa and 0.54 appm He/dpa and at 600°C to 18 dpa and 4.17 appm He/dpa were examined to provide further understanding of the effect of helium generation on microstructural development and to further

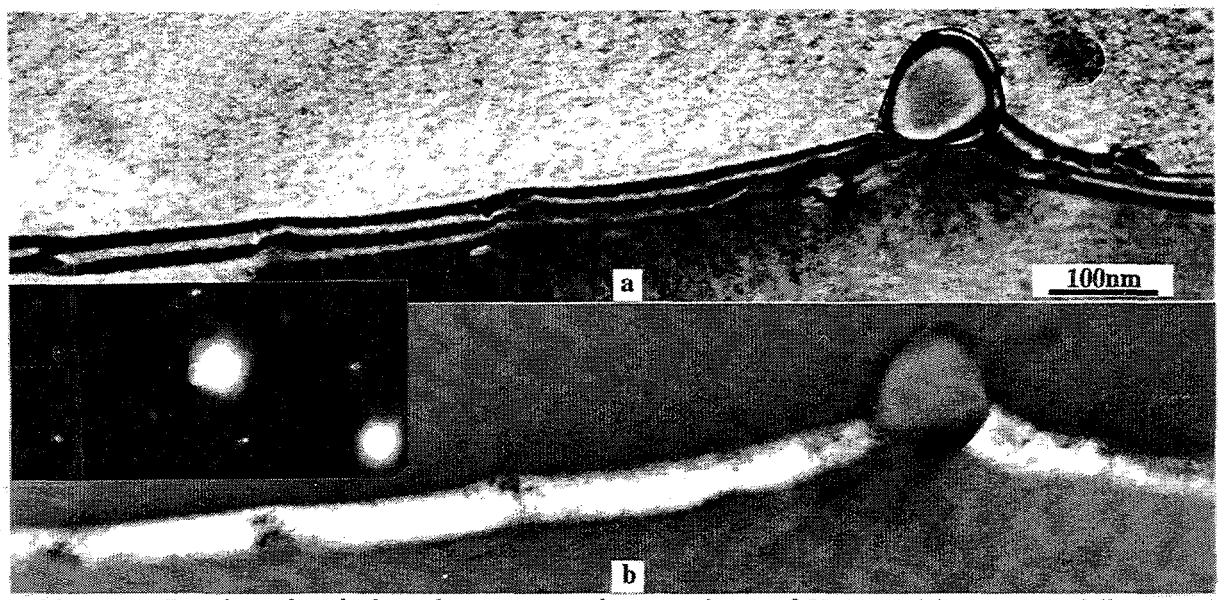

Figure 1. Imaging of grain boundary structure in a specimen of V-5Cr-5Ti heat BL-63 following annealing at 1050°C in bright field (a) and dark field (b).

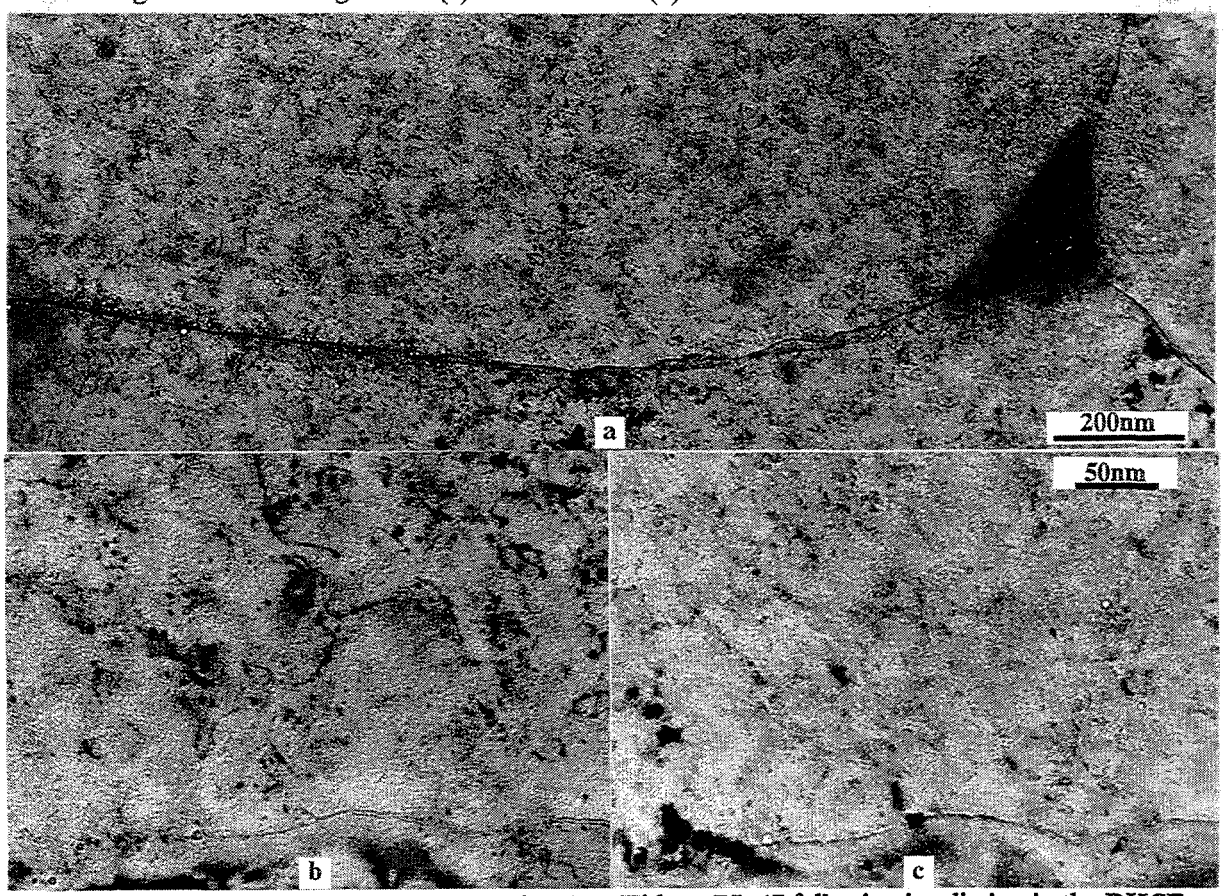

Figure 2. Microstructure of a specimen of V-5Cr-5Ti heat BL-47 following irradiation in the DHCE experiment at 425°C to 31 dpa and 0.39 appm He/dpa showing bubbles near grain boundaries at low magnification in (a) and structure near a grain boundary at higher magnification in dislocation contrast (b) and void contrast (c).

elucidate precipitation response. It was found that both conditions contained bubbles or voids, but densities and sizes were low. A low magnification example for the condition containing about 75 appm He is given in Figure 3 (a), and only a low density of small bubbles on the order of 7 nm can be identified in the matrix. However, careful comparison of boundary features in the two conditions, shown in Figures 3 (b) and (c) indicate a different distribution of helium bubbles. A few bubbles as large as 7 nm can be identified in the upper center of Figure 3 (b) for the specimen containing 10 appm He whereas a much higher density of smaller 3.5 nm bubble-like features can be observed in Figure 3 (c) for the specimen containing 75 appm He. Therefore, higher helium levels appear to promote local regions of higher densities of smaller bubbles, with maximum bubble sizes about the same in both cases.

Microstructural evolution at 600°C differed from that at 425°C primarily with regard to precipitate development. Dislocation structure consisted of loops and curved dislocation line segments, typical of climbing dislocations. Precipitates were elongated and as large as 40 nm long and 7 nm wide, and were easily imaged using, for example, ¾ <200>. However, differences could not be identified as function of helium production. Examples of the microstructures are provided in Figures 3 (d) and (e) for the specimen from packet 5C1 containing 10 appm He and in Figures 3 (f) and (g) for the specimen from packet 5C2 containing 75 appm He. In both cases, $\vec{g}$ = <200> contrast was used for the bright field image and $\vec{g}$ = ¾ <200> for the precipitate dark field image. The corresponding diffraction pattern is inset into Figure 3 (e) showing the typical elongation of the diffraction spot. Note that the operating $\vec{g}$ is perpendicular to the sense of elongation, indicating that the shape is probably plate-like, seen on edge. It is anticipated that this phase is TiP[6] based on the ¾[200] reflection, but similar morphologies have been identified previously as Ti_5Si_3.[4] Therefore, further investigation is necessary to identify the precipitate.

Discussion

The microstructural examinations reported here, although incomplete, agree with previously reported results on these or similar specimens.[4-6] However, the precipitate development found as a function of irradiation temperature and heat-to-heat variations in minor impurities should be taken into account because precipitation involves different chemical species at different temperatures. Such a response can arise because a precipitate becomes unstable above a critical temperature, but disappearance of a phase at lower temperatures is unusual unless precipitate dissolution is occurring due to cascade mixing, a phenomenon not generally found unless the irradiation temperatures are very low, and often leading to amorphization.

This work provides the novel observation that from the DHCE experiment it is found that increased helium levels may lead to a higher density of smaller helium bubbles in localized regions that can be overlooked because of their size. Mechanical property testing appears to show however that such increases in bubble density have little effect on deformation response.[8]

CONCLUSIONS

Collaborative microstructural examinations have been performed on a V-5Cr-5Ti control specimen of heat BL-63 following annealing at 1050°C, and specimens of V-4Cr-4Ti heat BL-47 irradiated in three conditions from the DHCE experiment: at 425°C to 31 dpa and 0.39 appm He/dpa, at 600°C to 18 dpa and 0.54 appm He/dpa and at 600°C to 18 dpa and 4.17 appm He/dpa. Results demonstrate that images of grain boundaries in BL-63 showing continuous coatings of unexpected phases are probably a result of double diffraction. Double diffraction effects must be ruled out before such images can be accepted as arising from precipitation. In BL-47 irradiated in DHCE, increases in helium generation may have

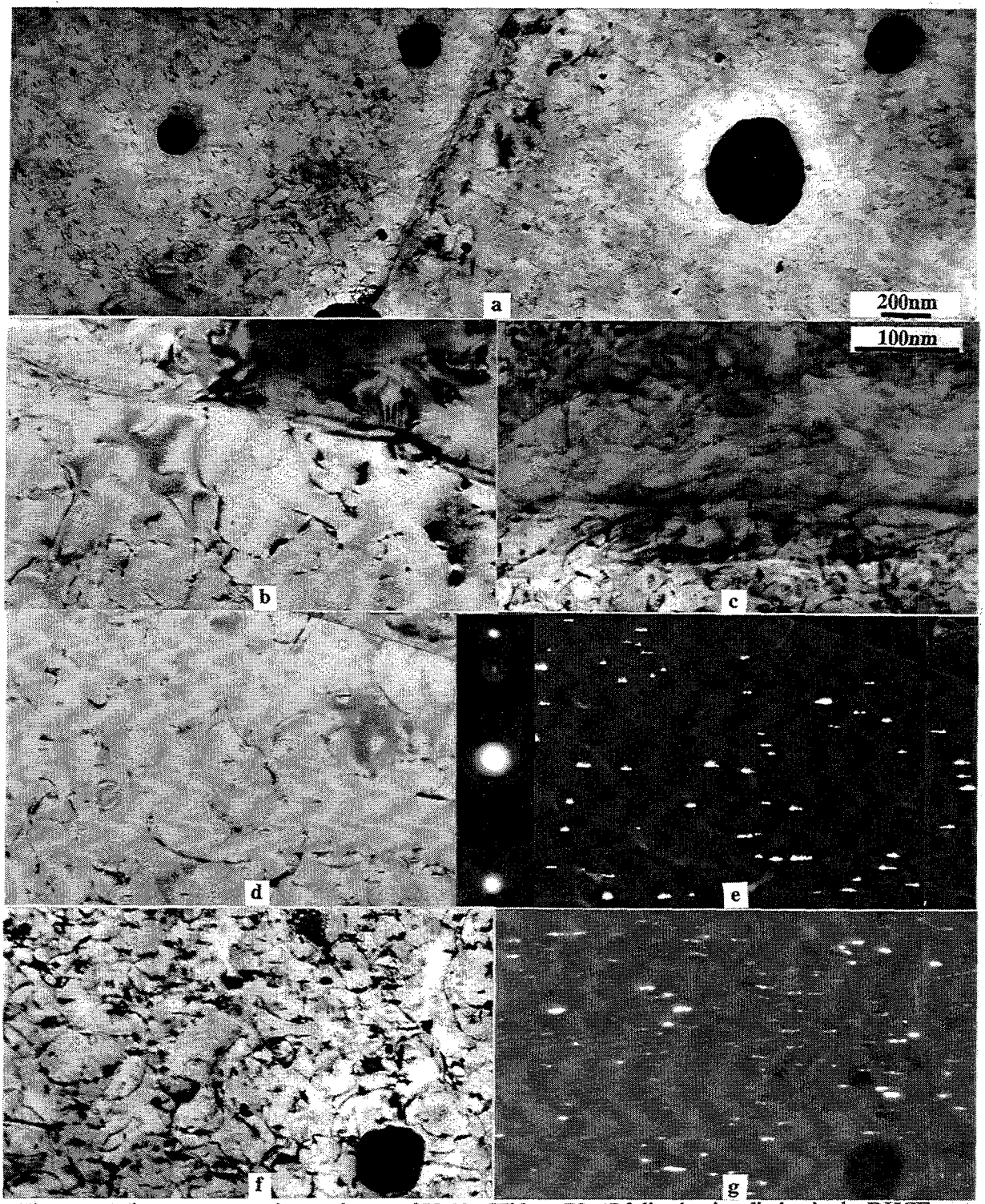

Figure 3. Microstructures of a specimens of V-5Cr-5Ti heat BL-47 following irradiation in the DHCE experiment at 600°C to 18 dpa and 0.54 or 4.17 appm He/dpa showing bubbles near grain boundaries at low magnification with 75 appm He in (a), bubbles near a grain boundary at higher magnification with 10 appm He in (b) and 75 appm He in (c), dislocation and precipitate structures with 10 appm He in (d) and (e) and with 75 appm He in (f) and (g).

resulted in high densities of smaller bubbles. However, precipitation response as a function of temperature is not completely understood.

Future work

It is planned to shift this collaborative work to the JEOL 2010F at PNNL in order to provide microchemical analysis when specimens and funding are available.

Acknowledgements

The authors acknowledge the help of Larry Nowicki for specimen transfers and support.

REFERENCES

1. B. A. Loomis, A. B. Hull, and D. L. Smith, J. Nucl. Mater., 179-181 (1992) 148.

2. H. M. Chung, J. Gazda, L. J. Nowicki, J. E. Sanecki, and D. L. Smith, DOE/ER-0313/15, 207

3. D. S. Gelles and Huaxin Li, DOE/ER-0313/19, 22

4. H. M. Chung, B. A. Loomis, H. Tsai, L. J. Nowicki, J. Gazda, and D. L. Smith, DOE/ER-0313/16, 204

5. H. M. Chung, L. J. Nowicki, J. Gązda, and D. L. Smith, DOE/ER-0313/17, 211.

6. H. M. Chung and D. L. Smith, J. Nucl. Mater., 191-194 (1992) 942.

7. H. M. Chung, B. A. Loomis, and D. L. Smith, J. Nucl. Mater., 212-215 (1994) 804.

8. H. M. Chung, B. A. Loomis, L. J. Nowicki, and D. L. Smith, DOE/ER-0313/19, 77.

2.0 SILICON CARBIDE COMPOSITE MATERIALS

HIGH THERMAL CONDUCTIVITY SiC/SiC COMPOSITES FOR FUSION APPLICATIONS -- J. C. Withers, W. Kowbel, and R. O. Loutfy (MER Corp., Tucson AZ); G. E. Youngblood (Pacific Northwest National Laboratory)* and C. Wong (General Atomics, San Diego CA)

OBJECTIVE

The objective of this work is to examine SiC composites fabricated by various processing methods designed to improve composite thermal conductivity. Specifically, it is desired to increase the thermal conductivity of these composites to meet requirements for advanced fusion energy systems.

EXTENDED ABSTRACT

SiC/SiC composites are considered for fusion applications due to their neutron irradiation stability, low activation, and good mechanical properties at high temperatures. The projected magnetic fusion power plant first wall and the divertor will operate with surface heat flux ranges of 0.5 to 1 and 4 to 6 MW/m^2, respectively. To maintain high thermal performance at operating temperatures the first wall and divertor coolant channels must have transverse thermal conductivity values of 5 to 10 and 20 to 30 W/mK, respectively [1]. For these components exposed to a high energy neutron flux and temperatures perhaps exceeding 1000°C, SiC/SiC composites potentially can meet these demanding requirements. The lack of high-purity SiC fiber and a low through-the-thickness (transverse) thermal conductivity are two key technical problems with currently available SiC/SiC. Such composites, for example produced from Nicalon^{TM} fiber with a chemical vapor infiltrated (CVI) matrix, typically exhibit a transverse conductivity value of less than 8 W/mK (unirradiated) and less than 3 W/mK after neutron irradiation at 800°C [2].

A new SiC/SiC composite fabrication process has been developed at MER. First, a carbon/graphite precursor fabric is directly converted to a high-purity SiC fabric by using a chemical vapor reaction (CVR) process. A matrix of crystalline SiC is added by a hybrid CVI-polymer infiltration and pyrolysis (PIP) process. Crystalline matrix conversion is enhanced by B-doping the starting liquid polymer prior to infiltration and pyrolysis. Because of the high thermal stability of the CVR-reacted SiC fabric, high temperature anneals can be used to further enhance the composite thermal and mechanical properties. For instance, Figure 1 compares the stress-strain curves from 4-pt. bend tests for SiC/SiC made with CVR converted SiC fabric with either a standard CVI matrix or two different hybrid PIP/CVI matrices. The two PIP/CVI matrices were fabricated with either a 3- or 6-cycle PIP infiltration followed by a final heat treatment at 1400°C. The composite with a CVI matrix alone exhibited low strength and brittle fracture. In contrast, both composites with PIP/CVI hybrid matrices exhibited much higher bend strengths and non-brittle fracture. These latter curves are comparable to curves obtained for conventional 2D plain weave Nicalon/CVI composites [2].

In Figure 2, the effect of heat treatment temperature and doping on the measured room temperature thermal diffusivity for the 3-cycle PIP processed composite are illustrated. For reference, the thermal diffusivity values of Nicalon/CVI and Nicalon/PIP without doping or heat treatment also are given. Heat treatment more than doubles the thermal diffusivity values of either the doped or undoped CVR-fiber/PIP matrix composites, while doping alone appears to also double these values. Notably, the thermal diffusivity values of the doped and heat treated CVR-fiber/PIP composite are more than double that of the Nicalon/CVI reference material. Further optimization of the thermal transport properties is achieved when additional PIP infiltration cycles and a final CVI treatment are included. As an example, a RT thermal diffusivity value of 0.28 cm^2/s, equivalent to a thermal conductivity value of 45 W/mK, has been attained. This value indicates

---

* Pacific Northwest National Laboratory (PNNL) is operated for the U.S. Department of Energy by Battelle Memorial Institute under Contract DE-AC06-76RLO-1830.

that by using a combination of doping and heat treatment methods, SiC/SiC thermal conductivity can be improved sufficiently to meet the thermal transport goals for potential use in a high flux radiation environment. Future work will be directed to testing the thermal performance of these materials after irradiation.

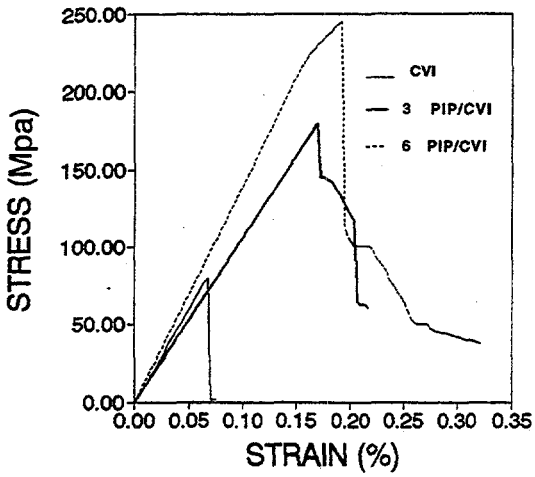

Figure 1. Comparison of stress-strain curves for SiC/SiC made by three different processes. The two PIP/CVI materials each had a final 1400°C heat treatment.

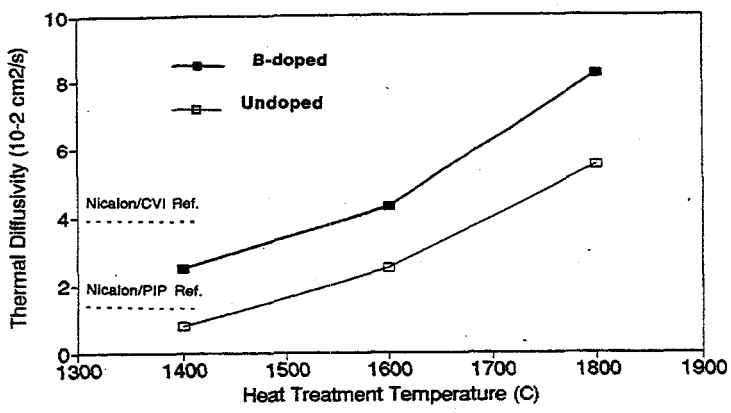

Figure 2. Effect of heat treatment on RT thermal diffusivity of undoped and boron-doped SiC/SiC composites made using 3 PIP cycles. For reference, the RT thermal diffusivity values of conventional Nicalon/CVI and Nicalon/PIP composite materials are shown.

This work was performed by MER Corp. under DOE Contract No. DE-FG02-94ER81487 and is to be published in the Proceedings for the IEA International Workshop on SiC/SiC Ceramic Composites for Fusion Structural Application, Ispra, Italy, October 1996.

REFERENCES

1. Clement Wong, "Thermal Conductivity of SiC and SiC-Composites and Design Implications," presented at SiC/SiC Workshop held in Richland, WA April 18-19, 1995.

2. G. W. Hollenberg, C. H. Henager, Jr., G. E. Youngblood, D. J. Trimble, S. A. Simonson, G. A. Newsome and E. Lewis, "The Effect of Irradiation on the Stability and Properties of Monolithic Silicon Carbide and SiCf/SiC Composites up to 25 dpa," J. Nucl. Mater. 219, 70-86 (1995).

CREEP BEHAVIOR FOR ADVANCED POLYCRYSTALLINE SIC FIBERS - G. E. Youngblood and R. H. Jones (Pacific Northwest National Laboratory),[1] G. N. Morscher[2] (Case Westerm Reserve University) and Akira Kohyama (Institute of Advanced Energy, Kyoto University, Kyoto 611, Japan)

OBJECTIVE

The objective of this work is to examine irradiation enhanced creep behavior in advanced polycrystalline SiC fibers.

SUMMARY

A bend stress relaxation (BSR) test has been utilized to examine irradiation enhanced creep in polycrystalline SiC fibers which are under development for use as fiber reinforcement in SiC/SiC composite. Qualitative, S-shaped 1hr BSR curves were compared for three selected advanced SiC fiber types and standard Nicalon CG fiber. The temperature corresponding to the middle of the S-curve (where the BSR parameter m = 0.5) is a measure of a fiber's thermal stability as well as its creep resistance. In order of decreasing thermal creep resistance, the measured transition temperatures were Nicalon S (1450 °C), Sylramic (1420 °C), Hi-Nicalon (1230 °C) and Nicalon CG (1110 °C).

PROGRESS AND STATUS

Introduction

As part of the Joint DOE/Monbusho Program to support materials development for fusion energy, PNNL has initiated a systematic study of the potential effects of irradiation creep in SiC/SiC composites and SiC fibers [1,2]. A previous report described a simple bend stress relaxation (BSR) test designed to examine the creep behavior of irradiated and unirradiated SiC fibers [3]. This report presents some new thermal creep (BSR) results for several unirradiated advanced SiC fiber types. The selected advanced fibers, namely Nicalon S™ and Hi-Nicalon™ manufactured by Nippon Carbon Co. and Sylramic™ manufactured by Dow Corning Corp, were all textile grade types suitable for incorporation into SiC_f/SiC composite. A planned test matrix designed to examine the creep behavior of these advanced fibers during irradiation also is presented.

Theoretical and Experimental Review

Theoretical and experimental details of the BSR test, developed initially by researchers at NASA Lewis [4], were presented previously [3]. Briefly, an initial elastic bend strain is applied to a single fiber by wrapping several coiled loops onto a SiC mandrel of radius R_o. The loops are captured by a SiC sleeve that slips over the mandrel. For the test designed to examine the potential effects of irradiation enhanced creep, the fiber loops will be subjected to a specific time (t), temperature (T), and irradiation dose (ϕ) at the fixture imposed strain $e_o = r_f/R_o$, where e_o represents the maximum strain at the outer edge of the coiled fibers and r_f is the fiber radius. To separate thermal from irradiation creep effects, thermal control BSR tests are carried out without irradiation for equivalent times and temperatures.

---

[1]Pacific Northwest National Laboratory is operated for the U. S. Department of Energy by Battelle Memorial Institute under Contract DE-AC06-76RLO 1830.

[2] Resident Research Associate at NASA Lewis Research Center, Cleveland OH).

In both these tests, a BSR parameter "m" quantifies the stress relaxation that occurs during either treatment:

$$m = 1 - R_o/R_{(T \text{ or } \phi)} \approx 1/[1+(e_c/e_o)] \quad (1).$$

In Eq. (1), R_T or R_ϕ is the arc radius of a relaxed fiber segment measured at room temperature after the thermal or the irradiation treatment, respectively. In the approximation, e_c is representative of the tensile creep strain that would result in a constant stress creep test for exposure temperatures and times equivalent to the BSR test temperatures and times and where the stress is taken equal to e_oE and E is the elastic modulus [5]. Thus, a constant strain BSR fiber creep experiment can yield basic creep data, i.e., stress and time dependence exponents and thermal activation energies. Unlike a conventional constant stress creep test, a fiber BSR test can be conveniently designed to take place in a reactor, thus its utility for examining the potential effects of irradiation enhanced creep. In BSR tests, values of m will range from 0 to 1 with m = 1 or 0 indicating the occurrence of no relaxation or complete relaxation by creep, respectively, while intermediate values of m indicate partial relaxation. The temperature dependence of m itself gives a convenient qualitative ranking of the creep resistance of various fiber types. Furthermore, Morscher and DiCarlo [4] have shown that the drop off in fiber strength with increasing temperature correlates with the transition temperature range of the BSR parameter m. Thus, a quantitative measure of the fiber thermal stability is the temperature at which m = 0.5 for a particular exposure time, i.e., 1 hr, 100 hr, 1000 hr, etc.

If actual creep strains are desired, Eq. (1) can be inverted to estimate e_c from measured m-values for either thermal creep (TC)- or irradiation creep (IC)- BSR tests. Then the irradiation dependent strain increment $\Delta e = e_c(\phi,T,t,e_o) - e_c(T,t,e_o)$ for an irradiation fluence (or dose) ϕ and is given by

$$\Delta e = e_o\{1/m(\phi,T,t,e_o) - 1/m(T,t,e_o)\} \quad (2).$$

The term in brackets is the difference in reciprocal m-values for the IC- and the TC-BSR tests for equivalent treatment temperature T, time t and maximum applied fiber strain e_o.

In this reporting period, several TC-BSR tests were carried out after heat treating the fiber coils for one and 100 hour periods in argon in a muffle tube furnace. Some of the TC-BSR tests were carried out in the same fixtures as will be used later in the IC-BSR tests; other tests were carried out by NASA Lewis in a similar BSR test rig. For all cases, e_o was about 0.2%.

The fibers tested at PNNL or NASA Lewis were selected from the same fabrication lots. Further characterization of representative fibers selected from these lots is being carried out at PNNL. Average fiber diameters are being determined by optical or SEM images of typical fiber cross-sections, densities by a liquid gradient column, and room temperature tensile strengths by using a Micropull™ device designed for this purpose.

Results and Discussion

The measured, lot specific fiber properties are given in Table 1 and are marked with an asterisk. The listed property values not marked with an asterisk were provided by the manufacturer and pertain to production fiber properties.

Table 1. Properties of SiC Fibers Selected for the IC-BSR Tests

Property		Nicalon CG	Hi-Nicalon	Sylramic	Nicalon S
Fiber diameter	(um)	14*	12*	10*	11*
Density	(g/cm^3)	2.55*	2.74*	3.0	3.10
Tensile strength	(GPa)	3.0*	3.4*	3.1	2.6
Tensile modulus	(GPa)	190	270	400	420
Elongation	(%)	1.4	1.0	0.8	0.6
Chemical composition	Si (wt %)	56.6	62.4	69	68.9
	C	31.7	37.1	29	30.9
	O	11.7	0.5	-	0.2
	C/Si (atomic)	1.31	1.39	1.0	1.05
Crystallite grain size	(nm)	<2*	5-10*	500	11
Thermal Stability	(°C)	1110*	1230*	1420*	1450*

* measured values for these fiber lots. Other values were provided by the manufacturer.

In Figure 1, the 1 hr BSR parameter m is plotted as a function of reciprocal temperature for the three advanced SiC fibers as well as for commercially available ceramic grade Nicalon CG fiber.

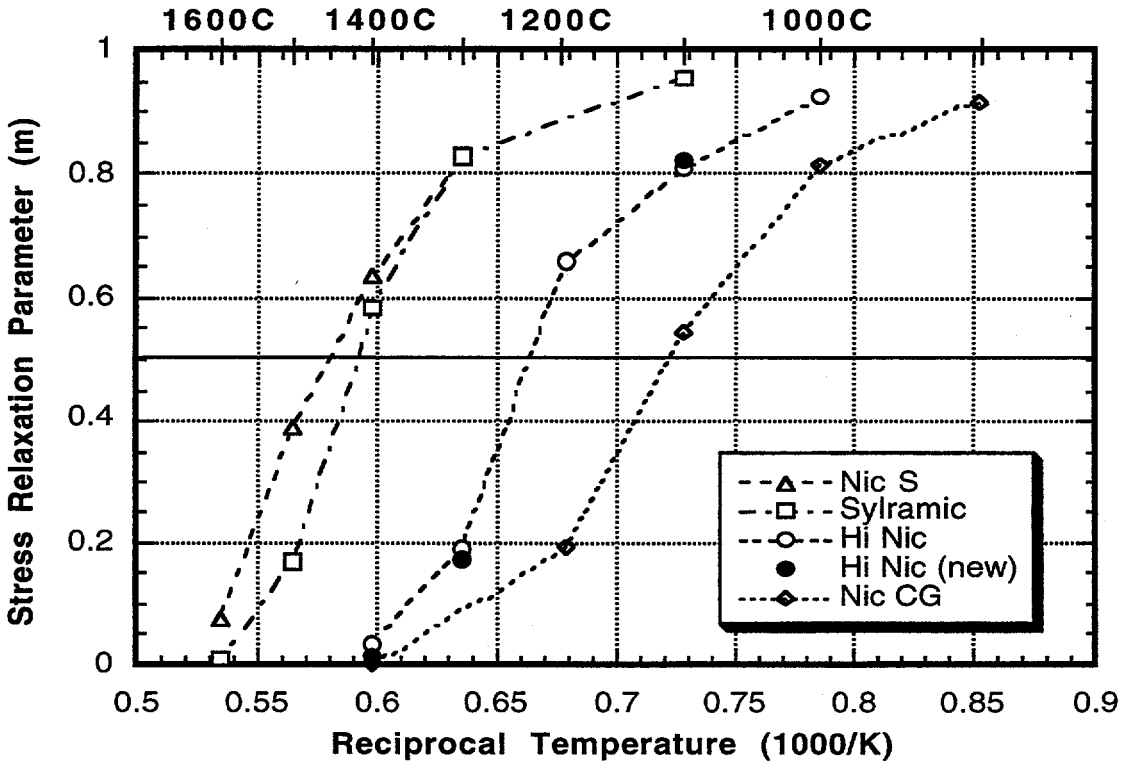

Figure 1. Comparison of one hour BSR thermal creep results for advanced SiC and Nicalon CG fibers ($e_o = 0.2\%$).

Qualitatively, the S-shaped curves have similar shapes. The transition from a slightly crept fiber ($m > 0.9$) to a near totally crept fiber ($m < 0.1$) takes place over about 350°C for all these fibers. The S-shaped curve for the fibers exhibiting the highest creep resistance are shifted to the left. Thus, in order of decreasing creep resistance, Nicalon S has the highest creep resistance, slightly higher than Sylramic, both of which are higher than Hi-Nicalon which is higher than Nicalon CG. The trends exhibited by these data generally agree with the trends delineated by Morscher and DiCarlo [6]; that is, lower oxygen content is the primary determinant of high creep resistance, while lower excess carbon content and near stoichiometric composition also contribute to a higher creep resistance in a SiC type fiber. Additional m-values for 20 and 100 hr exposures at 1000 and 1100°C were reported previously [3]. When compared to the corresponding 1000 and 1100°C 1 hr. m-values, the 20 and 100 hr values would be displaced to lower temperatures, i.e., to the right of these 1 hr data, as expected.

For each S-curve, the temperature where $m = 0.5$ is estimated and listed in Table 1 as the fiber "thermal stability." The data for the Hi-Nicalon fiber were obtained for two different lots. Although the common 1 hr m-values are in good agreement for these two different lots, the measured tensile strength (3.4 GPa) for the "new" lot of Hi-Nicalon fiber is somewhat greater than the listed production tensile strength value of 2.8 GPa. It is possible that the thermomechanical properties of Hi-Nicalon have a sensitive dependence upon fabrication details, which were still in a state of development when these fibers were obtained. Therefore, the higher strengths measured for the new lot of Hi-Nicalon may indicate some optimizing in its fabrication has taken place. For instance, Yun et al [7] have shown that annealing Hi-Nicalon in argon for one hour at 1500°C (well above its fabrication curing temperature of about 1300°C) significantly increases its average grain size and creep resistance while the tensile strength decreases.

CONCLUSIONS

The 1 hr TC-BSR test results indicated that the three advanced SiC fibers selected for later irradiation creep testing (Nicalon S, Sylramic and Hi-Nicalon), exhibited greater thermal creep resistance than standard Nicalon CG fiber, as expected. Using the temperatures at which $m = 0.5$ as a quantitative measure of thermal stability and creep resistance, the selected fibers ranked in order of highest thermal creep resistance first: Nicalon S (1450°C), Sylramic (1420°C), Hi-Nicalon (1230°C) and Nicalon CG (1110°C).

FUTURE WORK

To optimize SiC_f/SiC composite properties for fusion energy applications, it might be desirable to include a final high temperature anneal after fabrication. In particular, Hi-Nicalon strength and creep resistance have been shown to be sensitive to such a treatment, as noted above. Therefore, annealed Hi-Nicalon will be added to future fiber BSR testing. Also in the next reporting period, the 100 hr TC-BSR testing will be completed and reported for the selected SiC fibers.

The planned IC-BSR test matrix is presented in Table 2. The first IC-BSR irradiation cycle is scheduled to start in January, 1997 in the ATR reactor in Idaho Falls. Its irradiation test temperature will be 370°C, well below thermal creep regime temperatures. However, if irradiation creep is temperature independent down to 370°C, as preliminary data suggest [1], any observed creep will be totally irradiation induced. The following three tests will examine fiber creep in the more fusion relevant temperature range (800 - 1000°C), a range where both thermal and irradiation induced creep could be important. These latter tests will examine the dose dependence to 25 dpa-SiC as well as the applied strain dependence from 0.1 to 0.25%.

Table 2. SiC Fiber IC-BSR Test Matrix

Irrad Temp (°C)	Dose (dpa-SiC)	Time (hrs)	Applied Strain (%)	Initial Stress* (MPa)	Facility-Start Date
370	2	1500	0.2	400-800	ATR-Jan 97
1000	2	1500	0.1, 0.2, 0.25	200-1000	ATR-Jul 97
800	10	6400	0.1, 0.2, 0.25	200-1000	HFIR-Jan 98
1000	25	6400	0.1, 0.2, 0.25	200-1000	HFIR-Jan 98

* Depends on the fiber elastic modulus.

REFERENCES

1. F. A. Garner, G. E. Youngblood and M. L. Hamilton, "Review of Data on Irradiation Creep of Monolithic SiC," Fusion Materials Semiannual Progress Report for Period Ending December 31, 1995. DOE/ER--0313/19.

2. M. L. Hamilton, C. A. Lewinsohn, R. H. Jones, G. E. Youngblood, F. A. Garner and S. L. Hecht, "Progress in the Development of a SiC_f/SiC Creep Test," Fusion Materials Semiannual Progress Report for Period Ending June 30, 1996. DOE/ER--0313/20.

3. G. E. Youngblood, M. L. Hamilton and R. H. Jones, "Technique for Measuring Irradiation Creep in Polycrystalline SiC Fibers," Fusion Materials Semiannual Progress Report for Period Ending June 30, 1996. DOE/ER--0313/20.

4. Gregory N. Morscher and James A. DiCarlo, "A Simple Test for Thermomechanical Evaluation of Ceramic Fibers," *J. Amer. Ceram. Soc.,75(1),136-40 (1992).*

5. James A. DiCarlo, "Creep Limitations of Current Polycrystalline Ceramic Fibers," *Composites Science and Technology 51, 213-222 (1994).*

6. Gregory N. Morscher and James A. DiCarlo, "Creep and Stress Relaxation Properties in Relation to Microstructure for SiC Fibers," *HITEMP Review Vol. III, Oct. 25-27, 1993. NASA CP19117.*

7. H. M. Yun, J. C. Goldsby and J. A. DiCarlo, "Effects of Thermal Treatment on Tensile Creep and Stress-Rupture Behavior of Hi-Nicalon SiC Fibers," *Ceram. Eng. Sci. Proc. 16(5), 987-996 (1995).*

THERMOGRAVIMETRIC AND MICROSCOPIC ANALYSIS OF SiC/SiC MATERIALS WITH ADVANCED INTERFACES - C. F. Windisch Jr., R. H. Jones (Pacific Northwest National Laboratory)* and L. L. Snead (Oak Ridge National Laboratory)

OBJECTIVE

The objective of this effort is to determine the chemical stability of SiC/SiC composites with advanced fiber/matrix interfaces in Ar+O_2 environments.

SUMMARY

The chemical stability of SiC/SiC composites with fiber/matrix interfaces consisting of multilayers of SiC/C/SiC and porous SiC have been evaluated using a thermal gravimetric analyzer (TGA). Previous evaluations of SiC/SiC composites with carbon interfacial layers demonstrated the layers are not chemically stable at goal use temperatures of 800-1100°C and O_2 concentrations greater than about 1 ppm. No measurable mass change was observed for multilayer and porous SiC interfaces at 800-1100°C and O_2 concentrations of 100 ppm to air; however, the total amount of oxidizable carbon is on the order of the sensitivity of the TGA. Further studies are in progress to evaluate the stability of these materials.

INTRODUCTION

A previous analysis (1) of the chemical stability of SiC/SiC in inert gas containing impurity levels of O_2 suggested that composite material with C as the fiber/matrix interfacial debond layer may not be suitably stable in fusion relevant environments. This study, which was only based on chemical stability and did not include radiation effects, predicted that O_2 concentration in an inert gas must be kept to less than 1 ppm to obtain a 10 year lifetime. While it may be possible to achieve less than 1 ppm O_2 in small laboratory equipment, the concentration would be difficult to achieve in a large engineering device. Therefore, materials with advanced fiber/matrix interfacial debond layers are being developed which minimize the amount of carbon in the interface. Two such composites are the multilayer approach where the interface debond layer is several layers of SiC/C/SiC where the C layer is very thin. This material has been made by Hypertherm. A second approach utilizes defective or porous SiC as the interfacial debond layer. Samples with this interface were made at ORNL by the forced CVI method.

Thermogravimetric analysis (TGA) was previously used to quantify carbon oxidation in the interface during exposure to oxygen gas at varying conditions of temperature and partial pressure of oxygen (2). This approach was found to be very useful in studies on SiC/SiC with 1-μm thick interfaces. Linear TGA mass losses as a function of time, with slopes dependent on both temperature and oxygen partial pressure, were measured in these previous experiments and used to conclude that the mass losses were limited primarily by the carbon oxidation reactions at the gas/carbon interface. It was hoped that TGA studies on the ORNL SiC/SiC materials, with their compositionally more complex interfaces, would be similarly informative.

EXPERIMENTAL

TGA studies were performed using a TA Instruments SDT 2960 analyzer. SiC/SiC samples, about 0.30 cm x 0.50 cm x 0.25 cm in size, were ramped from room temperature to the temperature of interest at 65°C/minute and then held at this temperature for 24 h, during which time the mass of the sample was monitored. Gas flow through the instrument was maintained at 0.1 L/min. Other than the tests in air, all

---

* Pacific Northwest National Laboratory (PNNL) is operated for the U.S. Department of Energy by Battelle Memorial Institute under Contract DE-AC06-76RLO-1830.

gases tested were premixed concentrations of oxygen in argon. Optical microscopy and scanning electron microscopy (SEM) were performed on selected samples before and after TGA analysis.

RESULTS

Multilayer Interface SiC/SiC

TGA data for all the experiments in this study, illustrated for two sets of conditions in Figures 1a and 1b, contained a region at less than 200 minutes dominated by an instrumental artifact. In this region, the mass appears to decrease rapidly by about 0.1 to 0.3 mg and then increase by about the same amount. (The system achieves the set temperature at about 12-17 minutes into the run, or at the approximate position of the "peak" in the data.) Several runs on control samples (no SiC/SiC) exhibited the same response, so all data below 200 minutes were considered to be subject to too much error to be useful. Data above 200 minutes showed some trends that appeared to depend on temperature and oxygen partial pressure. However, caution must be taken not to misinterpret the >200-minute data as well since the experimental uncertainty from several control runs was estimated to be $\pm$ 0.05 mg compared to the observed mass change, which was 0.1 mg at the most between 200 and 1440 minutes.

As shown in Figures 1a and 1b, the TGA data between 200 and 1440 minutes was different for Ar at 800°C and air at 1100°C. In Ar, the data exhibit a slow mass loss (Figure 1a). In air, they show a mass gain (Figure 1b). A transition from one form of behavior to the other appeared to occur at about 100 ppm oxygen. The TGA data in Ar may indicate a slow mass loss in the absence of oxygen. However, since the total mass loss in these tests was only about 0.05 mg, or about the same magnitude as the uncertainty, this conclusion is questionable. An approximate calculation was performed to determine the maximum amount of carbon in the sample that could burn out and cause this mass loss, even though it is uncertain what the burnout mechanism could be in the absence of oxygen. Using geometric measurements on previously tested SiC/SiC composite samples and assuming similar geometries for the ORNL materials, it can be shown that about 0.2 mm^3 of the samples is interface material. However, only a fraction of the interface material is carbon (about 30% for the multilayer interface and 15-20% for the porous interface). For the multilayer interface material, it is estimated that only 0.12 mg of carbon was present in an entire sample. This amount is larger than the mass losses observed in the present study suggesting that loss of interfacial carbon could explain the results. However, the data are still too close to the experimental uncertainty to produce reliable conclusions.

At 100 ppm oxygen and above at 1100°C, a gradual mass gain was observed as illustrated in Figure 1b. The rate of mass gain also appeared to increase with increasing oxygen partial pressure. The magnitude of the mass gain was small, but was larger than the experimental uncertainty at the higher oxygen partial pressures (air, Figure 1b). A thin interference-type coating was also observed over the whole surface of samples that showed a mass gain. For this reason, we believe the mass gains are real and reflect the growth of a film, probably SiO_2, that results from the reaction of the SiC and oxygen. Attempts to use the TGA data to quantify the kinetics of the film formation were not successful. The "slopes" of the mass gain region (200 to 1440 minutes) do, indeed, increase with increasing oxygen (i.e. more reaction with more oxygen) but it was difficult to model this increase, probably because the film growth kinetics was linear-parabolic. Linear-parabolic kinetics would be expected to show the most dramatic effects of temperature and oxygen partial pressure near the transition zone (when the curve changes from linear to parabolic control), and this behavior is probably observed at times shorter than 200 minutes where the large instrumental artifact also occurs.

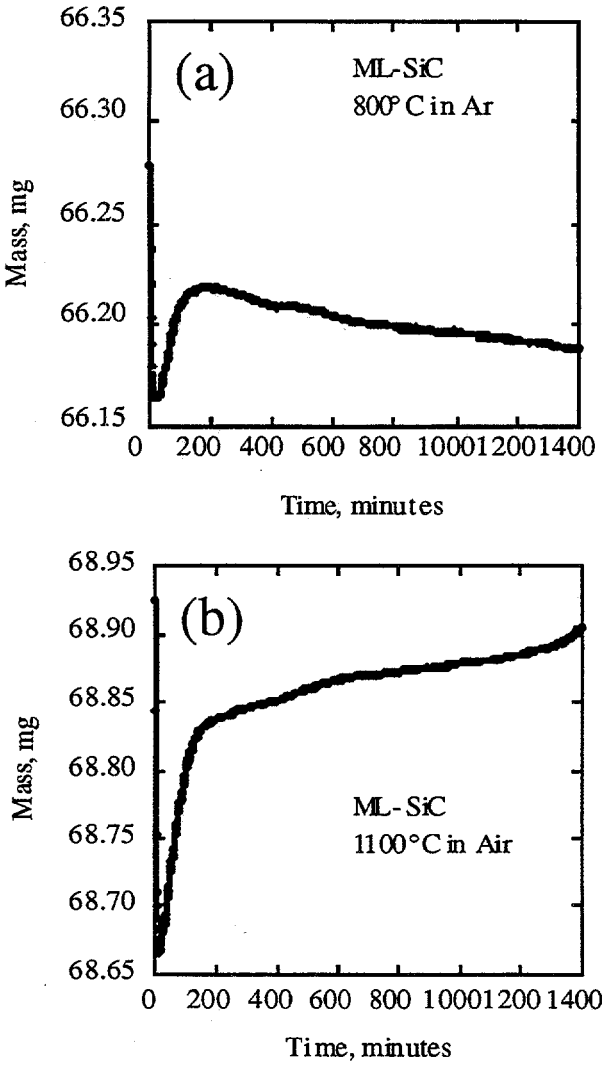

Figure 1. TGA Data for Multilayer Interface SiC/SiC (a) at 800°C in Ar and (b) at 1100°C in Air.

Porous Interface SiC/SiC

As shown in Figures 2a and 2b, the porous and multilayer interface SiC/SiC show essentially the same behavior as a function of temperature and oxygen partial pressure. This is consistent with the behavior arising largely from either instrumental factors or reactions of the entire sample surface (which is similar for both samples) rather than from the interface (which is different). Both of these possibilities were discussed in detail above, for the multilayer interface SiC/SiC material.

If the mass gains observed for the samples at higher temperatures and oxygen partial pressures are due to the growth of an SiO_2 film over the whole sample, the data are not useful for quantifying effects on the interface material. Attempts to use optical microscopy and SEM to observe changes in the interface have not been successful to date. As shown in Figure 3, the interface is less than 100 nm thick, close to the resolution limit of the techniques. Samples tested in air have not yet been evaluated and these may show some effects

around the ends of the interfaces that could relate to "pinching" from SiO_2 previously observed in thin-interface materials and associated with mitigating interface reactions. Future work will study this possibility. At this point, however, it does not appear that either microscopy or our TGA instrument can be used to say much about reactions of the interface material.

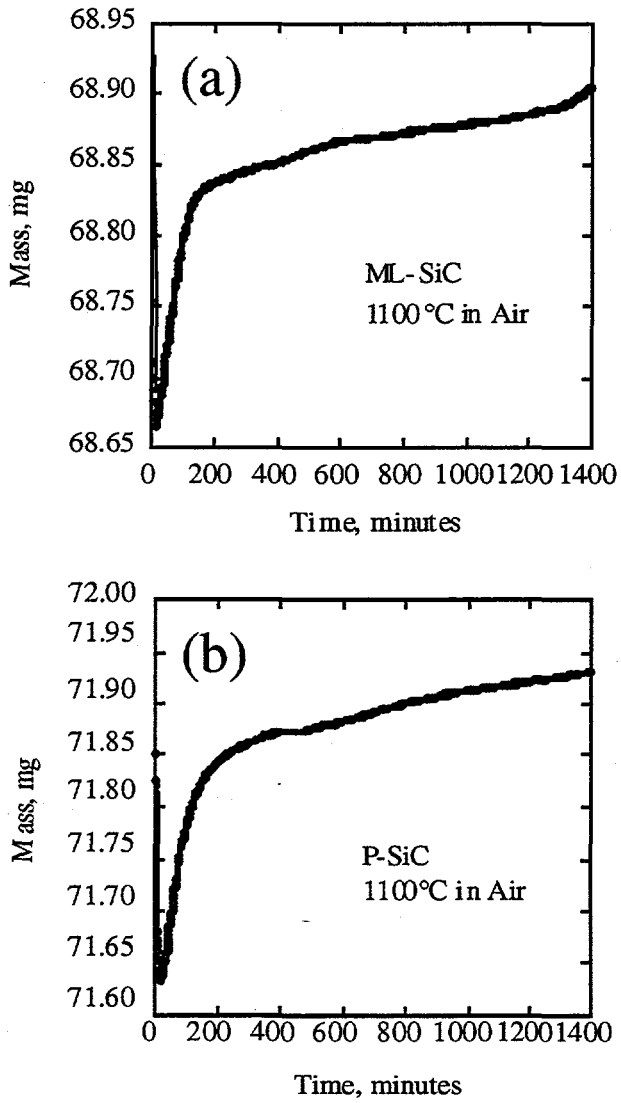

Figure 2. Comparison of TGA Data for (a) Multilayer and (b) Porous Interface SiC/SiC at 1100°C in Air.

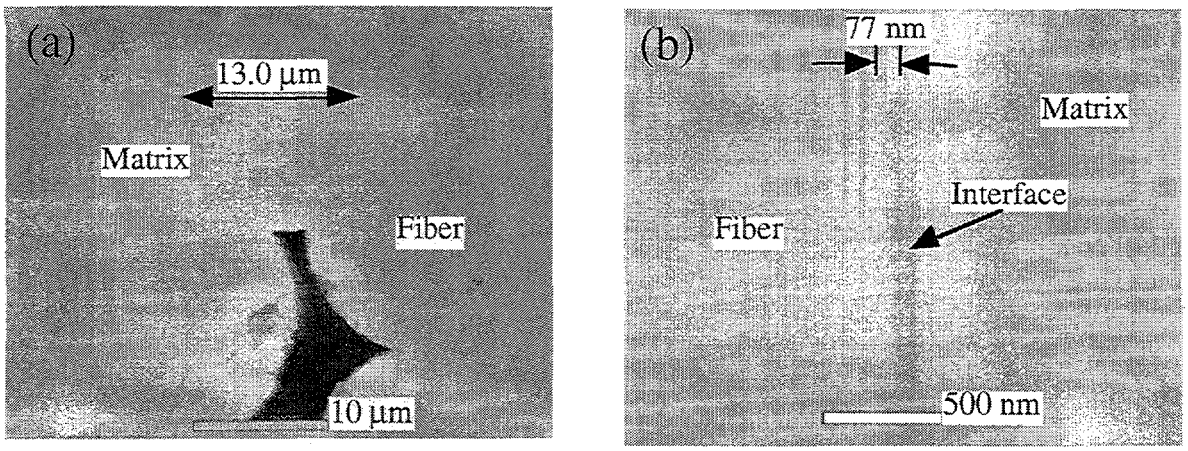

Figure 3. SEM Images of Porous Interface SiC/SiC Illustrating the Difficulty in Resolving the Interface.

FUTURE WORK

Additional microscopy work will be performed in cases where reaction of the SiC/SiC and oxygen was observed to determine whether any "pinching" of the interfaces occurs that could, possibly, slow the interface reaction kinetics, similar to mechanisms proposed for other SiC/SiC materials. Crack growth rate studies are being considered since the crack velocity for these materials has been shown to be sensitive to the interface oxidation.

REFERENCES

1. C. H. Henager, Jr., C.F. Windisch, Jr., and R. H. Jones, "Time Dependent Bridging and Life Prediction for SiC/SiC in a Hypothetical Fusion Environment", Fusion Materials Semiannual Progress Report for Period Ending June 30, 1996, DOE/ER-031/20.

2. C.F. Windisch, Jr., C. H. Henager, Jr., G. D. Springer and R. H. Jones, "Oxidation of the Carbon-Interface in Nicalon-Fiber-Reinforced Silicon Carbide Composite", J. Am. Ceram. Soc., in press.

THRESHOLD IRRADIATION DOSE FOR AMORPHIZATION OF SILICON CARBIDE — L. L. Snead and S. J. Zinkle (Oak Ridge National Laboratory)

OBJECTIVE

The amorphization of silicon carbide under neutron irradiation is a concern at low irradiation temperatures. The objective of this work is to present a summary of the data on amorphization due to ion beam irradiation and to propose a model which describes the damage threshold as a function of temperature for ion and neutron irradiated material.

SUMMARY

The amorphization of silicon carbide due to ion and electron irradiation is reviewed with emphasis on the temperature-dependent critical dose for amorphization. The effect of ion mass and energy on the threshold dose for amorphization is summarized, showing only a weak dependence near room temperature. Results are presented for 0.56 MeV silicon ions implanted into single crystal 6H-SiC as a function of temperature and ion dose. From this, the critical dose for amorphization is found as a function of temperature at depths well separated from the implanted ion region. Results are compared with published data generated using electrons and xenon ions as the irradiating species. High resolution TEM analysis is presented for the Si ion series showing the evolution of elongated amorphous islands oriented such that their major axis is parallel to the free surface. This suggests that surface or strain effects may be influencing the apparent amorphization threshold. Finally, a model for the temperature threshold for amorphization is described using the Si ion irradiation flux and the fitted interstitial migration energy which was found to be ~0.56 eV. This model successfully explains the difference in the temperature-dependent amorphization behavior of SiC irradiated with 0.56 MeV silicon ions at 1×10^{-3} dpa/s and with fission neutrons irradiated at 1×10^{-6} dpa/s irradiated to 15 dpa in the temperature range of ~340 ±10K.

PROGRESS AND STATUS

Introduction

An understanding of the microstructural evolution of SiC under irradiation is critical to the application of these materials in fusion systems. At the expected application temperatures for SiC (<1200°C) the most significant microstructural changes occur in the lower temperature regime. Specifically, at temperatures under 100°C, volumetric swelling due to point defect induced strain has been seen to reach 3%.[1, 2] At these low temperatures, amorphization of the SiC is also possible, which would lead to a substantial volumetric expansion of ~15%,[3-5] along with correspondingly large changes in mechanical properties such as hardness and modulus.[3, 4, 6] Specifically, Snead et al.[6] found that the elastic modulus for chemically vapor infiltrated SiC decreased from 400 GPa in the unimplanted region, to ~275 GPa in the amorphized region. Likewise, the hardness was seen to decrease from 41 GPa to 32 GPa. Similar behavior has been recently reported by other authors[5] for ion irradiated SiC.

Numerous studies[3, 7-14] have shown that SiC becomes amorphous during ion-beam irradiation at temperatures between 77 K and room temperature for damage levels of approximately 0.1 to 0.5 atomic displacements per atom (dpa.) To date there has been no demonstration of neutron induced amorphization of SiC, although it is worth noting that there is a lack of low temperature high dose neutron irradiation data. The majority of studies relating to SiC amorphization have utilized low-energy (<1 MeV) ion-beams[8-14] with a few researchers studying the amorphization threshold using high energy electrons.[15-19] These electron and ion irradiation studies have typically been carried out at temperatures between liquid nitrogen and 470 K. Amorphization was not observed in SiC irradiated with fission neutrons (damage rate ~ 10^{-7} dpa/s) at ~420 K to damage levels in excess of 1 dpa.[20]

In the past ten years there has been a growing interest in the effect of irradiation temperature on the amorphization of silicon carbide. Specifically, Kinoshita[15] and Matsunaga[16] used 1 MeV electron irradiation to measure the damage threshold for amorphization from liquid nitrogen temperature to room temperature. Inui[17-19] has used 2 MeV TEM electrons and Weber[5, 21-24] has used a 1.5 MeV Xe beam in conjunction with (non damaging) TEM to study amorphization. In all cases the critical threshold for amorphization was measured as a function of temperature. It was observed that there is a temperature-independent amorphization dose at low temperatures followed by a temperature above which the damage level required to amorphize SiC increases rapidly. In each case an apparent asymptotic increase in the critical dose for amorphization occurred, yielding a critical temperature above which amorphization is apparently not possible. This value is reported to be significantly lower for electron irradiations compared to ion irradiations at the same damage rate of ~1×10^{-3} dpa/s. The critical temperatures above which amorphization does not occur has been reported to range between 290 K and 340 K for electrons,[17-19] ~420 K for Si ions,[25] and ~490 K for Xe ions.[23] It is noted that both Weber's[21, 23] and Matsunaga's[16] work did not observe a significant difference in amorphization threshold between α and β SiC, whereas Inui reported ~50 K lower threshold temperature for α-SiC.[17]

Experimental

The materials chosen for this study were Cree Systems single crystal 6-H alpha SiC, Cercom hot pressed β-SiC, and Carborundum sintered α-SiC (Hexaloy). Four ion beams were selected for implantation in orientations both normal and parallel to the basal plane. Specifically, 3.6 MeV Fe and 0.56 MeV Si ions were implanted as single beams, with a dual beam of 1.8 MeV Cl and 1.0 MeV He. The silicon beam was produced in the NV-500 accelerator at the SMAC user facility at ORNL while the Fe, Cl and He ion beams were produced in the Triple Ion Beam Facility at ORNL. In both facilities, samples were heat sinked to a thermalizer block and temperatures measured using thermocouples either in contact with the thermalizer block or a backing to which the block was clamped. Typical ion beam fluxes were 7.1×10^{11} to 2.6×10^{12} ion/cm^2 -s, producing peak displacement damage rates of ~0.2 to 1×10^{-3} dpa/s. Cross sectional transmission electron microscopy was performed on all samples. The determination of amorphization was made by bright and dark field imaging and the presence of spot-free, diffuse diffraction patterns. The amorphized band was measured and compared with the TRIM-92[26] code to determine the critical dose for amorphization. The damage calculations were obtained assuming a sublattice-averaged threshold displacement energy of 40 eV. High resolution TEM was performed with a JEOL 4000 microscope, while conventional microscopy was performed using a Philips CM-12 microscope. Samples prepared for microscopy were mechanically thinned and ion milled with argon ions at 6 keV and 15° using a liquid nitrogen cooled stage during milling. A final mill was performed at 3 keV, 9° for 10 minutes at ambient temperature to reduce surface amorphization associated with argon implantation.

Two TEM discs each of Carborundum sintered α-SiC (Hexaloy) and hot pressed β-SiC produced by Cercom were irradiated in the target region of the High Flux Isotope Reactor in an aluminum capsule that was in direct contact with the reactor coolant water, producing a specimen irradiation temperature of ~340K. The fast neutron (E>0.1 MeV) fluence was ~1.5×10^{26}/m^2 corresponding to a displacement level of ~15 dpa at a damage rate of ~1×10^{-6} dpa/s. Densities on these specimens were obtained using density gradient columns using mixtures of tetrabromethane-methylene iodide or ethylene bromide-bromoform for the unirradiated and irradiated samples, respectively. The accuracy of the measurement was better than 0.001 g/cc and was found to be reproducible in repeated measurements and consistent for duplicate irradiated samples.

RESULTS AND DISCUSSION

Amorphization of the single crystal SiC due to 3.6 MeV Fe ion irradiation at room temperature is shown in Figure 1. The upper cross-sectional micrograph shows the highest fluence specimen (5.7×10^{15} ions/cm^2), which amorphized over the entire range. The electron diffraction pattern for the amorphous region is inset into Fig. 1a. At a fluence of 2.0×10^{15} ions/cm^2 (Fig. 1b), amorphization only occurred over a ~0.7 μm wide band centered near the peak damage region. Amorphization was not observed at any depth at the lowest Fe ion fluence shown in Fig. 1c (1.4×10^{14} ions/cm^2), which produced 0.05 dpa in

the peak damage region. Similar results were obtained for CVD SiC irradiated with Fe ions at the same three fluences.[25] No significant difference was found in the amorphization behavior of the Cree single crystal 6H-SiC, CVD SiC or Cercom hot pressed β-SiC. Figure 1 also demonstrates the swelling associated with the amorphization of SiC. By comparison of Fig. 1a (totally amorphous) with the non-amorphized sample (Fig. 1c), it is seen that amorphization has caused a significant volumetric expansion, with a resultant 0.27 μm movement of the free surface to the left. From this free surface "step-height" movement a volumetric swelling of ~15% was calculated due to the crystal-to-amorphous transformation.[25] Part of the original surface is missing from Fig. 1b so the volumetric expansion associated with the 0.7 μm amorphous band is not evident. From a comparison of the visible damage depths for the three Fe ion irradiation fluences, the amount of volumetric swelling associated with amorphization was calculated to be ~17%.[25]

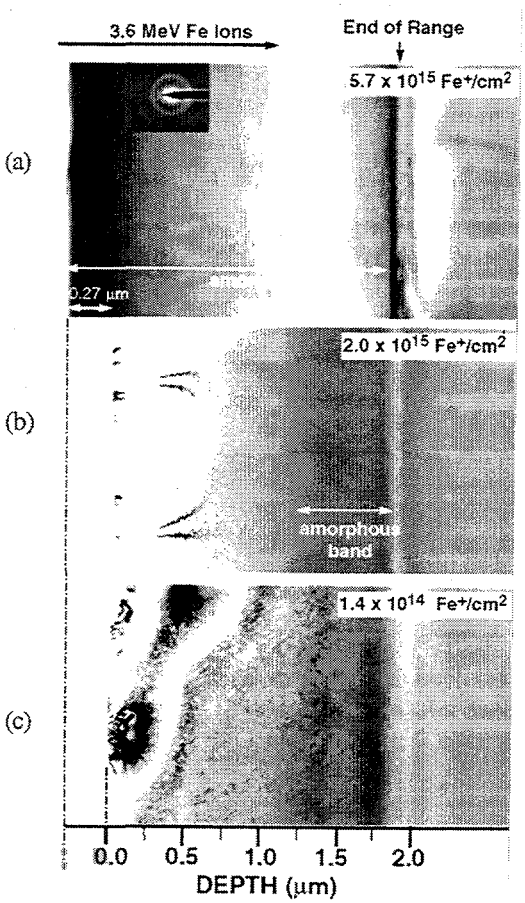

Figure 1. 3.6 MeV Fe ion amorphized SiC
He ion single crystal 6H-SiC.

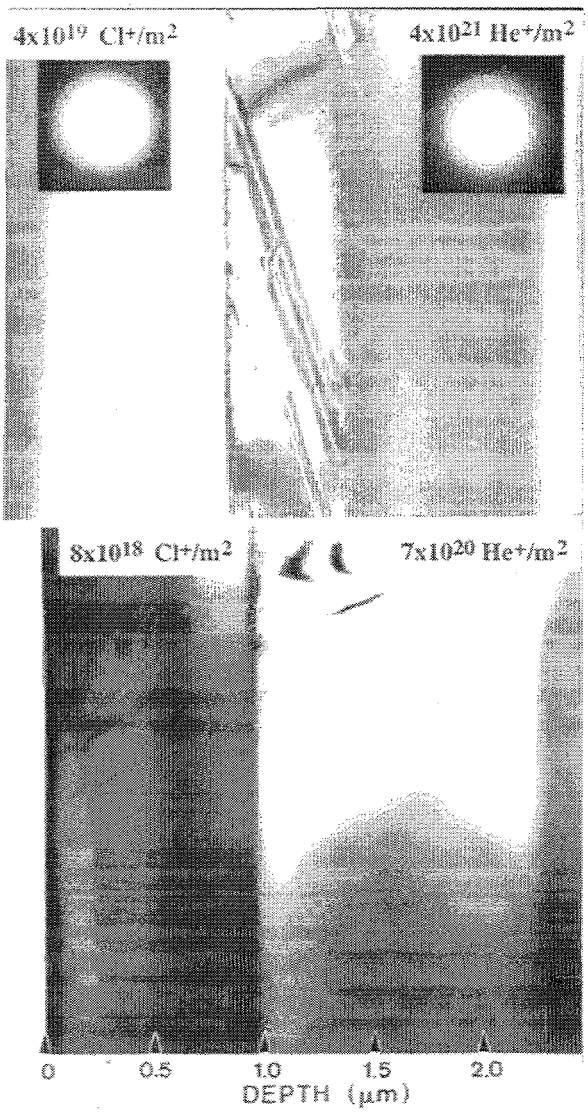

Figure 2. 1.8 MeV Cl and 1 MeV
amorphized β-SiC.

Figure 2 shows the effect of a room temperature simultaneous irradiation of 1.8 MeV Cl and 1.0 MeV He ions into a β-SiC sample.[25] The Cl beam had a damage range of nearly 1 μm, and the He beam produced damage up to ~2 μm. The upper micrograph of the figure is for the higher dose condition, and it is seen that amorphization has occurred over all but the near-surface regions of the Cl plus He ion irradiated region (~1.0 μm) and over the last third of the He ions irradiated region (maximum range ~2.4 μm due to density decrease associated with amorphization.) The lower ion doses shown in the bottom of this figure exhibit amorphization only near the end of the Cl and He ion ranges. Figure 2 also shows the effect of volumetric expansion, visible through the free surface movement. A measured swelling associated with amorphization of 17% (±3%) was measured for these specimens. The measured volume change associated with amorphization in SiC of 17% for the Fe, Cl and He ion irradiation is somewhat lower than the 22±3% reported by Weber,[5] but in good agreement with the value of 15% reported by McHargue.[4]

A matrix of samples was irradiated from room temperature to 400°C at several different Si ion fluences. Figure 3 shows examples of two different specimens that were irradiated to a Si ion fluence of 1.0×10^{15} ions/cm^2 at room temperature and 200°C. The room temperature specimen contained a band of material starting at about mid-range (~0.3μm) that appeared to be amorphous under ordinary bright field imaging conditions. However, through high resolution imaging a small volume fraction (<5%) of dispersed islands of crystalline material was observed at the beginning half of the "amorphous" band and was absent at the end of the ion range. These crystalline islands account for the weak diffraction spots seen in the diffuse rings of the upper diffraction pattern of Fig. 3 and indicate that the material was on the verge of total amorphization. The 200°C irradiated sample given in the lower part of Fig. 3 shows no evidence of amorphization for equal dose rates (1×10^{-3} dpa/s), indicating a temperature dependent dynamic recovery.

The measured threshold for amorphization as a function of temperature for the Si ions and the other ions is given in Figure 4. As discussed previously, the presence of Fe and Si ions did not have any measurable effect on the threshold amorphization dose, whereas Cl ions significantly reduced the threshold dose for amorphization in the implanted ion region.[7, 25] This enhancement of amorphization is clearly demonstrated in Fig. 4 for the Cl irradiated material near room temperature. The remaining data in Fig. 4 were all taken from the unimplanted regions. Figure 4 shows a rapid increase in the critical amorphization dose with increasing temperature. At 420 K, no amorphization was observed in either the implanted or unimplanted regions at the highest Si ion dose studied, which was equivalent to 20 dpa.

These temperature dependent results are qualitatively consistent with previous studies which have used an in-situ technique for measuring the temperature dependent amorphization in SiC. For the in-situ approach, an irradiating beam is passed through, or partially through, a thin section of material with real-time observation of the microstructural evolution using TEM. Specifically, Kinoshita[15] and Matsunaga[16] used

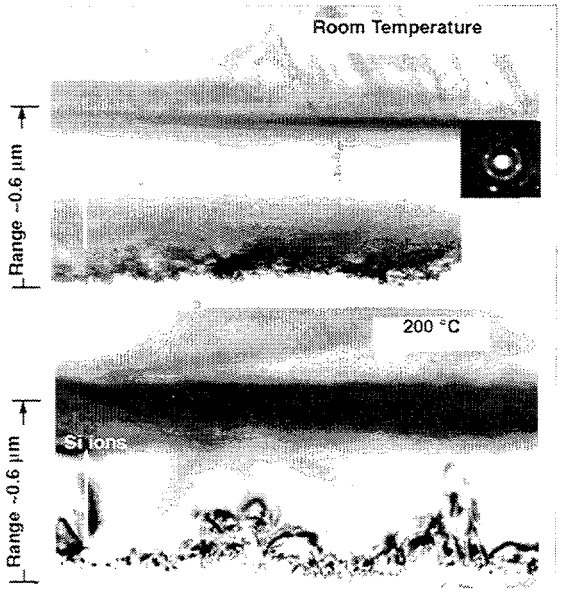

Figure 3. Cross sectional TEM of Si ion implanted SiC.

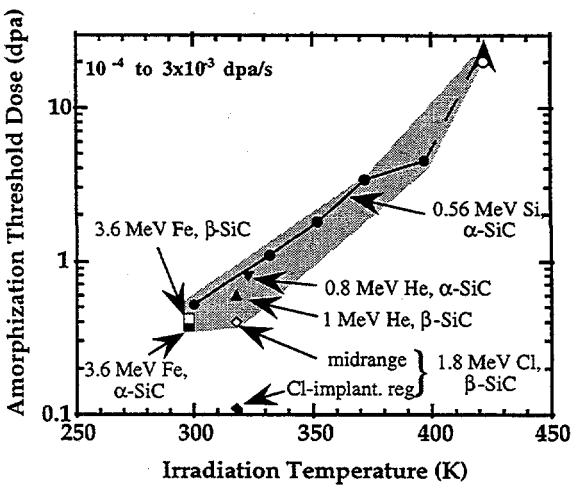

Figure 4. Amorphization threshold of SiC as a function of irradiation temperature.

1 MeV electrons while Inui[17-19] has used 2 MeV electrons to both damage and image the samples. Weber[5, 21-24] used a 1.5 MeV Xe beam in conjunction with TEM. In these examples Inui found the amorphization dose threshold below room temperature to be approximately 1 dpa for α-SiC[17] and about 0.5 dpa for highly faulted β-SiC.[18] Weber[21] found the amorphization threshold near room temperature to be about 0.2 dpa for 1.5 MeV Xe ions. Figure 5 compares the data from the Si ion irradiations with the data from Inui and Weber, all of which were obtained at a damage rate near 1×10^{-3} dpa/s. All of the data in Fig. 5 have been plotted assuming an average displacement energy of 40 eV.

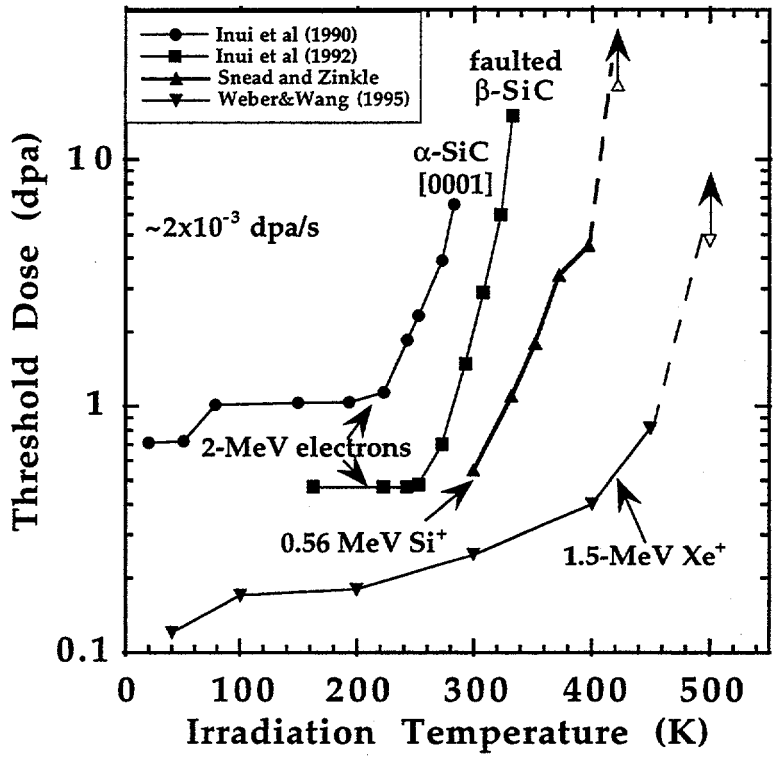

Figure 5. Temperature dependent critical dose for amorphization of SiC[25].

The results of Fig. 5 raise interesting questions regarding the mechanism for amorphization in SiC. Because amorphization has occurred under electron irradiation it is apparent that the SiC crystal, in the cubic or hexagonal form, can be driven amorphous by simple defect accumulation alone. The Xe ions, which can transfer much higher energies to the lattice atoms than the electrons (or the Si ions), are apparently capable of amorphizing SiC to a much higher temperature than electrons at the same damage rate. While the Xe ions will cause relatively large cascades compared to Si ions, no cascades can form for the low energy transfer electron irradiations. This supports the possibility of amorphization beginning within cascade structures which would also explain why the Xe ions produce amorphization to a higher temperature than the Si ions. Alternatively, it is possible that the heavier Xe ions simply create a higher concentration of "stable" interstitials than the Si ions or electrons on a dpa-normalized basis, thus driving the temperature threshold higher.

A potential problem in comparing the amorphization threshold data sets presented in Fig. 5 is whether the in-situ approach of Inui and Weber[5, 17-19, 21-24] can be directly compared with the ex-situ measurements of the present study. In other words, are there technique-dependent effects occurring for one or both types of amorphization measurements. One example of an experimental artifact is demonstrated by observing a series of high resolution TEM images from the Si implanted, single crystal β-SiC. In general, there is a fairly rapid transition from crystalline material into the amorphous band (see Figs. 1-3). As expected from the damage gradient of the ion profile,[7] this transition region is wider at the near-surface side of the

amorphization band compared to the end of the band (larger gradient in damage.) Figure 6 shows a HRTEM bright field image of the crystalline to amorphous transition region at the end of the amorphous band for a 6H-SiC sample irradiated with Si ions normal to the c-axis at 60°C. Fairly large areas of amorphous regions are seen, mixed into the crystal structure, which is consistent with the statistical nature of a point defect accumulation driven amorphization. Of particular interest in this micrograph is the shape and orientation of the amorphous areas, which appear to form as island structures with the major radii aligned parallel to the surface of the specimen. This phenomenon was observed in all amorphized specimens studied at both the beginning and end of the amorphized region from 60°C to 125°C for the Si ion irradiated specimens as well as the room temperature 6H SiC and CVD SiC specimens irradiated with 3.6 MeV Fe. These anisotropic amorphous structures occur when the beam is injected normal to the

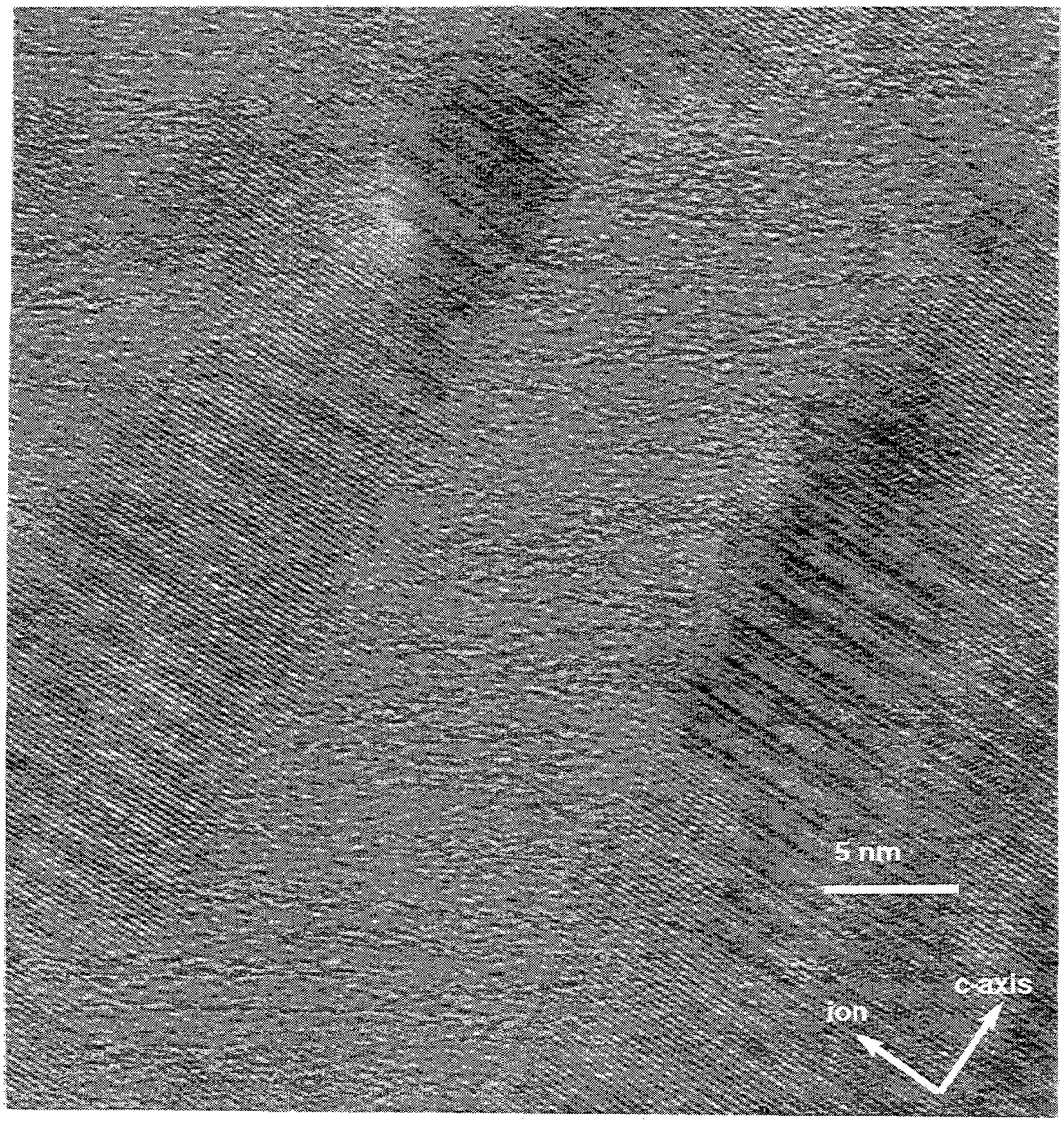

Figure 6. HRTEM image showing large island amorphous structures in 60°C Si Irradiated SiC.

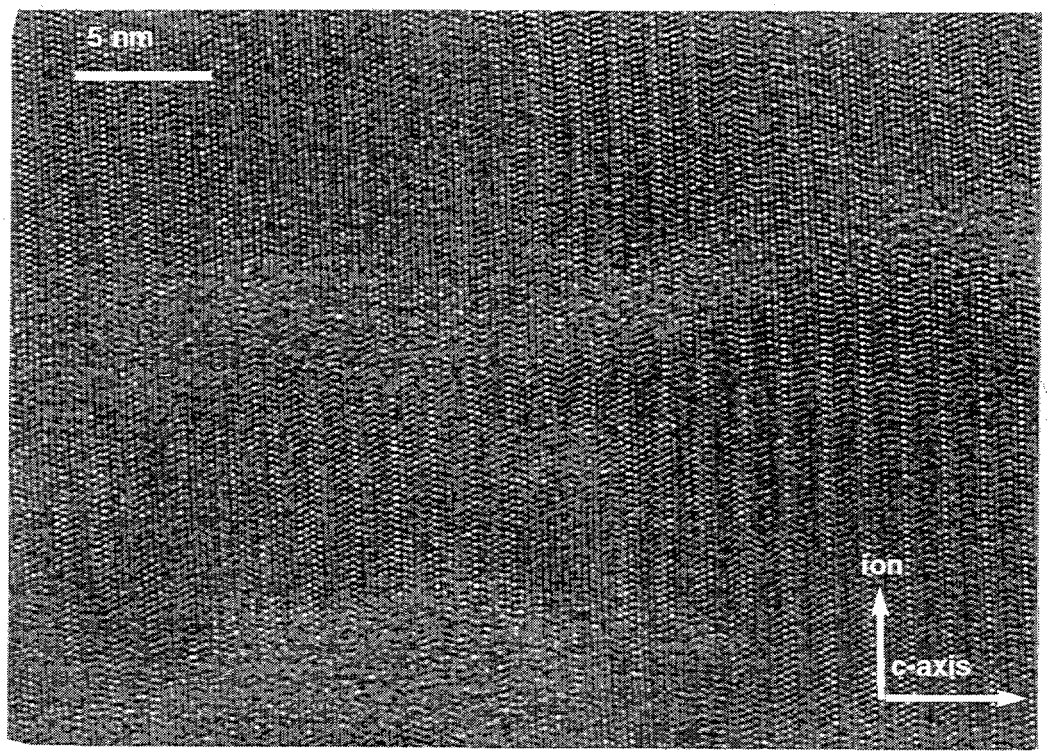

Figure 7. HRTEM image of Si irradiated SiC showing nucleation of island amorphous structures.

c-axis (as in Fig. 6) or parallel to the c-axis and therefore is not a crystallographic orientation phenomenon. Figure 7 shows another bright field micrograph illustrating that the formation of these islands occurs on a very fine scale, eventually growing and linking with other islands.

In order to quantify this effect, a series of micrographs were taken at the beginning and end of the amorphized band for specimens irradiated with Si ions at 60 and 125 °C. Amorphous islands were identified using the complete loss of lattice fringes as the criteria, and the major and minor radius of each amorphous pocket was measured. Typically, about 50 islands were measured from at least three separate areas on each specimen. Results of this analysis showed that the aspect ratio (major/minor radius) was fairly constant independent of the temperature and location of the amorphous band. Specifically, the aspect ratio was found to be 3.3 and 3.1 for the beginning and end of the amorphous band for the 60°C Si ion irradiated material and 3.2 and 3.6 at the beginning and end of the amorphous band for the 125°C irradiated material, respectively.

The anisotropic geometry of these islands relative to the surface of the specimens raises the question of whether there is a strain effect on the evolution of the amorphous structure. There is obviously a large

lattice strain induced in the crystal to amorphous transition both from point defect accumulation and the amorphous pockets. Also, the presence of the free surface should affect the nature of the strain field. The obvious question from these results is whether the formation and connection of the amorphous pockets are being affected in a substantial way by this phenomenon. For example, it has been shown that the amorphization threshold is reduced in Cl ion implanted SiC.[7] Amorphous regions could nucleate first in such an implanted region causing a large stress field due to the associated volumetric expansion and contribute to drive the surrounding material amorphous. The presence of the free surface and/or the expansion of the material in a direction towards the surface could affect this strain field and the subsequent amorphization.

Chemical rate theory models have been developed by several authors which can be fitted to experimental amorphization data. However, these models contain numerous parameters which are not well known and generally do not have analytical solutions. More simplistic analytical models have been developed.[21] However, these models have yielded unrealistically low activation energies for amorphization (below 0.1 eV), considering that the recovery processes occur near or above room temperature.

The data of Fig. 5 have been analyzed with an analytical approximation based on the rate theory model of Motta and Olander[27] developed for electron induced amorphization of intermetallic precipitates in zircaloy. This model is analogous to well known rate theory results for point defect concentrations in irradiated metals and is based on the free energy increase associated with point defect accumulation, and is therefore not appropriate if in-cascade amorphization occurs. The assumption of point defect driven amorphization is supported by the molecular dynamics simulations[28] and high-resolution TEM observations[18,23] which indicate that amorphization in SiC proceeds gradually by point defect accumulation processes, as opposed to heterogeneous in-cascade amorphization. There is no evidence for the spontaneous creation of amorphous zones in displacement cascades in irradiated SiC,[23,28] though this should still be considered an open question.

Specifically, the model[27] as applied to amorphization in SiC uses the temperature dependent term for the critical damage for amorphization (see Fig. 5) which is given by (1) :

(1) $$d(T) = \frac{A}{\sqrt{\phi}} e^{-\frac{E_m^i}{2kT}}$$ (2) $$dpa_{crit} = d(T) + a$$

The critical dose for amorphization as given in Fig. 5 can be described by the sum of this temperature dependent term and the temperature independent term obtained at low temperatures as shown in equation (2).

The interstitial migration energy, E_i^m, is found from the slope of the experimental amorphization data, as plotted in Figure 8. The interstitial migration energy for the silicon ion irradiation was calculated to be 0.56 eV and is in agreement with the data sets of Inui[17] and Weber[5] on α-SiC. The data by Inui[19] on highly faulted β-SiC is significantly higher than this value, however. All the data sets of this figure are at approximately the same displacement rate (~2×10^{-3} dpa/s) rendering the pre-exponential term in equation (1) constant.

The physical explanation for the temperature-dependent behavior of the Motta and Olander amorphization model is associated with interstitial migration that assists restoration of chemical order in the lattice. We assume that amorphization occurs via chemical disordering on both the Si and C sublattices in SiC. Experimental measurement of the threshold energy to induce amorphization in SiC during cryogenic temperature electron irradiation is needed to determine the validity of this assumption. The migration energy of 0.56 eV is tentatively attributed to the slower interstitial specie (presumably Si). As shown in Fig. 5, both α-SiC electron [17] and β-SiC Xe ion[21] irradiation studies observed a step in the amorphization dose at low temperature (~70K) which may be due to migration of the faster interstitial specie, or perhaps recovery of close pair Frenkel defects.

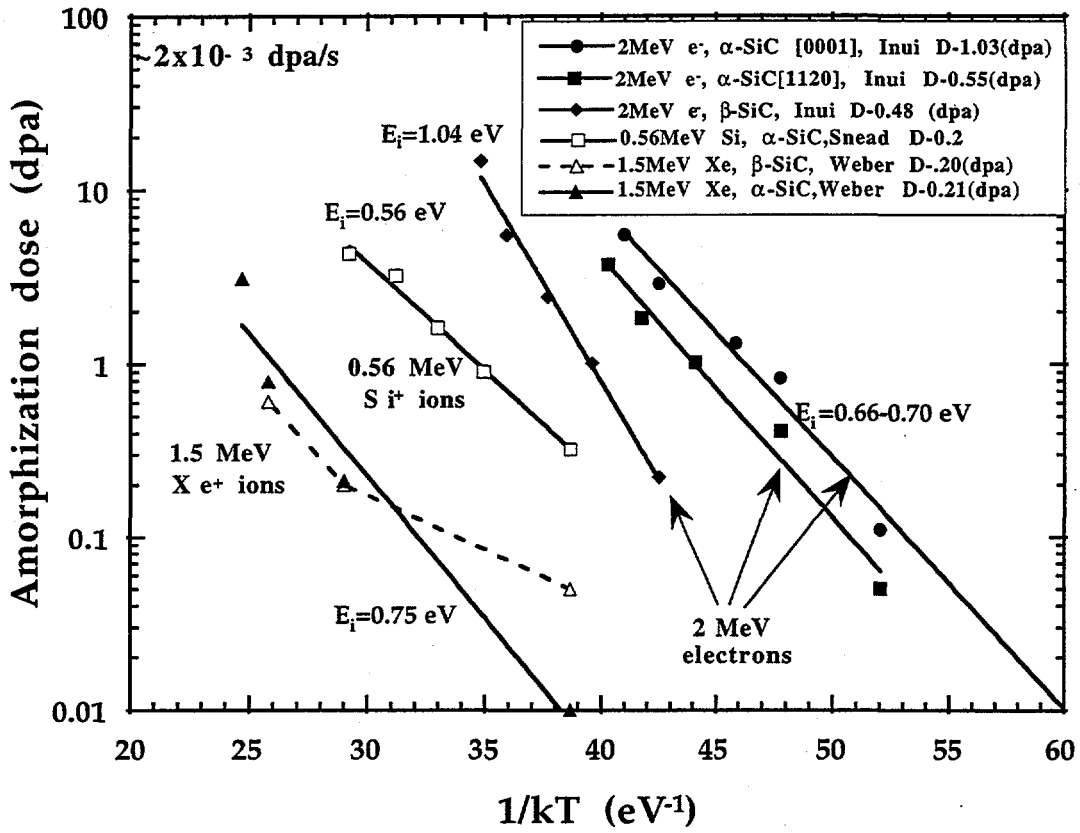

Figure 8. Interstitial migration energy determination for amorphization of SiC.

Referring again to Fig. 5, it is seen that for all the data sets used, amorphization has occurred in the temperature independent region at a displacement dose (d_0) of less than 1 dpa. The temperature above which amorphization is not observed is ~ 300 K for electron irradiated material, ~ 420 K for Si ions, and ~500 K for Xe ions. The SiC material which was neutron irradiated in this study to a dose of approximately 15dpa yielded density changes of 10.1% for the Cercom β-SiC and 11.1% for the Carborundum α-SiC. While both values are significantly higher than expected for simple "point defect "swelling from the previous neutron irradiation data for swelling in silicon carbide, it is less than the 15% swelling level reported for complete amorphization. However, given this large swelling which has occurred it is likely that the samples include pockets of amorphization. The neutron irradiation temperature for these samples was ~ 350 K.

Given that the fast neutron irradiation of SiC should produce a damage spectrum closer to the ion irradiated material than the simple point defect only spectrum of the electron irradiation it might be expected that complete amorphization should have occurred during neutron irradiation at the ~350 K neutron irradiation. The apparent partial retention of the crystal structure for the neutron irradiated SiC specimens can be explained with the above rate theory model by noting that the damage rate for the neutron irradiation was $\sim 1 \times 10^{-6}$ dpa/s which is three orders of magnitude lower than the Si ion irradiation. Using the 0.56 eV migration energy calculated from the Si ion data and using the respective damage rates, equation (2) can be used to plot the calculated threshold dose profile for amorphization at two different damage rates, as shown in Figure 9. This plot includes the silicon ion irradiation data along with its calculated profile and the data point for which amorphization was not observed (20 dpa and 420 K.)

The threshold dose profile for the fission neutron damage rate of $\sim 1 \times 10^{-6}$ dpa/s is calculated with the derived 0.56 eV interstitial migration energy, and migration energies ± 0.05 eV from this value, to

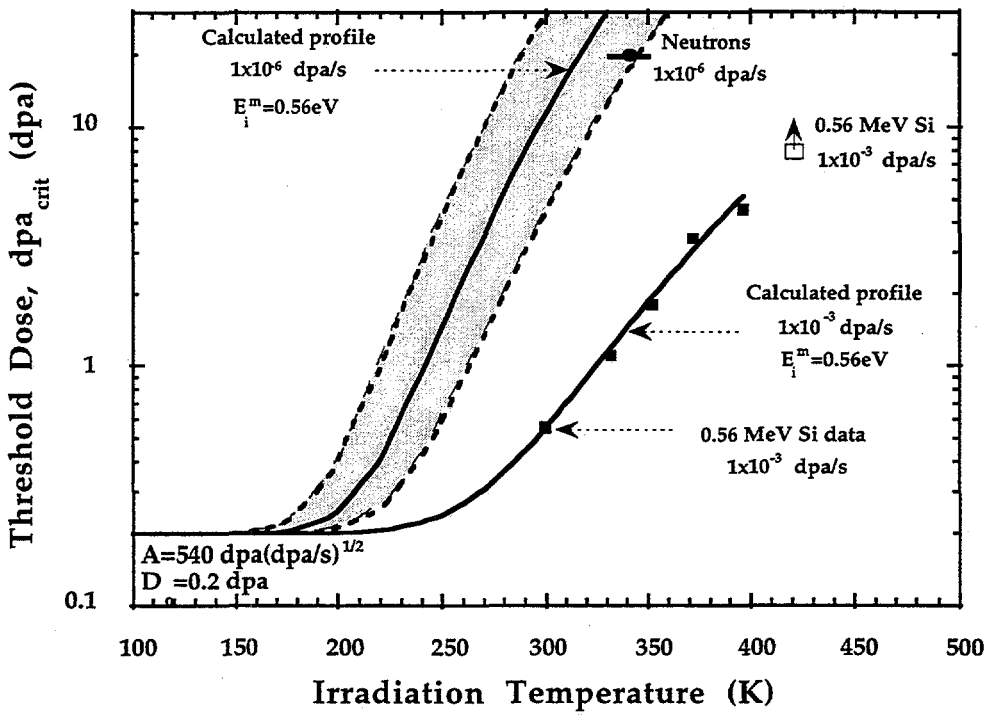

Figure 9. Predicted flux dependence of the critical dose for amorphization of SiC.

demonstrate sensitivity to this variable. Given the nature of the calculation of the interstitial migration energy, such an uncertainty is conceivable. However, assuming a migration energy of 0.56 eV, it is seen that for the ~340 K fission neutron irradiation temperature and ~1×10^{-6} dpa/s damage rate, it would require between 30 and 50 dpa to completely amorphize the SiC. For comparison it would require <2 dpa at the Si ion dose rate of ~1×10^{-3} dpa/s. While this model appears to adequately describe the temperature dependence of amorphization at moderate temperatures, it is not entirely satisfying in that it does not exhibit the "critical temperature" asymptotic behavior which is suggested by the data. As the temperature is increased and the exponential term approaches unity, the critical dose for amorphization approaches a constant value of $d_o + A/\sqrt{\phi}$. Modification of the Motta and Olander model is necessary to correct this nonphysical predicted amorphization behavior at very high temperatures. The inadequacy of the present model at very high temperatures is seen by noting the unamorphized Si ion irradiated data point irradiated to 20 dpa at 420 K. The extrapolated Si ion model would fall to the right of this data point (implying the material should have amorphized) and continue to flatten towards a constant value just mentioned.

CONCLUSIONS

(1) There is apparently no PKA spectrum effect in this study on the low temperature (temperature independent) amorphization of SiC when irradiating with He, Si, Cl and Fe atoms. However, published low temperature 2 MeV electron and 1.5 MeV Xe irradiations suggest that the low-temperature amorphization dose decreases by about a factor of 5 as the irradiation source is changed from electrons to ions.

(2) The critical temperature for amorphization of SiC with 0.56 MeV Si of ~420 K shows an exponential dependence with an apparent critical temperature threshold above which amorphization dose not take place at a damage rate of ~2×10^{-3} dpa/s. This compares with the published amorphization temperature thresholds for 2 MeV electron and 1 MeV Xe ions of ~300 K and 500 K respectively at a similar damage rate.

(3) A possible experimental artifact was observed which may affect the calculation of critical dose for amorphization in ion implanted specimens. Specifically, amorphized islands were seen to form with their major radii parallel to the free surface of the specimen. These islands have an aspect ratio of ~3 which are independent of temperature and crystal orientation. Formation of these islands raises the question of whether surface or strain effects alter the apparent amorphization thresholds in the bulk irradiation method presented here and the thin foil in-situ method which has been used by other workers. A determination of the adequacy of this implantation technique for determining amorphization threshold should be conducted and compared with the in-situ "thin foil" technique.

(4) A swelling of approximately 10% was measured for sintered α-SiC and hot pressed β-SiC neutron irradiated to 15 dpa at ~350 K. This amount of swelling is about a factor of three higher than previously reported for neutron irradiation at similar temperatures. However, this amount of swelling is less than the ~15 to 20% level of swelling observed in completely amorphized ion-irradiated material. It is likely that partial amorphization characterized by amorphous islands is present in the material. XRDA and TEM analysis will be performed to determine the extent of amorphization in the room temperature irradiated samples.

(5) A model for the critical dose for amorphization based on the free energy increase associated with point defect accumulation in metals is applied to the temperature dependent critical dose for amorphization. An interstitial migration energy of 0.56 eV was calculated based on the Si ion (10^{-3} dpa/s) irradiations and adequately describes the transition from the temperature independent to temperature dependent regimes of amorphization. However, the model does not adequately describe the higher temperature asymptotic amorphization dose behavior. Extrapolation of this model to the dose rate for the neutron irradiated samples (10^{-6} dpa/s) successfully predicts the observed lack of complete amorphization in these specimens. Assuming this dose rate and the interstitial migration energy of 0.56 eV, it would require between 30 and 50 dpa to have reached total amorphization for the material neutron irradiated at ~340 K. Presently, a neutron irradiation capsule identical to the one used in this study is in the HFIR reactor and will achieve 60 dpa. Examination of the SiC specimens from this capsule should provide interesting information on the validity of the fitted rate-controlling interstitial migration energy, and whether SiC can be amorphized during high-dose neutron irradiation at ~340 K.

REFERENCES

1. W. Primak, L.H. Fuchs, and P.P. Day, Phys. Rev., **103**(5), 1184-1192 (1956).
2. R. Blackstone, J. Nucl. Mater., **39**, 319-322 (1971).
3. C.W. White et al., Nucl. Instrum. Meth. B, **80/81**, 41-146 (1989).
4. C.J. McHargue and J.M. Williams, Nucl. Instrum. Meth., **B80/81**, 889-894 (1993).
5. W.J. Weber et al., accepted for publication, J. Nucl. Mater. (1996).
6. L.L. Snead, S.J. Zinkle, and D. Steiner, J. Nucl. Mater, **191-194**, 560-565 (1992).
7. L.L. Snead and S.J. Zinkle, *MRS Symposium #373 on Microstructure of Irradiated Materials* (1995) Materials Research Society, Pittsburgh, PA., I. M. Robertson et al., eds.
8. R.R. Hart, H.L. Dunlap, and O.J. March, Rad. Effects, **9**, 261-266 (1971).
9. J.M. Williams, C.J. McHargue, and B.R. Appleton, Nucl. Instrum. Meth., **209/210**, 317-323 (1983).
10. J. Spitznagel et al., Nucl. Instrum. Meth., **B16**, 237-243 (1986).
11. J.A. Edmond et al., J. Mater. Res., **3**, 321-328 (1988).
12. N.G. Chechenin et al., Nucl. Instrum. Meth., **B65**, 341-344 (1992).
13. L.L. Horton et al., Nucl. Instrum. Meth, **B65**, 345-351 (1992).
14. R.G. Vardiman, *Mat. Res. Soc. Symp.*, 1989.

15. C. Kinoshita et al., in *Proceedings of the 11th International Conference on Electron Microscopy* (1986), Japanese Society of Electron Microscopy.
16. A. Matsunaga et al., J. Nucl. Mater., **179-181**, 457-460 (1991).
17. H. Inui, H. Mori, and H. Fujita, Phil. Mag., **B 61**, 107 (1990).
18. H. Inui, H. Mori, and T. Sakata, Phil. Mag., **B 66**(6), 737-748 (1992).
19. H. Inui et al., Phil. Mag., **B 65**, 1 (1992).
20. S.D. Harrison and J.C. Corelli, J. Nucl. Mater., **99**, 203-212 (1981).
21. W.J. Weber and L.M. Wang, Nucl. Instrum. Meth., **B 106**, 298-302 (1995).
22. W.J. Weber and N. Yu, Accepted Nucl. Instrum. Methods B, (1996).
23. W.J. Weber, L.M. Wang, and N. Yu, Nucl. Instrum. Meth., **B 116**, 322-326 (1996).
24. W.J. Weber. *13th Internation Cong. on Defects in Insulating Materials* (1996).
25. S.J. Zinkle and L.L. Snead, Nucl. Instrum. Meth. B, **116**, 92-101 (1996).
26. J.F. Ziegler, J.P. Biersak, and U.L. Littmark, Pergamon, New York (1985).
27. A.T. Motta and D.R. Olander, Acta Metta. Mater., **38**, 2175-2185 (1990).
28. T.D. de la Rubia, M.-J. Caturla, and M. Tobin. in *Microstructure of Irradiated Materials* (1995) Boston, MA., I. M. Robertson et al., eds.

STORED ENERGY IN IRRADIATED SILICON CARBIDE — L. L. Snead and T. D. Burchell (Oak Ridge National Laboratory)

OBJECTIVE

A short discussion of the possibility for the release of stored energy (Wigner energy) from irradiated silicon carbide is presented. The objective of this work was to provide a basis to decide if further study into this area is warranted.

SUMMARY

This report presents a short review of the phenomenon of Wigner stored energy release from irradiated graphite and discusses it in relation to neutron irradiation silicon carbide. A single published work in the area of stored energy release in SiC is reviewed and the results are discussed. It appears from this previous work that because the combination of the comparatively high specific heat of SiC and distribution in activation energies for recombining defects, the stored energy release of SiC should only be a problem at temperatures lower than those considered for fusion devices. The conclusion of this preliminary review is that the stored energy release in SiC will not be sufficient to cause catastrophic heating in fusion reactor components, though further study would be desirable.

PROGRESS AND STATUS

The production of interstitial-vacancy pairs in graphite by neutron irradiation was postulated by E. P. Wigner in 1942. Later, it was pointed out by L. Szilard that when these defects recombine the defect formation energy of approximately 8 eV will be recovered (released). These two phenomenon became known as the Wigner Effect and the Szilard Complication, respectively. The potential danger of stored energy release during reactor operation was discovered early in the operation of the air cooled graphite production reactors at Windscale in the United Kingdom. To prevent the build-up of excessive amounts of stored energy the reactors were routinely thermally annealed to reduce the extent of the 200°C release peak. The Windscale reactors were successfully annealed on numerous occasions. However, the 1957 Windscale reactor 1 graphite fire was initiated by an anomalous stored energy release during a scheduled anneal.

Because of the wide scale use of graphite in gas cooled reactors a significant study was undertaken in the UK and the US into the stored energy release of irradiated graphite. It is now well understood that for low irradiation temperatures (<150°C,) the mobility for interstitial carbon is small and huge interstitial concentrations build-up between the graphite basal planes. For lower doses these defects remain as mono-interstitials though as the damage level is increased more complex groups are formed.[1] Because it is more difficult to recombine complex defects a temperature-dependent saturation occurs in the total stored energy available for release. If the temperature of the material is increased above the irradiation temperature the carbon interstitials increase in mobility and can recombine with interstitials releasing their formation energy. In recombining, approximately 8 eV is liberated leading to total stored heats of as much as 2,600 J/g (for graphite irradiated at 30°C.)[2] As the irradiation temperature is increased the equilibrium concentration of carbon interstitials falls off rapidly thereby reducing the total energy stored in the graphite. The decrease in the amount of stored energy accumulated is shown in Fig. 1.[3] While this figure does not show the saturation levels, it appears that there is less than 20% of the stored energy in material irradiated at 180°C as compared to materials irradiated at 25°C.

While a significant amount of energy can be stored in the crystal of irradiated graphite (and silicon carbide), the more critical issue is the kinetics of energy release. For the case of graphite irradiated at low temperature, and to low dose, the stored energy is released primarily in two peaks located at between 100 and 200°C. In order for graphite, or any material, to have an uncontrolled temperature increase due to the release of stored energy, the amount on energy release must exceed the specific heat at that temperature. As illustrated in Fig. 2,[3] the integral of the area between the energy release curve for an irradiated sample and the unirradiated specific heat can be used to calculate the stored-energy driven temperature rise. As

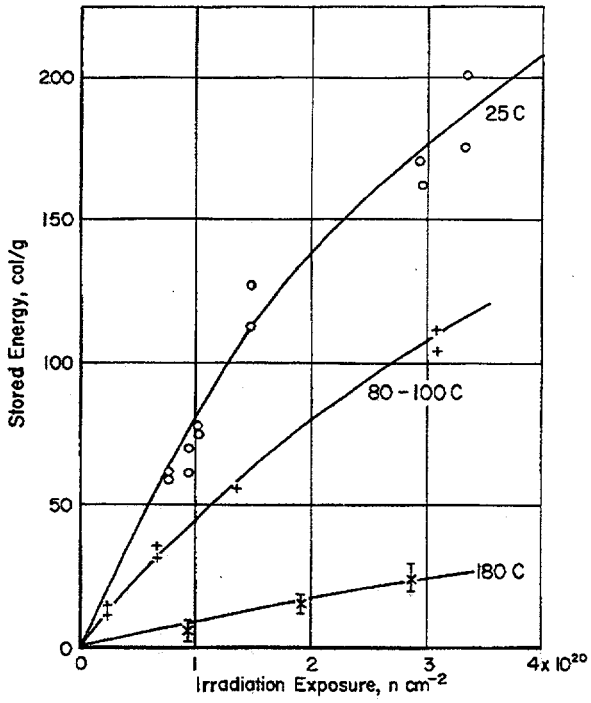

Figure 1. Stored energy in irradiated graphite.[3]

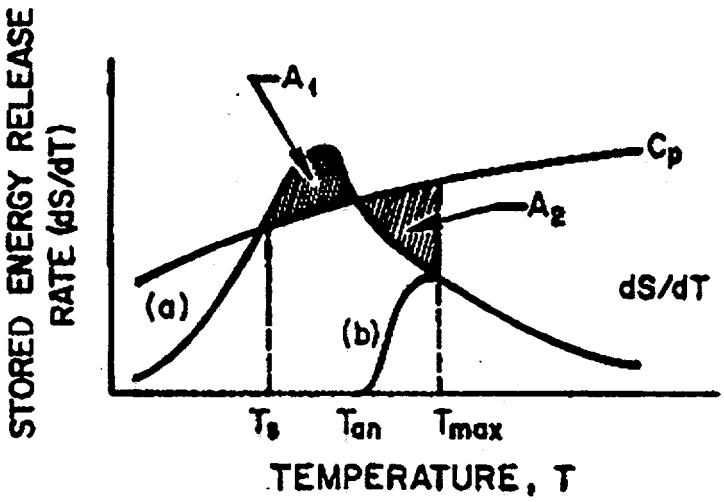

Figure 2. Schematic of stored-energy driven temperature rise.[3]

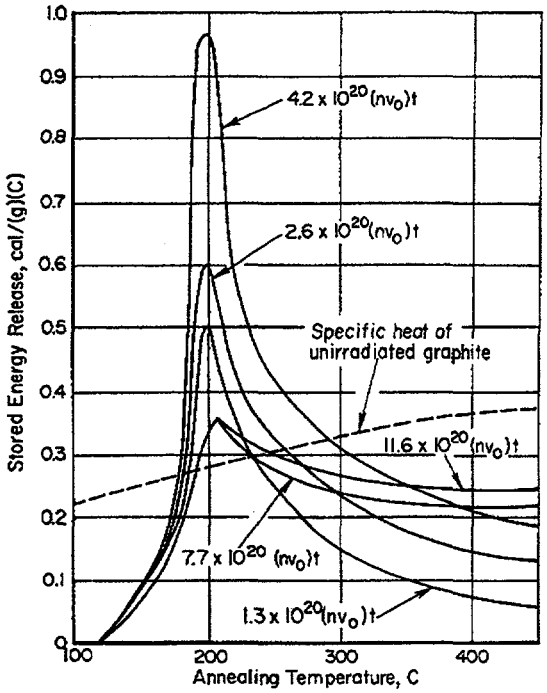

Figure 3. Stored energy release in graphite irradiated at 30°C.[4]

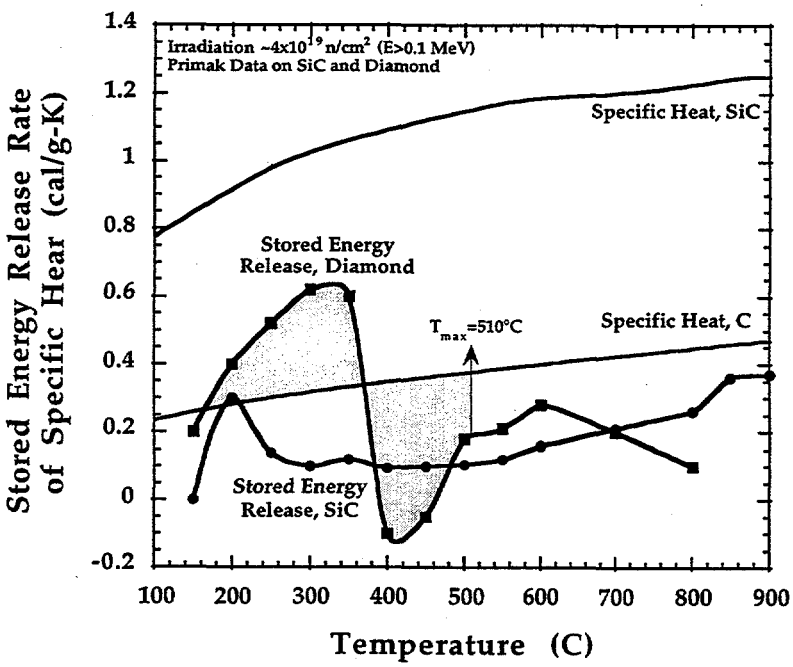

Figure 4. Energy release curves for diamond and silicon carbide.[5]

irradiation dose for graphite is increased and the defect structures become more complex, the release peaks broaden so that significant stored energy release occurs as high as 400-500°C. This is demonstrated in Fig. 3 for graphite irradiated in a fluence range of 1.3 and 11.6×10^{20} $(nv_o)t$.[4] It is seen in this figure that the potential sample temperature rise, as indicated by the integrated area above the specific heat, is greatest at the intermediate fluence of 4.2×10^{20} $(nv_o)t$. As the fluence increases from this point the energy release is substantially decreased due to the broadening of the release peaks.

The only published research on the release of stored energy in irradiated silicon carbide was carried out by Primak.[5] In this work, the energy release was measured for silicon carbide and diamond (which is very similar to graphite) using a differential thermal analysis apparatus at a heating rate of 20-40 degrees Celsius per minute. Single crystal SiC was irradiated in the cooled test hole facility of the Hanford reactor to a total dose of 255 MWd/at, or a "damaging" flux quoted as 4.3×10^{19} n/cm^2. The term "damaging" flux was described elsewhere[6] as 0.01 to ~10 MeV. Using a correction, and the 20% uncertainty in the fluence stated by Primak[5], the assumed E>0.1 MeV fluence for this study was $3.6 \pm 0.7 \times 10^{19}$ n/cm^2.

Plots the energy release data of Primak[5] and the specific heats of both carbon and silicon carbide are in Fig. 4. Two observations can be made from this data. First, the majority of the stored energy release of diamond occurs in the lower temperature regime as expected from previous work with graphite. In this case a stored energy driven temperature rise of approximately 125°C would occur for the diamond sample. Second, the data shows that the stored energy release for SiC at low temperatures is less than for diamond. It was also shown by Primak[5] that irradiated SiC has a much broader (and flatter) range in activation energies, which peaked above 3 eV as compared to the 1.5 eV peak of diamond.

The stored energy release characteristics of SiC will be a function of the total stored energy (dose and temperature dependent) and the release kinetics. For the stored energy rate (dS/dT) to exceed the specific heat of SiC requires both the accumulation of sufficient damage, and for its release over a relatively narrow temperature window. It is probably that Primak's data (~0.04 dpa) was for material below its saturation neutron damage dose. By applying the well established relationship between thermal conductivity and the total stored energy in graphites[7], and applying our experience with radiation damage in SiC, we are able to extrapolate Primak's data to a postulated saturation damage dose. If this is assumed to be the case for SiC, the saturation in stored energy should occur at, or less than, 0.1 dpa for temperatures under 200°C. The saturation of thermal conductivity by 0.1 dpa is demonstrated in Fig. 5 for irradiation temperatures in the range of 80-200°C.[8] To first order, the data of Primak can be scaled by a factor of two to estimate the amount of stored energy released in SiC at saturation. This is shown in Fig. 6. From the figure it is seen that a factor of two would yield an energy release well below the specific heat of SiC. A more pessimistic scenario is also shown in Fig. 6, where Primak's release curve is arbitrarily increased by a factor of five. Such a release would cause a temperature increase from about 240 to 300°C (T_{max}). It is important to note that this simple scaling does not account for any broadening in the release peaks which were discussed previously. However, this represents a conservative assumption as the effect would be to flatten the energy release curve.

CONCLUDING REMARKS

It appears that the release of Wigner energy is not a concern for using SiC as a structural material in fusion reactors for the following reasons.

(1) Existing data, while very limited, indicates that the energy release from SiC is less than that for graphite. Moreover, the significantly higher specific heat of silicon carbide compared to graphite suggests that the potential problem for SiC is considerably less than that of graphite. If Wigner energy release were a problem, an engineering solution such as annealing cycles (similar to those used to mitigate Wigner energy in gas cooled reactors) may be employed.

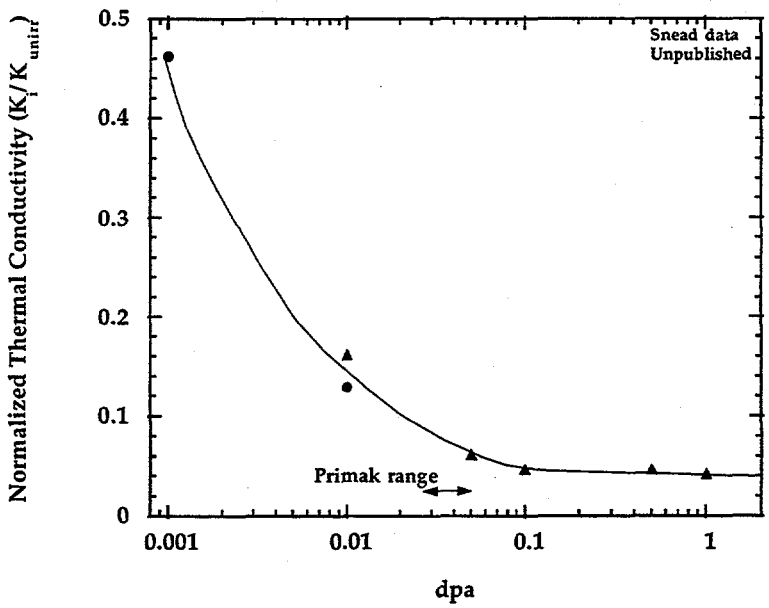

Figure 5. Thermal conductivity degradation for Morton CVD SiC under irradiation.[8]

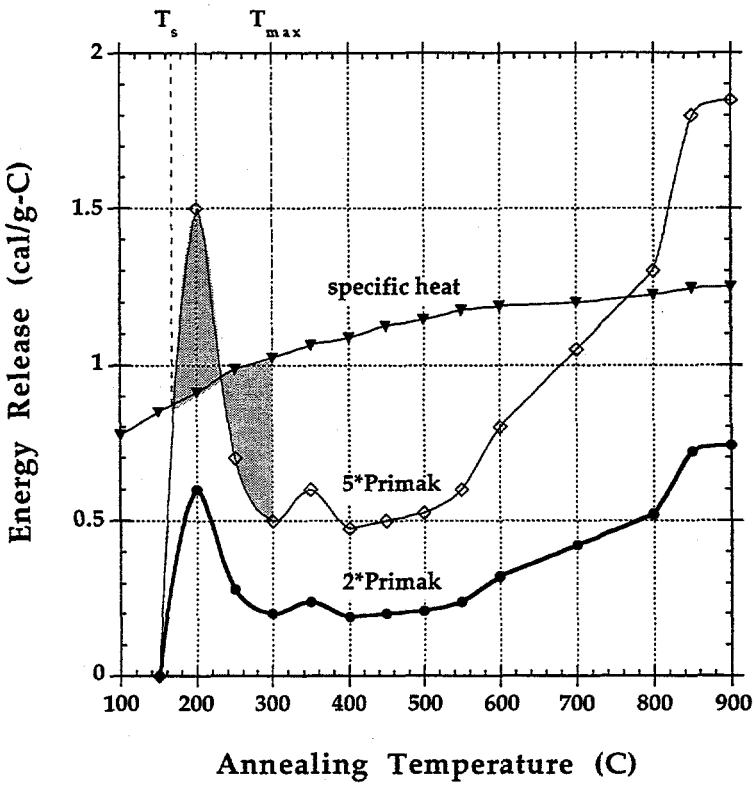

Figure 6. Assumed levels of stored energy release at saturation for SiC.

(2) The energy release peaks for SiC appear to be fairly broad and flat allowing the energy release due to recombination of defects to occur over a wide temperature range. This is in stark contrast to graphite, which releases the majority of its stored energy in the temperature range of 100 to 250°C. This former release characteristics suppresses spontaneous temperature rise in the case of SiC. Such behavior is probable for all ceramic materials because of the difference between the weak Van der Walls bonding of interstitials between basal planes of graphite and the covalent bonds in SiC or ionic bonding of other ceramics.

(3) It is unlikely that components of a fusion system which will see significant neutron flux will be at temperature less than 300°C. The data presented in this paper were in for materials irradiated somewhere between 80 and 150°C, and should therefore have significantly greater amounts of stored energy owing to the reduced interstitial mobility at these temperatures. For this reason, the total stored energy will be less at the elevated operating temperatures of fusion systems. However, if SiC is to be used for heating or diagnostic systems where it is cooled below 150°C, stored energy may be a consideration.

It is possible that the assumptions made for the saturation of stored energy of SiC based on Primak's data are in error, either because of to problems in using the analog between thermal conductivity saturation and stored energy saturation, or in determining the fluence of Primak's data. While it is unlikely that these errors will be large enough to alter our conclusion that stored energy in SiC is not a major issue in fusion systems, a series of simple experiments would confirm our conclusions.

REFERENCES

1. G. R. Hennig and J. E. Howe, *Interpretation of Radiation Damage to Graphite*, in *First Geneva Conference on the Peaceful Uses of Atomic Energy* 7 (1955) 666-675.
2. R. E. Nightingale, J. M. Davidson, and W. A. Sunder, *Damage Effects to Graphite Irradiated up to 1000°C in Second United Nations Conference on the Peaceful Uses of Atomic Energy*, 1958, Geneva, Switzerland.
3. J.W.H. Simmons, International Series of Monographs in Nuclear Energy, Vol. 102, Pergamon Press, 1965 .
4. W. K. Woods, L. P. Bopp, and J. F. Fletcher, *Irradiation Damage to Artificial Graphite*, in *First Geneva Conference on the Peaceful Uses of Atomic Energy* 7 (1955) 455-471.
5. W. Primak, L. H. Fuchs, and P. P. Day, Phys. Rev. **103**(5), 1184-1192 (1956).
6. W. Primak, Nucl. Sci. and Eng. **2**, 320-333 (1957).
7. T. D. Burchell, *Radiation Damage in Carbon Materials*, in *Physical Processes of the Interaction of Fusion Plasmas with Solids*, W.O. Hofer and J. Roth, eds., 1996, Academic Press, pp. 341-384.
8. L. L. Snead, unpublished data.

EFFECTS OF NEUTRON IRRADIATION ON THE STRENGTH OF CONTINUOUS FIBER REINFORCED SiC/SiC COMPOSITES -- G. E. Youngblood, C. H. Henager, Jr., and R. H. Jones (Pacific Northwest National Laboratory)*

OBJECTIVE

The objective of this work is to assess the development of continuous, fiber-reinforced SiC_f/SiC composites for structural applications in advanced fusion energy systems.

SUMMARY

Flexural strength data as a function of irradiation temperature and dose for a SiC_f/SiC composite made with Nicalon-CG fiber suggest three major degradation mechanisms. Based on an analysis of tensile strength and microstructural data for irradiated Nicalon-CG and Hi-Nicalon fibers, it is anticipated that these degradation mechanisms will be alleviated in Hi-Nicalon reinforced composites.

PROGRESS AND STATUS

Introduction

This paper updates previously reported results [1, 2] on the mechanical properties of irradiated, continuous fiber-reinforced silicon carbide composite (SiC_f/SiC). In this composite, hereafter referred to as reference SiC_f/SiC, the Nicalon^{TM}-CG fibers were coated with a 150 nm thick pyrolytic carbon interphase prior to a chemical vapor infiltration (CVI) deposition of the matrix. Bend bar samples made from reference SiC_f/SiC were irradiated in four different experiments in either the FFTF or the EBR-II fast reactors at temperature and dose ranges covering 430°C to 1200°C and 4 to 80 dpa-SiC, respectively. Only after the accumulation of a considerable amount of mechanical property data obtained by using a consistent set of test procedures on this single type of irradiated material is it now possible to analyze in detail this material's irradiation performance and its degradation mechanisms.

A substantial degradation in mechanical and thermal properties at radiation damage levels as low as 1 dpa-SiC was reported for a type of SiC_f/SiC similar to reference SiC_f/SiC [3, 4]. However, irradiation experiments to higher doses have shown that the degradation tends to saturate at a relatively low dose and further degradation remains relatively small [2]. The degradation of reference SiC_f/SiC was shown to be primarily connected to the poor irradiation performance of the Nicalon-CG type fibers, although additional microcracking in the matrix also was observed. In separate studies of irradiated fiber bundles, it was shown that Nicalon-CG fibers shrink and densify [5] while their strengths decrease during irradiation [6]. As a result, the ultimate bend strength of irradiated reference SiC_f/SiC probably is degraded by both fiber strength loss and decoupling from the matrix. A modest reduction in the matrix cracking stress (defined here as the maximum stress where stress remains proportional to strain) and an overall reduction of the modulus, both of which depend upon the irradiation temperature and dose, also were observed. Notably, catastrophic brittle failure never was observed in the tested reference SiC_f/SiC bend bars. In spite of the fiber/matrix debonding and loss of fiber strength, the irradiated bend bars still exhibited a strength greater than the matrix cracking stress and a large strain-to-failure. Nevertheless, these high dose studies concur with several low dose studies that to achieve acceptable radiation performance in a SiC_f/SiC composite, a fiber more radiation tolerant than Nicalon-CG must be used.

---

* Pacific Northwest National Laboratory (PNNL) is operated for the U.S. Department of Energy by Battelle Memorial Institute under Contract DE-AC06-76RLO-1830.

In a study comparing the irradiation performance of several types of SiC-based fibers, the Hi-Nicalon^{TM} fiber was shown to exhibit a minimum density increase (+0.7 ± 0.4%) and a 40% increase in tensile strength after irradiation at 1000°C to a dose of 43 dpa-SiC [6]. Osborne, et al. [7, 8] noted similar trends for low temperature (100°C), low dose (<1 dpa-SiC) irradiations. Apparently, the Hi-Nicalon fiber behaves much differently than the Nicalon-CG fiber during low and high temperature irradiations. In either case, it exhibits a marked improvement in irradiation stability over that of Nicalon-CG fiber.

It is the goal of this report to combine and analyze all of the irradiation behavior data obtained at PNNL for the reference SiC_f/SiC. From this analysis, reasons why a composite reinforced with Hi-Nicalon fiber should exhibit enhanced mechanical properties as well as improved irradiation performance over that of the reference composite are given.

Materials

Several plates of reference SiC_f/SiC composite were fabricated by Dupont using the isothermal CVI process and Nicalon-CG fabric with a 2D 0-90° plain weave pattern. The plates nominally contained 40 volume percent fiber which were laid up as eight fabric plys through the plate thickness. During the CVI process, the deposition layers grow outward from the individual fibers until they intersect and eventually seal off the gas flow, thus ending the process. A radial, columnar polycrystalline microstructure, essentially 100% ß-SiC, is formed; however the grains are expected to contain a high concentration of stacking faults [9]. Because of the fabric weave and the matrix growth patterns, a bimodal distribution of residual macroporosity develops. It consists of linear pores which lie within and parallel to the fiber yarns with dimensions similar to that of a single fiber and laminar-shaped pores which lie between the fabric plies with dimensions similar to the fabric unit cell (≈ 1 mm^2). The latter pores are responsible for the somewhat weaker shear strength for a 2D weave composite. The smaller linear pores within the fiber bundles are primarily responsible for the permeable nature of these composites. The total macroporosity typically represents 10-15% of the structure volume. In Reference 2 (Fig. 4), a complete set of optical micrographs which depict the micro- and macro-structures for both unirradiated and irradiated reference SiC_f/SiC are presented.

For comparison, a similar composite plate with Hi-Nicalon replacing the Nicalon-CG fabric also was obtained from Dupont. Another difference with this advanced material was a thicker graphite interface layer (≈ 1000 nm) was applied to the fibers. The plates were cut into a large number of rectangular flexure bars measuring 3.2 x 6.4 x 38 mm^3. All bars were cut normal to the weave pattern so that about 20% of the fiber yarns were parallel to the lengths of the flexure bars.

Both the Nicalon-CG and Hi-Nicalon fibers, produced as textile-grade yarns by Nippon Carbon Co. of Japan, are polymer-derived. Nicalon-CG is a Si-C-O fiber (12 ± 2 wt% O, C:Si = 1.3) whose microstructure consists of small, nanocrystalline (≈ 2 nm) ß-SiC grains within a somewhat amorphous Si-C-O matrix. Due to a different curing step in its manufacture, Hi-Nicalon has a significantly lower oxygen content (<0.5 wt% O) than Nicalon-CG and a somewhat higher carbon to silicon ratio (C:Si = 1.4). The Hi-Nicalon fiber microstructure consists of nanocrystalline (5-10 nm) ß-SiC grains separated by thin (1-2 nm) turbostratic graphite layers [10]. Each of the yarns contains 500 individual fibers and have an elliptical cross-section with about a 1.2 mm width and a 6/1 aspect ratio. Other relevant properties for both unirradiated and irradiated Nicalon-CG and Hi-Nicalon fibers are presented in Table 1 and will be discussed later.

Irradiation and Test Conditions

The composites and fibers were irradiated in either the FFTF or the EBR-II reactors under conditions described previously [2]. Bend bar specimens were irradiated at 430, 500, 800, 1000 and 1200°C to doses of from 4 to 80 dpa-SiC. Four-point flexure stress-strain curves were used to determine the ultimate bend strengths, the matrix cracking stresses and the bend modulus of the reference SiC_f/SiC material for the given

irradiation conditions. To simulate material properties expected under actual operating conditions in a fusion environment, these curves were acquired at the temperatures of the irradiations, again as reported previously [2]. Flexure data also have been obtained at ambient and 500°C for the unirradiated SiC_f/SiC composite made with Hi-Nicalon fabric. This material will be irradiated in the HFIR reactor at 500°C to a dose of about 10 dpa-SiC. Tensile strength and modulus data, collected at ambient using a Micropul^{TM} device described elsewhere [6], are given in Table 1 for both unirradiated and irradiated Nicalon-CG and Hi-Nicalon fibers.

Table 1. Nicalon-CG and Hi-Nicalon Fiber Properties.

Property	Nicalon-CG (unirrad.)	Nicalon-CG (irrad.)	Hi-Nicalon (unirrad.)	Hi-Nicalon (irrad.)	Ref.
Density	2.58 g/cc	+5.8 ± 0.2%		not in	(a)
	" "	+5.3 ± 0.2%		not in	(b)
	2.54 g/cc	14.7 ± 0.9%		not in	(c)
	2.57 g/cc	+9.5 ± 1.0%	2.76 g/cc	+0.7 ± 0.3%	(d)
	" "	to be measured	2.74 g/cc	to be measured	(e)
Crystallite Size (nm)	<2	5+	5-10	5-10	(d)
		not in	3.1	2.8	(e)
Strength (GPa)	3.0 ± 1.6	1.9 ± 0.6	2.4 ± 0.8	3.4 ± 0.7	(d)
	" "	to be measured	" "	to be measured	(f)
		not in	2.9 ± 0.8	3.7	(e)
Elastic Mod. (GPa)	160	180	210	260	(d)
			280	300	(f)

(a) FFTF at 430°C, 5.3 dpa-SiC [5]; (b) FFTF at 430°C, 26 dpa-SiC [5];
(c) EBR-II at 850°C, 25 dpa-SiC [1]; (d) EBR-II at 1000°C, 43 dpa-SiC [6];
(f) EBR-II at 800°C, 80 dpa-SiC [new data]; (e) HIFR at 100°C, 2.5 dpa-SiC [8];

Results and Discussion

From Table 1, it is noted that the Nicalon-CG fiber density increases significantly for a broad range of radiation conditions. Also, the tensile strength of the fiber decreased from 3.0 GPa to 1.9 GPa while the elastic modulus increased slightly from 160 to 180 GPa for the unirradiated and irradiated condition of 1000°C/43 dpa-SiC, respectively. Osborne, et al. [7], presented evidence that Nicalon-CG contains an amorphous SiO_xC_y phase that is unstable under irradiation. This phase converts to crystalline SiC and CO gas, which causes Nicalon-CG fiber to densify (and shrink) and to become weaker. Observations by TEM [10] showed that the Nicalon-CG crystallite size increased from about 2 nm (unirradiated) to 5 nm (irradiated at 1000°C, 43 dpa-SiC), which supports Osborne's findings.

In contrast, the Hi-Nicalon density slightly increased while little change in the crystallite size was observed for the 1000°C/43 dpa-SiC irradiation. Surprisingly, the tensile strength increased by 40% from 2.4 to 3.4 GPa while the elastic modulus increased slightly from 210 to 260 GPa for the unirradiated and irradiated conditions, respectively. Osborne, et al. [8], also observed a strength increase for Hi-Nicalon from 2.9 GPa to 3.6 GPa for quite different irradiation conditions (100°C/2.5 dpa-SiC). Apparently, the Hi-Nicalon fiber exhibits much more radiation tolerance than Nicalon-CG fiber for a broad range of irradiation conditions.

In Figure 1, the 4-pt flexure strengths of unirradiated and irradiated reference SiC_f/SiC are presented in a 3D plot. The independent irradiation/test temperature and dose variables form the horizontal axes and the dependent flexure strength variable forms the elevation axis. Qualitative strength contours and constant dose

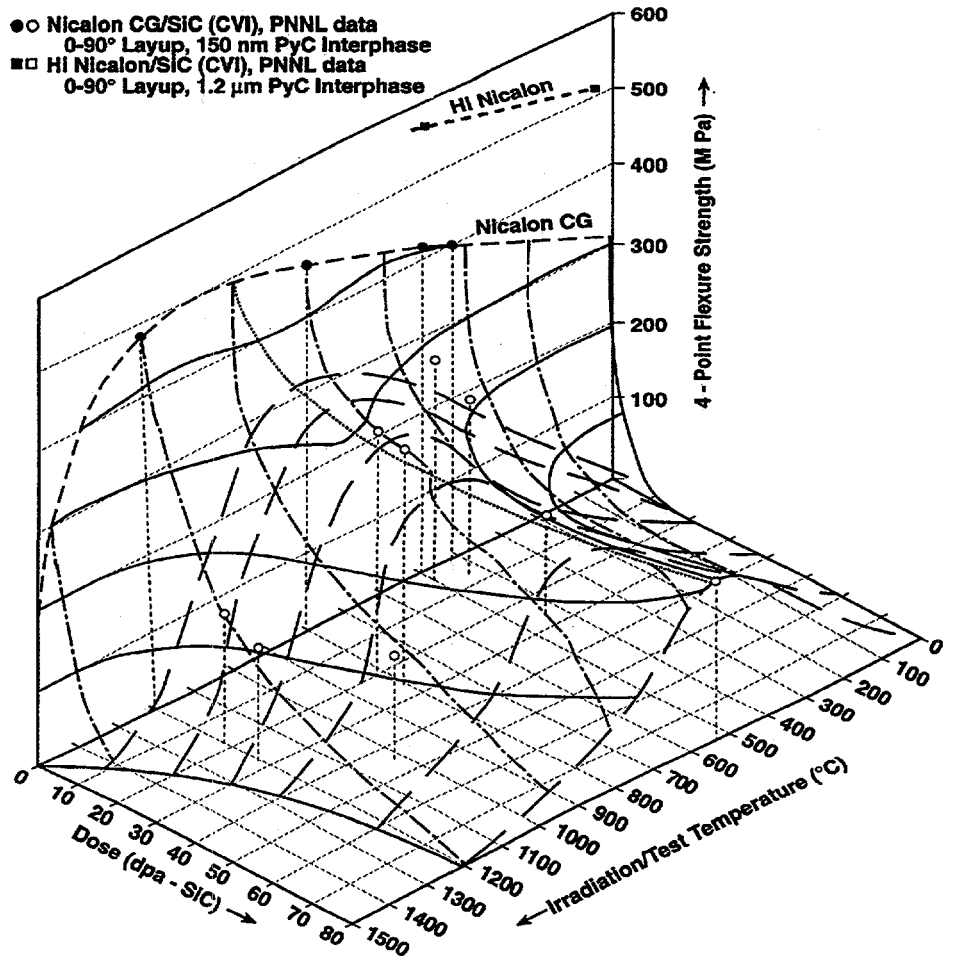

Figure 1. Proposed Strength-Irradiation Dose-Temperature Surface for Reference SiC_f/SiC Composite

and temperature lines have been added to suggest a hypothetical 3D surface which represents the strength dependence on irradiation dose and temperature for the reference SiC_f/SiC material.

Guided by a limited amount of data, this hypothetical surface nevertheless depicts three topological features which are characteristic of the irradiated reference SiC_f/SiC strength behavior. In particular, these major features are suggested to be due to the following three different types of degradation mechanisms: (1) For the unirradiated reference SiC_f/SiC, the strength gradually increases with temperature from 300 MPa at ambient up to a maximum value of 510 MPa at about 1000-1200°C, then it steeply drops off with further temperature increase. This temperature dependence closely follows the bend strength-temperature curve for similar SiC_f/SiC composite presented by Lamicq, et al. [11]. The strength for monolithic SiC also increases with temperature at about the same rate; but in contrast, it continues to increase up to and above 1500°C [1]. Therefore, the steep drop-off must be related to the characteristic loss in tensile strength of the Nicalon-CG fiber for temperatures exceeding about 1100°C. From the 3D plot, as the irradiation dose increases the temperature where the strength drop-off commences gradually diminishes. A dotted "optimum composite strength" ridge-line is shown starting at 500 MPa (1000°C/0 dpa-SiC) and gradually dropping but proceeding out to 210 MPa (550°C/80 dpa-SiC). This ridge-line behavior reflects a combination of the irradiation instability and the loss in strength at high temperature of the Nicalon-CG fiber. (2) For low

irradiation doses, the strength drop-off initially is rather steep for all irradiation temperatures. While depending somewhat on the irradiation temperature, the rate of drop-off slows considerably for doses above about 1-2 dpa-SiC. This initial steep drop-off with dose appears to reflect the characteristic defect accumulation which saturates at doses below about 1 dpa-SiC for irradiated SiC. For instance, irradiated monolithic SiC exhibits roughly an initial 25% loss in flexural strength by 4.3 dpa-SiC, but retains its strength with further irradiation [1]. Also, the Nicalon-CG fiber itself probably continues to slowly lose strength with increasing irradiation time (proportional to dose) as it recrystallizes. The composite strength dose dependence also reflects this slower form of fiber strength degradation. (3) The difference between the SiC matrix swelling due to irradiation and the shrinkage of the irradiated Nicalon-CG fiber is greater for lower irradiation temperatures. Therefore, considerable debonding of the fiber from the matrix is expected at lower irradiation temperatures at fairly low doses. This causes the composite strength drop-off with dose to be much steeper. A strength "depression" in the 3D surface is expected at higher doses and lower temperatures. There is no data for reference SiC_f/SiC irradiated to high doses at temperatures below 550°C, so the magnitude of the low temperature depression is speculative.

In a previous report [12], it was recommended that at least six flexure samples be tested for each condition to achieve reliable and reproducible (± 10%) average strength values for SiC_f/SiC composite. Much of the data used in this analysis were taken from earlier studies where only 2-4 bar samples for each condition were used, so the strength values must be considered qualitative. Importantly, test conditions themselves were always the same, thus the temperature- and dose-dependent trends depicted by the 3D strength surface are expected to be reliable for the SiC_f/SiC material.

With reference to these three degradation features and the relevant properties of unirradiated and irradiated Nicalon-CG and Hi-Nicalon fibers already presented in Table 1, the strength behavior of SiC_f/SiC composite should be improved by replacing Nicalon-CG with Hi-Nicalon fiber. In fact, for unirradiated SiC_f/SiC made with Hi-Nicalon fiber this is the case (See Fig. 1). Between ambient and 500°C, the strengths of the Hi-Nicalon composite increased with temperature from 505 to 560 MPa, which represents about a 40% strength increase over that of reference SiC_f/SiC. Based on the improved thermal creep stability of Hi-Nicalon over that of Nicalon-CG fiber [13], the related composite strength "drop-off" temperature is expected to be increased by about 120°C for the Hi-Nicalon composite. The steep strength drop-off with irradiation dose exhibited by reference SiC_f/SiC, primarily due to the loss of strength of the Nicalon-CG fiber (especially at higher temperatures), also should not be observed for the Hi-Nicalon composite since the Hi-Nicalon fiber actually exhibited an increase in strength with irradiation. Finally, the low temperature strength depression, caused by larger differential swelling and debonding between the composite matrix and fiber during irradiation, should not be as severe for the Hi-Nicalon composite since the Hi-Nicalon fibers shrink very little with dose. Furthermore, other properties of the more crystalline Hi-Nicalon fiber, such as elastic modulus and thermal expansion, more closely match those of the ß-SiC matrix; so load transfer between the fiber and matrix should remain more uniform over a range of temperature and load conditions. Thus, the optimum "ridge-line" should be broader, have higher strength values and be shifted to higher temperatures for all doses for the Hi-Nicalon composite.

It has been shown that each of the three degradation mechanisms responsible for the topological features depicted by the 3D strength-temperature-dose surface for reference SiC_f/SiC should be alleviated by replacing the Nicalon-CG with Hi-Nicalon fiber. Other advanced fibers with more crystalline microstructures made up of pure ß-SiC, such as Nicalon-S or Sylramic^{TM} fiber, should promote similar improvements in irradiated SiC_f/SiC composite.

An important issue not discussed to this point is the effect of the composite interphase type and thickness. To attain the overall strength improvement in these Hi-Nicalon composites, a 1.2 μm thick carbon interphase was used. Potentially, the thicker interphase could be a problem due to the dimensional

instability of graphite in an irradiation environment. This potential problem will be closely analyzed after the upcoming HFIR irradiations of this material. Other interface strategies, for instance utilizing porous SiC or multiple C/SiC/C layers in place of the graphite layer, currently are being developed by others [14].

CONCLUSIONS

The irradiation performance of reference SiC_f/SiC is characterized by a 3D strength-temperature-dose surface that exhibits three types of degradation mechanisms. Each of the three proposed degradation mechanisms for irradiated reference SiC_f/SiC composite should be alleviated by replacing Nicalon-CG with Hi-Nicalon fiber.

FUTURE WORK

The irradiation effects on a Hi-Nicalon SiC_f/SiC composite will be reported at the conclusion of the Jupiter P3-3 test cycle (February to December 1997, 500°C/10 dpa-SiC, in the HFIR reactor) in early 1998.

REFERENCES

1. G. W. Hollenberg, C. H. Henager, Jr., G. E. Youngblood, D. J. Trimble, S. A. Simonson, G. A. Newsome and E. Lewis, "The Effect of Irradiation on the Stability and Properties of Monolithic Silicon Carbide and SiC_f/SiC Composites up to 25 dpa," *J. Nucl. Mater.*, 219, 70-86 (1995).

2. G. E. Youngblood, C. H. Henager, Jr., D. J. Senor and G. W. Hollenberg," Effects of Neutron Irradiation on Dimensional Stability and on Mechanical Properties of SiC/SiC Composites," p. 321 in Fusion Materials, Semiannual Progress Report for Period ending September 31, 1994, DOE/ER-0313/17.

3. L. L. Snead and O. J. Schwarz, "Advanced SiC Composites for Fusion Applications," *J. Nucl. Mater.*, 219, 3-14 (1995). Also p.274 in Fusion Materials, Semiannual Progress Report for Period ending September 30, 1994, DOE/ER-0313/17.

4. L. L. Snead, D. Steiner and S. J. Zinkle, "Measurement of the Effect of Radiation Damage to Ceramic Composite Interfacial Strength," *J. Nucl. Mater.*, 191-194, 566-570 (1992).

5. G. E. Youngblood, D. J. Senor and G. W. Hollenberg, "Dimensional Stability of SiC-Type Fibers Neutron Irradiated to High Doses," p. 417 in Fusion Materials, Semiannual Progress Report for Period ending March 31, 1995, DOE/ER-0313/18.

6. D. J. Senor, G. E. Youngblood, J. L. Brimhall, D. J. Trimble, G. A. Newsome, and J. J. Woods, "Dimensional Stability and Strength of Neutron-Irradiated SiC-Based Fibers," accepted for publication in *Fusion Technology* and based on a Poster presentation at the 12th Topical Meeting of Fusion Energy at the 1996 American Nuclear Society Annual Meeting, 16-20 June, Reno, NV.

7. M. C. Osborne, L. L. Snead and D. Steiner, "Tensile Behavior of Irradiated SiC Fibers," *J. Nucl. Mater.*, 219, 63-69 (1995).

8. M. C. Osborne, D. Steiner and L. L. Snead, "Neutron Irradiation Effects on Hi- Nicalon Silicon Carbide Fibers," p. 136 in Fusion Materials, Semiannual Progress Report for Period ending June 30, 1996, DOE/ER-0313/20.

9. G. E. Youngblood and W. Kowbel, "Improvement of the Thermal Conductivity of SiC_f/SiC

Composite," p.107 in Fusion Materials, Semiannual Progress Report for Period ending December 31, 1995, DOE/ER-0313/19.

10. G. E. Youngblood, R. H. Jones and A. Hasegawa, "Microstructural Effects of Neutron Irradiation on SiC-Based Fibers, p. 101, ibid.

11. Pierre J. Lamicq, Gerald A. Bernhart, M. M. Dauchier and Jean G. Mace, "SiC/SiC Composites," *Am. Ceram. Soc. Bull.*, 65 (2), 336-38 (1986).

12. G. E. Youngblood, C. H. Henager, Jr. and R. H. Jones, "Specimen Size Effect Considerations for Irradiation Studies of SiC/SiC, p. 140 in Fusion Materials, Semiannual Progress Report for Period ending June 30, 1996, DOE/ER-0313/20.

13. G. E. Youngblood and R. H. Jones, "Status of Measuring Irradiation Creep in SiC Fibers," this Report.

14. L. L. Snead, private communication.

THE MONOTONIC AND FATIGUE BEHAVIOR OF CFCCs AT AMBIENT TEMPERATURE AND 1000°C - N. Miriyala, P. K. Liaw, and C. J. McHargue (University of Tennessee), and L. L. Snead (Oak Ridge National Laboratory).

OBJECTIVE

To develop a fundamental understanding of the fabric orientation effects on the monotonic and fatigue behavior of continuous fiber-reinforced ceramic-matrix composites (CFCCs) at ambient and elevated temperatures.

SUMMARY

Metallographically polished flexure bars of Nicalon/SiC and Nicalon/alumina composites were subjected to monotonic and cyclic-fatigue loadings, with loading either parallel or normal to the fabric plies. The fabric orientation did not significantly affect the mechanical behavior of the Nicalon/SiC composite at ambient temperature. However, the mechanical behavior of the Nicalon/alumina composite was significantly affected by the fabric orientation at ambient temperature in air and at 1000°C in argon atmosphere. In addition, there was a significant degradation in the fatigue performance of the alumina matrix composite at the elevated temperature, owing to creep in the material and degradation in the fiber strength.

PROGRESS AND STATUS

Introduction

It is generally observed that unidirectionally reinforced composites exhibit good strength and toughness when the load is applied parallel to the fiber orientation, but perform poorly when the load is applied normal to the fibers. Hence, in applications where multi-axial stresses are expected, two dimensional (2-D) or three dimensional (3-D) reinforcement is commonly used [1, 2]. The 2-D composites are usually manufactured by first making a woven or braided-fabric preform, which is then infiltrated with the matrix, using liquid or vapor infiltration techniques [3, 4]. However, the interlaminar strength of these composites is often poor, which may lead to significant differences in the mechanical behavior of the material, depending on whether the load is applied parallel or normal to the fabric plies. Accordingly, it is the objective of the current study to systematically investigate the effects of fabric orientation on the mechanical behavior of two of the commercially available 2-D CFFCs, namely, Nicalon/silicon carbide (SiC) and Nicalon/alumina composites manufactured by DuPont-Lanxide Corporation.

In our previous studies [5, 6], the monotonic and fatigue behavior of the two composites was studied at ambient temperature. It was observed that the fabric orientation significantly affected the mechanical behavior of the Nicalon/alumina composite, while the effects were insignificant for the Nicalon/SiC composite. However, it was not possible to develop an understanding of the damage mechanisms in the two materials, as unpolished specimens were used in the experiments. In the present study, carefully polished flexure specimens were used to perform the mechanical tests. The monotonic and fatigue behavior of the Nicalon/SiC composite was studied at ambient temperature. For the Nicalon/alumina composite, the monotonic and fatigue tests were performed at ambient temperature in air, and at 1000°C in argon atmosphere. The specimen fracture surfaces were examined under a scanning electron microscope to understand the damage mechanisms operative under both static and cyclic-fatigue loadings.

Experimental Details

Materials

The material details have already been described in previous progress reports [5, 6] and, hence, only a brief mention of them will be made here. The Nicalon/SiC composite, fabricated by an isothermal chemical vapor infiltration (ICVI) process, was provided by AlliedSignal Engines, Phoenix, AZ. A 2-D braided Nicalon fabric was used as the preform, which was first given an interfacial coating of carbon (approximately 0.4 to 0.5 μm) by a CVD process, prior to the infiltration of SiC matrix. The SiC matrix was infiltrated by the decomposition of methyltrichlorosilane, in the presence of hydrogen, at 1100 to 1200°C. The nominal fiber volume percent in the composite was approximately 40.

The Nicalon/alumina composite, fabricated by a direct molten metal oxidation (DIMOX) process, was supplied by Westinghouse Electric Corporation, Orlando, FL. A 12-harness satin woven Nicalon fabric in a 0/90 sequence was used as the preform in this composite. The fabric preform was given a duplex coating of boron nitride (BN) and silicon carbide (SiC) via chemical vapor deposition (CVD). The duplex-coated preform was then placed in contact with molten aluminum at 900 to 1100°C in air. The matrix in the composite was formed by the growth of alpha alumina, starting from the alloy/preform interface. The nominal fiber volume percent in the composite was approximately 35.

Flexure testing

The Nicalon/SiC flexure bars were 50 mm long, 2 mm wide and 2 mm thick, while the Nicalon/Alumina samples were 50 × 3 × 3 mm [5, 6]. The details of the MTS servohydraulic system used to perform the mechanical tests can be obtained from references 5 and 6. During the monotonic and fatigue tests, loads were applied to the specimens either parallel or perpendicular to the fabric plies. Accordingly, the specimen configurations were referred to as edge-on and transverse, depending on whether the load was parallel or normal to the fabric plies, respectively [6]. The ambient-temperature monotonic and fatigue tests were conducted in air, while the high-temperature tests were performed at 1000°C in argon atmosphere. The monotonic tests were conducted under displacement control at a crosshead displacement rate of 0.5 mm/min. The cyclic-fatigue tests were conducted under load control using a sinusoidal wave form. The loading frequency was 0.5 Hz up to 1000 cycles, and then gradually increased to 5 Hz and maintained at that frequency till the completion of tests. A load-ratio (minimum load/maximum load) of 0.1 was used in all the cyclic fatigue tests. The fatigue run-out was set at one million cycles, which corresponded to approximately 56 hours of testing.

Metallographic Examination

Unsevered composite specimens, after unloading at periodical intervals during the fatigue tests, as well as the specimen fracture surfaces following the monotonic and fatigue tests, were examined under a Hitachi S-800 Scanning Electron Microscope (SEM) at the High Temperature Materials Laboratory (HTML) of the Oak Ridge National Laboratory (ORNL), to observe the damage mechanisms in the two materials investigated. A Macintosh personal computer was interfaced to the SEM to digitally capture the images using the Adobe Photoshop software (version 2.5).

Results and Discussion

Nicalon/SiC Composite

From our previous studies on the mechanical behavior of the Nicalon/SiC composite [5,6], it was observed that the flexural strength in the edge-on orientation was 234 ± 27 MPa, while the strength was 241 ± 23 MPa in the transverse orientation. It was also evident that the difference in flexural strength between the two orientations was insignificant, considering the scatter in the strength data and the porosity content. Stress-life (S-N) tests were also performed at ambient temperature, and it was noted that specimen failure did not occur even when the maximum stress during the tests was about 190 MPa (80 % of the monotonic

strength), in both orientations [6]. From the effective modulus and midspan deflection trends, it appeared that the fabric orientation did not significantly affect the fatigue behavior of the Nicalon/SiC composite. The slope of the load versus midspan deflection values decreased after the first loading cycle in all the samples. After a relatively steep drop of up to 10% in the first ten cycles, the decrease in effective modulus was less precipitous as the loading continued. It appeared that much of the damage in the composite material occurred in the first few cycles. However, an understanding of the damage mechanisms was lacking since unpolished specimens were used in performing the mechanical tests. To meet this objective, metallographically polished flexure specimens were used to perform the monotonic and fatigue tests in the present study.

The fracture surfaces after monotonic loading, in both edge-on and transverse orientations, were fibrous, indicating substantial fiber pullout. Matrix cracking was observed mostly in the transverse fiber tows (yarns oriented at 90° to the long axis of the specimen and intersecting the bottom surface in the edge-on orientation, or the cross-section in the transverse orientation). The interlaminar pores appeared to have acted as stress concentration sites, and microcracks initiated from these pores (Figure 1), and propagated primarily into the transverse fiber tows. These cracks linked up to cause specimen failure. Specimen separation was observed to be primarily along the interlaminar pores (Figure 2). Matrix cracking in the transverse fiber tows, fiber breakage and interlaminar cracking appear to be the main failure mechanisms in the composite material, under monotonic loading, in both orientations. However, from the examination of specimen surfaces, it appeared that interlaminar porosity played a bigger role than matrix cracking in the material failure [7].

The specimens subjected to cyclic-fatigue loading were periodically unloaded from the test machine to observe damage progression in the material. Although the effective modulus trends indicated that the degradation in material load bearing capability occurred during the early stages (< 10 cycles) of fatigue loading, the SEM examination did not reveal any cracking in the material. It may, however, be noted that the specimens used in the present investigation were very small (50 × 2 × 2 mm). Consequently, the damage evolution was limited, since only a small fraction of the bend bar volume is subjected to the maximum tensile stress in a flexure test. However, matrix cracking was readily observed on the specimen surfaces after about 1,000 loading cycles (Figure 3). Cracks appeared to have initiated from the interlaminar pores and propagated primarily into the transverse fiber tows in both orientations. In some samples, matrix cracking in the transverse fiber tows appeared to link up some of the smaller interlaminar pores, forming a weak layer in the material (Figure 4).

Nicalon/Alumina Composite

The flexural strength of the composite was significantly higher in the edge-on orientation, compared to the transverse orientation, at both ambient and elevated temperatures. In the edge-on orientation, the ultimate flexural strength values were 474 ± 7 MPa and 468 ± 18 MPa, respectively, at room temperature and 1000°C. In contrast, for the transverse orientation, the room-temperature flexural strength was 330 ± 20 MPa, while the high-temperature strength was 346 ± 13 MPa. The flexural stress-strain curves at 1000°C are presented in Figure 5. It can be seen from Figure 5 that the stress-strain curves were non-linear in both orientations.

While the flexural strength and the strain to failure values were higher in the edge-on orientation, compared to the transverse orientation, the proportional limit (the stress at which the stress-strain curve deviates from linearity) was approximately the same (70 MPa) for both orientations. The stress-strain curves, and the proportional limit, at ambient temperature were similar to those at 1000°C [8, 9].

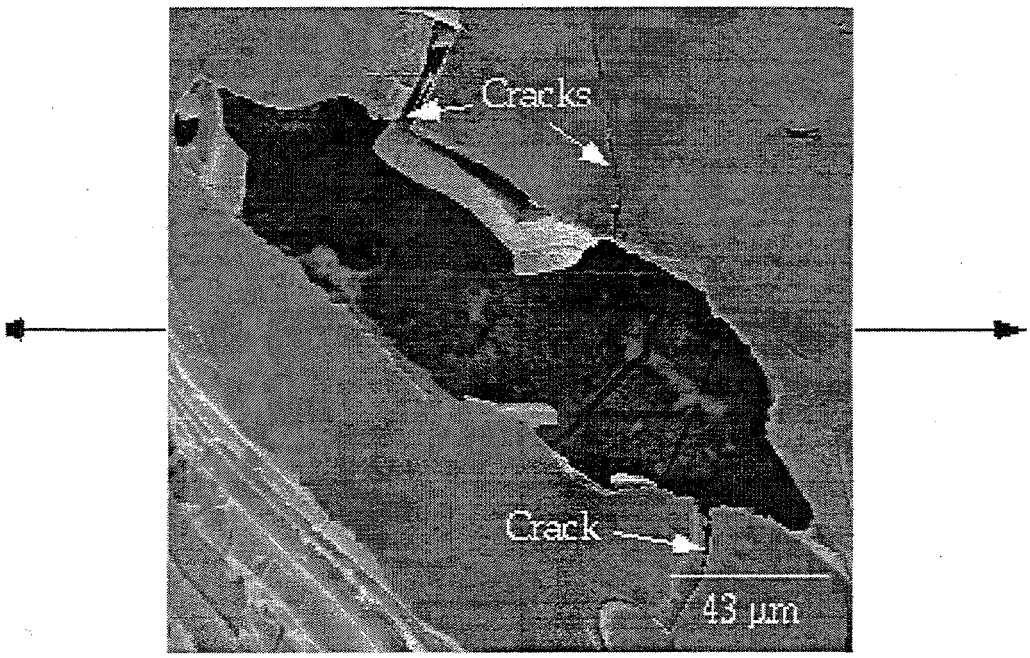

Figure 1. Crack initiation from interlaminar pore, on the tensile (bottom) surface) of an edge-on specimen monotonically loaded to failure .

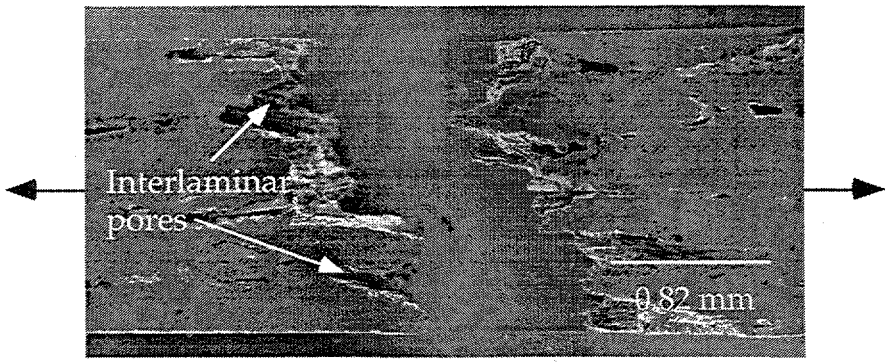

Figure 2. Tensile surfaces of an edge-on specimen separated along the interlaminar pores after monotonic loading.

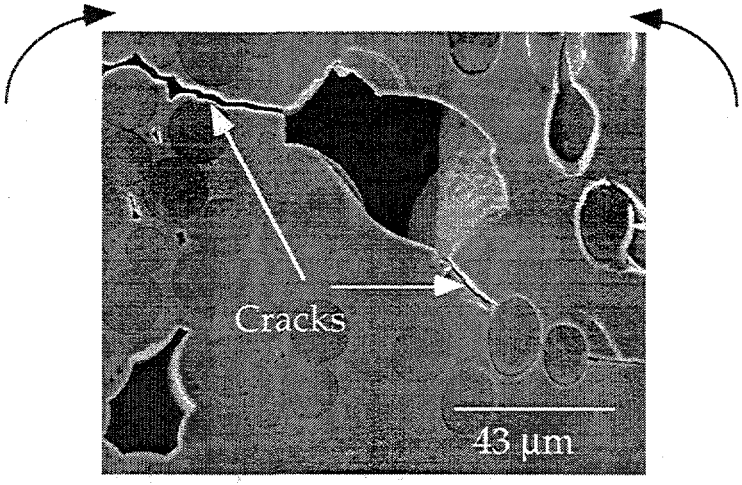

Figure 3. Cracks initiated from an interlaminar pore propagating into a transverse fiber tow in a transversely loaded specimen subjected to fatigue loading.

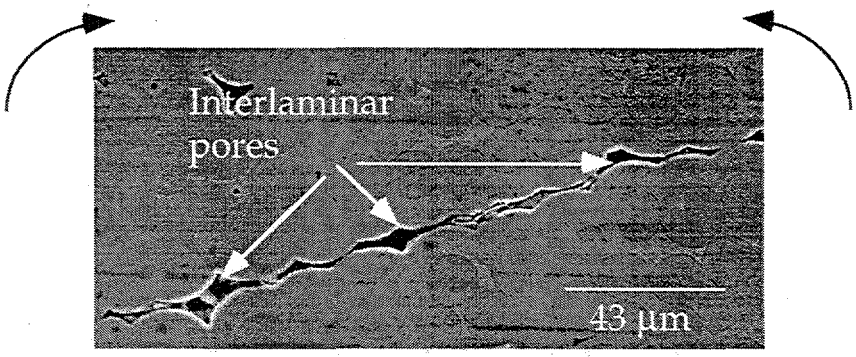

Figure 4. Matrix cracking in a transverse ply linking up interlaminar poresin a transversely loaded specimen subjected to fatigue loading.

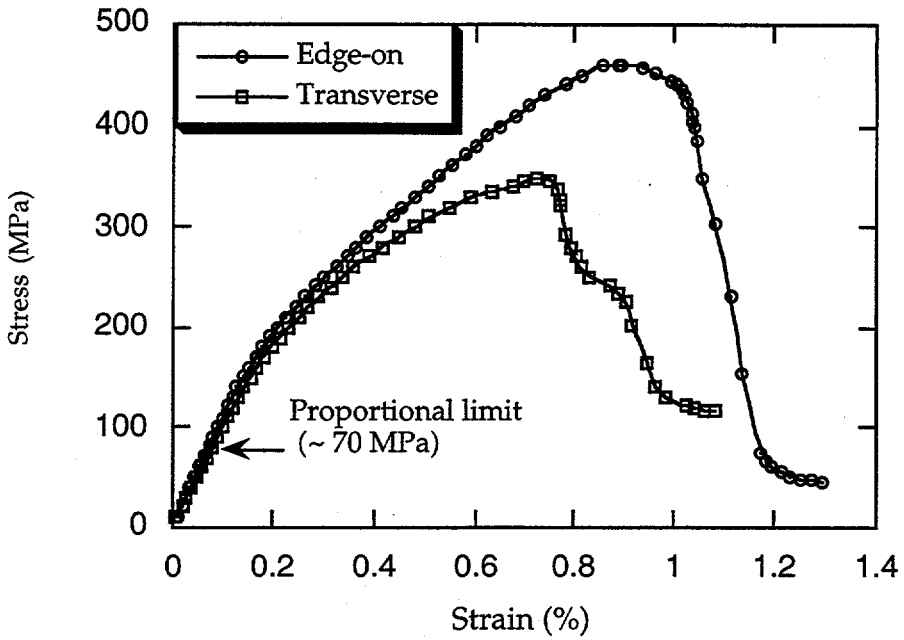

Figure 5. Stress-strain curves for the Nicalon/alumina composite in the edge-on and transverse orientations at 1000°C in argon atmosphere.

Fractography revealed that the failures modes in the edge-on and transverse orientations were significantly different. The edge-on specimens failed in a predominantly tensile mode, with cracking in the 90° fiber bundles preceding the failure of the 0° fibers. In most cases, the specimen broke into two pieces (Figure 6). In the transverse orientation, cracking initiated in the 90° tows, and some of these cracks developed into interlaminar cracks, leading to collapse rather severance of the specimens (Figure 7). Multiple matrix cracking and interfacial bonding were observed in all the samples. It was also observed that the cracks in the 90° fiber tows propagated primarily along the fiber-matrix interface. For a given orientation, the failure modes were similar at ambient and elevated temperatures.

While the monotonic behavior of the composite was not affected by the test temperature, there was a significant degradation in the fatigue behavior of the material, particularly in the edge-on orientation, due to the prolonged exposure to elevated temperatures. The stress versus number of cycles (S-N) curves for the composite at ambient and elevated temperatures are shown in Figure 8. It can be seen from Figure 8 that, at room temperature, in the edge-on orientation, the ratio of endurance limit (the stress at which the specimen survives 1 million cycles) to flexural strength was approximately 0.67, while the ratio was only 0.45 at 1000°C. The corresponding ratios in the transverse orientation were 0.77 and 0.69, respectively, at ambient and elevated temperatures. Thus, the degradation in the fatigue behavior appears to be more severe in the edge-on orientation compared to the transverse orientation. It is also apparent from Figure 5 that, at room temperature, the endurance limit was significantly higher in the edge-on orientation, compared to the transverse orientation. In contrast, the endurance limit at 1000°C was approximately the same in both orientations. It is important to note that, at room temperature, the specimens tested in the edge-on orientation were subjected to much higher stress levels than the transversely oriented specimens. At these higher stress levels, the 0° fibers failed gradually, leading to specimen severance, while the transverse specimens, subjected to much lower stress levels, failed by interlaminar cracking, followed by specimen collapse. At 1000°C, however, the stress levels used in both orientations are comparable. While the S-N line slopes for the transverse orientation at room temperature and 1000°C are comparable, the slope is much

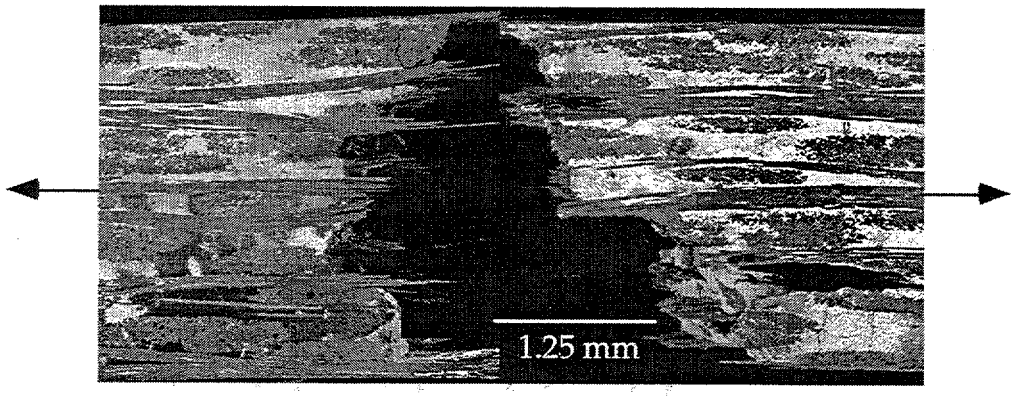

Figure 6. Tensile (bottom) surfaces of an edge-on specimen monotonically loaded at ambient temperature.

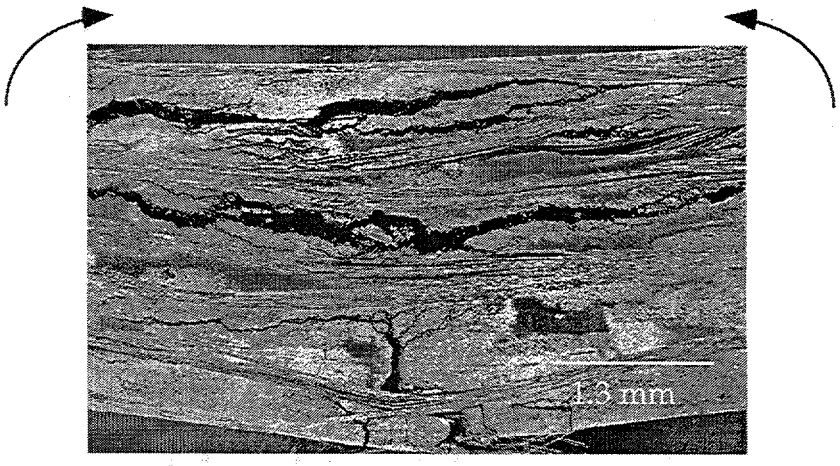

Figure 7. Cross-section of a transverse specimen monotonically loaded at ambient temperature.

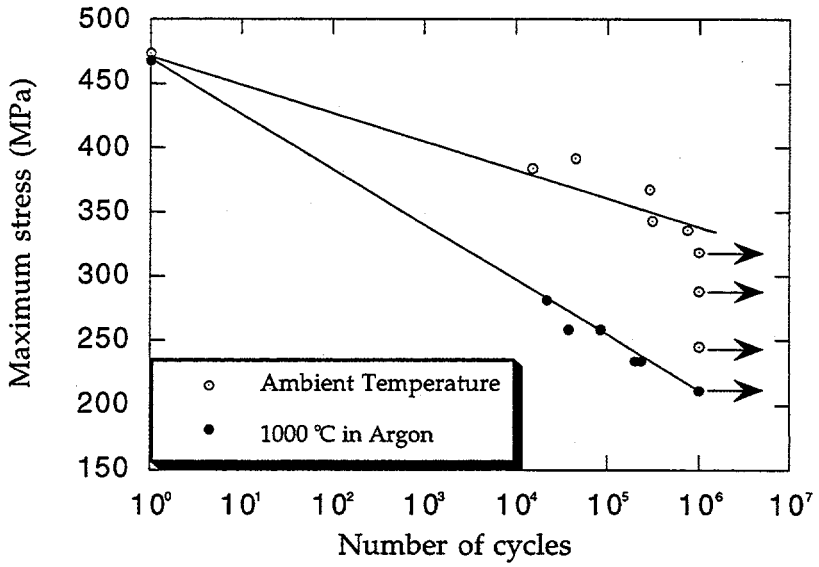

(a)

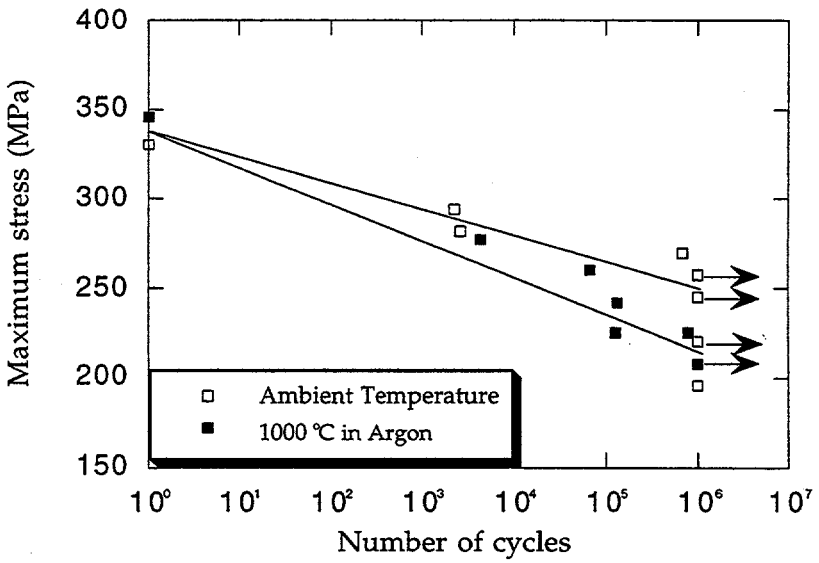

(b)

Figure 8. Stress versus life curves for the Nicalon/alumina composite at ambient temperature and 1000°C in (a) edge-on orientation and (b) transverse orientation.

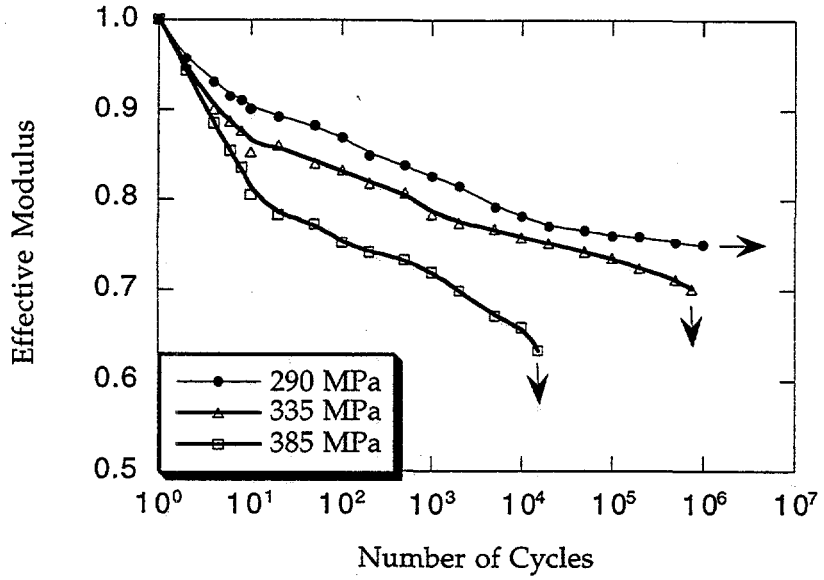

(a)

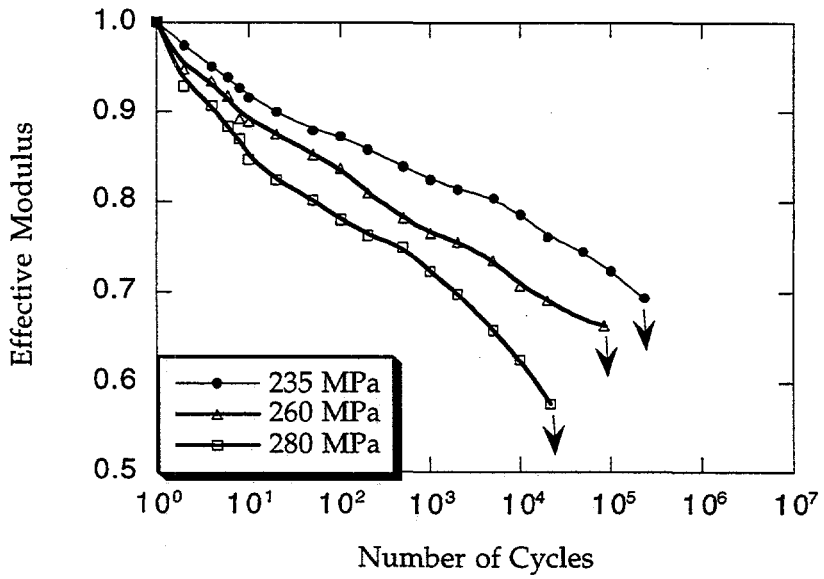

(b)

Figure 9. Reduction in effective modulus upon cyclic loading in the edge-on orientation at (a) ambient temperature and (b) 1000°C in argon atmosphere.

steeper at the high temperature, compared to that at the ambient temperature, for the edge-on orientation. Some specimens were loaded to the stress levels used in the fatigue experiments at 1000°C and held at a constant stress for about 50 hours or till the specimen failure, whichever occurred earlier [9]. It was noticed that the midspan deflection values increased significantly, particularly at the higher stress levels, in the first few hours of testing. It is also well known that the Nicalon^{TM} fibers degrade in strength, upon prolonged exposure to elevated temperatures [10]. We believe that the creep in the material and the fiber degradation are responsible for the poor fatigue behavior of the composite at the elevated temperature, particularly in the edge-on orientation.

The effective modulus value trends for the Nicalon/alumina composite, in the edge-on orientation, at room temperature and 1000°C, respectively, are plotted in Figures 9. It can be seen from Figure 9 that the effective modulus values continued to drop after the first cycle, in both orientations, at ambient as well as elevated temperatures. The initial drop in the effective modulus values (< 1000 cycles) was observed to be due to cracking in the 90° fiber bundles, in both orientations, at ambient as well as elevated temperatures. These cracks then penetrated into 0° fiber tows in the edge-on orientation, but propagated as interlaminar cracks in the transverse orientation. For a given orientation, the failure modes at room temperature and 1000°C were similar. However, the creep of the specimens and degradation of the Nicalon fibers contributed to more precipitous drop in the effective modulus values at the high temperature.

CONCLUSIONS

The monotonic and fatigue behavior of the Nicalon/SiC composite at ambient temperature appears to be unaffected by the orientation of fabric plies to the applied loads. There was a large scatter in the flexural strength values, owing to the variation in porosity content and distribution. Upon cyclic-fatigue loading, the effective modulus of the composite decreased after the first loading cycle in both orientations. After a relatively steep decrease in the modulus values in the first ten cycles, the modulus values decreased more gradually upon further cycling. The specimen failure after monotonic and cyclic-fatigue loadings, in both orientations, occurred due to matrix cracking in the transverse fiber tows, interlaminar cracking, and fiber breakage.

The flexural strength of the Nicalon/alumina composite was significantly higher in the edge-on orientation, compared to the transverse orientation, at ambient and elevated temperatures. While the monotonic behavior was unaffected by the exposure to 1000°C, there was a significant deterioration in the fatigue behavior of the material, particularly in the edge-on orientation, at the elevated temperature, compared to the behavior at the ambient temperature. The edge-on specimens failed by cracking in the 90° fiber tows, followed by the failure of the 0° fibers. In contrast, the cracking in the 90° bundles was followed by interlaminar cracking in the transverse orientation. The creep in the material, and the degradation of the Nicalon fibers, further contributed to the poor fatigue behavior at 1000°C.

FUTURE WORK

Monotonic and fatigue tests will be performed on the Nicalon/SiC composite at 1000°C in argon atmosphere. In addition, the influence of span-to-thickness ratio, on the monotonic and fatigue behavior of both composites, will be evaluated. Finally finite element method (FEM) analysis will be performed to help explain some of the experimental results.

ACKNOWLEDGMENTS

This research is supported by the Department of Energy under Contract No. Martin Marietta 11X-SV483V to the University of Tennessee. P. K. Liaw is also supported by the National Science Foundation under Contract No. EEC-9527527 to the University of Tennessee with M. Poats as the program manager. We are grateful to E. E. Bloom and A. F. Rowcliffe of the Oak Ridge National Laboratory for their continued support and understanding. Thanks are due to J. A. Morrison of Westinghouse Electric Corporation and J. Armstrong of AlliedSignal Engines for providing the composite materials used in the present study. We are also indebted to T. A. Long, G. L. Jones, and D. E. Fielden of the University of Tennessee, and A. M. Williams, J. W. Jones, D. W. Coffey, and M. K. Ferber of the Oak Ridge National Laboratory for their help and advice in performing this work.

REFERENCES

1. N. Miriyala and P. K. Liaw, JOM, September 1996, p 44.

2. A. G. Evans and D. B. Marshall, Acta Metall. 37 (1989), p 2567.

3. A. S. Fareed, D. J. Landini, T. A. Johnson, A. N. Patel, and P. A. Craig, SME Paper EM92-216, 1992.

4. T. M. Besmann, B. W. Sheldon, R. A. Lowden, and D. P. Stinton, Science, 253 (1991) p. 1104.

5. N. Miriyala, P. K. Liaw, C. J. McHargue, and L. L. Snead, Fusion Materials Semiannual Progress Report for Period Ending December 31, 1995, DOE/ER-0313/19, p. 115.

6. N. Miriyala, P. K. Liaw, C. J. McHargue, and L. L. Snead, Fusion Materials Semiannual Progress Report for Period Ending June 30, 1996, DOE/ER-0313/20, p. 130.

7. N. Miriyala, P. K. Liaw, C. J. McHargue, and L. L. Snead, "The Monotonic and Fatigue Behavior of Continuous Fiber-Reinforced Ceramic-Matrix Composites (CFCCs)," Final Report for SURA/UT/ORNL Summer Cooperative Research Program, September 1996.

8. N. Miriyala, P. K. Liaw, C. J. McHargue, L. L. Snead, and A. S. Fareed, Ceramic Transactions 74 (1996), p. 447.

9. N. Miriyala, P. K. Liaw, C. J. McHargue, L. L. Snead and J. A. Morrison, "The Monotonic and Fatigue Behavior of a Nicalon/Alumina Composite at Ambient and Elevated Temperatures," Ceram. Eng. Sci. Proc. 18 (1997), in press.

10. G. Simon and A. R. Bunsell, J. Mater. Sci. 19 (1984), p 3649.

3.0 FERRITIC/MARTENSITIC STEELS

DEVELOPMENT OF OXIDE DISPERSION STRENGTHENED FERRITIC STEELS FOR FUSION -

D.K. Mukhopadhyay, F.H. Froes (University of Idaho) and D. S. Gelles (Pacific Northwest Laboratory)[a]

OBJECTIVE

The objective of this research is to develop low activation oxide dispersion strengthened fully ferritic steels for first wall applications in a fusion power system.

SUMMARY

Uniaxial tension creep response is reported for an oxide dispersion strengthened (ODS) steel, Fe-13.5Cr-2W-0.5Ti-0.25 Y_2O_3 (in weight percent) manufactured using the mechanical alloying process. Acceptable creep response is obtained at 900°C.

PROGRESS AND STATUS

Introduction

An ODS ferritic steel has been developed in order to optimize this class of materials for first wall applications of a fusion power system.[1] This was accomplished by developing an alloy composition to be in line with low activation criteria, but with the minimum chromium content to insure fully delta-ferrite stability. The alloy composition selected was Fe-13.5Cr-2W-0.5Ti-0.25Y_2O_3. The objective of the present investigation was to determine the creep response of the ODS alloy in order to demonstrate its potential for high temperature applications.

Experimental Procedure

A SATEC creep frame, with 20:1 lever arm, was used for creep testing. A schematic of the test stand used for creep testing is shown in Figure 1. The test specimen was connected to the balance beam through the load train, a system of pull rods and couplings manufactured from alloy Inconel 718. A knife edge alignment coupling was used in the load train to facilitate self-alignment. The specimen was heated in a three zone tubular split furnace in an inert atmosphere chamber to prevent oxidation of the specimen. The inert atmosphere chamber was made of an Al_2O_3 retort which was sealed at both ends by stainless steel end caps with a metal bellows at the top cap. Strain was measured using an extensometer attached to a Linear Variable Differential Transformer (LVDT) located away from the high temperature zone. The mechanical linkages, attached to the specimen were also made of Inconel 718.

Specimens were made from two batches of rod material described previously as samples 1 and 2.[1] Specimens were 1.50 inches long, with a gauge section 1.020 inches long and 0.170 inches in diameter, with grip sections 0.250 inches in diameter. Specimen temperature was continuously monitored during heat up and throughout the test with two type-K thermocouples, one attached at the top and the other at the bottom of the specimen gauge length. The temperature gradient between the top and bottom of the specimen was minimized during the test, and did not exceed 2°C. The average specimen

---

[a]Operated for the U.S. Department of Energy by Battelle Memorial Institute under Contract DE-AC06-76RLO 1830.

temperature was maintained to within ±20°C of the desired test temperature for the duration of the test.

The specimen was loaded in the creep frame and the extensometer was attached tightly. The Al_2O_3 retort was then inserted and sealed with the endcaps. The endcaps were then attached to the hose supplying coolant to keep the endcaps cool during creep testing. Argon gas was used to create an inert atmosphere environment inside the retort. The specimens were heated to the desired test temperature in 2-4 h and then were held for about 1 h at the test temperature to equilibrate and stabilize the specimen temperature. Predetermined loads were then applied.

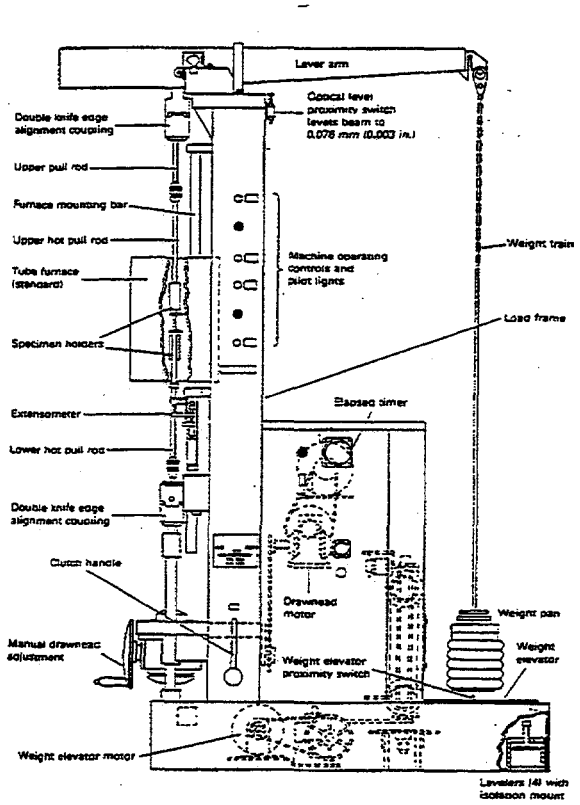

Figure 1 Schematic of the SATEC creep frame.

Results

Creep Test Results

Specimens were tested in argon at 650°C and 900°C at stresses ranging from 90 MPa to 350 MPa with specimens being tested to failure in all cases. Table 1 provides test parameters, elongation and rupture time for each specimen.

Table 1: Creep test parameters and test results

Sample No.	Test No.	Stress (MPa)	Temperature (°C)	Elongation (%)	Rupture Time (h)
#1	1	90	900	36	520
	2	150	900	25	22
#2	3	150	900	10	2
	4	350	650	6	14

Figures 2 and 3 show creep plots of strain vs. time for two test specimens from sample # 1. About 36% strain was observed during creep test No. 1 which failed after 520 h (Figure 2). Creep test no. 2 which lasted 22 h (Figure 3), however, showed 25 % strain before failure. Figures 4 and 5 show the plots of creep strain vs. time for two test specimens from sample # 2. Creep test no. 3 which lasted for about 2 h (Figure 57) showed only 10 % elongation. Creep test no. 4 which lasted for about 14 h showed only 6 % elongation before failure.

Fractography of creep specimens after failure

Scanning electron microscopy (SEM) examination demonstrated necking during creep rupture testing of sample # 1/test # 1 at 900°C, 90 MPa. The necking clearly indicated good ductility for sample # 1. However, SEM examination of sample # 2/test # 1 showed no necking during creep rupture testing at 900°C, 150 MPa, which confirmed the reduced ductility for sample # 2.

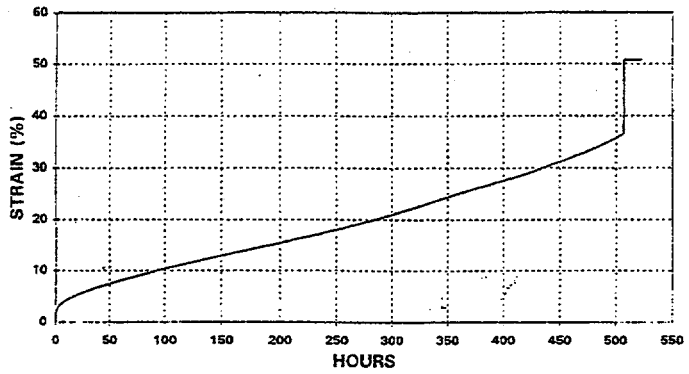

Figure 2 Creep Strain Versus Time in Sample #1 at 900°C and 90 MPa.

Discussion

The creep test performed on sample # 1 at 900°C at 90 MPa indicates a 520 h rupture life with an elongation of 36% before failure (Figure 2). Therefore, good strength and ductility can be obtained in this class of alloys at high temperature. Comparison of the creep rupture results between sample # 1 and sample # 2 indicates that the creep ductility in sample # 2 is much lower than that observed in sample # 1. This may be due to the presence of higher levels of oxygen and nitrogen in sample # 2 which may decrease the ductility of the alloy. Analyses of the powders for the sample materials are given in Table 2.[2]

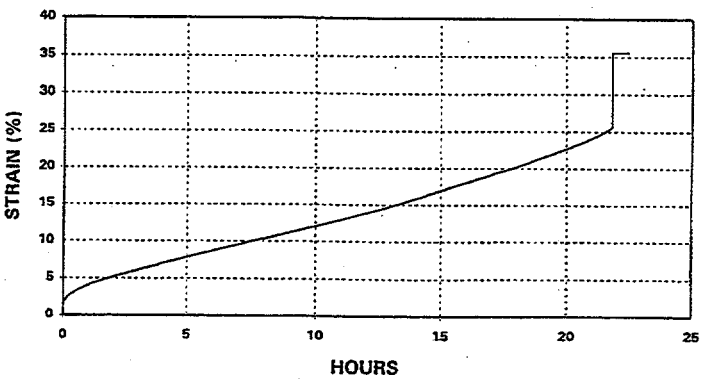

Figure 3 Creep Strain Versus Time in Sample #1 at 900°C and 150 MPa.

Nitrogen additions can cause strengthening due to nitride formation. However, nitrogen should be discouraged due to long lived radioactive isotope production. Our results indicate that nitrogen additions decrease the time to rupture and ductility. Therefore minimum levels of nitrogen are recommended.

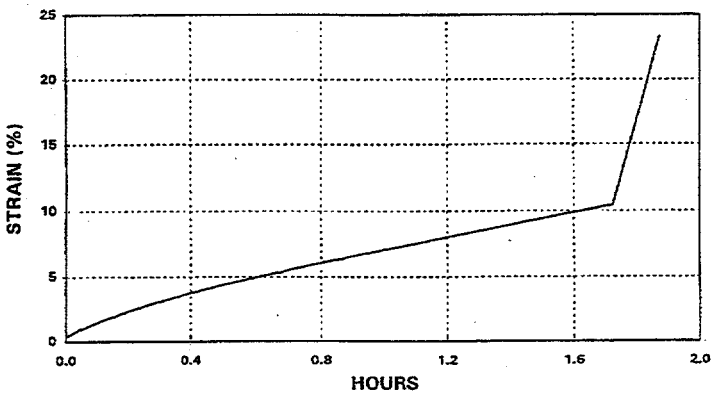

Figure 4 Creep Strain Versus Time in Sample #2 at 900°C and 150 MPa.

The merit of the new low activation ODS alloy can be demonstrated using a Larson-Miller plot. Figure 6, a Larson-Miller plot of stress rupture data plotting rupture stress as a function of temperature and time to rupture shows a summary of creep rupture values of the present ODS alloy (sample # 1 and sample # 2), MA 957,[3] MA 956,[4] two similar ODS steels developed in Japan by Asabe[5] and Ukai,[6] a Belgian ODS steel,[7] and HT-9

Table 2. Interstitial element analysis (in wt%) of the powders before consolidation.

Sample No.	Condition	Carbon	Oxygen	Nitrogen
#1	10h SPEX milled	0.055	0.84	0.281
#2	50h attritor + 10h SPEX milled	0.070	1.24	0.404
#3	25h attritor milled	0.084	1.33	0.078

martensitic steel.[8] From this it can be seen that despite limited data, the new low activation alloy compares favorably with similar ODS ferritic alloys MA956 and MA957, which are far superior to martensitic steels.

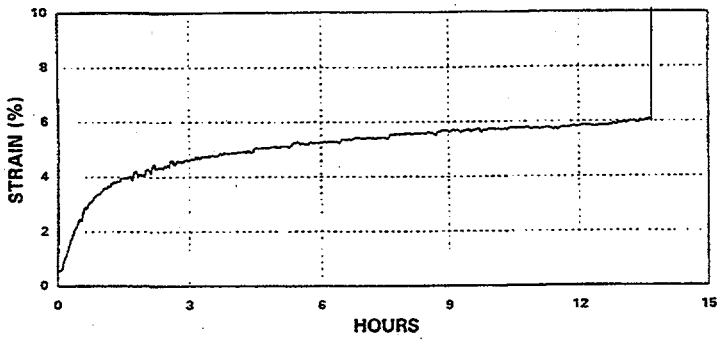

Figure 5 Creep Strain Versus Time in Sample #2 at 650°C and 350 MPa.

The plot indicates a higher stress rupture value of sample # 1 than that of sample # 2 and that may be due to the higher interstitial content in sample # 2. The creep resistance of both MA956 and MA957 were lower than that of sample # 1 and sample # 2. The Larson-Miller plot also indicates that the creep resistance of martensitic steel is much lower than that of sample # 1 and sample # 2. The very fine and uniform dispersion is mainly responsible for the superior creep resistance of the present ODS alloy.

CONCLUSIONS

An optimized low activation grade ODS ferritic steel of composition (Fe-13.5Cr-2W-0.5Ti-0.25Y_2O_3) has been tested in uniaxial creep in order to provide comparison with similar composition. Results of tests at 900°C demonstrate that this alloy has creep properties similar other alloys of similar design and can be considered for use in high temperature fusion power system designs.

FUTURE WORK

This work is completed.

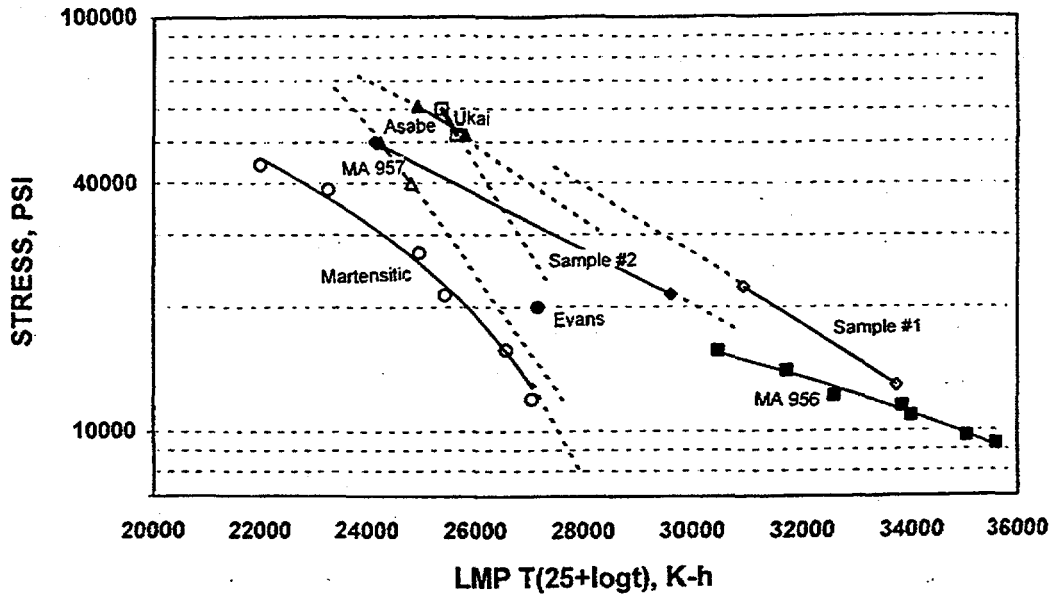

Figure 6 Larson-Miller Plot Comparing the Creep Strength of the new ODS Ferritic Steel with those of Similar Steels.

ACKNOWLEDGEMENTS

One of the authors, D.K. Mukhopadhyay, would like to acknowledge the financial support of a Pacific Northwest National Laboratory Research fellowship. DJ Chriswell assisted with the set up and operation of the creep machine.

REFERENCES

1. D. K. Mukhopadhyay, C. Suryanarayana, F. H. Froes and D. S. Gelles, DOE/ER-0313/19, (1996) 142.
2. D. K. Mukhopadhyay, Development of Low Activation Oxide Dispersion Strengthened Ferritic Steels for Fusion Reactors, doctoral dissertation, College of Graduate Studies, University of Idaho, July 1996.
3. J.J. Fisher, U.S. Patent, 4,075,010 (February 21,1978).
4. Engineering Data Sheet of INCOLOY alloy MA 956 published by International Nickel Co., WV, USA.
5. K. Asabe, M. Nakanishi and S. Tanoue: The Sumitomo Search, No. 45, March 1991, p. 65.
6. S. Ukai, M. Harada, H. Okada, M. Inoue, S. Nomura, S. Shikakura, K. Asabe, T. Nishida and M. Fujiwara: J. Nucl. Mater., 204, 1993, p. 65.
7. R.W. Evans, J. Preston, B. Wilshire and E.A. Little: J. Nucl. Mater., 195, 1992, p. 24.
8. J. L. Straalsund and D.S. Gelles, presentation at the Topical Conference on Ferritic Alloys for Use in Nuclear Energy Technologies, Snowbird, Utah June 1983, HEDL-SA-2771 FP.

FRACTURE TOUGHNESS OF THE IEA HEAT OF F82H FERRITIC/MARTENSITIC STAINLESS STEEL AS A FUNCTION OF LOADING MODE - Huaxin Li, D. S. Gelles (Pacific Northwest Laboratories)[a] J. P. Hirth (Washington State University--Pullman) and R. H. Jones (Pacific Northwest Laboratories)[a]

OBJECTIVE

The purpose of this research is to compare mixed mode fracture toughness response on the IEA heat of F82H with previous measurements on a small heat given a different heat treatment.

SUMMARY

Mode I and mixed-mode I/III fracture toughness tests were performed for the IEA heat of the reduced activation ferritic/martensitic stainless steel F82H at ambient temperature in order to provide comparison with previous measurements on a small heat given a different heat treatment. The results showed that heat to heat variations and heat treatment had negligible consequences on Mode I fracture toughness, but behavior during mixed-mode testing showed unexpected instabilities.

PROGRESS AND STATUS

Introduction

We have reported previously on mode I, mode III and mixed-mode I/III fracture toughness for heat #8033 from Nippon Kokkan Corporation (NKK).[1-3] That work was based on material given a laboratory heat treatment optimized for strength and designed for martensitic steels that were not given progressive hot deformation treatments [1000°C/20h/AC + 1100°C/7min/AC + 700°C/2h/AC]. Therefore, the results obtained did not apply directly to the large IEA heats of F82H made available for international testing.[4,5] The present effort is intended to extent these earlier results by duplicating the mode I and mixed-mode tests to the IEA heat in the standard as-received heat treatment conditions [1040°C/40min/AC + 750°C/1h/AC].

Experimental Procedures

Specimens were prepared from 15 mm plate of F82H received directly from Dr. A. Hishinuma of JAERI. This plate was from lot 1, heat 9741, plate RB802-3-14. Details for this material have been published previously.[4,6] Only specimen crack angles of 0° (mode I) and 35° (mixed-mode I/III) were used, and the heat treatment condition was as-received. Specimens were 12.7 mm thick and therefore, specimens for this study were almost the thickness of those from heat #8033 which were 14 mm thick. Both specimen geometries meet the plane strain condition as specified in ASTM E399. Specimen testing followed standard procedures.[1]

Results

Two tests were performed on the IEA F82H heat in mode I (crack angle 0°) and two tests were

---

[a]Operated for the U.S. Department of Energy by Battelle Memorial Institute under Contract DE-AC06-76RLO 1830.

performed in mixed mode I/III (crack angle 35°), all at room temperature. The results of the mode I test are provided in Table 1, with the value obtained for the small heat tested previously provided for comparison. Tests in mixed mode produced unstable crack propagation, making measurements of fracture toughness and tearing modulus impossible. Comparison of the results in Table 1 between the IEA heat and the small NKK heat shows that both materials behave similarly, with values from the small heat intermediate between the measurements made on the large heat both for fracture toughness and tearing modulus. This is shown more clearly in Figure 1 which provides data for mode I and mixed mode I/III toughness as a function of crack angle.

Table 1. Results of fracture toughness and tearing modulus for Mode I specimens of the IEA heat of F82H.

Specimen ID	J (KJ/m^2)	T ($KJ/m^2/mm$)
IEA-1	273	264
IEA-2	328	248
Heat 8033	284	263

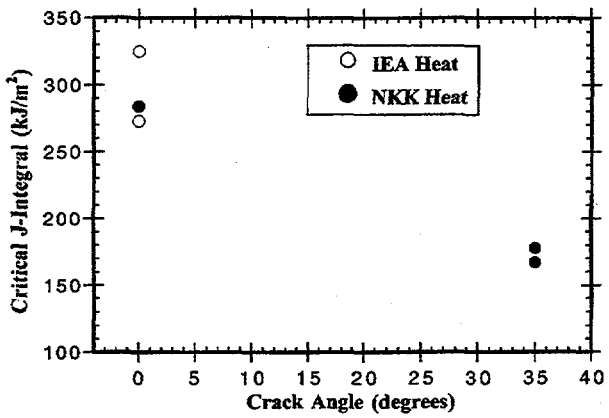

Figure 1 Fracture toughness for F82H as a function of crack angle

The cause of unstable crack propagation during mixed-mode testing is not yet understood. A test trace is shown in Figure 2 for specimen IEA-9, and reveals that testing proceeded normally until after the 28th compliance unloading step, needed to quantify crack propagation, when the crack advanced suddenly to failure.

Fractographic examinations revealed the expected dimple rupture response in specimen IEA-2 tested in mode I, but unexpected response in specimen IEA-8, tested in mixed mode. This unexpected response was in two forms. Areas of the fracture surface were found to have failed by brittle transgranular cleavage, and, in large dimples created on other parts of the fracture surface, features as large as several microns could be identified. Examples are provided in Figures 3 through 5. Figure 3 shows the area of the specimen adjacent to the fatigue crack at low magnification, with the fatigue crack at the bottom, a region adjacent that failed by dimple rupture, and the upper region which failed by cleavage fracture. The cleavage fracture response is shown in greater detail in Figure 4. Figure 5 provides an example of large features found in a large dimple that can be expected to have been the

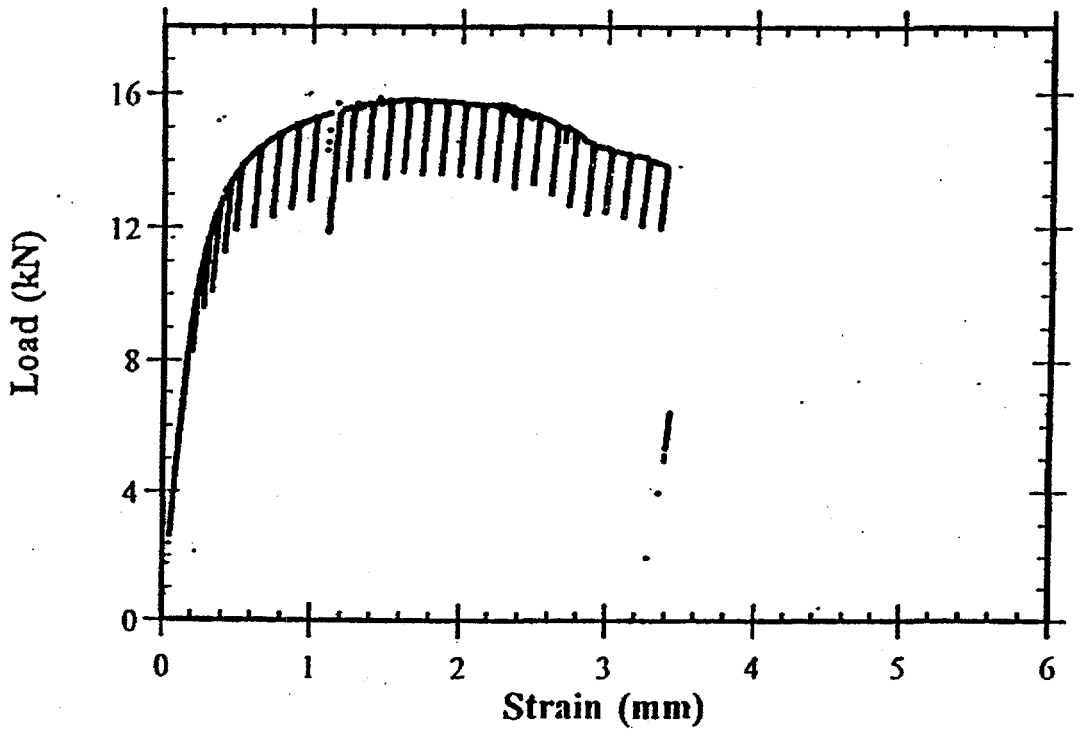

Figure 2 Test trace for mixed-mode specimen IEA-9.

cause of cavitation.

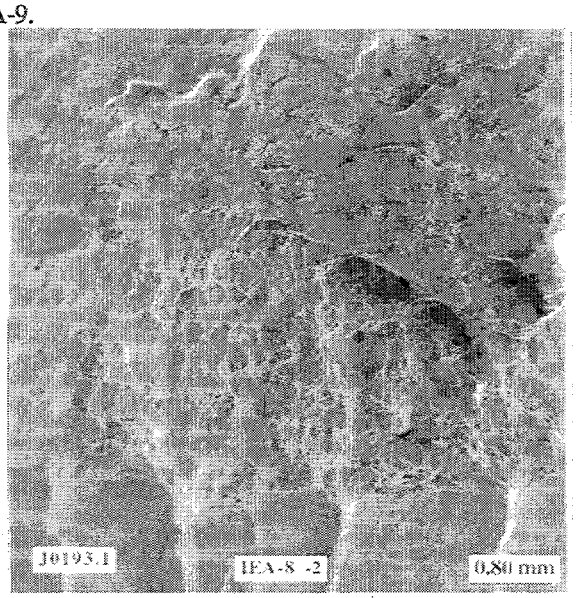

Figure 3 Fracture Surface of Specimen IEA-8 Showing the Fatigue Surface at the Bottom.

Discussion

Tests to determine mixed-mode I/III fracture toughness of the IEA heat of F82H have provided unexpected response. Mixed-mode tests on the small NKK heat of F82H had given stable cracking response, whereas tests on the large heat did not. Also, brittle fracture appearance was very different for the two heats. The IEA heat is found to fail during mixed mode testing by transgranular cleavage at room temperature. It had been shown in the laboratory heat that mixed-mode (Heat 8033) response at low temperature (-90°C) produced an intergranular brittle fracture appearance which differed from that of mode I behavior, which was transgranular.[3] It was assumed from that work that the brittle response for mixed-mode I/III testing would always develop a tendency for intergranular failure. Therefore, both the unstable cracking and transgranular cleavage during unstable crack propagation were unexpected.

The cause of this unexpected response is not yet understood. The possibility of flawed material or incorrect heat treatment can be discounted because mode I testing was successful, providing similar

results for both heats of material. Also, the observation of crack nucleation sites that were larger than expected in the IEA heat of F82H is in agreement with material characterization studies from Europe which showed that inhomogeneities were limited and generally ≤ 10 μm, but with some complex oxides of Al, Ta, Ti and/or Zr as large as 60 μm.[7]

CONCLUSION

The effect of heat-to-heat and heat treatment variations has been studied by performing critical J integral tests in mode I (J_{IC}), and in mixed-mode I/III (J_{MC}) at ambient temperature, for the IEA heat of the reduced activation ferritic/martensitic stainless steel F82H in a standard heat treatment, and by comparing with previous measurements on a small heat given a different heat treatment. The results showed that heat-to-heat variations and heat treatment had negligible consequences on mode I behavior, but behavior during mixed-mode testing showed unexpected instabilities.

FUTURE WORK

This work will be continued within the limits of available funding.

ACKNOWLEDGEMENTS

The material was supplied by Dr. A. Hishinuma of JAERI whose help is gratefully acknowledged. This research was supported by the Office of Fusion Energy of the U. S. Department of Energy under Contract DE-AC06-76RLO 1830 with Battelle Memorial Institute.

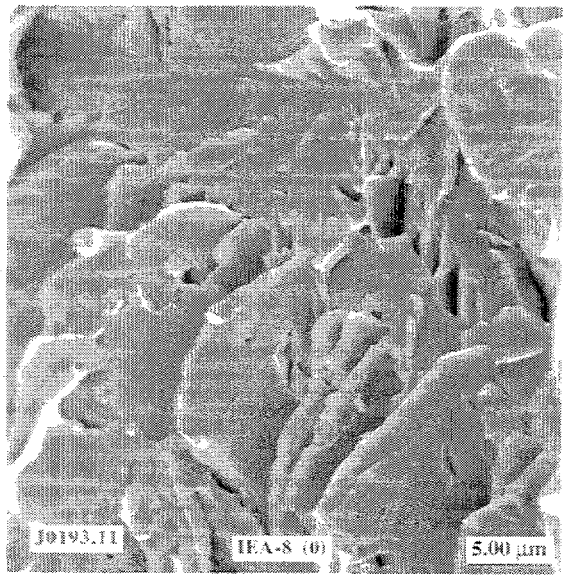

Figure 4 Example of Intergranular Brittle Cleavage in Specimen IEA-8.

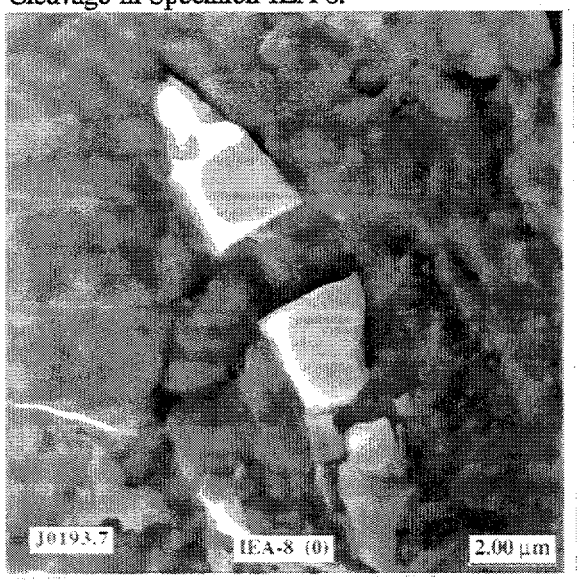

Figure 5 Example of Particles in a Large Dimple that were Possible Responsible for Cavitation.

REFERENCES

1. Huaxin Li, R. H. Jones, J. P. Hirth, and D. S. Gelles, DOE/ER-0313/14, 165.

2. Huaxin Li, R. H. Jones, J. P. Hirth, and D. S. Gelles, DOE/ER-0313/15, 134.

3. Huaxin Li, R. H. Jones, P. J. Hirth and D. S. Gelles, DOE/ER-0313/17, 99.

4. A. Hishinuma in Proceedings of the IEA Working Group Meeting on Ferritic/Martensitic Steels held June 24, 1994 in Sun Valley, ID. ORNL/M-3777

5. Y. Takagi and A. Hishinuma in Proceedings of the IEA Working Group Meeting on

Ferritic/Martensitic Steels held February 1, 1995 in Oak Ridge, TN. ORNL/M-4230

6. K. Shiba in Proceedings of the IEA Working Group Meeting on Ferritic/Martensitic Steels held September 19-20, 1995 in Baden, Switzerland, ORNL/M-4939.

7. R. Lindau in Proceedings of the IEA Working Group Meeting on Ferritic/Martensitic Steels held September 19-20, 1995 in Baden, Switzerland, ORNL/M-4939.

SUMMARY OF THE IEA WORKSHOP/WORKING GROUP MEETING ON FERRITIC/MARTENSITIC STEELS FOR FUSION

– R. L. Klueh **(Oak Ridge National Laboratory)**

OBJECTIVE

The objective of this report is to describe the working group meeting and workshop held to review planned and completed work that is being undertaken to prove the feasibility of using ferritic/martensitic steels for fusion applications.

SUMMARY

An International Energy Agency (IEA) Working Group on Ferritic/Martensitic Steels for Fusion Applications, consisting of researchers from Japan, the European Union, the United States, and Switzerland, met at the headquarters of the Joint European Torus (JET), Culham, United Kingdom, 24-25 October 1996. At the meeting, preliminary data generated on the large heats of steel purchased for the IEA program and on other heats of steels were presented and discussed. The second purpose of the meeting was to continue planning and coordinating the collaborative test program in progress on reduced-activation ferritic/martensitic steels. The next meeting will be held in conjunction with the International Conference on Fusion Reactor Materials (ICFRM-8) in Sendai, Japan, 23-31 October 1997.

PROGRESS AND STATUS

Introduction

The IEA Working Group on Ferritic/Martensitic Steels for Fusion under the auspices of the IEA Executive Committee for the Implementing Agreement on Fusion Materials met at JET Headquarters, Culham, UK, 24-25 October 1996. Researchers from Japan (3), the European Union (4), the United States (3), and Switzerland (1) participated. Russian Federation participation was invited, but no one from there attended the meeting. The objective of the Working Group is the establishment and coordination of an international collaborative test program to determine the feasibility of using ferritic/ martensitic steels for fusion.

This was the sixth meeting of the Working Group, which was formed as a result of a workshop on ferritic/martensitic steels in Tokyo in October 1992. At the first meeting following the Tokyo workshop, the Working Group developed specifications for large heats of reduced-activation steels and outlined a collaborative research program. Two 5-ton heats of the IEA-modified F82H steel and two 1-ton heats of JLF-1 steel were produced, fabricated into plates, and distributed to the participants of the collaboration. Subsequent meetings were used to plan a test program and to coordinate the acquisition of the data needed to prove feasibility for the steels for fusion.

The Culham meeting was a follow up to the meeting at Baden, Switzerland, 19-20 September 1995, at which the first data on the new large heats were presented; the Culham meeting was planned to expand on the review of data on the new heats, since the amount of data generated was expected to increase during the following year. The meeting was also set to review the status and future direction of the programs in Japan, Europe, and the United States in a continuing effort to coordinate the collaborative program.

Research and Development Activities

The first day of the Culham meeting consisted of a workshop on research results obtained on the large IEA heats of F82H and JLF-1 and research results on other ferritic/martensitic steels that have an impact on the objective of the Working Group. A range of properties have been examined for the large modified IEA heats of F82H and JLF-1 reduced-activation martensitic steels. These presentations are discussed in the first section below, followed by a section summarizing the work on other reduced-activation steels and non-reduced-activation steels. A report that includes copies of handouts of viewgraphs used for the presentations is available [1].

Experimental Work on IEA Heats

K. Ehrlich reviewed the studies of nine institutes throughout Europe that had combined to evaluate the homogeneity of chemical composition and mechanical properties of the plates from the IEA F82H heat. The plates are homogeneous, with little variation in grain size, hardness, and tensile properties through the thickness of the 7.5-and 15-mm plates produced from the large heat (the 15-mm plate is slightly stronger than the 7.5-mm plate). Heat treatment characteristics were determined for the steels in an effort to ascertain how optimum properties can be developed. Included in these studies were determinations of austenitization and tempering behavior, and a continuous cooling transformation diagram was determined. The properties of the IEA F82H steel was compared with other reduced-activation steels and the MANET conventional Cr-Mo steel. The IEA modified F82H heat had better Charpy properties than the MANET, but creep-rupture strength and the yield and tensile strength below 500°C of the IEA F82H were slightly less than those for the MANET. The ductility of the IEA F82H exceeded that for the MANET.

K. Shiba reported on the range of mechanical and physical properties planned and being carried out on the modified IEA F82H heat by JAERI. The planned mechanical properties test matrix includes tensile, creep, Charpy impact, fracture toughness (K_{1c} and J_{1c}), fatigue, and hardness tests. These properties are being determined on the as-heat treated base metal and on weldments; tensile, Charpy impact, and fracture toughness data are also being determined on thermally aged base metal and weldments. The following physical properties are also to be determined: density, specific heat, thermal conductivity, thermal expansion, electrical conductivity, melting point, Young's modulus, Poisson's ratio, and magnetic hysteresis. Much of this characterization work has already been accomplished [1].

Other JAERI studies on the modified F82H were presented by A. Hishinuma. These included studies on the effect of tantalum and titanium on grain size and Charpy impact behavior. There were also studies on radiochemical analysis of impurities in the steel, vacuum properties (gas desorption), and corrosion behavior in high-temperature water. The corrosion tests were at 250 and 280°C and showed the effect of dissolved oxygen on the behavior.

D. S. Gelles reported on mixed-mode fracture toughness of the modified IEA F82H and compared the results with previous results reported in Baden on a small heat of F82H with a different heat treatment. The previous results indicated that there was an effect of crack angle, and the toughness in the mixed mode is less than for either Mode I or Mode III. The IEA heat gave similar results for Mode I fracture toughness tests, but there were differences for mixed-mode I/III for the two materials. Tests are continuing to determine the cause of the differences.

P. Spatig reported on a program to study the effect of helium on the properties of the IEA F82H. To determine hardening effects, helium is to be injected into tensile specimens in either the PIREX facility in Switzerland or the duel-ion beam in Karlsruhe. For comparison, pre-injected specimens will be irradiated in the Studvik reactor in Sweden. Specimens irradiated in PIREX have been tested, and specimens are presently being irradiated in the Studvik reactor. Spatig also discussed studies under way to determine activation volumes for irradiated specimens using stress relaxation tests.

A. Kohyama reported on the extensive studies of the large heats of the JLF-1 steel. Just as is the case for the F82H, Monbusho researchers have conducted a range of microstructural and mechanical properties studies on the base metal and on TIG and EB weldments. Tensile, Charpy impact, and creep tests were conducted.

In general, the results of these tests indicate that the new IEA heats have properties comparable or better than those of the commercial steels they would replace.

Experimental Work on Other Heats of Steel

Several reports concerned information gathered on irradiated properties of other heats of reduced-activation and conventional steels, including F82H and JLF-1 heats other than the large IEA heats.

A. Kohyama summarized studies of Cr-W-V steels containing 2.25-12% Cr (including JLF-1 and F82H) irradiated in FFTF/MOTA. Tensile, Charpy, irradiation creep, and microstructural studies were conducted at 370-600°C and up to 60 dpa. One interesting observation was that hardening, as measured in a tensile test, appears to go through a maximum with dose, which was also reflected in the shift in the transition temperature of the Charpy tests.

D. S. Gelles reported Charpy impact data for PNNL reduced-activation steels containing 2-12% Cr and different levels of manganese irradiated to 10 and 30 dpa in FFTF/MOTA at ≈370°C. There was no change in properties between 10 and 30 dpa. Manganese additions in the 9-12% Cr steels caused a change from cleavage to intergranular fracture. It was concluded that the 7-9Cr steels show the most promise.

K. Shiba reported on the tensile and fracture toughness properties of a heat of F82H irradiated in HFIR over the range 200-500°C. Experiments to asses helium effects using boron doping were also reported. Different levels of ^{10}B were added to F82H, and the steels were irradiated in the JMTR to 0.05-0.6 dpa at 400 and 550°C. No effect of helium was observed on tensile properties, but there appeared to be a slight effect on the Charpy behavior.

A. Kohyama reported on work by Kimura, Morimura, and Matsui of Tohuku University on the effect of helium implantation on the DBTT of a 9Cr-2WVTaB steel. TEM disks were implanted with 120 appm He in a cyclotron at 36 MeV at ≈220°C to 0.048 dpa. A small punch test was used to estimate an increase in yield stress of ≈104 MPa and a shift in the DBTT of ≈50°C. The changes were attributed to the possibility of enhanced hardening by helium.

M. G. Horsten reported on irradiation studies of tensile and fracture toughness measurements of modified 9Cr-1Mo and Sandvik HT9 irradiated at ≈80 and 300°C in the High Flux Reactor (HFR) at Petten. Tensile tests from room temperature to 600°C showed that the high-temperature damage (300°C irradiation) was more stable than low-temperature damage (80°C irradiation). The toughness of the modified 9Cr-1Mo was superior to that of HT9.

R. L. Klueh reported on the tensile and Charpy impact properties of the ORNL reduced-activation steels with 2.25-12% Cr irradiated in FFTF/MOTA to 27-29 dpa. The 9Cr-2WVTa steel continued to show excellent impact properties. The shift in transition temperature was only 32°C after ≈28 dpa, although there appeared to be a slight increase in the shift with increasing fluence. However, even after the 32°C shift, the DBTT after irradiation was lower than the DBTT of modified 9Cr-1MoVNb or Sandvik HT9 before irradiation (these steels showed shifts of ≈45 and 160°C, respectively, for these irradiation conditions).

K. Ehrlich presented the latest Charpy impact data from a continuing irradiation experiment in HFR, in which the conventional steels MANET I and II and the reduced-activation steels OPTIFER Ia and II, F82H, and ORNL 9Cr-2WVTa are being irradiated. Data obtained after irradiation to 2.5 dpa at 300°C were reported; previously, data were reported to 0.8 dpa. The reduced-activation steels again performed better than the MANET steels, and the 9Cr-2WVTa steel again showed the smallest change in Charpy properties.

Fracture Assessment

An integrated approach to assessing fracture-safe margins of fusion power plant structures was presented by G. R. Odette. The types of data on irradiated and unirradiated specimens required to apply the methodology were outlined, and examples of the application of the technique were described. This approach has been formalized in a paper, copies of which were distributed to participants at the meeting.

Collaboration: Planning and Status

On the second day of the meeting, the status and future direction of the programs in Europe, Japan, and the United States were reviewed by W. Dietz, A. Hishinuma, A. Kohyama, and R. L. Klueh, in a continuing effort to coordinate the collaborative program [1].

A major question concerning the use of ferritic/martensitic steels for fusion has concerned the interaction of a ferromagnetic structural material with the magnetic fields of a fusion power plant and how the ferromagnetic material will affect plasma control. Up until now, this question has been addressed by design studies. In his discussion of the JAERI program, A. Hishinuma presented information on JAERI plans for an experimental study of this problem. JAERI will produce a simulated ferritic steel vacuum vessel by covering the inner surface of the vacuum vessel of their JFT-2M with F82H. Using this vessel, they hope to measure the effects of the ferromagnetic material on the operation of the machine. They also have plans for simulating a ferritic steel blanket module. Diagrams of the JFT-2M vessel with the proposed F82H modifications are shown in the attachment.

During the discussion of the proposed JAERI program, it was recognized by the Working Group that a timely assessment of the effect of a ferritic steel blanket structure on the ability to control a plasma is of utmost importance in verifying the feasibility of using ferritic steels for fusion. The program will also provide invaluable information on the development of large-scale fabrication technology of martensitic steels, because the project will require studies on the production of large heats of steel and the welding and joining of large structures. The Working Group and the fusion community will look forward to seeing the results of the JAERI study, because of the important contribution it will make toward our understanding of the martensitic steels for fusion applications.

Areas requiring coordination by the Working Group in the future were discussed. These include work on corrosion and hydrogen embrittlement and on creep-fatigue studies being carried out in the different programs. Action items were recommended on these subjects. In the near future, the Japanese and the European Union programs intend to purchase new large heats for component studies, and they intend to coordinate the specification effort for these heats. The need for a compilation of the data being obtained on the new heats of steels was considered. A data base for F82H already exists at JAERI, and an action item was proposed for investigating the use of this data base by fusion programs throughout the world.

Next Meeting

The next meeting was tentatively set for 3-4 November 1997 in Japan in conjunction with ICFRM-8 (23-31 October 1997). The Japanese delegation suggested that the meeting be held near the site of a Japanese steel plant, so that a tour of the facility could be made, thus providing an opportunity for the group to become informed on the technology of steelmaking to be used to produce ferritic/ martensitic steels for fusion applications.

References

[1] R. L. Klueh, Proceedings of the IEA Working Group Meeting on Ferritic/Martensitic Steels, ORNL/M-5674.

FURTHER CHARPY IMPACT TEST RESULTS OF LOW ACTIVATION FERRITIC ALLOYS, IRRADIATED AT 430°C TO 67 DPA - L. E. Schubert, M. L. Hamilton, and D. S. Gelles (Pacific Northwest National Laboratory)[a]

OBJECTIVE

The objective of this work is to evaluate the effects of neutron irradiation in low activation ferritic alloys, by examining the shift of the ductile to brittle transition temperature (DBTT) and the reduction of the upper shelf energy (USE) in miniature Charpy V-notch (CVN) specimens.

SUMMARY

Miniature CVN specimens of four ferritic alloys, GA3X, F82H, GA4X and HT9, have been impact tested following irradiation at 430°C to 67 dpa. Comparison of the results with those of the previously tested lower dose irradiation condition indicates that the GA3X and F82H alloys, two primary candidate low activation alloys, exhibit virtually identical behavior following irradiation at 430°C to ~67 dpa and at 370°C to ~15 dpa. Very little shift is observed in either DBTT or USE relative to the unirradiated condition. The shifts in DBTT and USE observed in both GA4X and HT9 were smaller after irradiation at 430°C to ~67 dpa than after irradiation at 370°C to ~15 dpa.

PROGRESS AND STATUS

Introduction

Two low activation ferritic steels have been identified for application as structural materials in a fusion reactor. These are F82H and GA3X, in the 7-9Cr range, strengthened by additions of W. This document reports results of CVN impact tests on miniature specimens of these alloys that had been irradiated in-core in the FFTF, in the MOTA 2A and 2B experiments to ~67 dpa at 430°C. Two additional alloys, HT9 and GA4X, were irradiated and tested for comparison. Nominal alloy compositions are 7.8Cr-2W for F82H, 9Cr-2W for GA3X, 11Cr-2W for GA4X, and 12Cr-1Mo-0.5W for HT9. Each alloy also contains 0.2-0.3V. Note that while GA3X was designed to be a 9Cr alloy, and that the current work reports results of tests conducted on a 9Cr heat of GA3X, the results reported in reference 1 were obtained from specimens of an experimental heat obtained from General Atomics which had only 7.5Cr. Previous irradiations were accomplished below core at 370°C to ~15 and ~30 dpa.

Experimental Procedure

Previous reports[1,2,3] on six low activation ferritic alloys described the experimental procedures. The specimens utilized were about one third the size of the ASTM standard CVN specimen.[4] Specimens of two of the alloys (GA3X and HT9) were fatigue precracked before irradiation. The GA4X was expected to exhibit a duplex microstructure; therefore precracking of the specimens of this alloy was not conducted. The F82H specimens were not precracked prior to irradiation. Impact tests were conducted inside a hot cell using a remotely operated vertical drop tower. The fracture energy was calculated from the load versus time record of each impact. The method of calculation and data analysis as well as the details of the system have been described previously.[3,5,6,7]

---

[a]Operated for the U.S. Department of Energy by Battelle Memorial Institute under Contract DE-AC06-76RLO 1830.

Specimen temperature control is described in the references cited and is estimated at an accuracy of ±3°C. This value should be doubled for temperatures below -100°C due to difficulties associated with the very cold equipment.

Results

Tests were conducted on each alloy over a range of temperatures in order to establish full DBTT curves. The data are plotted in Figures 1-4 with the data from control specimens and from the specimens tested after the previous irradiation at 370°C to ~15 dpa. Of these four alloys, the two higher chromium alloys, HT9 and GA4X, exhibited large increases in the DBTT and a significant drop in the USE when compared to the control data, but neither were as severe as was exhibited after irradiation at 370°C. For the two alloys with lower chromium content, the GA3X exhibited the same DBTT as after irradiation at 370°C to ~15 dpa, but a somewhat lower USE. The USE determined for the GA3X at the 15 dpa level was ~20% greater than the control data. The USE determined for the GA3X at the 67 dpa level had decreased ~10% from the 15 dpa USE value, but it was still about 10% above the USE value for the unirradiated control specimens. The results obtained on the F82H specimens were qualitatively the same for both irradiation conditions, but since the previously tested specimens were precracked and the current specimens were only notched, quantitative comparison is not possible. The results of the notch-only specimen tests indicate essentially the same behavior both for the unirradiated control specimens and for the specimens irradiated to 67 dpa.

Discussion

Impact tests have also been performed on other low activation ferritic alloys being studied; a comparison is shown in Figure 5 with data obtained on a similar 9Cr-2WVTa alloy irradiated in the same reactor at ~365°C to ~15 dpa.[8] Note that these data were obtained on notched specimens rather than precracked specimens. The figure shows that while the impact behavior of the alloys was virtually identical in the unirradiated condition, the 9Cr-2WVTa alloy exhibited a DBTT shift of ~30°C (using notched specimens) while the F82H exhibited virtually no shift (using precracked specimens). The major difference between these two alloys is the presence of tantalum in the 9Cr-2WVTa, thus there appears to be reason to speculate that the larger DBTT shift in the 9Cr-2WVTa alloy might result from the presence of the tantalum.

CONCLUSION

Impact tests were performed on four ferritic alloys irradiated at 430°C to ~67 dpa in order to determine behavior in reduced activation alloys. Impact property degradation was no different in the 7-9Cr alloys than had been observed after irradiation at 370°C to ~15 dpa, and was minimal. Degradation in the 11-12Cr alloys was more significant, but less was observed than after irradiation at 370°C to ~15 dpa. The results support the earlier conclusions that the impact behavior of the GA3X and F82H alloys is superior to that of the GA4X and HT9 alloys, that on the basis of the impact data, both the GA3X and F82H alloys appear to warrant further consideration as potential structural materials in fusion reactors, and that chromium content of about 9% appears to be optimum for Fe-Cr-W/V ferritic alloys.

FUTURE WORK

Scanning electron microscopy will be performed on fracture surfaces from the specimens tested in this work to determine the fracture mode.

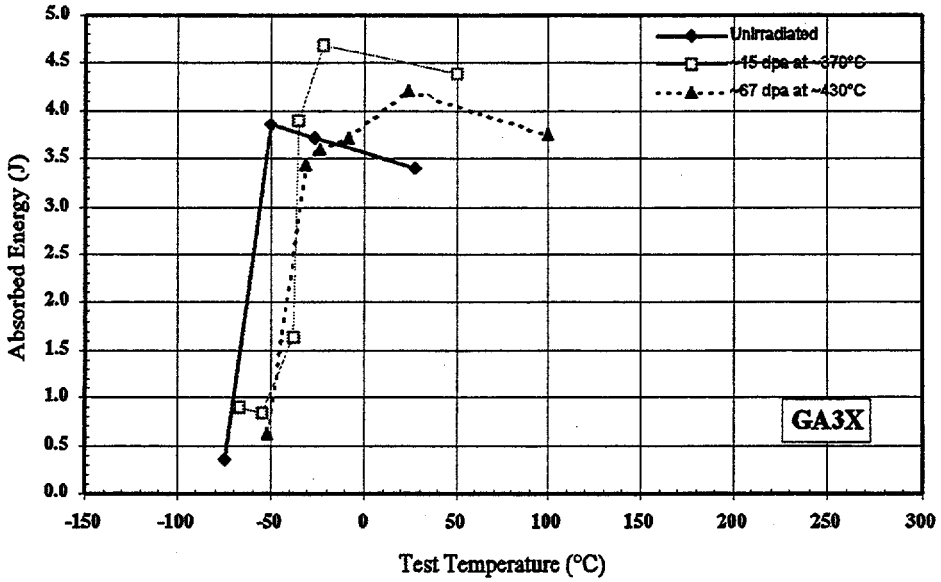

Figure 1. Test results of impact tests of precracked, miniature CVN specimens of alloy GA3X, Fe-0.15C-9.0Cr-2.0W-0.3V.

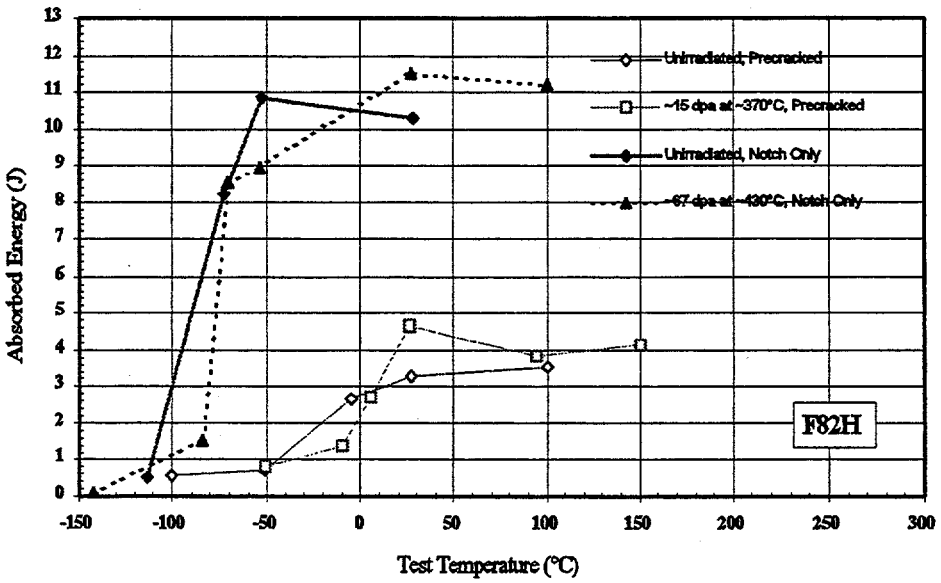

Figure 2. Test results of impact tests of precracked and notch-only, miniature CVN specimens of alloy F82H, Fe-0.10C-7.8Cr-2.0W-0.5Mn-0.2V.

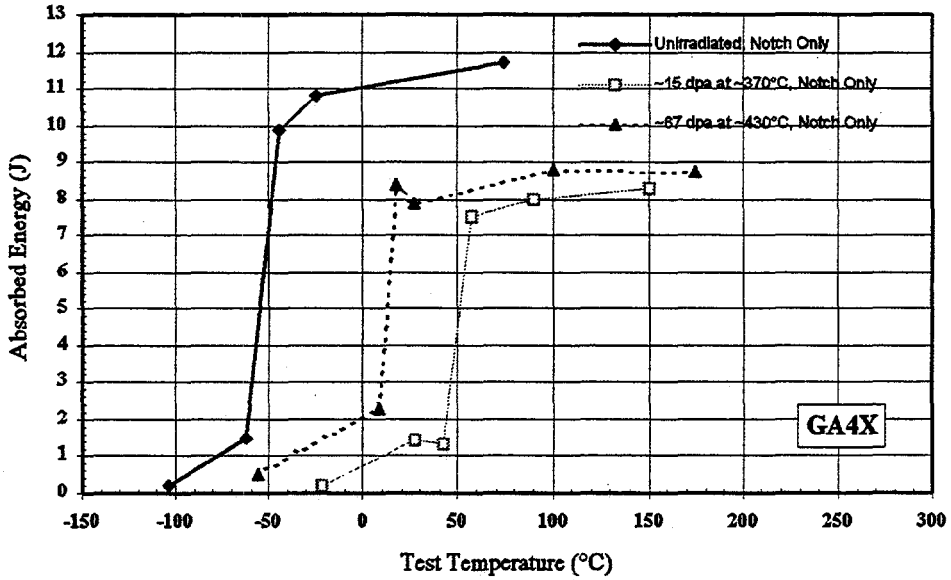

Figure 3. Test results of impact tests of miniature CVN specimens of alloy GA4X, Fe-0.14C-11.0Cr-2.0W-0.3V.

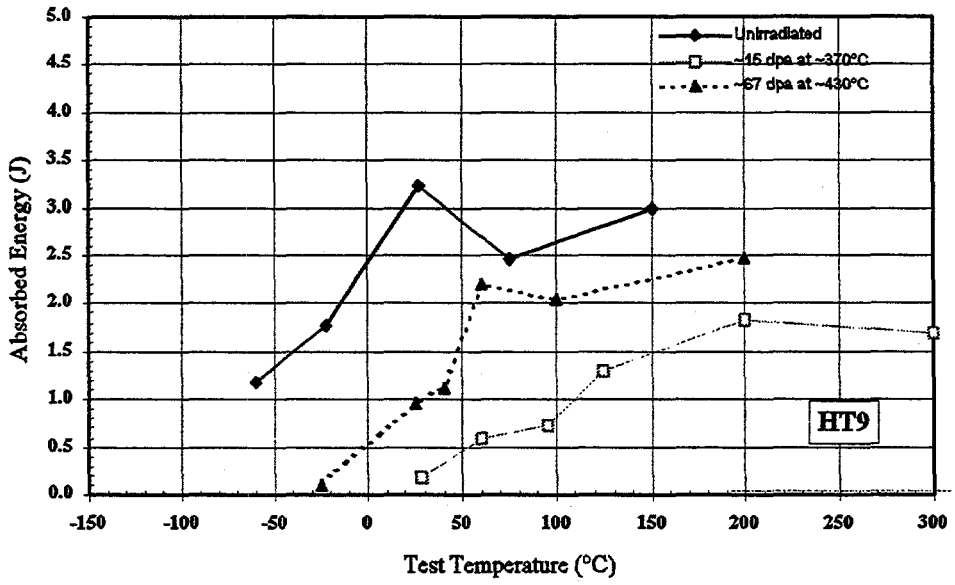

Figure 4. Test results of impact tests of precracked, miniature CVN specimens of alloy HT9, Fe-0.20C-12.1Cr-1.0Mo-0.6Mn-0.5Ni-0.5W-0.3V.

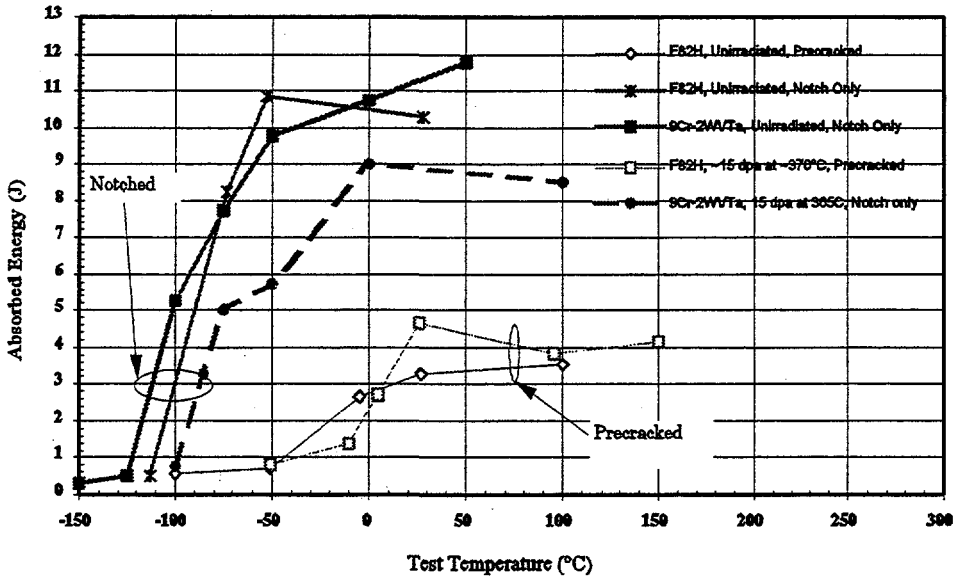

Figure 5. Comparison between impact data from F82H and 9Cr-2WVTa.

REFERENCES

1. L. E. Schubert, M. L. Hamilton, D. S. Gelles, "Charpy Impact Test Results for Low Activation Ferritic Alloys Irradiated to 30 dpa," Fusion Reactor Materials Semiannual Progress Report for the Period Ending December 31, 1995, DOE/ER-0313/19, p. 133.

2. N. S. Cannon, W. L. Hu, and D. S. Gelles, "Charpy Impact Test Results for Low Activation Ferritic Alloys," Fusion Reactor Materials Semiannual Progress Report for the Period Ending March 31, 1987, DOE/ER-0313/2, p. 119.

3. L. E. Schubert, M. L. Hamilton, D. S. Gelles, "Charpy Impact Test Results of Four Low Activation Ferritic Alloys Irradiated at 370°C to 15 dpa," Fusion Reactor Materials Semiannual Progress Report for the Period Ending June 30, 1996, DOE/ER-0313/20, p. 171.

4. "Standard Test Method for Notched Bar Impact Testing of Metallic Materials," Designation: E 23, The American Society for Testing and Materials.

5. W. L. Hu and N. F. Panayotou, "Miniature Charpy Specimen Test Device Development and Impact Test Results for the Ferritic Alloy HT9," Alloy Development for Irradiation Performance Semiannual Progress Report for the Period Ending September 30, 1981, DOE/ER-0045/7, p. 235.

6. L. E. Schubert, "Effects of Specimen Size Reduction on the Transition Curve of the Charpy V-Notch Impact Test," M.Sc. Thesis, Nuclear Engineering, A. S. Kumar--Advisor, UMR, May 1995.

7. W. L. Hu, "Miniature Charpy Impact Test Results for Irradiated Ferritic Alloys," Alloy Development for Irradiation Performance Semiannual Progress Report for the Period Ending September 30, 1982, DOE/ER-0045/9, p. 255.

8. R. L. Klueh and D. J. Alexander, Journal of Nuclear Materials 233-237 (1996) 336-341.

THE EFFECT OF FUSION-RELEVANT HELIUM LEVELS ON THE MECHANICAL PROPERTIES OF ISOTOPICALLY TAILORED FERRITIC ALLOYS - G. L. Hankin (I.P.T.M.E., Loughborough University, England), M. L. Hamilton, D. S. Gelles (Pacific National Northwest Laboratory), and M. B. Toloczko (Washington State University)

OBJECTIVE

The purpose of this work was to determine the influence of helium level on the mechanical properties of a set of isotopically tailored ferritic alloys following irradiation.

SUMMARY

The yield and maximum strengths of an irradiated series of isotopically tailored ferritic alloys were evaluated using the shear punch test. The composition of three of the alloys was Fe-12Cr-1.5Ni. Different balances of nickel isotopes were used in each alloy in order to produce different helium levels. A fourth alloy, which contained no nickel, was also irradiated. The addition of nickel at any isotopic balance to the Fe-12Cr base alloy significantly increased the shear yield and maximum strengths of the alloys, and as expected, the strength of the alloys decreased with increasing irradiation temperature. Helium itself, up to 75 appm over 7 dpa appears to have little effect on the mechanical properties of the alloys.

PROGRESS AND STATUS

Introduction

It is expected that the most significant difference between fission and fusion reactor environments is the high rate of transmutant helium generation resulting from fusion spectra [1]. In the worst case in a high nickel content alloy, the rate for helium generation in a fast reactor is ~0.5 appm He/dpa which compares with an expected level of ~10 appm He/dpa for iron-based alloys proposed for first wall applications in fusion reactors. Many of the previous experiments devised to study the effect of helium levels relevant to fusion reactor materials used complex alloys which had sometimes experienced different neutron irradiation spectra and flux levels in order to simulate the expected conditions. These experiments were not always successful since potential effects of the helium were masked by the more dominant effects of neutron flux and temperature history [2]. Helium production at a rate of 10 appm He/dpa, can be achieved in HFIR by the addition of 1.5% ^{59}Ni [3].

A recent study [4] reported on a simple, one variable experiment which was devised in order to study the effects of different helium levels on the microstructures that evolved in a set of isotopically tailored ferritic alloys, nominally of composition Fe-12Cr-1.5Ni. The rate of helium evolution was varied from 0.3 to 10.7 appm/dpa without changing the neutron spectrum or the atomic displacement rate, by varying the isotopic content of the nickel. The same composition and initial microstructure was maintained for the nickel containing alloys. The first Fe-12Cr-1.5Ni variant contained the ^{59}Ni isotope which undergoes an (n,a) reaction to form helium. This idea had been tested and proven in a previous series of FFTF irradiations on Fe-Cr-Ni austenitic alloys [5]. The second alloy contained ^{60}Ni which produces very little helium (~2 appm He after 7 dpa) and the third alloy contained natural nickel which produces an intermediate level of helium after the delayed development of ^{59}Ni. The fourth alloy, which was included to clarify the role of nickel on the properties of these alloys, contained no nickel.

This paper reports on the shear punch testing of the same set of alloys. Of particular interest are the trends in some of the mechanical properties of the ferritic alloys as a function of helium content.

Experimental Procedure

Specimens were irradiated side-by-side in the HFIR-MFE-JP23 experiment at four different temperatures to ~7 dpa. Based on results from previous irradiation experiments, it is expected that sufficient dose to initiate void swelling in ferritic/martensitic alloys would have been experienced by this point [4].

The shear punch test is essentially a blanking operation which is common to sheet metal forming. A 1 mm diameter punch is driven at a constant rate of 0.127 mm/min. (0.005 in./min.) through a TEM-sized disk (nominally 0.25 mm thick and 2.8 mm in diameter). The load on the punch is measured as a function of punch travel, which is taken to be equivalent to the cross head displacement [6]. This assumes that the test machine and punch are completely stiff relative to the response of the test specimen. A plot of punch load versus punch displacement was obtained for each specimen.

With the exception of one set of irradiated aluminium alloys [8], shear punch testing has thus far only been carried out on unirradiated materials. A new test facility was set up and a detailed procedure was written to accommodate the shear punch testing of highly irradiated specimens. All tests were conducted under ambient conditions and the results of each test were recorded by computer and simultaneously recorded on a chart recorder.

The curve obtained from a shear punch test is of a similar form to that obtained from a tensile test. Initially a linear relationship exists between load and punch displacement during which no plastic deformation occurs. This is followed by a deviation from linearity or yield point when permanent penetration of the punch into the specimen occurs. Beyond the yield point, further deformation forms a shear process zone between the die and punch. Work hardening compensates for thinning until a maximum load is achieved [6]. The points of interest on the curve were the yield load and maximum load. Effective shear yield strength (τ_{sy}) and an effective maximum shear strength (τ_{sm}) can be evaluated from these values, respectively, by the following equation [7]:

$$\tau_{sy,sm} = P/(2\pi rt)$$

where P is the appropriate load, r is the average of bore and punch radii and t is the specimen thickness. Previous work has shown that an empirical relationship can be developed between data from shear punch testing and that from tensile testing [7,8,9]. In this instance, however, no tensile data were available and the shear punch test was used only as a tool to identify trends in the mechanical properties that might occur as a result of differing helium levels.

Results

Two tests per specimen condition were performed with good reproducibility in the data: effective shear strength typically varied by no more than 30 MPa between duplicate specimens. Figure 1 shows a summary of τ_{sy} as a function of helium content. Figure 2 shows a similar plot for τ_{sm}. Data from the unirradiated material is included in Figures 1 and 2 with the corresponding data from the irradiated material.

It is evident from the plots of τ_{sy} and τ_{sm} that the addition of nickel to the Fe-12Cr base alloy significantly increases the strength of both the unirradiated and the irradiated alloys, especially for irradiation temperatures of 300 and 400°C. The yield and maximum shear strengths are increased by ~100% for the unirradiated condition, a result which is independent of the nickel isotope balance used.

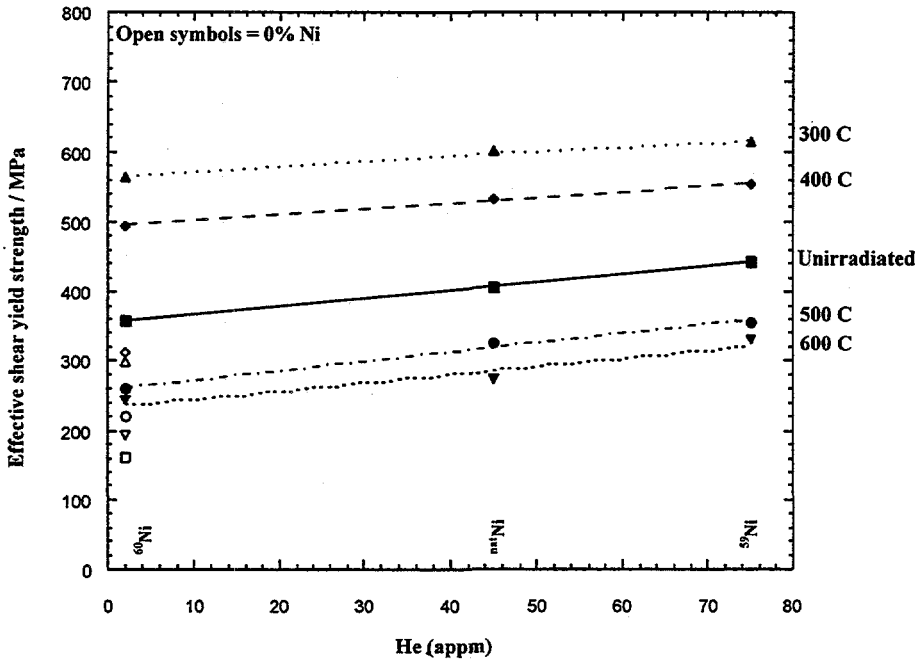

Figure 1 - Effective shear yield strengths (τ_{sy}) in Fe-12Cr-1.5Ni as a function of helium content (an open symbol signifies the control alloy [Fe-12Cr] at the same condition as the corresponding filled symbol).

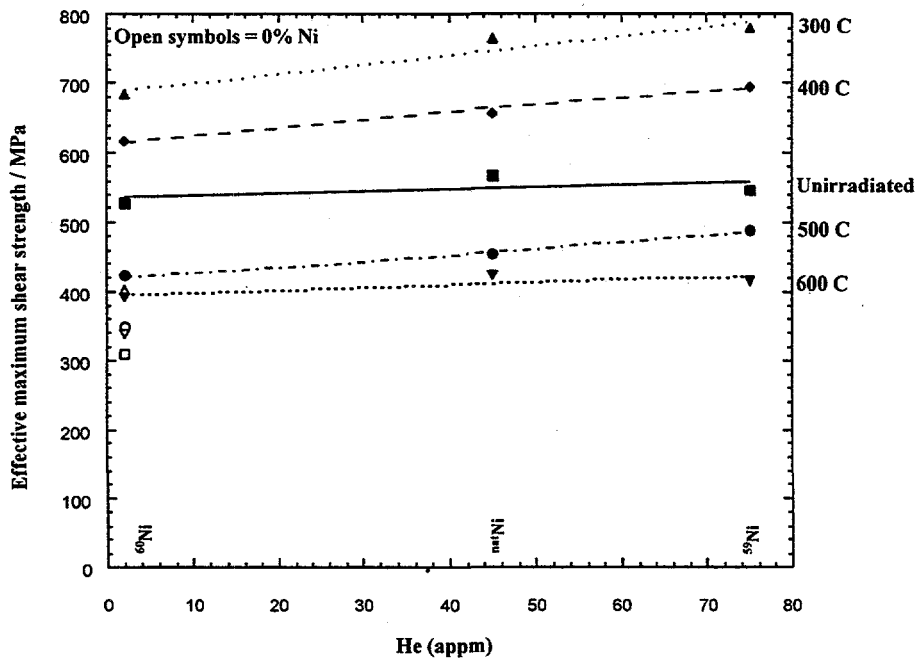

Figure 2 - Effective maximum shear strengths (τ_{sm}) in Fe-12Cr-1.5Ni as a function of helium content (an open symbol signifies the control alloy [Fe-12Cr] at the same condition as the corresponding full symbol).

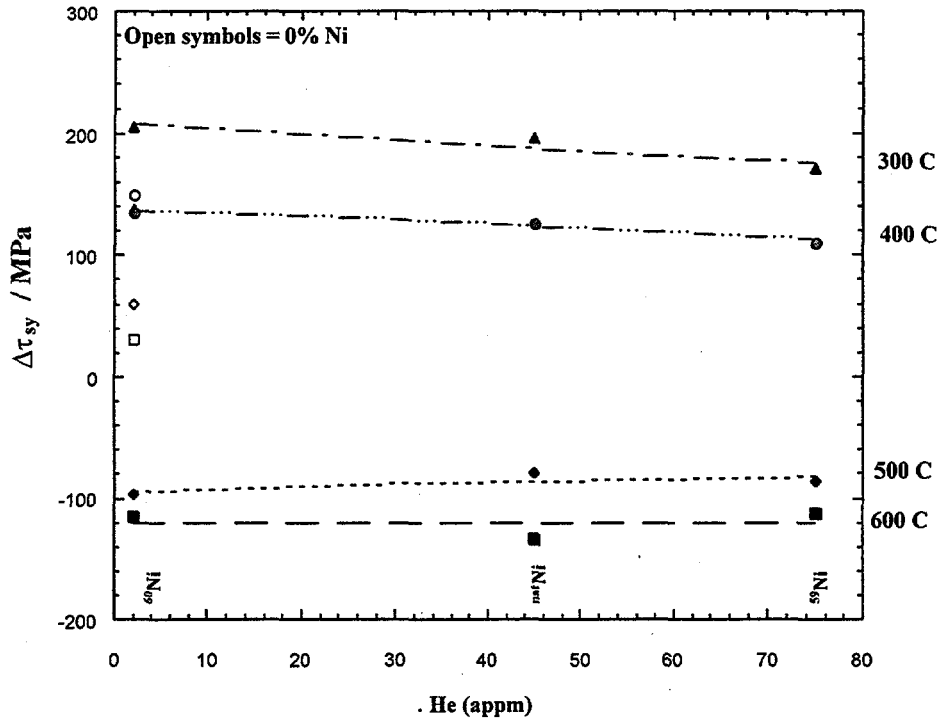

Figure 3 - Change in τ_{sy} with respect to the unirradiated condition as a function of helium content.

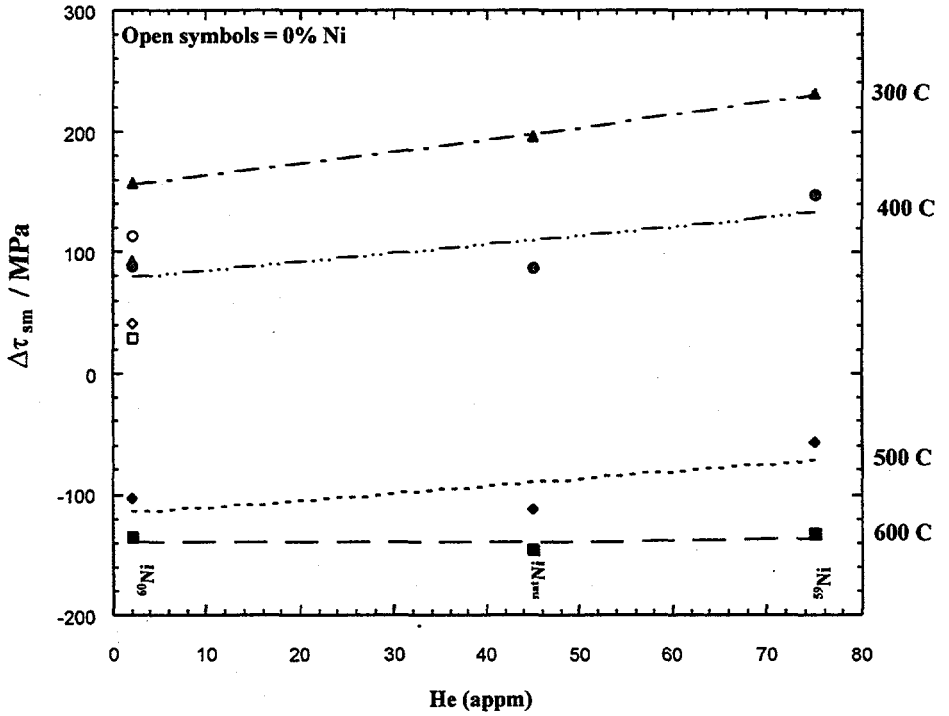

Figure 4 - Change in τ_{sm} with respect to the unirradiated condition as a function of helium content.

The strength of all alloys decreased with increasing irradiation temperature. The highest strength was observed for alloys irradiated at 300°C. The alloys irradiated at 500 and 600°C experienced an overall decrease in strength when compared to the unirradiated condition.

A small increase in both τ_{sy} and τ_{sm} is observed with increasing helium content in the irradiated alloys. Since the same trend is echoed in the data for the unirradiated material, however, it cannot be attributed to the helium level, but rather to another factor inherent to the alloys. Figures 3 and 4 show the change in τ_{sy} and τ_{sm} with respect to the unirradiated condition ($\Delta\tau_{sy}$ and $\Delta\tau_{sm}$ respectively) versus helium content for each irradiation temperature. While a shallow negative gradient is observed for the lower irradiation temperatures for $\Delta\tau_{sy}$, the trend is reversed in Figure 4 for $\Delta\tau_{sm}$.

Discussion

It is clear from Figs. 1 and 2 that nickel additions significantly increase τ_{sy} and τ_{sm} of the alloys before irradiation. This is true for all irradiation temperatures as well as in the unirradiated condition, which suggests that the strengthening action was present at least in part, prior to irradiation and can probably be attributed primarily to solution strengthening/precipitation hardening due to the addition of nickel. The slight variability observed in the strength for each isotopic variation is currently unexplained, but may arise from variability in impurity levels associated with the isotopic additions.

Irradiation at 300 and 400°C both caused an increase in strength when compared to the unirradiated material with the greatest strengthening occurring at 300°C. This is in agreement with the microstructural analysis carried out by Gelles [4] on the same set of alloys. The microstructure of the material irradiated at 300°C exhibited a dense distribution of fine precipitates, small voids and small dislocation loops. Each of these features would be expected to produce an increase in the strength of the alloy. The material irradiated at 400°C showed a more coarse microstructure, with larger and fewer precipitates and fewer, but more developed, dislocation loops. The material irradiated at 500 and 600°C showed an overall reduction in strength when compared with the unirradiated condition. Although the microstructures have not been studied for the alloys irradiated at 500 and 600°C, it is expected that further coarsening and increased loop and precipitate growth will have occurred.

The plot of $\Delta\tau_{sy}$ versus helium content (Fig. 3) shows a shallow positive gradient for materials irradiated at the lower temperatures. This trend is reversed, but has a slightly steeper gradient, in the plot of $\Delta\tau_{sm}$ versus helium level (Fig. 4). The variation in $\Delta\tau_{sy}$ over the range of helium levels for irradiation at a given temperature is only ~30 MPa, which is essentially the same as the scatter in the data for a given test condition (±20 MPa). It is therefore difficult to draw any conclusions, other than that helium levels up to 75 appm have little or no influence on the mechanical properties over the range of temperatures considered.

CONCLUSIONS

The shear punch testing of a series of isotopically tailored Fe-12Cr-1.5Ni ferritic alloys showed that helium levels up to 75 appm have little, if any, effect on the effective shear yield and maximum shear strengths. The strengthening effect of nickel was evident prior to irradiation and the strength of the irradiated Fe-12Cr-1.5Ni ferritic alloys shows a strong dependence on irradiation temperature, decreasing with increasing irradiation temperature.

FUTURE WORK

Chemical analysis of the unirradiated controls is planned to investigate the possible effect of variation in impurity levels.

REFERENCES

1. Odette, G.R., Maziaz, P.J. and Spitznagel, J.A., "Fission-Fusion Correllations for Swelling and Microstructure in Stainless Steels: Effect of the Helium to Displacement Per Atom Ratio," p. 1289 in J. of Nucl. Matl., (104), 1981.
2. Garner, F.A., Sekimura N., Grossbeck, M.L., Ermi, A.M. Newkirk, J.W., Watanabe, H., and Kiritani, M., "Influence of details of reactor history on microstructural development during neutron irradiation," p. 206 in J. of Nucl. Matl., (205), 1993.
3. Odette, G.R., "New Approaches to Simulating Fusion Damage in Fission Reactors," p. 1011 in J. of Nucl. Matl., (141-143), 1986.
4. Gelles, D.S., "The Consequences of Helium Production on Microstructural Development in Isotopically Tailored Ferritic Alloys," to be included in Fusion Reactor Materials Semiannual Progress Report for the period ending 30 June 1996, DOE/ER-0313/20 and submitted for consideration as part of the proceedings of the 18th International Conference on Effects of Radiation on Materials.
5. Materials Science and Technology, "A Comprehensive Treatment," Ch.6, Vol. 10A, Cahn, R.W., Haasen, P., Kramer, E.J., Eds., VCH Verlagsgesellschaft GmbH, 1994.
6. Lucas, G.E., Odette, G.R. and Sheckherd, J.W., "Shear Punch and Microhardness Tests for Strength and Ductility Measurements," p. 112 in The Use of Small Scale Specimens for Testing Irradiated Material, ASTM STP 888, Philadelphia, 1986.
7. Hamilton, M.L., Toloczko, M.B., Lucas, G.E., "Recent Progress in Shear Punch Testing," p. 46 in Miniaturized Specimens for Testing of Irradiated Materials, Hans Ullmaier and Peter Jung, Eds., Forschungszentrum Jülich GmbH, January, 1995.
8. Hamilton, M.L., Toloczko, M.B., Edwards, D.J., Sommer, W.F., Borden, M.J., Dunlap, J.A., Stubbins, J.F., Lucas, G.E., "Correlation Between Shear Punch and Tensile Data for Neutron Irradiated Aluminium Alloys," Effects of Radiation on Materials: Seventeenth International Symposium, ASTM STP 1270, David S. Gelles, Randy K. Nanstad, Arvind S. Kumar and Edward S. Little, Eds., American Society for Testing and Materials, Philadelphia, 1996, in press.
9. Toloczko, M.B., Hamilton, M.L., Lucas, G.E., "Ductility Correlations Between Shear Punch and Uniaxial Tensile Data", J. of Nucl. Matl., in press.

IRRADIATION CREEP OF VARIOUS FERRITIC ALLOYS IRRADIATED AT ~400°C IN THE PFR AND FFTF REACTORS - M. B. Toloczko and F. A. Garner (Pacific Northwest National Laboratory, Richland, WA 99352) and C. R. Eiholzer (Westinghouse Hanford Company, Richland, WA)

To be presented at the 8th International Conference on Fusion Reactor Materials in Sendai, Japan, October 1997.

Extended Abstract

Three ferritic alloys were irradiated in two fast reactors to doses of 50 dpa or more at temperatures near 400°C. One martensitic alloy, HT9, was irradiated in both the FFTF and PFR reactors. PFR is the Prototype Fast Reactor in Dourneay, Scotland, and FFTF is the Fast Flux Test Facility in Richland, WA. D57 is a developmental alloy that was irradiated in PFR only, and MA957 is a Y_2O_3 dispersion-hardened ferritic alloy that was irradiated only in FFTF. These alloys exhibited little or no void swelling at ~400°C.

Depending on the alloy starting condition, these steels develop a variety of non-creep strains early in the irradiation that are associated with phase changes. Each of these alloys creeps at a rate that is significantly lower than that of austenitic steels irradiated in the same experiments. The creep compliance for ferritic alloys in general appears to be ~0.5 x 10^{-6} MPa^{-1} dpa^{-1}, independent of both composition and starting state. The addition of Y_2O_3 as a dispersoid does not appear to change the creep behavior.

4.0 COPPER ALLOYS AND HIGH HEAT FLUX MATERIALS

EFFECT OF TEST TEMPERATURE AND STRAIN RATE ON THE TENSILE PROPERTIES OF HIGH-STRENGTH, HIGH-CONDUCTIVITY COPPER ALLOYS

— S. J. Zinkle and W. S. Eatherly (Oak Ridge National Laboratory)

OBJECTIVE

The objective of this report is to summarize recent tensile and electrical resistivity measurements on several different unirradiated commercial high-strength, high-conductivity copper alloys that are being considered for the divertor structure and first wall heat sink in ITER.

SUMMARY

The unirradiated tensile properties of wrought GlidCop AL25 (ITER grade zero, IG0), solutionized and aged CuCrZr, and cold-worked and aged and solutionized and aged Hycon 3HP™ CuNiBe have been measured over the temperature range of 20-500°C at strain rates between 4×10^{-4} s^{-1} and 0.06 s^{-1}. The measured room temperature electrical conductivity ranged from 64 to 90% IACS for the different alloys. All of the alloys were relatively insensitive to strain rate at room temperature, but the strain rate sensitivity of GlidCop Al25 increased significantly with increasing temperature. The CuNiBe alloys exhibited the best combination of high strength and high conductivity at room temperature. The strength of CuNiBe decreased slowly with increasing temperature. However, the ductility of CuNiBe decreased rapidly with increasing temperature due to localized deformation near grain boundaries, making these alloy heats unsuitable for typical structural applications above 300°C. The strength and uniform elongation of GlidCop Al25 decreased significantly with increasing temperature at a strain rate of 1×10^{-3} s^{-1}, whereas the total elongation was independent of test temperature. The strength and ductility of CuCrZr decreased slowly with increasing temperature.

PROGRESS AND STATUS

Introduction

High-strength, high-conductivity copper alloys have been selected for first wall heat sink and divertor structural applications in the proposed International Thermonuclear Experimental Reactor (ITER) [1,2]. The divertor structure poses a particularly challenging operating environment, where good mechanical properties (strength, fatigue, etc.) and high thermal conductivity are required. The proposed operating temperatures for the divertor structure and first wall heat sink range from ~100 to 350°C. Three different copper alloys are under consideration for fusion energy high heat flux applications, namely dispersion strengthened copper (Cu-Al_2O_3), CuCrZr and CuNiBe.

The purpose of the present report is to summarize recent tensile measurements performed on unirradiated specimens of these three alloys in ITER-relevant thermomechanical conditions. The reference thermomechanical conditions for the proposed ITER applications are as-wrought for the dispersion-strengthened copper, and solutionized and aged for the CuCrZr and CuNiBe alloys. At the present time, there are no known tensile data for solutionized and aged CuCrZr or CuNiBe over the temperature range of 100-350°C which is of interest for ITER. Tensile measurements were performed at temperatures between 20 and 500°C and at strain rates between 4×10^{-4} and 0.06 s^{-1} in order to identify key trends in the deformation behavior. Room temperature electrical resistivity measurements were also performed in order to obtain thermal stress figures of merit for the different alloys.

Experimental Procedure

Four different copper alloy heats were selected for the tensile measurements. The dispersion strengthened (DS) copper specimens were cut from a 2.5 cm thick plate of GlidCop Al25 DS copper produced by SCM Metal Products (now known as OMG Americas), which was fabricated according to

"ITER grade 0" [3] specifications (heat #C-8064). This alloy contains 0.25 wt.% Al in the form of finely dispersed aluminum oxide particles. The copper cladding on the plate surface was machined off prior to specimen fabrication. The tensile axis of the specimens were oriented along the longitudinal direction of the wrought plate. The Cu-0.65%Cr-0.10%Zr specimens were obtained from a 2 cm thick plate that was originally fabricated under the trade name of Elbrodur G by KM-Kabelmetal, Osnabrück, Germany as an F37 (cold-worked and aged) temper, heat #AN4946. A 2 × 3 × 5 cm piece from this plate was solution annealed in flowing argon for 1 hour at 980°C, water quenched, then aged in flowing helium at 475°C for 2 hours (furnace cool) at ORNL, in accordance with the draft ITER heat treatment specifications. Two different Hycon 3HP™ Cu-2%Ni-0.35%Be heats produced as 2.5 cm thick plates by Brush-Wellman were investigated. A cold-worked and aged plate (longitudinal orientation, heat #33667Y1) was fabricated to produce maximum strength while still providing reasonable conductivity [4], and is referred in the following as HT1 temper. In addition, a solutionized and aged (AT temper) plate of Hycon 3HP™ CuNiBe was obtained by heat treating a cold-worked and aged plate (heat #46546, designated HT2 in the following) at Brush-Wellman. Miniature SS-3 sheet tensile specimens with nominal gage dimensions 0.76 mm × 1.5 mm × 7.6 mm were electro-discharge machined from all four plates and tested without any subsequent heat treatment.

The tensile properties of the SS-3 sheet tensile specimens were determined at temperatures between 20 and 500°C at crosshead speeds ranging from 0.003 to 0.42 mm/s, which corresponds to initial strain rates of 3.9×10^{-4} to 0.056 s^{-1} in the gage region. The room temperature tests were performed in air, and the elevated temperature tests were performed in vacuum (10^{-6} to 10^{-5} torr). The specimens were held at the test temperature for 0.25 h prior to the start of each tensile test. One or two specimens were typically tested in an Instron servohydraulic machine for each experimental condition. The tensile properties were determined from graphical analysis of the chart recorder curves. A plastic deformation offset of 0.2% was used for measuring the yield strength.

Four-point probe electrical resistivity measurements were performed at room temperature on a minimum of 5 different SS-3 sheet tensile specimens for each of the alloys, using procedures summarized elsewhere [4]. The temperature was recorded for each measurement and the resistivity data were corrected to a reference temperature of 20°C using the copper resistivity temperature coefficient of $d\rho/dT = 6.7 \times 10^{-11}$ Ω-m/K. Nonuniformities in the width and thickness in the specimen gage region caused the typical experimental uncertainty of individual resistivity measurements to be ±0.5%.

Results

Table 1 summarizes the results of the room temperature electrical resistivity measurements. The relation 17.241 nΩ-m=100% IACS (international annealed copper standard) was used to convert the resistivity measurements to the familiar normalized conductivity scale. Previously reported results for the HT2 temper heat of Hycon 3HP™ CuNiBe [4] are also included in Table 1 for comparison. GlidCop Al25 exhibited the highest conductivity, followed by CuCrZr and CuNiBe. The measured values are in reasonable agreement with conductivities reported by the vendors. It is interesting to note that the AT heat treatment of the HT2 CuNiBe plate caused a reduction in the electrical conductivity.

The tensile properties obtained in the present study are summarized in Table 2. Additional data on the HT1 and HT2 heats of Hycon 3HP™ CuNiBe have been reported previously [4] for temperatures between 20 and 500°C at a strain rate of 1.1×10^{-3} s^{-1}. Figure 1 compares the 0.2% yield strength of the 4 different materials as a function of test temperature. All of the data in these two plots were obtained at an initial strain rate of 2.2×10^{-3} s^{-1} with the exception of the CuNiBe HT1 (heat #33667) data, which was obtained at a strain rate of 1.1×10^{-3} s^{-1}. The CuCrZr and GlidCop Al25 alloys exhibited similar yield strengths over the temperature range of 20-300°C, whereas both the AT and HT1 CuNiBe heats had much higher yield strengths. The yield strength of the CuNiBe AT temper was about 50 MPa lower than the parent HT2 temper [4] at room temperature. The AT and HT1 tempers had comparable strengths at temperatures ≥300°C. It is interesting to note that the strength of CuCrZr determined from these short term tensile tests was higher than that of GlidCop Al25 at 500°C. The

Table 1. Comparison of vendor data with electrical conductivities measured in the present study

Alloy	Nominal conductivity	Meas. resistivity at 20°C	Electrical conductivity
GlidCop Al25 (IG0)	86% IACS [5]	19.12 nΩ-m	90% IACS
CuCrZr (ITER SAA)	~80-83% IACS	20.67 nΩ-m	83% IACS
Hycon 3HP CuNiBe (AT)	65% IACS [5]	26.78 nΩ-m	64% IACS
Hycon 3HP CuNiBe (HT1)*	68% IACS [4]	26.27 nΩ-m	66% IACS
Hycon 3HP CuNiBe (HT2)*	74% IACS [4]	24.05 nΩ-m	72% IACS

*HT1= Hycon 3HP™ heat #33667 ; HT2= Hycon 3HP™ heat #46546

Table 2. Summary of tensile data from the present study (asterisks denote duplicate specimen averages)

	Temperature	σ_y (MPa)	UTS (MPa)	e_u (%)	e_{tot} (%)
GlidCop Al25 (IGO)					
3.9×10^{-4} s^{-1}	20°C	313	377	10.0	20.8
	200°C	263	314	11.9	35.0
	300°C	200	250	3.1	24.6
	500°C	75	104	30.3	68.0
2.2×10^{-3} s^{-1}	20°C	324	411	13.4	24.0
	200°C	287	333	8.4	26.4
	300°C	229	272	5.5	28.3
	500°C	92	134	4.0	45.0
0.056 s^{-1}	20°C	335	435	13.5	21.7
	200°C	292	359	10.7	27.2
	300°C	282	306	7.8	29.2
CuCrZr (ITER SAA)					
3.9×10^{-4} s^{-1}	20°C	300	407	15.4	23.2
	200°C	276*	359*	24.3*	42.2*
	300°C	253	313	12.0	23.0
2.2×10^{-3} s^{-1}	20°C	316	414	16.2	24.2
	200°C	280*	357*	13.8*	23.2*
	300°C	275*	332*	12.0*	23.7*
	500°C	197	223	11.4	30.0
0.056 s^{-1}	20°C	322	433	20.7	27.8
	300°C	264	330	14.3	24.3
CuNiBe (AT)					
3.9×10^{-4} s^{-1}	20°C	569	720	15.9	18.6
	200°C	550	672	14.9	16.0
	300°C	510	581	1.9	1.9
2.2×10^{-3} s^{-1}	20°C	564	723	15.3	18.0
	200°C	553	669	11.6	13.4
	300°C	545	595	2.6	2.8
	400°C	520	543	0.8	0.9
	500°C	(>420)**	—**	—**	—**
0.056 s^{-1}	20°C	596	728	17.5	18.5
	200°C	570	688	13.5	13.6
	300°C	543	621	6.0	6.0
	400°C	523	567	1.2	1.3
CuNiBe 33667 (HT1)					
3.9×10^{-4} s^{-1}	20°C	700	787	6.7	9.0
	300°C	649	712	2.1	3.2
2.2×10^{-3} s^{-1}	20°C	732	817	6.7	10.2
0.056 s^{-1}	20°C	728	769	9.8	13.3
	300°C	681	713	5.0	6.8

**broke in specimen grip pin hole; 2 different samples

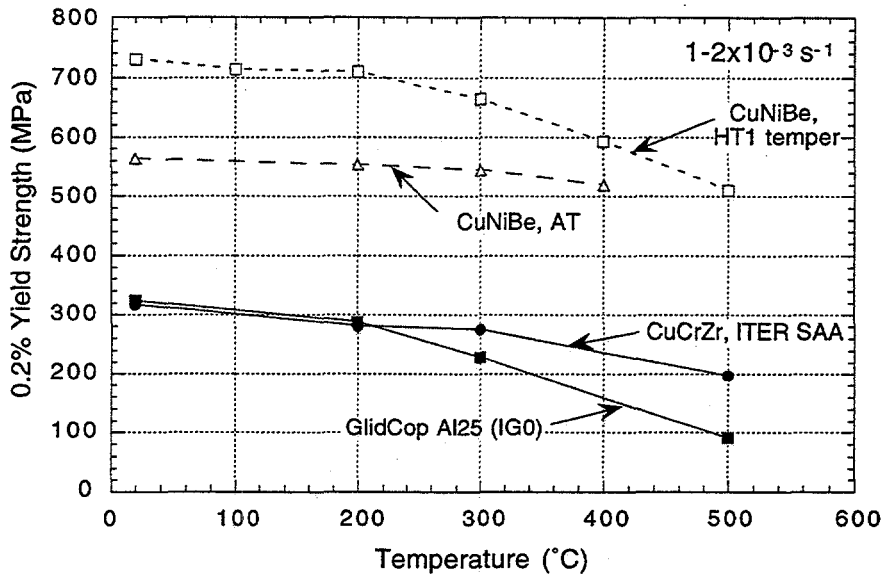

Fig. 1. Comparison of the temperature-dependent yield strengths of the four high-strength, high-conductivity copper alloy heats.

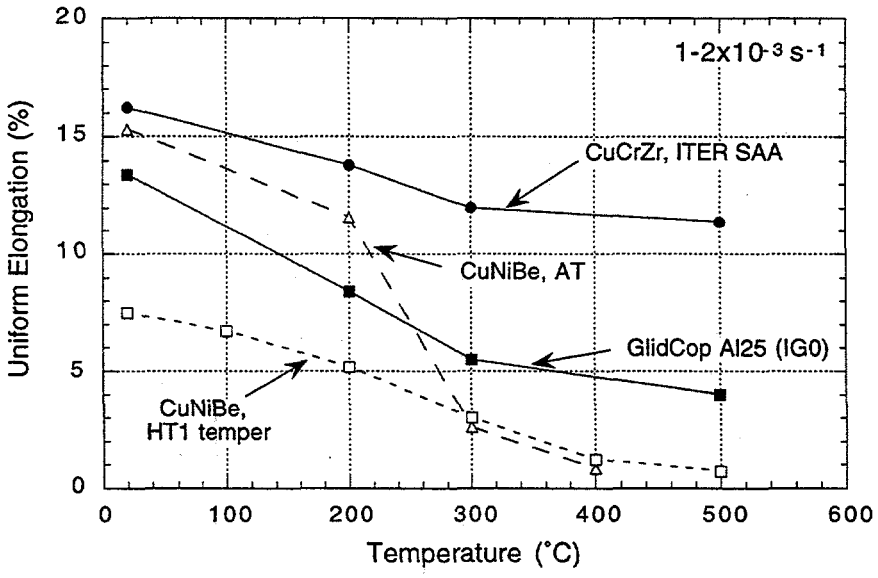

Fig. 2. Comparison of the temperature-dependent uniform elongations of the four high-strength, high-conductivity copper alloy heats.

strength of GlidCop dropped off more rapidly with increasing test temperature than any of the other alloys. For example, the measured yield strength for GlidCop Al25 at 300°C was 71% of its room temperature value. The corresponding 300°C yield strength ratios for the other alloys were 87% for CuCrZr and 91-97% for the two CuNiBe heats.

Figure 2 shows the uniform elongations as a function of temperature for the 4 different materials at a strain rate of 1 to 2 × 10^{-3} s^{-1}. All of the materials tested exhibited good ductility at room temperature. However, the behavior at elevated temperature was significantly different for each of the different alloys. The uniform elongation of CuCrZr decreased only slightly from ~16% at room temperature to ~12% at 500°C. In contrast, the uniform elongations of GlidCop and both CuNiBe heats decreased strongly with increasing test temperature. The uniform elongation of GlidCop Al25 decreased from ~13% at room temperature to ~4% at 500°C. The GlidCop Al25 total elongation remained high at all temperatures, with values between 25 and 45% at temperatures of 300-500°C (Table 1). The GlidCop elongation data indicate that necking (localized deformation) occurred at lower deformation levels with increasing test temperature, but high ductility was present in the necked region at all temperatures. The most severe elevated temperature embrittlement behavior occurred in the CuNiBe alloys, where the uniform elongation was reduced to <5% at a temperature of ~250°C. The decrease in uniform elongation in the CuNiBe alloys at elevated temperatures was accompanied by a pronounced decrease in the total elongation as well (cf. Table 2). Scanning electron microscopy of the fracture surfaces showed a transition from ductile transgranular failure at room temperature to intergranular failure (with localized ductile deformation) at elevated temperatures.

Figure 3 shows the effect of strain rate ($\dot{\varepsilon}$) on the measured yield strengths (σ_y) of the four materials tested at room temperature and 300°C. In general, all of the materials exhibited a very weak strain rate dependence, with a strain rate sensitivity parameter [6,7] of m~0.01, where $\sigma_y = C\dot{\varepsilon}^m$ and C is a constant. However, the strain rate sensitivity of GlidCop Al25 increased with increasing test temperature. A value of m=0.07 was measured at 300°C, which agrees well with another recent tensile test measurement on this alloy [8]. Previous work on GlidCop Al15 reported that m~0.1 for test temperatures of 400-650°C [9]. Due to the increased strain rate sensitivity of GlidCop at elevated temperatures, it can be seen in Fig. 3 that the yield strength of GlidCop Al25 at 300°C is comparable or greater than that of CuCrZr at a strain rate of 0.06 s^{-1}, but is 50 MPa weaker than CuCrZr at a strain rate of 4 × 10^{-4} s^{-1}. A qualitatively similar strain rate dependence was also observed for the ultimate tensile strengths of the 4 materials. The measured strain rate parameters obtained from the ultimate tensile strength data were m≤0.01 for all alloys except for GlidCop Al25, which exhibited m=0.03 and m=0.04 at room temperature and 300°C, respectively.

The uniform elongations of the alloys were somewhat more sensitive to strain rate than the yield and ultimate strengths. In all cases, the uniform elongation increased with increasing strain rate. The value of the uniform elongation strain rate exponent was m'~0.05 for all of the alloys at room temperature. A similar value was also obtained for CuCrZr tested at 300°C, whereas the value of m' increased to ~0.2 for the GlidCop and CuNiBe alloys tested at 300°C. The total elongation was not significantly affected by strain rate, with the notable exception of the CuNiBe specimens tested at elevated temperatures which exhibited an increase in total elongation with increasing strain rate.

Indications of an approach to superplastic deformation behavior were observed in the GlidCop Al25 and Kabelmetal CuCrZr specimens under certain combinations of strain rate and test temperature (Table 2). The GlidCop specimens exhibited a dramatic increase in uniform and total elongation at 500°C for the slowest strain rate investigated in this study, 4 × 10^{-4} s^{-1}. A somewhat less pronounced increase in ductility was observed for CuCrZr specimens tensile tested at 200°C at 4 × 10^{-4} s^{-1}. Further work is needed to determine if even higher levels of elongation can be achieved in these alloys through a suitable combination of strain rate and test temperature.

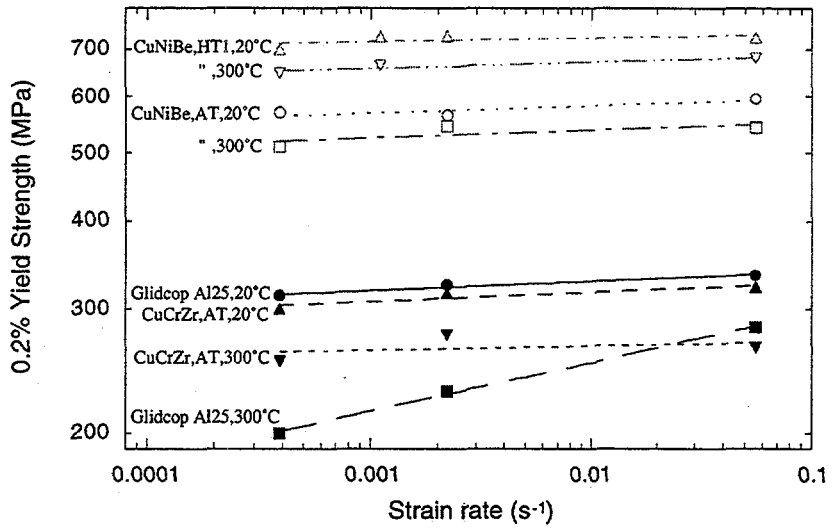

Fig. 3. Effect of strain rate on the yield strengths of the four high-strength, high-conductivity copper alloy heats at room temperature and 300°C.

Discussion

Table 3 compares the thermal stress figures of merit, $M=\sigma_y k_{th}(1-\nu)/\alpha E$, at room temperature and 300°C for the four materials tested in this study. The M values were calculated using the temperature-dependent pure copper data [1] for Young's modulus (E), Poisson's ratio (ν) and the coefficient of thermal expansion (α), and by utilizing the Wiedemann-Franz relation to convert the electrical conductivity measurements to thermal conductivity (k_{th}). The yield stress (σ_y) measured at a strain rate near 1×10^{-3} s^{-1} was used for the calculations. Table 3 also contains data for the HT2 temper of CuNiBe, which was the parent material for the AT specimens. The calculated thermal stress figures of merit decrease with increasing temperature for all of the alloys, mainly due to the decrease in yield strength. Small decreases in thermal conductivity and an increase in the Poisson's ratio also act to decrease the value of M at elevated temperatures, but they are partially balanced by a small decrease in Young's modulus [1]. The CuNiBe alloys exhibit the highest values for the thermal stress figure of merit over the temperature range of interest for ITER (100-350°C). However, their superior thermal stress behavior is seriously compromised by their increasingly poor ductility with increasing temperature above 250°C.

Table 3. Thermal stress figures of merit for high-strength, high conductivity copper alloys

Alloy	M at 20°C (kW/m)	M at 300°C (kW/m)
GlidCop Al25 (IG0)	36	25
CuCrZr (ITER SAA)	32	28
Hycon 3HP CuNiBe (AT)	45	44
Hycon 3HP CuNiBe (HT1)	60	54
Hycon 3HP CuNiBe (HT2)	56	49

The uniform elongation, yield strength and ultimate tensile strength increased with increasing strain rate for all of the alloys tested in this study. This simultaneous improvement in ductility and strength with increasing strain rate is a common feature in face-centered cubic metals, and may be contrasted with the decrease in ductility with increasing strain rate that occurs in body-centered cubic metals [10]. The strain rate sensitivity parameter is defined as [7]

$$m = \frac{1}{\sigma}\frac{\partial \sigma}{\partial \ln \dot{\varepsilon}} \tag{1}$$

Several phenomenological models have been developed which describe the combined effects of strain rate and test temperature on deformation behavior in metals. One of the earliest models [11,12] noted that most tensile data obtained on face centered cubic metals at low temperatures (below the creep regime) could be described by a "mechanical equation of state". Although it is generally recognized that a generalized mechanical equation of state cannot be formulated due to temperature-dependent changes in the deformation microstructure, the Zener-Hollomon model is useful for investigating strain rate sensitivity effects. The Zener-Hollomon parameter (P) is given by

$$P = \dot{\varepsilon} e^{Q/kT} \tag{2}$$

where $\dot{\varepsilon}$ is the strain rate and Q is an activation enthalpy for deformation. It was empirically noted that the flow stress was related to the Zener-Hollomon parameter by a simple power-law exponent [11]. From equation 1, it can be seen that this exponent is the strain rate sensitivity parameter, i.e. $\sigma = P^m$. A similar relation between strain rate and test temperature has been used for analyzing high temperature creep behavior in metals, and is known as the Sherby-Dorn equation [9,13].

$$\left(\frac{\sigma}{E}\right)^n = \frac{\dot{\varepsilon}}{A} e^{Q/kT} \tag{3}$$

where E is the temperature-dependent Young's modulus and n and A are constants. It can be readily seen that the stress exponent for the creep equation is simply the reciprocal of the strain rate sensitivity parameter, n=1/m. More sophisticated models have been forwarded in recent years which provide a better fit to experimental data, particularly near the threshold stress for creep initiation [14,15]. However, the key strain rate and temperature dependence is still reasonably approximated by eqns 1-3.

Figure 4 compares the yield strength versus reciprocal test temperature for the four copper alloy heats at a strain rate of 1 to 2×10^{-3} s^{-1}. All of the yield strength data have been normalized by the elastic modulus ratio E'=E(T)/E(20°C) so that the deformation activation energy can be readily obtained. A distinct change in slope occurs in all of the alloy curves at a temperature of ~300°C, which corresponds to a homologous temperature of 0.42 T_M where T_M is the melting temperature. GlidCop exhibited a somewhat higher slope in the low-temperature regime compared to the other alloys, which according to eqns 1-3 may be attributable to its higher strain rate sensitivity parameter m. The deformation activation energy determined from the low-temperature region of the curves in Fig. 4 was ~0.25 eV for all of the alloys. There were not sufficient data at temperatures above 300°C to accurately determine the deformation activation energy in the high-temperature regime. Analysis of the asymptotic slope obtained from the two highest temperature data points for the different alloys indicated that the high temperature activation energy was comparable to the copper self diffusion energy of 2.07 eV. This suggests that creep is the primary deformation mechanism in the tensile tests performed above 300°C.

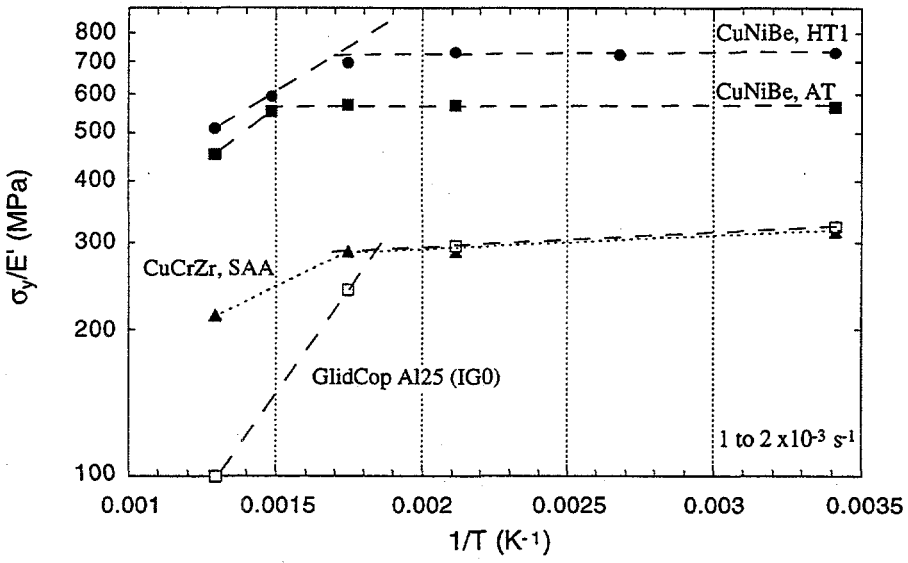

Fig. 4. Comparison of the temperature-dependent yield strengths of the four high-strength, high-conductivity copper alloy heats (normalized by elastic modulus ratio E'=E(T)/E(20°C)).

The present results demonstrate that GlidCop Al25 dispersion strengthened copper, CuNiBe and CuCrZr each exhibit different deformation behavior at elevated temperatures. The GlidCop Al25 and the two CuNiBe alloys exhibited significant reductions in uniform elongation with increasing temperature, whereas CuCrZr maintained high uniform elongation levels (>10%) up to 500°C (Table 1). The reduction in uniform elongation at elevated temperatures in the GlidCop Al25 and CuNiBe alloys was particularly severe at low strain rates. Previous tensile studies on wrought GlidCop Al15 and Al25 plates have observed a similar reduction in uniform elongation with increasing test temperature [16]. The GlidCop alloys did not exhibit a corresponding drop in total elongation at high temperatures, indicating that this alloy maintains good ductility in the necked region. On the other hand, the total elongation in the CuNiBe alloys decreased rapidly with increasing test temperature and the fracture mode changed from ductile transgranular failure at room temperature to ductile intergranular failure at temperatures above 300°C [4].

The solutionized and aged CuCrZr specimens were relatively insensitive to strain rate effects, and exhibited only a moderate decrease in strength and elongation with increasing temperature. There is some evidence that Zr additions can inhibit the intermediate temperature embrittlement that is sometimes observed in copper alloys [17-19]. The suppression of embrittlement in Zr-bearing copper alloys has been attributed to either trapping of surface-active bulk impurities such as sulfur [17,18] or else scavenging of atmospheric oxygen at grain boundaries [19]. However, it should be noted that a previous tensile property study on cold-worked and aged Elbrodur CuCrZr (produced by the same vendor as the present study) found low uniform elongations (<1%) and intergranular cracking for test temperatures between 300 and 700°C [20]. Further work is needed to determine the physical mechanisms responsible for low ductility in copper alloys at elevated temperatures.

Recent fracture toughness measurements on GlidCop Al15 and Al25 specimens have found that the fracture toughness decreases rapidly with increasing test temperature between 20 and 250°C [3,21,22]. However, Charpy impact tests of GlidCop Al25 did not show a decrease in absorbed energy for test temperatures up to 350°C [3,21]. The present results suggest that strain rate effects may be partially

responsible for this difference between the static fracture toughness tests (~10^{-5} s^{-1}) and the Charpy impact tests (~10 s^{-1}). The tensile strength and ductility of the GlidCop specimens would be significantly lower for the slow strain rates representative of static fracture toughness tests, particularly at elevated temperatures due to the increase in the strain rate sensitivity parameters (m and m'). Possible effects of testing environment (oxygen chemisorption) on the static fracture toughness test results also cannot be discounted, particularly since testing in vacuum at 150-250°C produced about a 50% increase in the measured fracture toughness of Al15 compared to air tests [21,22]. Since 0.5 monolayer of chemisorbed oxygen can reduce the surface energy of pure copper by about a factor of 2 and for copper this oxygen coverage occurs within ~500 s at a pressure of 10^{-9} torr [23], the partial pressure of oxygen should be less than ~10^{-9} torr in order to avoid oxygen effects in the static fracture toughness tests. It is worth noting that the typical oxygen partial pressure between pulses in present-day tokamaks is ~10^{-8} to 10^{-7} torr.

Finally, it must be noted that neutron irradiation at ITER-relevant temperatures of 100-250°C would produce significant increases in the strength and decreases in the ductility of these copper alloys [1,2,4]. Unfortunately, relatively little is known about the strain rate sensitivity of neutron irradiated copper alloys. Tensile testing of neutron irradiated specimens at several strain rates and test temperatures (up to the irradiation temperature) should be performed to increase the scientific understanding of deformation processes in radiation hardened copper alloys.

ACKNOWLEDGEMENTS

The GlidCop Al25 plate and Hycon 3HP™ CuNiBe solutionized and aged (AT) specimens for this study were provided by D. J. Edwards, Pacific Northwest National Lab. The two Hycon 3HP™ CuNiBe HT plates were supplied by David Krus, Brush-Wellman, Inc. The CuCrZr plate was supplied in the F37 temper condition by K. Slattery, McDonnell-Douglas.

REFERENCES

[1] S. J. Zinkle and S. A. Fabritsiev, Atomic and Plasma-Material Interaction Data for Fusion (supplement to Nuclear Fusion) 5 (1994) 163; also Fusion Materials Semiannual Progress Report for period ending March 31, 1994, DOE/ER-0313/16, pp. 314-341.
[2] S. A. Fabritsiev, S. J. Zinkle, and B. N. Singh, J. Nucl. Mater. 233-237 (1996), 127.
[3] R. R. Solomon, J. D. Troxell, and A. V. Nadkarni, J. Nucl. Mater. 233-237 (1996), 542.
[4] S. J. Zinkle and W. S. Eatherly, in Fusion Materials Semiannual Progress Report for Period ending June 30, 1996, DOE/ER-0313/20 (Oak Ridge National Lab, 1996), p. 207.
[5] D. J. Edwards et al., inFusion Materials Semiannual Progress Report for Period ending Dec. 31, 1995, DOE/ER-0313/19 (Oak Ridge National Lab, 1996), p. 165.
[6] G. E. Dieter, Mechanical Metallurgy, 2nd ed (McGraw-Hill, New York, 1976), p. 348.
[7] P. Haasen, Physical Metallurgy (Cambridge Univ. Press, New York, 1978), p. 26.
[8] T. P. Blair, personal communication from Westmoreland Mechanical Testing and Research, Inc., Youngstown, PA, to J. W. Davis, McDonnell-Douglas, Oct. 1996.
[9] J. J. Stephens, R. J. Bourcier, F. J. Vigil, and D.T . Schmale, Sandia National Lab Report SAND88-1351 (1988).
[10] A. N. Gubbi, A. F. Rowcliffe, W. S. Eatherly, and L.T. Gibson, in Fusion Materials Semiannual Progress Report for Period ending June 30, 1996, DOE/ER-0313/20 (Oak Ridge National Lab, 1996), p. 38.
[11] C. Zener and J. H. Hollomon, J. Appl. Phys. 15 (1944), 22.
[12] C. Zener and J. H. Hollomon, J. Appl. Phys. 17 (1946), 69.
[13] O. D. Sherby and A. K. Miller, J. Engineering Mater. Technology 101 (1979), 387.
[14] J. Rösler and E. Artz, Acta Metall. 38 (1990), 671.
[15] J. Groza, J. Mater. Engineering and Performance 1 (1992), 113.
[16] S. J. Zinkle, S. A. Fabritsiev, B. N. Singh, and D. J. Edwards, J. Nucl. Mater. (1997), to be submitted.

[17] M. Kanno, Z. Metallkde. 79 (1988), 684.
[18] R.D.K. Misra, V. S. Prasad, and P. R. Rao, Scripta Mater. 35 (1996), 129.
[19] P. Muthiah, A. Guha, and C.J. McMahon, Jr., Mater. Sci. Forum 207-209 (1996), 585.
[20] G. Piatti and D. Boerman, J. Nucl. Mater. 185 (1991), 29.
[21] D. J. Alexander, in Fusion Materials Semiannual Progress Report for Period ending June 30, 1996, DOE/ER-0313/20 (ORNL, 1996), p. 217.
[22] D. J. Alexander, S. J. Zinkle, and A. F. Rowcliffe in Fusion Materials Semiannual Progress Report for Period ending Dec. 31, 1996, DOE/ER-0313/21 (Oak Ridge National Lab, 1996), this report.
[23] S. J. Zinkle and E. H. Lee, Metall. Trans. A 21 (1990), 1037.

FRACTURE TOUGHNESS OF COPPER-BASE ALLOYS FOR ITER APPLICATIONS: A PRELIMINARY REPORT - D. J. Alexander, S. J. Zinkle, and A. F. Rowcliffe (Oak Ridge National Laboratory)

OBJECTIVE

The fracture toughness of several high-strength copper alloys was measured from room temperature to 250°C to determine their suitability for structural applications.

SUMMARY

Oxide-dispersion strengthened copper alloys and a precipitation-hardened copper-nickel-beryllium alloy showed a significant reduction in toughness at elevated temperatures (250°C). This decrease in toughness was much larger than would be expected from the relatively modest changes in the tensile properties over the same temperature range. However, a copper-chromium-zirconium alloy strengthened by precipitation showed only a small decrease in toughness at the higher temperatures. The embrittled alloys showed a transition in fracture mode, from transgranular microvoid coalescence at room temperature to intergranular with localized ductility at high temperatures. The Cu-Cr-Zr alloy maintained the ductile microvoid coalescence failure mode at all test temperatures.

PROGRESS AND STATUS

Introduction

High-strength copper alloys with high thermal conductivity are attractive candidates for some structural applications in ITER. Several classes of copper-based alloys are being examined to determine their fracture toughness at room temperature and up to 250°C.

The first class of copper alloys is dispersion strengthened by internal oxidation. One version of this alloy, called GLIDCOP AL-15, contains 0.15 wt % aluminum that has been internally oxidized to produce small Al_2O_3 particles in a copper matrix. Testing of unirradiated material was conducted to determine the fracture toughness as a function of test temperature and specimen orientation. Preliminary testing [1] had shown that the toughness of the AL-15 material decreased significantly as the test temperature increased from 22 to 250°C, although the tensile properties showed only a slight change over the same temperature range [2]. This suggested that an environmental effect might be responsible for the decrease in toughness at higher temperatures. Therefore, tests were carried out in vacuum to determine whether this could mitigate the decrease in toughness observed at higher temperatures. A second version of this alloy, GLIDCOP AL-25, which contains 0.25 wt % aluminum, was also examined.

A second class of alloys are strengthened by precipitation. Two alloys are being studied: Cu-Ni-Be [nominal composition Cu-2Ni-0.35Be (wt %)] and Cu-Cr-Zr (nominal composition Cu-0.65Cr-0.15Zr).

Experimental Procedure

The fracture toughness testing was conducted with small disk compact specimens 12.5 mm in diameter by 4.62 mm thick (0.491 by 0.182 in.) [designated 0.18 T DC(T) specimens]. All specimens were fatigue precracked at room temperature and then side grooved 10% of their thickness on each side prior to testing. Testing was conducted on an 89-kN (20-kip) capacity servohydraulic test machine in laboratory air, or on a 223-kN (50-kip) servohydraulic machine equipped with a vacuum chamber. The vacuum tests were conducted with a vacuum of better than 10^{-5} torr. A thermocouple was spotwelded to the specimen to monitor the temperature during each test. The J-integral-resistance (J-R) curves were obtained, in general accordance with ASTM E 813-89, Standard Test Method for J_{IC}, A Measure of Fracture Toughness, and ASTM E 1152-87, Standard Test Method for Determining J-R Curves, using a computer-controlled data acquisition and analysis system operating in strain control. The J-integral equations from E 1152-87 were used for the calculations. Tensile properties used in the analyses were taken from the literature [2-4].

Crack growth was monitored by the unloading compliance technique for all tests. An outboard clip gage was used that was seated in grooves machined on the outer diameter of the disk, above and below the loading holes. The experimental techniques developed for testing the small DC(T) specimens have been described elsewhere [5].

To mark the extent of crack growth for some of the preliminary testing the specimens were heat tinted by placing them on a hot plate and heating them until a noticeable color change had occurred. The specimens were cooled to room temperature and then broken open to allow the initial and final crack lengths to be measured. Later tests used fatigue crack extension at room temperature after the tests were completed to mark the final crack front. The crack lengths were measured from the fracture surfaces with a measuring microscope.

Specimens of the AL-15 material were fabricated from the middle of the thickness of an as-wrought plate measuring 165 mm wide by 12.7 mm thick by approximately 3 m long that was produced by SCM Metal Products, Inc. for the ORNL Fusion Energy Division in 1987 [3]. This plate had been warm worked during the consolidation of the -20 mesh powder. The plate was then extruded at about 820°C with an extrusion ratio of 25:1. Specimens were oriented in the T-L orientation so that crack growth was in the extrusion direction, or in the L-T orientation for crack growth perpendicular to the extrusion direction.

The AL-25 material was also fabricated by SCM Metal Products, Inc. The heat number was C-8064, and the material is referred to as IG0 (ITER Grade 0). The disk compact specimens were fabricated in stacks of 4 through the thickness of the plate, in either T-L or L-T orientations.

The Cu-Ni-Be alloy (C17510, trademark name Hycon 3 HP) was supplied by Brush-Wellman. Two heats were supplied in different strengths, primarily due to differences in their HT temper (cold-worked and aged) heat treatments. The high-strength heat 33667Y1 had a yield strength of about 720 MPa (104 ksi) at room temperature and an electrical conductivity of ~66% IACS. A second heat 46546AA2 in a slightly lower strength condition had a room-temperature yield strength of about 620 MPa (90 ksi) with a corresponding higher electrical conductivity of 72% IACS [4]. Specimens from both these heats were fabricated in stacks of 5 through the thickness of the nominally 25-mm-thick (1-in.) plates, in either the T-L or the L-T orientation, for crack extension parallel or perpendicular to the rolling direction, respectively.

The disk compact specimens prepared from the lower-strength heat 46546AA2 could not be successfully fatigue precracked. In all cases, the cracks deflected out of the plane of the starter notch, and began to grow perpendicular to the notch soon after they had initiated. This occurred for both specimen orientations, and persisted even when some specimens were side-grooved before precracking was attempted. This tendency for the crack to deflect out-of-plane has been observed previously for this material, in the L-T orientation [6]. The specimens from the high-strength material, heat 33667Y1, precracked readily, in either specimen orientation. Thus, all the data reported for alloy C17510 are from this high-strength condition and heat only.

The Cu-Cr-Zr alloy, called Elbrodur N, was provided by McDonnell-Douglas Aerospace in the form of plate 20.3 mm thick (0.8 in.). The material was produced by KobelMetall in the T37 temper (yield strength of 370 MPa) by solution annealing at 950 to 1000°C, water quench, cold work, and aging at 425 to 500°C. The specimens were fabricated as stacks of four through the thickness of the plate, in either the T-L or L-T orientations.

Results and Discussion

The results of the fracture toughness testing are summarized in Table 1. For the dispersion-strengthened AL-15 material, the fracture toughness decreased markedly as the test temperature increased. The toughness was also quite different depending on the specimen orientation, with specimens from the L-T orientation being much tougher than the T-L specimens. The toughness at room temperature was unaffected by the change from air to vacuum, but a higher toughness in vacuum than in air was observed at 250°C. The increase in test temperature from 25 to 250°C caused a significant decrease in the fracture toughness in either air or vacuum.

Table 1. Fracture Toughness of Unirradiated Copper Alloys

Material	Specimen	Orientation	Temperature (°C)	J_Q (kJ/m²)	K_{JQ} (MPa√m)	Tearing modulus (T)
GlidCop AL-15	FJ4	T-L	25	51	78	42
	FJ1		250	3	20	9
	GC1		250 vacuum	11	34	13
	GC5	L-T	25	241	168	87
	GC11		250 vacuum	220	161	75
	GC6		250	19	46	30
	GC7		250 vacuum	48	72	37
GlidCop AL-25	IG34	T-L	25	70	91	51
	IG35		250	7	28	16
	IG25	L-T	25	96	106	94
	IG26		250	13	38	26
Cu-Ni-Be	CL0	T-L	25	58	82	5
	CL2		150	23	51	4
	CT0	L-T	25	64	87	8
	CT6		250	6	26	1
Cu-Cr-Zr	CZ09	T-L	25	108	112	38
	CZ12		250	87	98	41
	CZ01	L-T	25	180	145	51
	CZ05		250	99	105	43

The significant decrease in the toughness of the oxide-dispersion strengthened alloys as the test temperature increases is a surprising response, as the change in the tensile properties over this same range of temperatures is modest (about 25%) [2]. These results are similar to toughness data reported by SCM Metal Products, Inc., for the AL-25 alloy [6], a higher alloyed variant of oxide-dispersion strengthened copper which has 0.25 wt % Al. Interestingly, impact tests of notched specimens of AL-25 [5] do not show a decrease in absorbed energy over a similar range of test temperatures. The fact that the toughness is degraded in the quasistatic fracture toughness test but not under dynamic conditions suggests that an environmental effect such as oxygen embrittlement of grain boundaries may be responsible for the drop in toughness at higher temperature. It was thought that the fracture toughness may not be so impaired in a vacuum environment. However, although there is a slight improvement in the toughness at 250°C under vacuum conditions as compared to air, the toughness is still much lower than one would expect on the basis of the small changes in the tensile properties over the same temperature range.

The results for GLIDCOP AL-15 show that the toughness of L-T specimens is much greater than that of T-L specimens. The processing used in the fabrication of this material results in the alignment of particles and the creation of an aligned grain structure parallel to the rolling or extrusion direction. Specimens in the T-L orientation will have crack extension parallel to this microstructure. This will result in a greatly reduced resistance to crack extension by providing a path that favors crack growth, whether by a ductile fracture mechanism, as will occur at room temperature, or by an intergranular mechanism, as occurs at high temperature.

The AL-25 material also shows a decrease in toughness at the higher test temperature (see Table 1). Again, the material in the L-T orientation is tougher than in the T-L orientation, although the difference is not a great as in the AL-15 material. The IG0 version of AL-25 incorporates cross-rolling of the plate during the size reduction process. Therefore, the grain elongation is less pronounced in the longitudinal direction, as compared to the AL-15 alloy.

Initial fractographic examinations of the AL-15 and AL-25 specimens showed a ductile microvoid coalescence mode of fracture for specimens tested at room temperature, in air or vacuum. A pronounced stretch zone was present at the tip of the fatigue precrack. Testing at 250°C in air or vacuum resulted in what appeared to be an intergranular fracture, with no stretch zone at the crack tip. The fracture mode did not resemble classic intergranular fracture, likely due to the anisotropic structure produced during fabrication of the oxide-dispersion strengthened material. It may in fact be intersubgranular, but is clearly very different than the microvoid coalescence observed at room temperature.

The Cu-Ni-Be material also shows a decrease in toughness when tested at higher temperatures, even at only 150°C (Table 1). Again, the L-T orientation appears to be tougher than the T-L orientation, although only limited testing has been conducted. Preliminary fractographic examination shows that at room temperature the fracture mode is microvoid coalescence, but at 250°C the fracture is intergranular. However, the intergranular fracture surface produced during the high-temperature fracture is a ductile one, with the grain boundaries covered with small, shallow dimples, much smaller than the transgranular dimples that formed for the specimen tested at room temperature. A similar transition in fracture morphology from ductile transgranular to ductile intergranular was observed in tensile tests performed on this same heat of material, although the transition in the tensile specimens only occurred for test temperatures above 300°C [4].

The Cu-Cr-Zr alloy generally had the best toughness of the alloys studied. At 250°C the toughness was only slightly lower than at room temperature. This material also showed some anisotropy, with the L-T orientation being tougher than the T-L orientation. However, the toughness was high in both orientations, and at 250°C this alloy showed much greater toughness than any of the other materials. Fractographic examination of the specimens tested at room temperature showed microvoid coalescence with a pronounced stretch zone at the precrack tip. At a test temperature of 250°C the fracture mode was again microvoid coalescence, but the dimples appeared to be shallower and less well-formed, and the stretch zone was much less apparent.

The beneficial effects of Zr additions on the high-temperature ductility and toughness of Cu-based alloys have been observed previously [8-12]. However, the mechanism by which the Zr improves the high-temperature ductility is not clear. Kanno [9] suggests that the Zr additions result in the formation of Zr sulphide particles, which getter the S and thus prevent S segregation to the grain boundaries. It was proposed that the presence of S produced intergranular

fracture and low ductility at high temperatures in Cu alloys that did not contain Zr. Misra et al. [10] examined a Cu-Co-Be alloy and suggested that the Zr segregates to the grain boundaries and prevents the dynamic embrittlement of these boundaries by oxygen which occurs in the absence of Zr.* They suggest either a reduction in the diffusivity of O due to the presence of Zr, or a scavenging effect of the Zr which will tie up the O. This suggests that if O is responsible for the reduced toughness observed in the copper alloys, the toughness should still be high when fracture occurs in a vacuum, if the partial pressure of O can thus be reduced to sufficiently low levels. Tests of a Cu-Co-Be-Ni alloy at 200°C supported this hypothesis, as no embrittlement was observed for tests in vacuum, but significant embrittlement was observed in air [11]. However, similar studies of a Cu-Cr alloy [12] attributed the high-temperature embrittlement to S, and the beneficial effect of Zr to the scavenging of the S. Thus, the embrittling mechanisms may differ in different alloy systems.

If the toughness is still low in vacuum, as was the case for the AL-15 material, then O may not be responsible, and surface-active impurities such as S present in the alloy may be causing embrittlement, if in fact the mechanism for the loss of toughness in the dispersion-strengthened alloys and the Cu-Ni-Be alloy is the same. Although the toughness of the AL-15 and AL-25 at 250°C in vacuum is higher than in air, the toughness is still much lower than would be expected from the tensile properties, so it is not clear which mechanism is responsible for embrittlement in the dispersion-strengthened materials.

Other elements have also been observed to prevent high-temperature embrittlement in Cu and Cu alloys, including Ti, B [13], Y [14], Ce, Ca, or La [15]. These effects were attributed to the removal of S from the alloys by the formation of sulphide particles, thus preventing grain boundary embrittlement by S at high temperatures [13-15].

If O is responsible for a dynamic embrittlement [10,11], then tests conducted at high strain rates should not show embrittlement, since sufficient time for diffusion of the O will not be available. To test this hypothesis, Charpy impact specimens were fabricated from the dispersion strengthened AL-25 alloy, in either the T-L or L-T orientations. Some of the specimens were fatigue precracked at room temperature prior to testing. The specimens were then tested with an instrumented Charpy impact test system at temperatures from 22 to 300°C. The results (see Fig. 1) show that no embrittlement is observed for the AL-25 material, in either the blunt-notched or fatigue-precracked condition. The precracked specimens absorbed much lower levels of energy, due in part to the sharper fatigue precrack, and in part to the reduced ligament remaining after the cracks were grown from the machined notch. However, the sharpness of the notch did not affect the trend of the results as a function of temperature, indicating that notch acuity is not a factor. The specimens in the L-T orientation showed higher energy absorption than the specimens in the T-L orientation, in agreement with the fracture toughness data, another indication of the anisotropy in these materials. These results are similar to data previously reported for AL-25 IG0 material by SCM Metal Products, Inc. [5].

The lack of embrittlement under dynamic testing conditions suggests that S is not responsible for the embrittlement observed in the dispersion-strengthened alloys, unless the S embrittlement mechanism is in some way time dependent. Again, it is not certain that all of these alloys are embrittled by the same mechanism. Further work is needed to determine the physical mechanism responsible for the dramatically lower fracture toughness observed for the GLIDCOP and Cu-Ni-Be alloys at 250°C.

It should be noted that most of the J-R data generated with this small disk compact specimen do not satisfy all of the validity requirements of the ASTM standards, and so these data are not valid. ASTM standard E 1152-87, Standard Test Method for Determining J-R Curves, sets three limits based on the specimen size. The maximum J-integral measurement capacity is given by the smaller of the following two equations:

*Note that "dynamic" is used in the sense that the presence of a stress is needed for embrittlement to occur, and not in reference to a strain rate during testing. This is compared to a "static" embrittlement, which would occur merely due to exposure to the embrittling species, even in the absence of an applied stress.

$$J_{max} = b\sigma_f/20 \text{ or} \quad (1)$$

$$J_{max} = B\sigma_f/20 , \quad (2)$$

where b = initial ligament size,
B = specimen thickness, and
σ_f = flow stress (average of yield and ultimate tensile stresses).

If the crack length to specimen width ratio (a/W) is 0.5, these are identical, as b will equal B for this specimen, in this case. For nearly all of the data, the measured J-integral values greatly exceed this limit. Only the lowest toughness materials have J-integral values low enough to satisfy these conditions. However, there is another even more limiting condition. The maximum allowable crack extension is limited to 0.1b. For an initial a/W value of 0.5, which was intended, the resultant maximum allowable crack extension is only 0.46 mm, well short of the second exclusion line at 1.5 mm of crack extension. If the initial crack length is greater than a/W = 0.5, as was nearly always the case, even less crack extension is allowed. For tough materials, the limit for crack extension will be reached when the J-R curve data are still on the blunting line, and stable tearing has not even begun to occur. Even for lower toughness conditions, only a few of the data points will be valid, and the bulk of the J-R curve is beyond the limit of validity. The values given in Table 1 have been generated by using all the data between the first and second exclusion lines to determine the curve fit for calculation of J_Q, even though these data are not all valid according to ASTM E 1152-87.

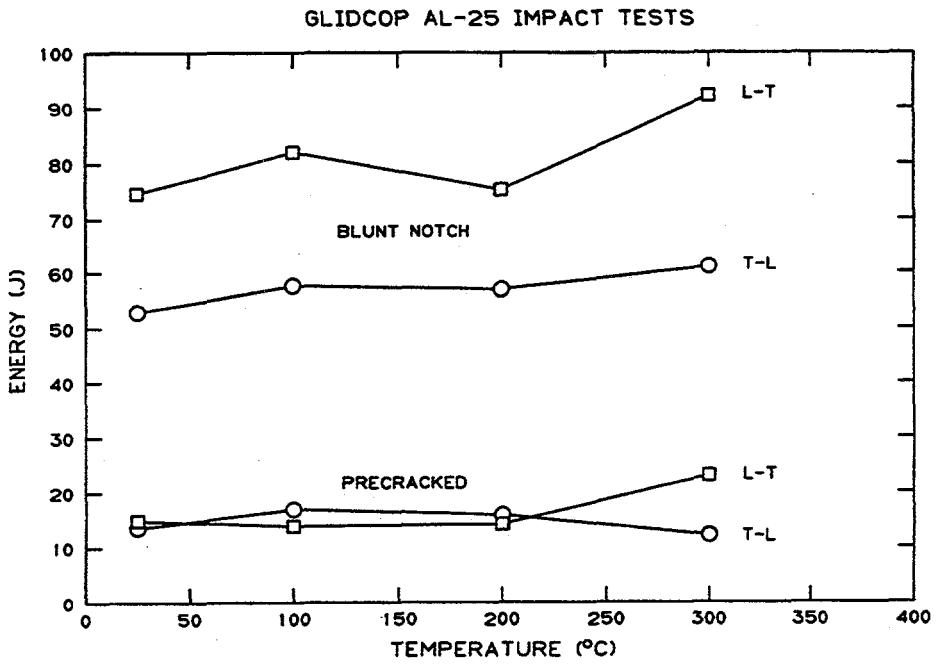

Fig. 1. Absorbed energy versus test temperature for impact tests of blunt-notched or precracked Charpy specimens of oxide-dispersion strengthened AL-25 copper alloy.

It must be emphasized that the J-R data, despite being invalid according to ASTM E 1152, are not incorrect. The size limitations imposed are conservative, and the J-integral values are quite likely still true measures of the materials' toughness, as long as the limits are not exceeded by too great a margin. The J-R curves are directly applicable to structures of the same thickness as the specimens, and are of great value in elucidating the materials' responses to test temperature. This will be useful information for evaluating candidate structural materials for ITER applications.

Summary

Fracture toughness tests have been conducted on several copper-based alloys being considered for applications in ITER, using small disk compact specimens, and the following preliminary results have been obtained.

1. Dispersion-strengthened copper alloys AL-15 and AL-25 show anisotropic fracture toughness, with higher toughness in the L-T orientation, and lower toughness in the T-L orientation. The anisotropy is significantly less in the AL-25 (IG0) alloy, presumably due to the cross-rolling during the alloy fabrication.

2. The fracture toughness of oxide-dispersion strengthened AL-15 and AL-25 decreases significantly as the test temperature increases from 22 to 250°C. The toughness at 250°C is higher for AL-15 specimens tested in vacuum than when tested in air, suggesting that environmental effects (oxygen chemisorption) may be at least partially responsible for the low toughness in air at 250°C. However, the reduction in toughness from room temperature to 250°C is much greater than one would expect, based on the modest changes in the tensile properties over this temperature range.

3. Impact tests of full-size Charpy impact specimens of AL-25 do not show embrittlement as the test temperature increases from 22 to 300°C. This is true for both blunt-notched and fatigue-precracked specimens.

4. The fracture toughness of a high-strength version of the Cu-Ni-Be alloy C17510 is anisotropic, with the L-T orientation being tougher than the T-L orientation. This material also shows a significant decrease in toughness as the test temperature in air increases from 22 to 250°C.

5. The fracture toughness of a Cu-Cr-Zr alloy is typically greater than that of the other alloys studied. In addition, this material shows only a small reduction in toughness as the test temperature increases from 22 to 250°C. Some anisotropy is present, with the L-T orientation being tougher than the T-L orientation.

6. The mechanism for the reduction in toughness of the dispersion- strengthened and the Cu-Ni-Be alloys is not clear. Different mechanisms may be operating in the different materials. The mechanism for the beneficial effect of Zr in the Cu-Cr-Zr alloy is also not certain, although it may be related to the formation of S-containing particles that thus prevent a sulphur-induced embrittlement from occurring at the grain boundaries.

REFERENCES

1. D. J. Alexander and B. G. Gieseke, "Fracture Toughness and Fatigue Crack Growth of Oxide-Dispersion Strengthened Copper," in *Fusion Materials Semiannual Progress Report for Period ending December 31, 1995*, DOE/ER-0313/19, 1996, pp. 189-194.

2. T. J. Miller, S. J. Zinkle, and B. A. Chin, "Strength and Fatigue of Dispersion-Strengthened Copper," *J. Nuc. Mat.*, 1991, Vol. 179-181, pp. 263-266.

3. S. J. Zinkle, Oak Ridge National Laboratory, personal communication, 1995.

4. S. J. Zinkle and W. S. Eatherly, "Tensile and Electrical Properties of Unirradiated and Irradiated HYCON 3HP™ CuNiBe," *Fusion Materials Semiannual Progress Report for Period Ending June 30, 1996*, DOE/ER-0313/20, pp. 207-216.

5. D. J. Alexander, "Fracture Toughness Measurements with Subsize Disk Compact Specimens," in *Small Specimen Test Techniques Applied to Nuclear Vessel Thermal Annealing and Plant Life Extension, ASTM STP 1204*, W. R. Corwin, F. M. Haggag, and W. L. Server, eds., American Society for Testing and Materials, Philadelphia, 1993, pp. 130-142; also published in *Fusion Reactor Materials Semiannual Progress Report for Period Ending March 31, 1992*, DOE/ER-0313/12, pp. 35-45.

6. R. R. Solomon, A. V. Nadkarni, and J. D. Troxell, SCM Metal Products, Inc., unpublished information presented at ITER Workshop, Gatlinburg, Tenn., November 7, 1995

7. H. A. Murray, I. J. Zata, and J. O. Ratka, "Fracture Testing and Performance of Beryllium Copper Alloy C17510," in *Cyclic Deformation, Fracture, and Nondestructive Evaluation of Advanced Materials: 2nd Volume, ASTM STP 1184*, M. R. Mitchell and O. Buck, eds., American Society for Testing and Materials, Philadelphia, 1994, pp. 109-133.

8. M. J. Saarivirta and P. P. Taubenblat, "Some High-Temperature Properties of Copper-Zirconium and Copper-Chromium High-Conductivity Alloys," *Trans. TMS-AIME*, 1960, Vol. 25, pp. 935-939.

9. M. Kanno, "Effect of a Small Addition of Zirconium on Hot Ductility of a Cu-Cr Alloy," *Z. Metallkunde*, 1988, Vol. 79, pp. 684-688.

10. R. D. K. Misra, C. J. McMahon, Jr., and A. Guha, "Brittle Behavior of a Dilute Copper-Beryllium Alloy at 200°C in Air," *Scripta. Metall. Mater.*, 1994, Vol. 31, pp. 1471-1474.

11. R. Muthiah, A. Guha, and C. J. McMahon, Jr., "An Example of Dynamic Embrittlement: Oxygen-Induced Cracking of a Cu-Be Alloy at 200°C," *Mat. Sci. Forum*, 1996, Vol. 207-209, Part 2, pp. 585-588.

12. R. D. K. Misra, V. Satya Prasad, and P. Rama Rao, "Dynamic Embrittlement in an Age-Hardenable Copper-Chromium Alloy," *Scripta Mater.*, 1996, Vol. 35, pp. 129-133.

13. H. Suzuki and G. Itoh, "A Study of Intermediate Temperature Embrittlement in Pure Copper," *J. Japan Inst. Metals*, 1984, Vol. 48, pp. 1016-1021.

14. M. Kanno and N. Shimodaira, "Improvement in Ductility at Intermediate Temperatures by a Small Addition of Yttrium in a Cu-30%Zn Alloy," *Scripta Metall.*, 1987, Vol. 21, pp. 1487-1492.

15. M. Kanno and N. Shimodaira, "Improvement in Hot Ductility in a Cu-4.4 mol%Sn Alloy by Adding a Small Amount of Third Elements," *Trans. Japan Inst. Metals*, 1987, Vol 28, pp. 742-748.

Recent Results on the Neutron Irradiation of ITER Candidate Copper Alloys Irradiated in DR-3 at 250°C to 0.3 dpa - DJ Edwards (PNNL), BN Singh, P. Toft and M. Eldrup (Risø National Laboratory)

OBJECTIVE

This particular experiment is one of three separate irradiations comprising the screening experiments on CuNiBe, CuCrZr and CuAl-25 aimed at helping decide which material should serve as the backup candidate to CuAl-25, the current primary candidate material.

SUMMARY

Tensile specimens of CuCrZr and CuNiBe alloys were given various heat treatments corresponding to solution anneal, prime-ageing and bonding thermal treatment with additional specimens re-aged and given a reactor bakeout treatment at 350^{0}C for 100 h. CuAl-25 was also heat treated to simulate the effects of a bonding thermal cycle on the material. A number of heat treated specimens were neutron irradiated at 250^{0}C to a dose level of ~ 0.3 dpa in the DR-3 reactor at Risø.

The main effect of the bonding thermal cycle heat treatment was a slight decrease in strength of CuCrZr and CuNiBe alloys. The strength of CuAl-25, on the other hand, remained almost unaltered. The post irradiation tests at 250^{0}C showed a severe loss of ductility in the case of the CuNiBe alloy. The irradiated CuAl-25 and CuCrZr specimens exhibited a reasonable amount of uniform elongation, with CuCrZr possessing a lower strength.

PROGRESS AND STATUS

Introduction

Because of their good thermal conductivity, copper alloys are being considered as heat sink materials for both first wall and divertor components of ITER (International Thermonuclear Experimental Reactor) [1,2]. The heat sink materials will have to be joined to the first wall and divertor materials at relatively high temperatures (900-1000^{0}C). During the joining process at these high temperatures, the microstructure of precipitation hardened (PH) alloys may change substantially, and consequently, these alloys may lose swelling resistance and become softer. Screening experiments were carried out at Risø to simulate the effect of bonding and bakeout thermal treatments on pre- and post-irradiation microstructures, mechanical properties and electrical resistivity of CuAl-25, CuCrZr and CuNiBe alloys. The present report describes the main results on the mechanical properties and electrical resistivity after irradiation at 250°C. A complete description of the microstructural analysis, mechanical properties and electrical resistivity measurements is in preparation [3].

Materials and Experimental Procedure

The materials used in the present investigations were oxygen-free high conductivity (OFHC) copper, CuCrZr, CuNiBe and CuAl-25 alloys. The OFHC-copper, CuCrZr and CuNiBe alloys were supplied by Tréfimétaux (France) in the form of 20 mm thick plates. The oxide dispersion strengthened (DS) copper (CuAl-25) was supplied by SCM Metals (USA) as GlidCop™ CuAl-25 in the form of rods in the as-wrought condition. The chemical composition of these alloys is listed in Table 1.

Table 1: Chemical Composition

OFHC-Cu:	Cu - 10, 3, < 1 and < 1 ppm of Ag, Si, Fe and Mg, respectively
CuCrZr:	Cu - 0.8% Cr, 0.07% Zr, 0.01% Si
CuNiBe:	Cu - 1.75% Ni, 0.45% Be
CuAl25	Cu - 0.25% Al as oxide particles (0.46% Al_2O_3)

Table 2: Summary of bonding and bakeout heat treatments* for CuCrZr, CuNiBe and CuAl-25 alloys

Type	Heat Treatment
A	Solution annealing at 950°C for 1 h followed by water quench
E	Prime ageing: heat treatment A + ageing at 475°C for 30 min. followed by water quench
B	Bonding thermal cycle: heat treatments A + E + annealing at 950°C for 30 min. followed by furnace cooling + re-ageing at 475°C for 30 min. followed by furnace cooling
C	Bakeout thermal cycle: heat treatment B + annealing at 350°C for 100 h followed by furnace cooling
C'	Bakeout thermal cycle: heat treatment E + annealing at 350°C for 100 h followed by furnace cooling
D	Annealing at 950° C for 30 min. (only for CuAl-25)
D'	CuAl-25 in the as-wrought condition, i.e. without any heat treatment

* - All heat treatments were done in vacuum (<10^{-4} torr)

Sheet tensile specimens (gage length = 7.0 mm) were cut from cold-rolled (~80%) sheets (~0.3 mm thick) of OFHC-copper, CuCrZr and CuNiBe alloys. Prior to irradiation, sheet tensile specimens of OFHC-copper were annealed at 550°C for 2 h in vacuum. Round tensile specimens of CuAl-25 (of gauge diameter 3 mm) were machined from the as-supplied rod, which was in the as-wrought condition (i.e. without cold-work). Prior to irradiation, all of the alloys were heat treated following the list in Table 2. All heat treatments were carried out in vacuum (<1.33 MPa or 10^{-5} torr).

Tensile specimens of pure copper, CuCrZr, CuNiBe and CuAl-25 alloys with the different heat treatments were irradiated at 250°C in the DR-3 reactor at Risø in the High Temperature Rig. During irradiation, temperature was measured, controlled (within ± 2°C) and recorded continuously. All specimens were irradiated at the same time to a fluence level of 1.5 x 10^{24} n/m^2 (E > 1 MeV), which corresponds to a displacement dose level of ~0.3 dpa (NRT). The neutron flux during

irradiation was approximately 2.5 x 10^{17} n/m^2 (E > 1 MeV) which corresponds to a displacement damage rate of ~5 x 10^{-8} dpa (NRT)/s.

Both unirradiated and irradiated tensile specimens were tested in an Instron machine at a strain rate of 1.2 x 10^{-3} s^{-1}. Tensile tests were carried out at 250°C in vacuum (<10^{-4} torr). The test temperature of 250°C was reached within 30 minutes. The cross-head displacement was measured and used to determine the stress-strain behaviour of the specimens. The fracture surfaces of the irradiated as well as unirradiated specimens were examined in a JEOL 840 scanning electron microscope.

All resistivity measurements were made at room temperature (23° C). In order to secure good electrical contacts, specimens were etched prior to resistivity measurements. The voltage connectors were either two sharply-pointed stainless steel pins which were pressed against the specimen, or (in a new specimen holder) spring loaded voltage probes, which gave a more well-defined and reproducible contact. The average resistivity of OFHC-copper (annealed at 550°C for 2 h) was found to be 1.682μΩ cm, which is in good agreement with the nominal resistivity of copper at room temperature of 1.698μΩ cm. The relative resistivity (RR) of the alloys was calculated from the following relationship: RR = R x t x w/ (R_{cu} x t_{Cu} x w_{Cu}), where R is the electrical resistance measured for the specimen of thickness t and width w. The index Cu refers to the values for the reference OFHC-Cu sample. The total uncertainty on each measurement was estimated to be less than 3%. The relative resistivity (RR) values for the various alloys quoted in Table 3 are the average values of six measurements made on each specimen.

Experimental Results

Results for the electrical resistivity and mechanical properties are presented in the following sections. The details of the microstructural analysis are provided in reference 3.

Pre- and Post-irradiation Electrical Resistivity

For comparison, resistivity measurements were carried out on unirradiated specimens with nominally the same heat treatments, although carried out in different batches. These measurements showed small variations in resistivity as shown in Table 3. The results on the unirradiated CuNiBe show that the HTB and HTE treatments decrease the resistivity as expected (see Table 3). Note, however, that the resistivity of the Tréfimétaux CuNiBe is much higher than that of two heats of Hycon 3HP® CuNiBe supplied by Brush Wellman Inc. (USA), another producer of CuNiBe alloys. The compositions and processing of the Brush Wellman heats have been optimized to yield a lower electrical resistivity while maintaining a reasonably high level of strength, though not as high as that of the Tréfimétaux CuNiBe. The relatively high resistivity of the Tréfimétaux CuNiBe suggests that a fraction of the beryllium and/or nickel (or other impurities) may still be in solid solution, and that the composition and thermal processing have yet to be optimized. However, note that the bakeout treatment had relatively little effect on the resistivity of the Tréfimétaux CuNiBe, indicative of the relative stability of the microstructure even when annealed at 350°C for 100 hours.

The irradiation of these alloys had little effect on the electrical resistivity. However, given that the precipitate density and size exhibited considerable change after irradiation [3], it is likely that the ballistic dissolution and re-precipitation of the precipitates still leaves solute elements in solid solution.

Table 3: Electrical resistivity measurements at room temperature for unirradiated and irradiated copper alloys given the indicated heat treatments.

Materials	Heat Treatment	Irradiation Dose (dpa)	Relative Resistivity† (RR)	Relative Conductivity (%)
OFHC-Cu	550°C/2 h	0	1.000	100
CuCrZr	A	0	2.09-2.16	46-48
CuCrZr	E	0	1.63-1.90	53-61
CuCrZr	B	0	1.40-1.73	58-71
CuCrZr	C	0	1.24-1.77	79-81
CuCrZr	C'	0	1.37-1.57	64-73
CuNiBe	A	0	2.96-3.23	31-34
CuNiBe	E	0	2.02-2.35	43-50
CuNiBe	B	0	2.01-2.38	42-50
CuNiBe	C	0	1.83-2.04	49-55
CuNiBe	C'	0	1.91-2.15	47-52
Hycon 3HP	CA*	0	1.55	65
Hycon 3HP	CK*	0	1.46	68
CuAl-25	D	0	1.13	88
CuAl-25	D'	0	1.15	87
CuCrZr	A	0.3	-	-
CuCrZr	E	0.3	1.52	66
CuCrZr	B	0.3	1.48	68
CuNiBe	A	0.3	3.22	31
CuNiBe	E	0.3	2.33	43
CuNiBe	B	0.3	2.22	45
Hycon 3HP	CA*	0.3	1.87	53

* Specimens from Oak Ridge National Laboratory, material originally from Brush Wellman Inc., Cleveland, Ohio; heat number 33667. CA and CK refer to different heat treatments that yield different starting conductivities and strengths.

† A range of values shows the measured variation in resistivity between different batches of samples with the same nominal heat treatment.

With the exception of the HTA specimens, the CuCrZr generally exhibited a lower resistivity than the CuNiBe alloys in each of the 5 heat treatments. In contrast to the CuNiBe, the bakeout treatment CuCrZr (HTC) clearly lowered the resistivity. Unlike the CuNiBe, irradiation improved the electrical resistivity of the CuCrZr alloy, but even this improvement still left the resistivity significantly higher than that of the CuAl-25 alloy. The results confirm the superior electrical resistivity of the CuAl-25 under these irradiation conditions. Transmutation effects are assumed to be minor for this low dose.

Pre- and Post-Irradiation Mechanical Properties

The mechanical properties of the three alloys show that irradiation can have a strong influence on the strength and ductility, with the CuNiBe showing the strongest susceptibility to irradiation effects.

The results for the individual alloys are summarized in the following sections, and the tensile data comparing the data for pure copper and the copper alloys are listed in Tables 4-6.

CuNiBe

The tensile results for the unirradiated CuNiBe specimens are provided in Figure 1 and Table 5, and show that the prime ageing treatment (HTE) yields the highest strength. The solution annealed (HTA) material possesses a higher yield strength compared to the annealed pure copper (Table 4) presumably due to the effect of solid solution strengthening. The HTB specimens exhibit a lower overall strength and higher ductility than the HTE specimens. It is significant to note that the denuded grain boundaries more prevalent in the HTB specimens [3] did not have any deleterious effect on the mechanical properties. The bakeout simulation (HTC) actually increases the strength somewhat. The effect of the bakeout simulation on specimens initially given heat treatment E is just the opposite, that is, the strength actually decreases somewhat.

Irradiation of these alloys reveals that the Tréfimétaux CuNiBe suffers a severe loss of ductility after irradiation (Figure 2, Table 6). The solution annealed (HTA) specimens exhibit a large increase in strength (178 vs. 655 MPa), but this is also accompanied by a large loss of ductility compared to the unirradiated state. The strength of the solution annealed specimens after irradiation is comparable to the specimens given the HTB and HTE treatments, indicative of the strong effect of irradiation-induced precipitation in these alloys [3]. The fracture surfaces of these alloys revealed that the failure mode changed from a completely ductile mode in the unirradiated state to a mixture of ductile intergranular and intergranular cleavage [3].

For comparison, specimens of a commercial CuNiBe (Hycon 3HP®) manufactured by Brush Wellman Inc. (USA) were also irradiated at 250°C to a dose level of 0.3 dpa and subsequently tested at 250°C (see Table 6 for tensile results). The material was in a fully hardened tempered condition (referred to as the HT temper in the United States), but the exact conditions are held proprietary by Brush Wellman. However, the HT temper normally involves solution annealing, cold working, and then ageing for several hours.

In the unirradiated condition the Hycon alloy has lower strength and noticeably less ductility. This changes after irradiation, however, since the irradiated CuNiBe (Hycon) exhibits somewhat lower yield strength and higher ductility than those measured in the Tréfimétaux CuNiBe (HTE). The results on CuNiBe (Hycon) reported in Table 6 are similar to those reported by Zinkle and Eatherly [4]. It should be emphasized here that it is not known how the Hycon 3HP® alloy would respond to the bonding thermal cycle (HTB), subsequent irradiation and post-irradiation mechanical testing.

Table 4: Tensile results for OFHC-copper in the unirradiated and irradiated (at 250°C to 0.3 dpa) conditions.

Material	Heat Treatment	Dose (dpa)	$\sigma_{0.05}$ (MPa)	$\sigma_{0.2}$ (MPa)	σ_{max} (MPa)	ε^{p}_{u} (%)	ε_{total} (%)
OFHC	550°C/2h	0	34	38	162	54.5	60.5
OFHC	550°C/2h	0.3	90	100	174	32.0	34.0

Table 5: Tensile results for unirradiated copper alloys with the pre-irradiation heat treatments described in Table 2. Tests were conducted at 250°C.

Material	Heat Treatment	$\sigma_{0.05}$ (MPa)	$\sigma_{0.2}$ (MPa)	σ_{max} (MPa)	ε^{P}_{u} (%)	ε_{total} (%)
CuCrZr	A	52	56	177	33.0	36.0
CuCrZr	B	94	100	219	27.3	31.3
CuCrZr	C	171	181	274	17.2	20.4
CuCrZr	C'	208	218	308	15.9	20.3
CuCrZr	E	135	140	261	22.6	25.5
CuNiBe	A	173	178	325	47.5	54.0
CuNiBe	B	455	480	665	24.6	30.5
CuNiBe	C	540	580	750	20.5	27.0
CuNiBe	C'	565	600	780	13.7	17.5
CuNiBe	E	610	630	825	15.0	19.0
(Hycon)*	Similar to HTE	575	620	690	3.0	5.3
CuAl-25†	D	306	315	326	1.5	18.5
CuAl-25†	D'	270	280	294	2.2	15.5

* Longitudinal direction, heat number 33667, proprietary HT heat treatment
† Round tensile geometry only

CuCrZr

The tensile curves shown in Figure 3 and the data listed in Table 5 for CuCrZr illustrate the differences that arise due to the 5 different heat treatments. The solution annealed CuCrZr does not exhibit the same degree of solution hardening as the solution annealed CuNiBe. In fact, its yield strength is very close to that of annealed OFHC-copper, but with noticeably less ductility. The lack of cold work in the HTB and the HTE samples illustrates the difference in strengthening that can be achieved in the two PH alloys. A cold working step prior to ageing the CuNiBe alloy is not required to achieve high strength, whereas its absence in CuCrZr leads to much lower strengths than can normally be achieved. All three heat treatments for the CuCrZr result in a material that possesses a high degree of work hardening, which the CuNiBe exhibits to a lesser extent, and is almost non-existent for CuAl-25 at 250°C. In both cases the bakeout treatment (or extra ageing) resulted in a significant increase in strength over the original starting state, and with little change in ductility.

The irradiated CuCrZr results are shown in Figure 4 and listed in Table 6. Clearly the irradiation of the solution annealed specimens has produced the same effect as in the CuNiBe, that is, radiation-induced precipitation that effectively doubles the strength. Irradiation of specimens given the other two heat treatments results in a large increase in yield strength, but little change in the ultimate strength.

Table 6: Tensile results for copper alloys irradiated at 250°C to 0.3 dpa with the pre-irradiation heat treatments described in Table 2. Tests were conducted at 250°C.

Material	Heat Treatment	$\sigma_{0.05}$ (MPa)	$\sigma_{0.2}$ (MPa)	σ_{max} (MPa)	ε^{P}_{u} (%)	ε_{total} (%)
CuCrZr	A	195	205	205	0.4	2.5
CuCrZr	B	215	224	223	4.0	5.0
CuCrZr	E	230	235	254	4.2	7.0
CuNiBe	A	590	655	670	0.7	1.9
CuNiBe	B	565	630	685	0.7	1.8
CuNiBe	E	625	690	705	0.3	1.5
CuNiBe (Hycon)*	Similar to HTE	530	620	655	2.1	3.1
CuAl-25†	D	280	303	328	1.8	15.3
CuAl-25†	D'	285	308	320	1.6	13.8

* Longitudinal direction, heat number 33667
† Round specimen geometry only

However, unlike the CuNiBe, this alloy still possesses a moderate amount of ductility in the HTB and HTE conditions, and retains some ability to work harden. The solution annealed condition has the lowest uniform elongation of the three irradiated conditions, and very little work hardening ability. The fracture surfaces for the CuCrZr show that before and after irradiation it still has a ductile failure mode, exhibiting a dimpled "knife edge" fracture surface due to the large reduction in area in the rectangular cross-section.

CuAl-25

The effect of annealing at 950°C for 30 min. (HTD) on the flow stress of CuAl-25 is very small (Table 5). It should be pointed out that unlike CuCrZr and CuNiBe alloys, the CuAl-25 does not seem to work harden during tensile deformation at 250°C. As in the unirradiated specimens, irradiated CuAl-25 exhibits little ability to work harden (Figure 4), which raises questions about its fracture toughness and resistance to crack growth. The fracture surfaces yield little information beyond the fact that the failure mode is ductile in nature, primarily because the grain size is too small to allow one to distinguish transgranular or intergranular failure.

Summary of Results

Of all the alloys, CuAl-25 proves to be the most stable in terms of the microstructure, mechanical properties and electrical resistivity. Based on these results the bonding thermal treatment should have little effect on the properties or microstructure of the DS copper alloys. However, the apparent lack of work hardening ability in CuAl-25 is a matter of concern. The case seems to be even worse in the case of irradiated CuNiBe, which loses not only its ability to work harden, but also its ability to deform plastically to any significant extent. The CuCrZr appears to be less susceptible to neutron irradiation effects at 250°C than CuNiBe, and still retains significant uniform elongation and some ability to work harden after irradiation. The poor behaviour of the CuNiBe after irradiation may be due to segregation at the grain boundaries, although there is not enough evidence to confirm this.

Irrespective of the initial state, the fracture surfaces from the CuNiBe revealed that failure occurred near or at the grain boundaries, and not within the bulk of the grains.

In both PH alloy systems (CuCrZr and CuNiBe) it is clear that the initial starting state has little effect on the final mechanical properties, even at a low dose of 0.3 dpa. The increase in yield strength observed for the HTB and HTE specimens of CuCrZr, along with the increase in conductivity, would indicate that irradiation resulted in further precipitation and coarsening that removes excess Cr and Zr from solution. Because of the different diffusion kinetics and the limited solubility of Cr in copper, the CuCrZr alloys respond differently to irradiation than the CuNiBe.

CONCLUSIONS

On the basis of the changes measured in the mechanical properties and electrical resistivity, the following conclusions can be drawn:

- The DS copper alloy CuAl-25 exhibits the greatest resistance to radiation-induced changes in microstructure and mechanical properties.
- The different heat treatments given to the CuNiBe and CuCrZr made little difference in the mechanical properties after irradiation at 250°C to 0.3 dpa.
- Irradiation of solution annealed CuNiBe and CuCrZr leads to radiation-induced precipitation that can produce strength levels near to that of the HTB and HTE specimens.
- CuCrZr appears to offer advantages over the CuNiBe because there remains a reasonable level of ductility and work hardening even after irradiation.
- The severe loss of ductility in the CuNiBe alloy due to neutron irradiation, regardless of the initial starting state, poses a serious concern for this alloy, particularly since the actual mechanism responsible for the poor behaviour remains unclear.

FUTURE WORK

The last irradiation experiment at 100°C on the same materials has been completed at Risø. Microstructural characterization , electrical resistivity, and mechanical testing have been completed on all of the specimens. Final analysis of the microstructural data is in progress.

ACKNOWLEDGMENTS

The present work was partly funded by the European Fusion Technology Program. The authors wish to thank B. F. Olsen, N.J. Pederson and J.L. Lindbo. DJ Edwards would like to thank Risø National Laboratory for the support and assistance during his visit. His work was also partly supported by the U.S. Department of Energy under contract DE-AC06-76RLO 1830 with the Battelle Memorial Institute at the Pacific Northwest National Laboratory. The authors would like to thank Dr. S.J. Zinkle for supplying the Hycon 3HP CuNiBe specimens.

REFERENCES

[1] ITER Joint Central Team, J. Nucl. Mater., 212-215 (1994) 3.

[2] J.W. Davis, D.E. Driemeyer, J.R. Haines and R.T. McGrath, J. Nucl. Mater., 212-215 (1994) 1353.

[3] B. N. Singh, D.J. Edwards, M. Eldrup and P. Toft, "Pre- And Post-Irradiation Properties Of Copper Alloys At 250°C Following Bonding And Bakeout Thermal Cycles", Risø - R - 937, Risø National Laboratory, Jan. 1997.

[4] S.J. Zinkle and W.S. Eatherly, Fusion Materials Semiannual Progress Report, DOE/ER-0313/20, (1996) 207.

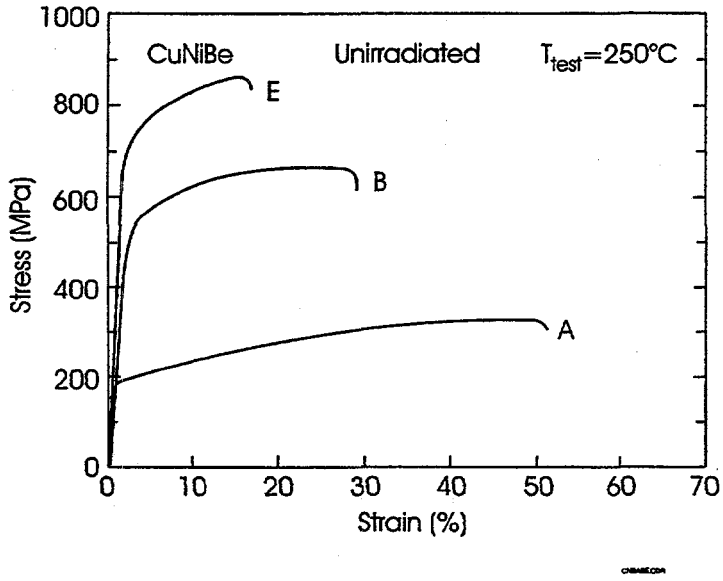

Figure 1 Tensile curves showing the influence of the different heat treatments on the deformation behavior of the CuNiBe alloy.

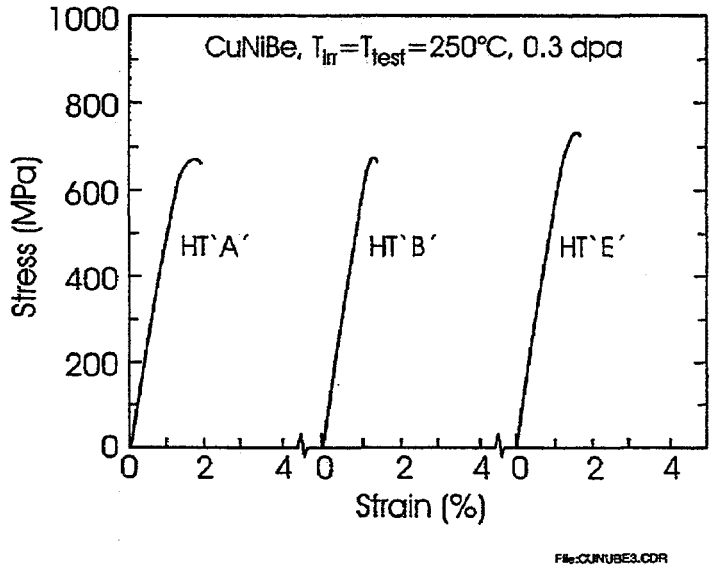

Figure 2 Tensile curves for the irradiated CuNiBe showing the severe loss of ductility after irradiation, regardless of the pre-irradiation heat treatments. Note that the post-irradiation strength is similar for all three heat treatments

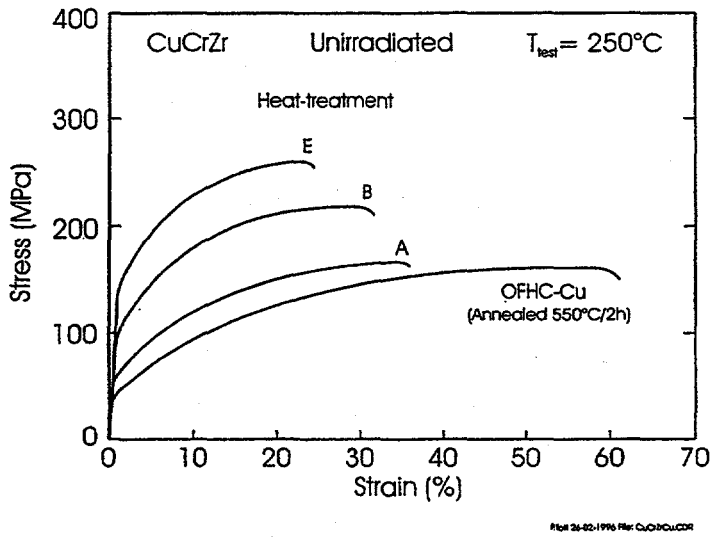

Figure 3 Tensile curves showing the influence of different heat treatments on the CuCrZr and a comparison with pure copper.

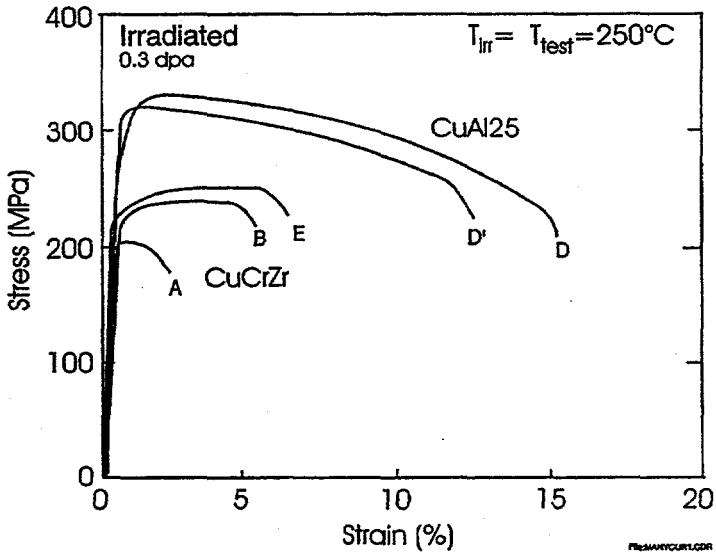

Figure 4 Comparison of the tensile behavior of CuCrZr to that of CuAl-25 after irradiation at 250°C to 0.3 dpa. Note that the CuCrZr still retains a measurable ability to work harden, whereas the CuAl-25 shows a very limited amount of work hardening.

IRRADIATION CREEP OF DISPERSION STRENGTHENED COPPER ALLOY —
A. S. Pokrovsky (Scientific Research Institute of Atomic Reactors), V. R. Barabash, S. A. Fabritsiev (D. V Efremov Institute of Electrophysical Apparatus), and M. L. Hamilton, C. R. Eiholzer, F. A. Garner, and D. J. Edwards (Pacific Northwest National Laboratory)

EXTENDED ABSTRACT

Dispersion strengthened copper alloys are under consideration as reference materials for the ITER plasma facing components. Irradiation creep is one of the parameters which must be assessed because of its importance for the lifetime prediction of these components.

In this study the irradiation creep of a dispersion strengthened copper (DS) alloy has been investigated. The alloy selected for evaluation, MAGT-0.2, which contains 0.2 wt.% Al_2O_3, is very similar to the GlidCop™ alloy referred to as Al20. Irradiation creep was investigated using He pressurized tubes. The tubes were machined from rod stock, then stainless steel caps were brazed onto the end of each tube. The creep specimens were pressurized by use of ultra-pure He and the stainless steel caps subsequently sealed by laser welding.

These specimens were irradiated in reactor water in the core position of the SM-2 reactors to a fluence level of 4.5-7.1 $\times 10^{21}$ n/cm^2 (E>0.1 MeV), which corresponds to ~3-5 dpa. The irradiation temperature ranged from 60-90°C, which yielded calculated hoop stresses from 39-117 MPa. A mechanical micrometer system was used to measure the outer diameter of the specimens before and after irradiation, with an accuracy of ±0.001 mm.

The irradiation creep was calculated based on the change in the diameter. Comparison of pre- and post-irradiation diameter measurements indicates that irradiation induced creep is indeed observed in this alloy at low temperatures, with a creep rate as high as ~2×10^{-9} s^{-1}. These results are compared with available data for irradiation creep for stainless steels, pure copper, and for thermal creep of copper alloys.

5.0 AUSTENITIC STAINLESS STEELS

Extreme Embrittlement of Austenitic Stainless Steel Irradiated to 75-81 Dpa at 335-360°C -
S. I. Porollo, A. N. Vorobjev and Yu. V. Konobeev (Institute of Physics and Power Engineering, Obninsk, Kaluga Region, Russia) and F. A. Garner (Pacific Northwest National Laboratory, Richland, WA USA)

To be presented at the 8th International Conference on Fusion Reactor materials in Sendai, Japan, Octobr 1997.

Extended Abstract

It is generally accepted that void swelling of austenitic steels ceases below some temperature in the range 340-360°C, and exhibits relatively low swelling rates up to ~400°C. This perception may not be correct at all irradiation conditions, however, since it was largely developed from data obtained at relatively high displacement rates in fast reactors whose inlet temperatures were in the range 360-370°C.

There is an expectation, however, that the swelling regime can shift to lower temperatures at lower displacement rates via the well-known "temperature shift" phenomenon. It is also known that the swelling rates at the lower end of the swelling regime increase continuously at a sluggish rate, never approaching the terminal 1%/dpa level within the duration of previous experiments.

This paper presents the results of an experiment conducted in the BN-350 fast reactor in Kazakhstan that involved the irradiation of argon-pressurized thin-walled tubes (0-200 MPa hoop stress) constructed from Fe-16Cr-15Ni-3Mo-Nb stabilized steel in contact with the sodium coolant, which enters the reactor at ~270°C. Tubes in the annealed condition reached 75 dpa at 335°C, and another set in the 20% cold-worked condition reached 81 dpa at 360°C. Upon disassembly all tubes, except those in the stress-free condition, were found to have failed in an extremely brittle fashion. The stress-free tubes exhibited diameter changes that imply swelling levels ranging from 9 to 16%. It is expected that stress-enhancement of swelling induced even larger swelling levels in the stressed tubes.

The embrittlement is explained in terms of the sensitivity of the swelling regime to displacement rate and the large, unprecedented levels of swelling reached at 335-360°C at these high neutron fluences. The failure mechanism appears to be identical to that observed at similar swelling levels in other austenitic steels irradiated in U.S. fast reactors at 400-425°C, whereby stress-concentration between voids and nickel segregation at void surfaces predisposes the steel to an epsilon martensite transformation followed by formation of alpha martensite at crack tips. The very slow strain rate inherent in such creep tests and the relatively high helium levels may also contribute to the failure.

The Independence of Irradiation Creep in Austenitic Alloys of Displacement Rate and Helium to dpa Ratio - F. A. Garner and M. B. Toloczko (Pacific Northwest National Laboratory, Richland, WA) and M. L. Grossbeck (Oak Ridge National Laboratory, Oak Ridge, TN)

To be presented at the 8th International Conference on Fusion Reactor Materials in Sendai, Japan, October 1997.

Extended Abstract

The majority of high fluence data on the void swelling and irradiation creep of austenitic steels were generated at relatively high displacement rates and relatively low helium/dpa levels that are not characteristic of the conditions anticipated in ITER and other anticipated fusion environments.

After reanalyzing the available data, this paper shows that irradiation creep is not directly sensitive to either the helium/dpa ratio or the displacement rate, other than through their possible influence on void swelling, since one component of the irradiation creep rate varies with to the instantaneous swelling rate.

Until recently, however, the non-swelling-related creep component was also thought to exhibit its own strong dependence on displacement rate, increasing at lower fluxes. This perception originally arose from the work of Lewthwaite and Mosedale at temperatures in the 270-350°C range. More recently this perception was thought to extend to higher irradiation temperatures.

It now appears, however, that this interpretation is incorrect, and in fact the steady-state value of the non-swelling component of irradiation creep is actually insensitive to displacement rate. The preceived flux dependence appears to arise from a failure to properly interpret the impact of the transient regime of irradiation creep.

THE COMPOSITIONAL DEPENDENCE OF IRRADIATION CREEP OF AUSTENITIC ALLOYS IRRADIATED IN PFR AT 420°C — M. B. Toloczko and F. A. Garner (Pacific Northwest National Laboratory), J. Standring (UKAEA, United Kingdom, retired), B. Munro and S. Adaway (AEA Technology, Dounreay, Scotland)

To be presented at the 8th International Conference on Fusion Reactor Materials in Sendai, Japan, October 1997.

Extended Abstract

Irradiation creep data are expensive and often difficult to obtain, especially when compared to swelling data. This requires that maximum use be made of available data sources in order to elucidate the parametric dependencies of irradiation creep for application to new alloys and to new environments such as those of proposed fusion environments.

One previously untapped source of creep data is that of a joint U.S./U.K. experiment conducted in the Prototype Fast Reactor (PFR) in Dounreay, Scotland. In this experiment, five austenitic steels were irradiated in a variety of starting conditions. In particular, these steels spanned a large range (15-40%) of nickel contents, and contained strong variations in Mo, Ti, Al, and Nb. Some alloys were solution-strengthened and some were precipitation-strengthened. Several were cold-worked.

These previously unanalyzed data show that at 420°C all austenitic steels have a creep compliance that is roughly independent of the composition of the steel at $2 \pm 1 \times 10^{-6}$ MPa^{-1} dpa^{-1}. The variation within this range may arise from our inability to completely separate the non-creep strains arising from precipitation reactions and the stress-enhancement of swelling. Each of these can be very sensitive to the composition and starting treatment of a steel.

IRRADIATION CREEP AND STRESS-ENHANCED SWELLING OF Fe-16Cr-15Ni-Nb AUSTENITIC STAINLESS STEEL IN BN-350 - A. N. Vorobjev, Yu. V. Konobeev and S. I. Porollo (Institute of Physics and Power Engineering, Obninsk, Russia), N. I. Budylkin and E. G. Mironova (Bochvar's Research Institute for Nonorganic Materials, Moscow, Russia), and F. A. Garner (Pacific Northwest National Laboratory)

To be presented at the 8th International Conference on Fusion Reactor Materials in Sendai, Japan, October 1997.

Extended Abstract

Irradiation creep and void swelling will be important damage processes for stainless steels when subjected to fusion neutron irradiation at elevated temperatures. The absence of an irradiation device with fusion-relevant neutron spectra requires that data on these processes be collected in surrogate devices such as fast reactors.

This paper presents the response of an annealed austenitic steel when exposed to 60 dpa at 480°C and to 20 dpa at 520°C. This material was irradiated as thin-walled argon-pressurized tubes in the BN-350 reactor located in Kazakhstan. These tubes were irradiated at hoop stresses ranging from 0 to 200 MPa. After irradiation, both destructive and non-destructive examination was conducted.

At 480°C and 60 dpa the swelling, as measured by both microscopy and density change, was very large and enhanced by applied stress, ranging from 20 to 30%. Swelling was much lower at 520°C and 20 dpa, but was also enhanced by stress. In both irradiation conditions, the creep rate was linear with applied stress. The creep-swelling coupling coefficient D in both irradiation conditions was found to have fallen to the low level characteristic of the swelling-dominated "creep disappearance" regime.

At 480°C microscopy examination showed that the stress-enhancement of swelling was reflected only in the void density and not the void size. Frank loops did not exist at this high dose and the network dislocation density was found to be independent of the stress level.

6.0 INSULATING CERAMICS AND OPTICAL MATERIALS

No contributions.

7.0 SOLID BREEDING MATERIALS

No contributions.

8.0 RADIATION EFFECTS, MECHANISTIC STUDIES, AND EXPERIMENTAL METHODS

ATOMIC SCALE MODELING OF DEFECT PRODUCTION AND MICROSTRUCTURE EVOLUTION IN IRRADIATED METALS* — T. Diaz de la Rubia, N. Soneda#, E Alonso, K. Morishita$, and Y. Shimomura♦ (Lawrence Livermore National Laboratory,l L-268, P.O. Box 808, Livermore, CA 94550)

SUMMARY

Irradiation effects in materials depend in a complex way on the form of the as-produced primary damage state and its spatial and temporal evolution. Thus, while collision cascades produce defects on a time scale of tens of picoseconds, diffusion occurs over much longer time scales, of the order of seconds, and microstructure evolution over even longer time scales. In this report we present work aimed at describing damage production and evolution in metals across all the relevant time and length scales. We discuss results of molecular dynamics simulations of displacement cascades in Fe and V. We show that interstitial clusters are produced in cascades above 5 keV, but not vacancy clusters. Next, we discuss the development of a kinetic Monte Carlo model that enables calculations of damage evolution over much longer time scales (1000's of s) than the picosecond lifetime of the cascade. We demonstrate the applicability of the method by presenting predictions on the fraction of freely migrating defects in α-Fe during irradiation at 600 K [1].

INTRODUCTION

Ferritic steels and V-based alloys are candidate materials for the first wall of fusion reactors. Their behavior under irradiation is one of the critical issues that must be considered in the final decision making process. In particular, degradation of mechanical properties due to embrittlement and swelling is one of the major concerns. Our recent work is aimed at understanding the fundamental aspects of defect production and microstructure evolution in these materials, and at developing physically-based predictive models of radiation-induced changes in mechanical properties. As a first step, we report here on the development of a hybrid approach that combines molecular dynamics (MD) with kinetic Monte Carlo (KMC) simulations [1]. This enables not only calculations of the primary damage state due to displacement cascades, but also a description of the fate of the cascade-produced defects over time scales comparable to actual experimental conditions. Such simulations can be used to predict, at the atomic scale, the formation of microstructural features such as impurity precipitates and voids during prolonged irradiation. Precipitates of impurities can act as obstacles for dislocation motion and are thought to be responsible for the increase in yield stress associated with embrittlement in these materials. Voids can nucleate at the site of transmutation He atoms, and are responsible for swelling.

In the past, MD simulations have been used extensively to model the primary damage state induced by displacement cascades in metals (for a review, see e.g. [2]). Because of the length and time scales of MD (100's of Å and tens of picoseconds), this is an appropriate tool for these calculations, but cannot be used to investigate the fate of the resulting defects and their role in producing microstructural and compositional changes. To overcome these limitations, a way of connecting the MD results to other simulation methods

---

* Work performed under the auspices of the U.S. Department of Energy by Lawrence Livermore National Laboratory under contract W-7405-Eng-48.

Permanent address: Central Research Institute of the Electric Power Industry, 2-11-1 Iwado-kita, Komae-shi, tokyo 201, Japan

$ Permanent address: University of Tokyo, 7-3-1 Hongo, Bunkyo-ku, Tokyo 113, Japan

♦ Permanent address: University of Hiroshima, 1-4-1 Kagamiyama, Higashi-Hiroshima 739, Japan

such as rate theory [3] or Monte Carlo calculations [4,5] is required. In particular, Monte Carlo simulations appear very promising because they provide the ability to perform atomic level studies of the defect kinetics and microstructural evolution over relevant length and time scales.

In this report, we present MD simulations of displacement cascades in Fe and V at energies from 100 eV to 20 keV. We then connect these results to KMC calculations that describe the long time-scale migration and evolution of these defects for the particular case of α-Fe at 600 K. To carry out the KMC calculations, we also perform studies of the formation and migration energy of point defects and defect clusters using the MD technique, and these results then serve to define the interaction rules for the KMC simulator. Results on the escape probability of defects from their nascent cascade, and on the fraction of freely migrating defects under these irradiation conditions are presented and compared to experiments.

2. MOLECULAR DYNAMICS SIMULATIONS OF DISPLACEMENT CASCADES

Collision cascades due to neutron irradiation produce defects in the matrix of structural materials. Information on the number of point defects and defect clusters as well as their spatial configuration provides the starting conditions for all further considerations regarding microstructural evolution. Our simulations were carried out with the MDCASK code [6) which can be used on either RISC workstations or massively parallel computers. The performance on a DEC workstation with the 300MHz Alpha chip is 1.2×10^{-4} CPU sec/atom-MD step, equivalent to the performance on a vintage 1988 Cray 2 supercomputer. On a Cray T3D parallel machine, the performance is 3×10^{-6} CPU-sec/atom/step on 128 processors. The largest MD simulation boxes used were cubes 250 Å on a side containing 500,000 atoms.

2.1. α-Fe

For the MD simulations presented here, the analytic EAM interatomic potential for α-Fe developed by Johnson and Oh [7] and modified by Guellil and Adams [8] was used after modifications to account properly for high energy scattering during the early stages of the cascade.

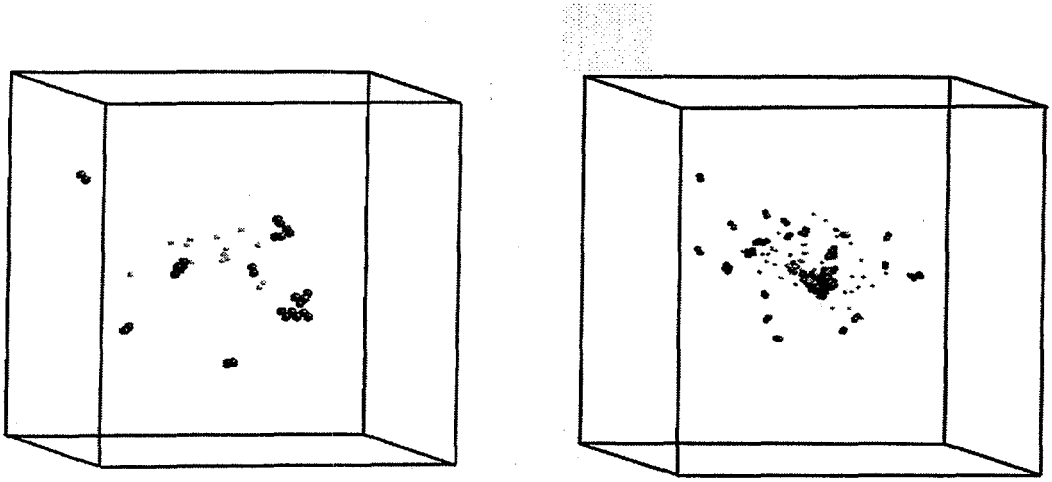

Figure 1. 5 and 20 keV displacement cascades in α-Fe. The blue spheres are interstitials and the small dots represent vacancies. A fraction of the interstitials is produced in clusters, but the vacancies are not.

Figure 1 shows a comparison of typical defect configurations produced by 5 and 20 keV displacement cascades 10 ps after the initiation of the recoil. Pairs of open circles are interstitial dumbbells, and small dots are vacancies. Fifteen Frenkel pairs are generated in this 5keV cascade simulation. Vacancies are located in the center region of the cascade, while isolated <110> interstitial dumbbells produced by replacement collision sequences (RCSs) can be found in the periphery. Two di-interstitials were also formed. On the other hand, the 20keV cascade shown in Fig 1b generated fifty five Frenkel pairs. Many mono-interstitial dumbbells are located at the edge of the cascade region, but large interstitial clusters are also present.

Detailed analysis of the cascade evolution process shows that these large interstitial clusters are formed at the interface of local subcascades. For the 20 keV case, the large interstitial cluster results from agglomeration of three smaller sub-clusters driven by the very high local stresses in the cascade periphery. No vacancy clusters were formed in any of these events. This is in sharp contrast to the case of Au where large vacancy loops are observed for 10 and 30 keV cascades [9], but agrees well with results in V [10].

The number of Frenkel pairs normalized by the number calculated by the modified Kinchin-Pease (or NRT) model [11] is plotted in Fig. 2 as a function of PKA energy. For very low PKA energies such as 100 and 200 eV, the results agree well with the NRT model. For higher PKA energies, however, the NRT model clearly overestimates the number of Frenkel pairs. In the 20 keV recoil events, the defect production efficiency is only 30% of the NRT model, which is consistent with experimental studies in Cu and Ag [12] and with previous MD simulations in many metals for PKA energies up to 25 keV [2]. Note that these results are based on the number of defects at 10 ps after event initiation. In order to calculate the fraction of freely migrating defects at elevated temperature, we need to consider how many of these defects undergo recombination within their nascent cascade and how many are able to escape. This issue is addressed section 3.

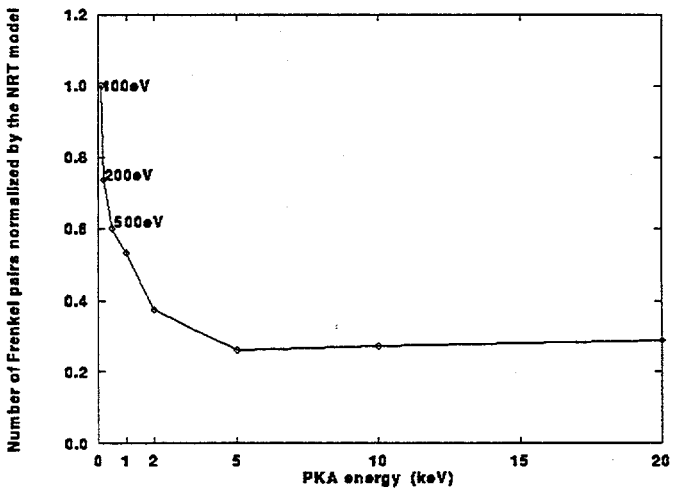

Figure 2. Defect production efficiency in α-Fe (Number of defects in MD cascades normalized by the NRT prediction) as a function of recoil energy

2.2 Vanadium

Vanadium-based alloys are strong candidate materials for the first wall of fusion reactors because of their low activation. It is therefore important to understand the form of the primary damage state in this materials in order to establish the conditions for further modeling of microstructure evolution under irradiation. We have carried out simulations of displacement cascades in V at energies from near threshold to 5 keV [10]. The simulations were carried out with the Johnson-Oh EAM-type potential [8] which was demonstrated to provide a good description of the formation and migration energies of vacancies, the melting point, and the fcc-bcc structural energy difference [10]. As for the case of Fe, the potential was modified at short range to account for scattering during the early collisional stages of the cascade.

The threshold energy for defect production was found to have a minimum value of 18 eV near the <100> direction and to increase to 80 eV 2° away from <111> towards <100> and 3° away from <100> toward <221>. As in the case of α-Fe, very few interstitial and vacancy clusters were found for any of the recoil events simulated. The largest cluster contained four interstitials in one of the 5 keV recoil events. No vacancy clusters larger than two were found.

3. Kinetic Monte Carlo Studies

As discussed in the introduction, interstitials, vacancies and some of their clusters are mobile at elevated temperatures. Therefore, soon after production in the cascade these defects begin to migrate and interact. Some of them will escape their nascent cascade to migrate over long distances in the matrix, thus contributing to the formation and evolution of microstructures such as impurity precipitates and voids. The estimation of the production efficiency of such defects, commonly termed Freely Migrating Defects (FMD), is a key requirement for the development of a quantitative understanding of the effect of particle irradiation on materials properties. In this section, we report on recent calculations of the production efficiency of FMDs in α-Fe at 600 K using kinetic Monte Carlo simulations [1]. The input data necessary for the KMC simulations, such as defect diffusivity, defect cluster binding energies, and the initial defect configurations produced by displacement cascades, were obtained by MD. The displacement cascade results were discussed in section 2. The mobility of the various point defects and defect clusters were also calculated and will be reported in the literature. For completeness, suffice to mention here that we found that small interstitial clusters are highly mobile and migrate by executing a random walk in one dimension.

For a given PKA energy, the starting defect microstructure is introduced at the center of the KMC computation box according to the spatial configuration obtained by the MD simulation of the corresponding displacement cascade. Then, the system is annealed at 600K for 1000 s, and the number of defects that are able to reach the edges of the KMC computational box (which is a cube 0.1 μm on a side) are counted to determine the escape fraction. We consider clusters that contain between 3 and 15 interstitials to execute a one-dimensional random walk. This is consistent with the ideas of Trinkhaus et al [13,14], who have reported that small interstitial clusters can unfault to form glissile dislocation loops and therefore migrate in one dimension. We didn't consider the migration of small vacancy clusters because their binding energies are small compared with the migration energy of the mono-vacancy, and are therefore expected to dissolve quickly at 600 K.

A typical defect evolution time-history during a 600 K anneal of a 20keV cascade shows that free mono-interstitials begin to migrate at $t = 1 \times 10^{-10}$ s. This causes an increase in the number of interstitials in clusters and a decrease in the number of free vacancies through recombination. At 1×10^{-8} s, the number of

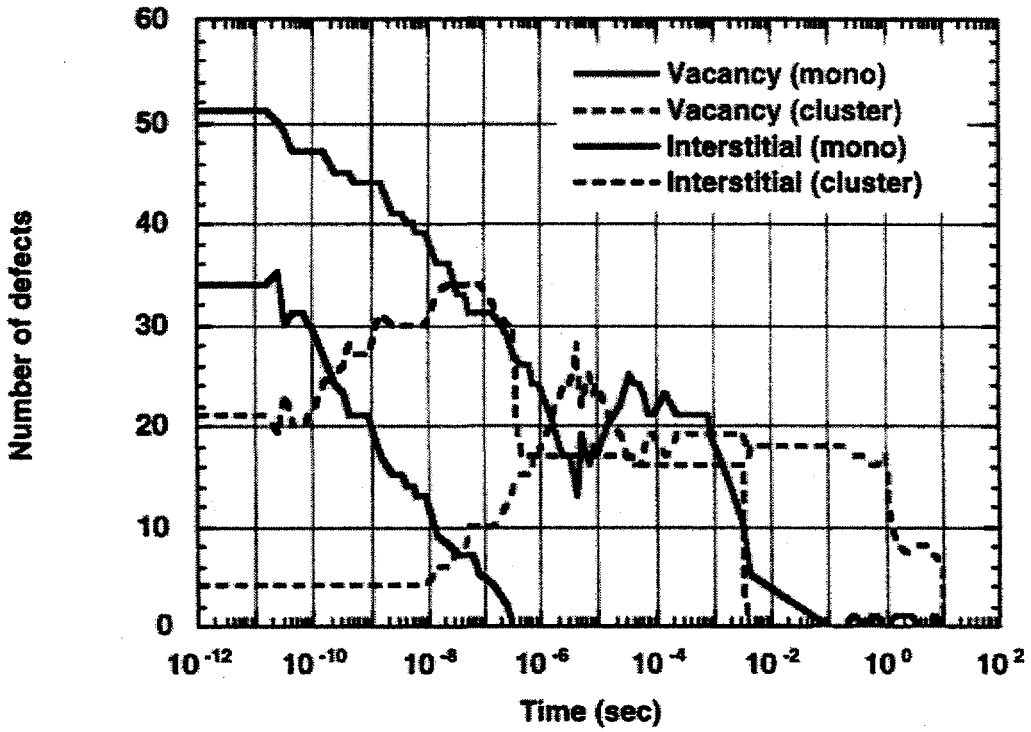

Figure 3. Time evolution of the defect microstructure produced by a 20 keV cascade in α-Fe during annealing at 600 K.

vacancies in clusters starts to increase, as a result of free vacancy migration. The number of free mono-interstitials becomes zero within 1 μs due to either recombination, clustering, or migration out of the KMC box. A large decrease observed in the number of interstitials in clusters at times around 1 μs and 10 ms arises from the escape of two large interstitial clusters from the box at these times. An increase in the number of free vacancies at 1x10-5 s is caused by dissociation of small vacancy clusters. Two large decreases in the number of vacancies in clusters at around 1 s and 10 s also arise from dissociation of vacancy clusters. The emitted mono vacancies from these clusters can migrate to the surface of the KMC computational box very quickly compared with the time scale of 1 s. All the defects annihilate by recombination or escape from the box within the first 10 s.

The results of these simulations show that a very small difference can be observed between the escape ratios of interstitials and vacancies for recoil energies greater than 10 keV. This is due to the formation of very large (>15) immobile interstitial clusters, an event which occurs with very small probability in all of the calculations performed here. For recoil energies less than 1keV, the escape ratios of vacancies and interstitials are identical and exceed 80%. This value decreases to about 65% as the recoil energy increases to 20keV. The sum of the escape ratios of mono- & di- interstitials, which can migrate three-dimensionally, and larger mobile interstitial clusters, which migrate one-dimensionally is the overall escape ratio of interstitials. For low recoil energies, the escape of mono- and di-interstitials is dominant. However, this tendency is reversed between 5 and 10 keV, and the escape ratio of mono- & di-interstitials becomes only

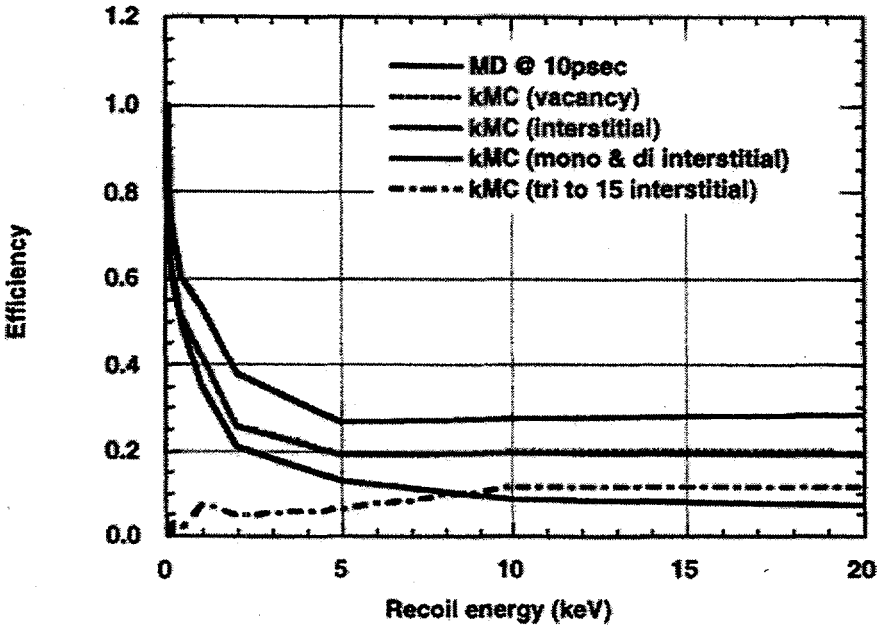

Figure 4. Freely Migrating Defect production efficiency in α-Fe during irradiation at 600 K as a function of recoil energy. At 20 keV, 60% of all defects produced escape their nascent cascade. The same number of vacancies and interstitials escape, but the 80% of the escaping interstitials do so as loops that glide in one dimension.

20% at 20 keV. On the other hand, all the vacancies escaping from the cascade are mono-vacancies, which migrate three-dimensionally. The FMD production efficiency is the product of the production efficiency in the cascade and the escape fraction, and is shown as a function of recoil energy at 600 K in Fig. 4. Total FMD production efficiencies for vacancies and interstitials decrease rapidly as the recoil energy increases, and saturate at about 20% of the NRT model predictions for the PKA energies larger than 5keV.

4. Summary

In summary, we have presented MD simulations of defect production in Fe and V at recoil energies typical from 100 eV to 20 keV. The simulations show that above 5 keV interstitials are produced in clusters with high probability, and that virtually no vacancy clusters result from these cascades. These results agree well with other MD simulations of cascades in α-Fe by Stoller et al. [15]. We have shown how the large local stresses within the cascade region can act to unfault small interstitial clusters resulting in the production of mostly glissile loops.

The MD results were used as input to KMC simulations of defect diffusion and interaction. The KMC simulations provide insight into the physical processes that take place within a few seconds following the displacement cascade. Our results show that for recoil energies less than 1 keV about 80% of the vacancies and interstitials produced in the cascade escape recombination . This value only decreases to 65% when the recoil energy increases to 20 keV. This high escape probability even in the case of dense displacement cascades is associated with the fact that in α-Fe many interstitials are produced in the form of small glissile loops, and the vacancies are all produced as isolated mono-vacancies and not as large collapsed Frank loops.

Two thirds of all escaping interstitials did so as gliding loops and only one third as three-dimensionally migrating self-interstitials. The production efficiency of freely migrating defects in Fe is 20% of the dpa standard for 20 keV recoils.

Work is under way to include the effect of sinks such as dislocations, grain boundaries, alloy components, and impurity atoms (e.g. He, C) in the KMC simulations of defect microstructure evolution. In addition, the role of inter-cascade annihilation (dose, dose rate) in the evolution of the system will be consider in the near future. Work is also under way to develop three-dimensional dislocation dynamics simulations to predict the changes in yield stress and strain hardening exponents as a fucntion of irradiation time associated with the evolving microstructure as obtained by the MD/KMC simulations.

REFERENCES

[1] Soneda, N. and Diaz de la Rubia, T., To be published.
[2] Diaz de la Rubia, T., 1996, *Annu. Rev. Mater. Sci.*, 26, 613.
[3] Phythian, W.J., Stoller, R.E., Foreman, A.J.E., Calder, A.F., and Bacon, D.J., 1995, *J. Nucl. Mater.*, 223, 245.
[4] Jaraiz, M., Gilmer, G.H., Poate, J.M., and Diaz de la Rubia, T., 1996, *Appl. Phys. Lett.*, 68, 409.
[5] Heinisch, H.L., 1995, *Nucl. Instr. and Meth. in Phys. Res. B*, 102, 47.
[6] Diaz de la Rubia, T. and Guinan, M.W., 1990, *J. Nucl. Mater.*, 174, 151.
[7] Johnson, R.A., and Oh, D.J., 1989, *J. Mater. Res.*, 4, 1195.
[8] Guellil, A.M., and Adams, J.B., 1992, *J. Mater. Res.*, 7, 639.
[9] Alonso, E., Tang, M., and Diaz de la Rubia, T. 1997, Mater. Res. Soc. Symp. Proc. in press.
[10] Morishita, K. and Diaz de la Rubia, T., 1996, Mater. Res. Soc. Symp. Proc. 396, 39.
[11] M.J. Norgett, M.T. Robinson and I.M. Torrens, *A proposed method of calculating displacements dose rates*, Nuc. Eng. and Design 33 (1975) 50-54
[12] R.S. Averback, R. Benedek and K.L. Merkle, *Phys. Rev. B* 18, 4156 (1978).
[13] Trinkhaus, H., Singh, B.N., Foreman, A.J.E., 1992, *J. Nucl. Mater.* 199, 5.
[14] Trinkhaus, H., Singh, B.N., Foreman, A.J.E., 1993, *J. Nucl. Mater.* 206, 200.
[15] Stoller, R.E., 1997, *J. Nucl. Mater.* 237, 999.

STOCHASTIC ANNEALING SIMULATIONS OF DEFECT INTERACTIONS AMONG SUBCASCADES- H. L. Heinisch (Pacific Northwest National Laboratory[1]) and B.N. Singh (Risø National Laboratory)

OBJECTIVE

The objective of this work is to determine the energy and temperature dependence of defect production and microstructure evolution for the development of fission-fusion correlations.

SUMMARY

The effects of the subcascade structure of high energy cascades on the temperature dependencies of annihilation, clustering and free defect production are investigated. The subcascade structure is simulated by closely spaced groups of lower energy MD cascades. The simulation results illustrate the strong influence of the defect configuration existing in the primary damage state on subsequent intracascade evolution. Other significant factors affecting the evolution of the defect distribution are the large differences in mobility and stability of vacancy and interstitial defects and the rapid one-dimensional diffusion of small, glissile interstitial loops produced directly in cascades. Annealing simulations are also performed on high-energy, subcascade-producing cascades generated with the binary collision approximation and calibrated to MD results.

PROGRESS AND STATUS

Even after the longest practical MD simulation, the defect clusters of a single cascade remain spatially localized in a "metastable" state far from the spatial and temporal uniformity required for the global picture to which rate theory may be applied. Atomic scale stochastic annealing simulation provides the necessary link between the localized, short-term, atomistic view of individual MD cascades and the spatially averaged global view required for the application of rate theory.

SUBCASCADE INTERACTIONS. Irradiations by high energy sources such as fusion neutrons, spallation neutrons, high energy protons and heavy ions produce a significant amount of damage in the form of high energy cascades that have multiple subcascades. It is important to know how the defect evolution within the high energy cascade is affected by the presence of subcascades in close proximity. Present computational resources are not capable of routinely generating high energy cascades by MD in the large numbers and arbitrary orientations required for good statistics. However, it should be possible to study the effects of subcascades on the annealing stage of high energy cascades by simply "constructing" multiple-subcascade cascades from a set of lower energy cascades, i.e., by placing individual cascades in close proximity and annealing them simultaneously. This procedure does not address the possible interactions among subcascades during the thermal spike or quenching stages.

Multiple-subcascade cascades in copper were approximated by replicating two 25 keV copper cascades [1] in several randomly chosen positions at a fixed separation distance to produce cascades with 2-5 "subcascades." The center-to-center separation of subcascades in this pseudo-cascade is 35 lattice parameters, slightly less than the average subcascade spacing determined in binary collision simulations of

---

[1]*Pacific Northwest National Laboratory is operated for the U.S. Department of Energy by Battelle Memorial Institute under Contract DE-AC06-76RLO 1830.*

copper cascades[2]. The pseudo-cascade also has been given a more compact configuration than the average cascade in copper to maximize possible effects of intersubcascade defect interactions. The results of annealing 100 such pseudo-cascades as a function of temperature are shown in Fig. 1. The fractions of surviving pairs and escaping defects are about 10% less than for the average of 100 anneals of the two individual 25 keV cascades (i.e. infinite separation), which is on the order of the standard deviation of the average values. Thus, there is only a minor effect of subcascade interaction during the annealing stage. There is a small systematic decrease in surviving and escaping defect fractions as a function of the number of subcascades per cascade, but there is essentially no effect of subcascade interaction on the average SIA and vacancy cluster sizes.

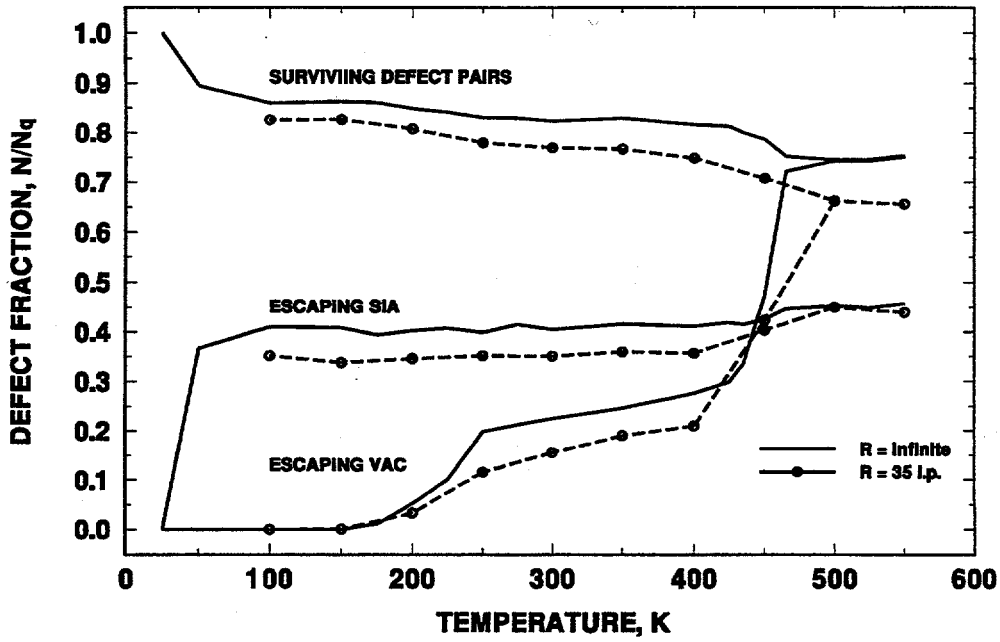

Figure 1. The fractions of point defects surviving recombination and of vacancies and interstitials escaping from 25 keV cascades in copper during the annealing stage, as a function of cascade annealing temperature. A comparison is made of annealing results for individual 25 keV copper cascades (R = infinite) and pseudo-cascades consisting of sets of five 25 keV "subcascades" having an average center-to-center separation of 35 lattice parameters (R = 35 l.p.). Each data point represents the average of anneals of 100 different arrangements of the five cascades.

APPROXIMATING HIGH ENERGY CASCADES. In light of the small amount of interaction observed among subcascades, it might be possible to estimate defect production and evolution in high energy, subcascade-producing cascades by linearly extrapolating from results at cascade energies near the subcascade threshold. However, even though MD has been used successfully to simulate cascades near threshold energies, those simulations are at the limit of computational capabilities, and only a small number of cascades can be produced at those energies. Also, at energies above the threshold, the size distribution of

subcascades may have significant influence on defect production and should be studied. Thus, it is of interest to develop easily-calculated approximations to high-energy cascades for such studies, especially for input to annealing simulations. A reasonable starting point is to use the binary collision approximation to simulate the collisional stage of the cascade. Variations of this approach have been employed, of necessity, several times in the history of radiation effects simulations [3,4,5].

A major advantage over the earlier attempts is that MD simulations now exist to which the binary collision calculations can be calibrated. A series of individual time steps of the two 25 keV cascades in copper discussed above have been analyzed to extract the collisional stage information that would be calculated in a binary collision approximation to this cascade. Thus, both the collisional stage configuration of displaced atoms and the post-quench defect configuration are known for the MD cascade. The ideal calibration would consist of a general algorithm for the transformation of the collisional stage displacement configuration to the quenched stage defect distribution. As a first attempt, the method of Ref. [5] was used. That is, exaggerated parameter values for defect mobility and interaction distances were applied to the binary collision results for a simulated time of about 10 ps, the typical duration of cascade evolution through the quenching stage. It is possible to choose "quenching" parameter values that give correct numbers of post-quench defects, but the cluster size distributions and the compactness of the post-quench vacancy distribution observed in the MD simulations cannot be achieved by this approach.

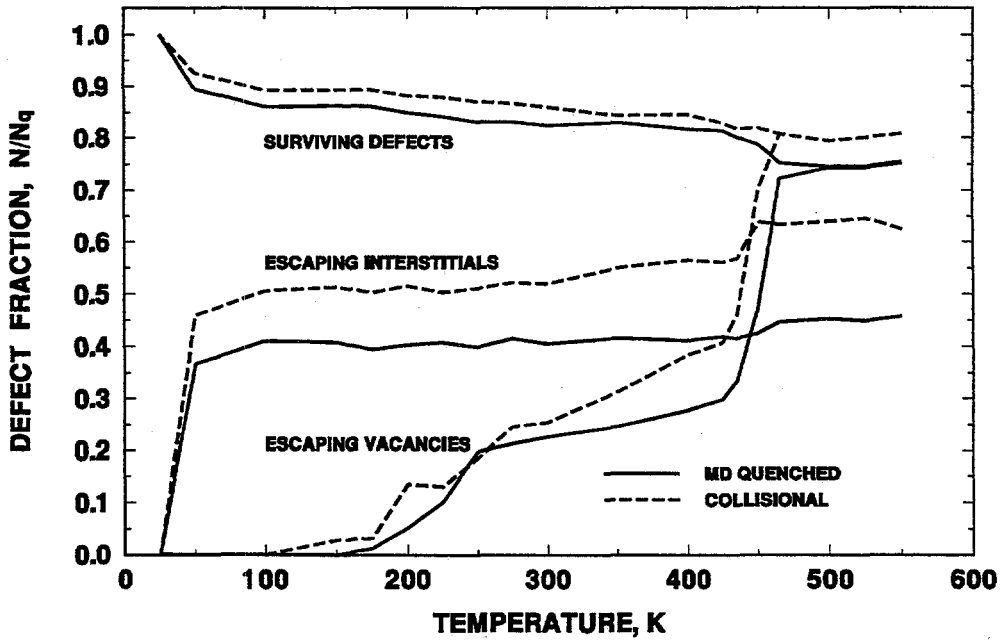

Figure 2. The fractions of point defects surviving recombination and of vacancies and interstitials escaping from 25 keV cascades in copper during the annealing stage, as a function of cascade annealing temperature. The solid lines are for the annealing of cascades fully quenched by MD, while the dashed lines are for the annealing of the same cascades that were artificially quenched from the collisional stage.

Obtaining the correct defect configuration after the artificial quenching stage may not be so important if the defect configuration following the subsequent annealing stage is well described. Thus, annealing simulations were performed for the 25 keV cascades artificially quenched from the collisional stage. Fig. 2 shows the results as a function of annealing temperature. These results are encouraging, being qualitatively similar to those obtained for the quenched MD cascades. The largest discrepancy is in the numbers of escaping SIAs, because fewer large, immobile SIA clusters form during the artificial quench. Because of the importance of the SIA and vacancy clusters and their stability and diffusion characteristics to the results of the annealing stage, a more realistic artificial quenching scheme is required, especially one that more specifically deals with the energy and particle transport properties of the material.

FUTURE WORK

The results discussed here were included in a presentation at the workshop on Defect Production, Accumulation and Materials Performance in Irradiation Environment, Davos, Switzerland, October 2-8, 1996. Proceedings will be published in the Journal of Nuclear Materials. Refinements of the model for high energy cascades are in progress, and annealing simulations of defect accumulation under ongoing irradiations are being developed.

REFERENCES

1. T. Diaz de la Rubia and M.W. Guinan, Mat. Sci. Forum **97-99** (1992) 23.

2. H.L. Heinisch and B. N. Singh, Phil. Mag. A **67**, 407 (1993).

3. J.R. Beeler, Proc. Int. Conf. on Radiation Induced Voids in Metals, Albany NY, June 1971, J.W. Corbett and L.C. Ianniello, eds. (1972) 684.

4. D.G. Doran and R.A. Burnett, in Interatomic Potentials and Simulation of Lattice Defects, P.C Gehlen, J.R. Beeler, R.I. Jaffee, eds., Plenum Press, NY, 1972, p. 403.

5. H.L. Heinisch, J. Nucl. Mater. **117** (1983) 46.

THE EFFECTS OF SELF-INTERSTITIAL CLUSTERS ON CASCADE DEFECT EVOLUTION BEYOND THE PRIMARY DAMAGE STATE - H. L. Heinisch (Pacific Northwest National Laboratory[1])

OBJECTIVE

The objective of this work is to determine the energy and temperature dependence of defect production and microstructure evolution for the development of fission-fusion correlations.

SUMMARY

The intracascade evolution of the defect distributions of cascades in copper is investigated using stochastic annealing simulations applied to cascades generated with molecular dynamics (MD). The temperature and energy dependencies of annihilation, clustering and free defect production are determined for individual cascades. The annealing simulation results illustrate the strong influence on intracascade evolution of the defect configuration existing in the primary damage state. Another factor significantly affecting the evolution of the defect distribution is the rapid one-dimensional diffusion of small, glissile interstitial loops produced directly in cascades. This phenomenon introduces a cascade energy dependence of defect evolution that is apparent only beyond the primary damage state, amplifying the need for further study of the annealing phase of cascade evolution and for performing many more MD cascade simulations at higher energies.

PROGRESS AND STATUS

Using MD, cascade simulations can follow the evolution of the cascade region through the quenching of the thermal spike (about 10 ps) and perhaps somewhat beyond (about 100 ps), depending on the energy. Once the cascade energy is dissipated during the quenching stage, little happens on the picosecond time scale. However, the cascade, consisting of a high concentration of defects in a small volume, is in a metastable state that continues to evolve by thermally activated diffusion, during which intracascade annealing results in recombination and clustering, as well as escape of some defects from the cascade region. Thus, simulating the annealing stage of cascade evolution offers the possibility of determining definitively the defect distributions individual cascades contribute to the global picture.

The annealing simulation code used for these studies and its input parameters are described in detail elsewhere [1]. The essential input parameters for the annealing simulations are the relative jump probabilities of the mobile defects at the temperature simulated and the critical reaction distances. Another element of the present annealing model is the dissolution of clusters. The relative frequency of single defect emission from a cluster as a function of cluster size is calculated using cluster binding energies from computer simulations [1].

The self-interstitial atom defects (SIA) are assumed to have two forms, depending on size. MD simulations of cascades in copper clearly show that SIA clusters exist in the primary damage state, i.e, that SIAs form clusters directly in cascades during the first 10 ps, and that the clusters collapse to glissile loops that move one-dimensionally. The present annealing model assumes that SIA clusters of size 1-3 are mobile in 3

---

[1]*Pacific Northwest National Laboratory is operated for the U.S. Department of Energy by Battelle Memorial Institute under Contract DE-AC06-76RLO 1830.*

dimensions and that SIA clusters of size 4-9 are mobile in 1 dimension. Clusters larger than size 9 are considered immobile. The activation energy for 1-dimensional glide is taken as 0.1 eV, about the same as for the motion of a single SIA, independent of size. This model is based on Trinkaus, Singh and Foreman's interpretations of MD simulations [2], which is probably correct in concept, but not quantitatively definitive. There still does not exist enough information, either from MD simulations or experiments to sufficiently determine the characteristics of the formation of glissile SIA loops in cascades and their kinetics during the annealing stage. Stochastic annealing simulations, however, provide an excellent tool for studying the sensitivity of the effects of glissile loop properties on the annealing stage.

Figure 1 shows the fraction of surviving defect pairs and the fractions of escaping vacancies and SIAs after the annealing stage of two 25 keV cascades simulated with MD in copper as a function of temperature. The average fractions are determined relative to the number of defects remaining

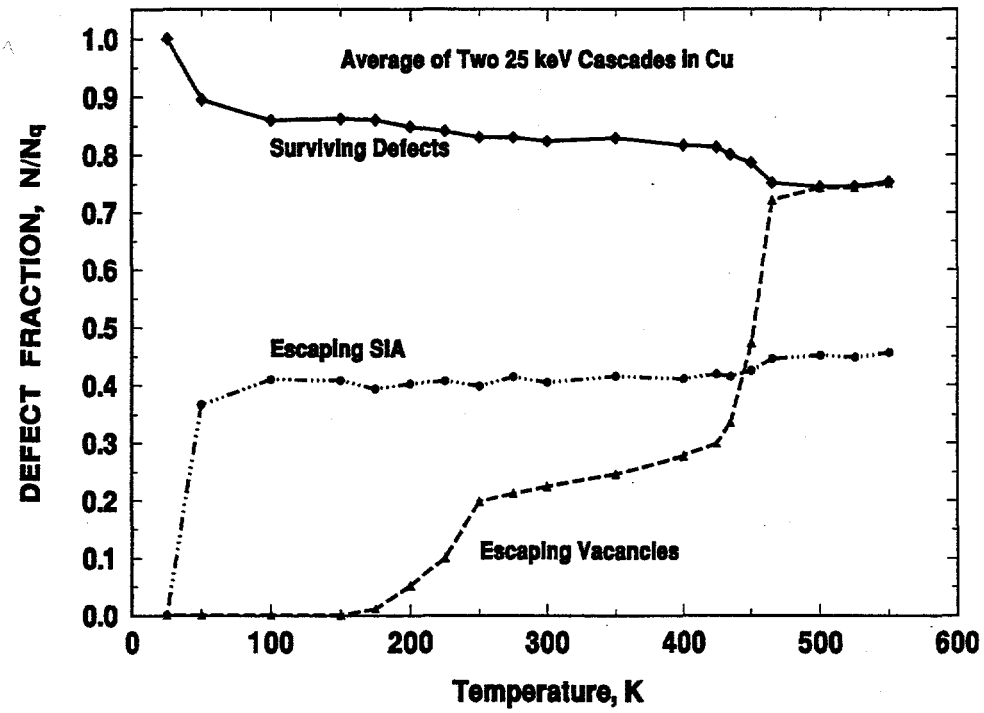

Figure 1. The fractions of point defects surviving recombination and of vacancies and SIAs escaping from 25 keV cascades in copper during the annealing stage, as a function of cascade annealing temperature. Each data point is the average of 100 anneals of each of two 25 keV cascades in copper generated in MD simulations.

in the cascades after quenching (i.e. at the end of the MD simulations) for 100 separate anneals of each of the two cascades. During the annealing stage, about 20% of the initial defects recombine and about 40% of the SIAs escape the cascade, with weak dependence on the temperature. The other 40% of the initial SIAs remain in the cascade region as immobile clusters. Approximately 60% of the SIAs that escape are in the form of small glissile loops moving in 1-dimensional random walks. Almost all the recombination

occurs as a result of the diffusion of the SIAs. An increasing fraction of the original mobile vacancies escapes the cascade at temperatures from 175-250 K. From 250-400 K small clusters also start to dissolve. Above 450 K all vacancy clusters are unstable and readily dissolve, resulting in slightly more recombination and escape of all remaining vacancies.

The situation depicted in Fig. 1 changes significantly when the size limit for glissile loops is changed in the annealing model. The same information in Figure 1 is plotted in Figure 2 for four values of the size limit for glissile SIA loops. The curve labeled G=9 refers to the escaping SIAs in the "standard" model which has glissile loops of size 4-9, as depicted in Figure 1. The curve labeled G=none is when no glissile loops are permitted and only SIA clusters of size 1-3 are mobile, moving in three dimensions. The fraction of SIAs that escape the cascade region varies from 10-80%, depending on the size of SIA clusters that are assumed to be glissile loops in the annealing model. It is obvious that few clusters consisting of more than 20 SIAs are formed in these cascades, even during the annealing stage. Because of this narrow size range, the upper limit for glissile loop formation has a large impact.

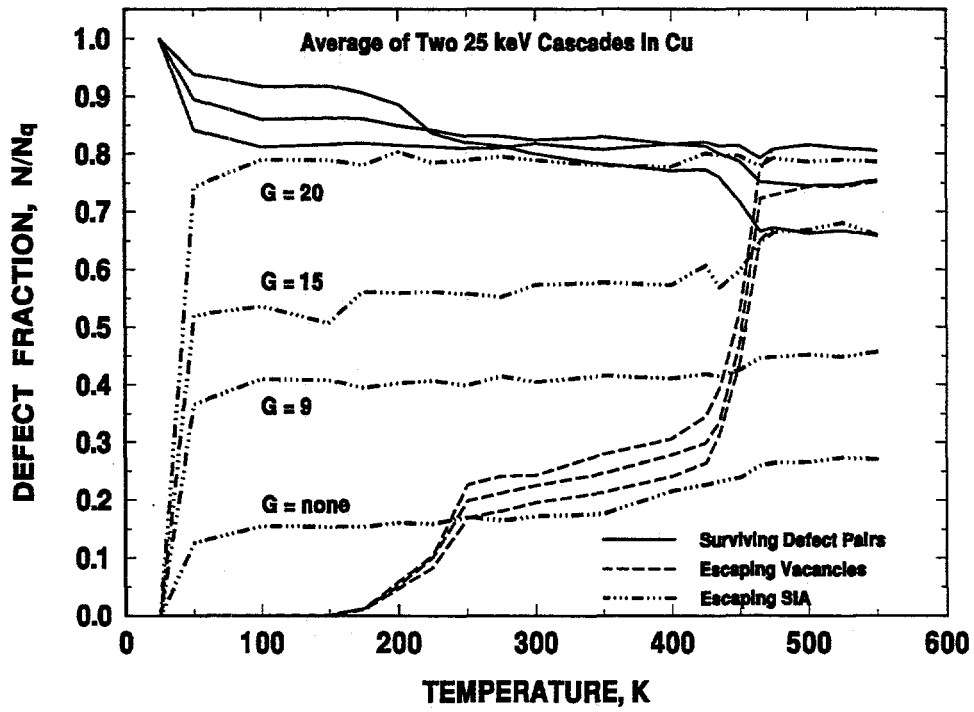

Figure 2. The fractions of surviving and escaping defects as a function of temperature for 25 keV cascades as in Fig. 1. The effects of changing the size limit for glissile SIA loops on the annealing behavior is illustrated.

DISCUSSION

Figure 2 reveals the importance of knowing the characteristics of SIA loop formation and kinetics in cascades. It is also of interest to note from Fig. 2 that the fractions of surviving defects and escaping

vacancies vary much less with the glissile SIA loop size limit than does the fraction of escaping SIAs, implying that the glissile SIA loops have few interactions with the vacancy population, and that recombination is due almost entirely to the diffusion of the small SIA clusters. This vividly illustrates the significant difference between the 1-dimensional random walk of glissile SIA loops and the 3-dimensional random walk of the small SIA clusters.

Sensitivity to the glissile SIA loop size limit during the annealing stage also implies a possible energy dependence in the global field of defects that has gone unrecognized. The probability of producing large SIA clusters is smaller for lower energy cascades. Even in the energy range of 5-25 keV the ratio of mobile to immobile SIAs that are formed may vary significantly. This energy sensitivity also affects the rates of SIA survival, which depend on the relative numbers of SIAs in glissile loops. It is likely that SIA loops up to size 20 and larger are glissile, and also likely that the migration energies of glissile loops increase with size. Additional MD simulations can shed considerable light on this key issue.

Determining glissile loop characteristics may now be the most important issue for annealing simulations, but it is not the only important issue. Virtually all the activation energies and pre-factors for the diffusion and emission processes need to be evaluated using consistent simulation approaches, and they need to be checked against experimental information where possible. Critical reaction distances need to be evaluated carefully as well. Atomic-scale defect studies need to be carried out to verify the use of homogeneous random hops in the annealing simulations, or to determine what correlated motions of defects are required to accurately model the annealing stage. Finally, but very important, is the need to establish a data base containing many more higher energy cascades than presently exist for each material of interest. Energies should range up to, and perhaps beyond, the threshold for subcascade formation, which is approximately 25 keV for copper [3]. Although the damage energy and the number of initially displaced atoms in cascades of the same energy have fairly narrow distributions, the distribution of sizes and shapes, which can affect defect interactions during the annealing stage, is quite broad [3]. The two 25 keV cascades used in this work so far are both somewhat compact, so some conclusions drawn from the results here may not be representative of the average behavior. In general, the higher the cascade energy, the less likely any single cascade, or small sample of cascades, can be considered to be typical of the entire distribution.

FUTURE WORK

The results discussed here were included in a presentation at the Symposium on Microstructure Evolution During Irradiation, 1996 Fall MRS Meeting, Dec. 2-6, 1996, Boston, and will appear in the proceedings. These results were also discussed at the workshop on Defect Production, Accumulation and Materials Performance in Irradiation Environment, Davos, Switzerland, October 2-8, 1996. Proceedings will be published in the Journal of Nuclear Materials. Annealing simulations are in progress on a library of cascades in copper generated by Alan Foreman et al. at Harwell. We are also working on annealing studies of cascades in iron and other materials in collaboration with the University of Liverpool.

REFERENCES

1. H. L. Heinisch and B. N. Singh, J. Nucl. Mater. **232** (1996) 206.

2. H. Trinkaus, B.N. Singh and A.J.E. Foreman, J. Nucl. Mater. **206** (1993) 200.

3. H.L. Heinisch and B. N. Singh, Phil. Mag. A **67**, 407 (1993).

9.0 DOSIMETRY, DAMAGE PARAMETERS, AND ACTIVATION CALCULATIONS

NEUTRON DOSIMETRY AND DAMAGE CALCULATIONS FOR THE EBRII COBRA-1A IRRADIATIONS

L. R. Greenwood and R. T. Ratner (Pacific Northwest National Laboratory)

OBJECTIVE

To provide dosimetry and damage analysis for fusion materials irradiation experiments.

SUMMARY

Neutron fluence measurements and radiation damage calculations are reported for the joint U. S. and Japanese COBRA-1A1 and 1A2 irradiations in the Experimental Breeder Reactor II. The maximum total neutron fluences at midplane were 2.0E+22 and 7.5E+22 n/cm^2, for the 1A1 and 1A2 irradiations, respectively, resulting in about 8.0 and 30.3 dpa in stainless steel.

PROGRESS AND STATUS

The COBRA-1A (Cold B7A Radiation Assembly) subassembly X516, consisting of seven B7A capsules (denoted B388 to B394), was irradiated in EBR-II core position 2B1 from November 26, 1992, to April 1, 1993 for a net exposure of 88.6 EFPD (effective full power days) at a nominal power of 62.5 MW. Three of the capsules, B392-394 (denoted as COBRA-1A1) were then removed from the reactor for analysis. The remaining four capsules, denoted as COBRA-1A2, then continued irradiation in core position 2B1 until September 26, 1994, for a net exposure of 337.3 EFPD. A complete description of the COBRA experimental matrix has been published previously.[1]

Neutron dosimetry capsules designed to measure the neutron energy spectra were located at six different locations, one in irradiation 1A1 (B392) and the rest in 1A2 (B389). Twenty dosimetry capsules designed to measure the neutron fluence gradients were also placed at different locations throughout the subassembly, sixteen in 1A2 and four in 1A1. The precise locations of the capsules are listed in Table 1. The spectral capsules contained small wires of Fe, Ni, Ti, Cu, Nb, 80.2 Mn-Cu, 0.1% Co-Al, ^{235}U, ^{238}U, and ^{237}Np. The gradient capsules contained only Fe and 0.1% Co-Al wires.

After irradiation, each dosimetry capsule was opened in a hot cell and each individual monitor wire was gamma counted to determine the residual activation. The measured activities were converted to activation rates by correcting for nuclear burnup, gamma self-absorption, decay during and after irradiation, isotopic abundance, and atomic weight. Burnup corrections are based on an iterative procedure for the thermal/epithermal monitor reactions. The resultant estimates of the thermal/epithermal neutron fluences were then used to calculate burnup corrections for the threshold fast neutron monitor reactions. Burnup corrections were $< 10\%$ for the thermal/epithermal reactions and were negligible for the threshold reaction rates. The activation rates are listed in Table 1 for the six neutron spectral locations. The full gradient data are shown in Figure 1. It is interesting to note that the ^{59}Co(n,γ) activation rates increase away from core center due to the rapidly increasing epithermal neutron flux. All activity values are normalized to full reactor power of 62.5 MW and have a net absolute uncertainty of about 5%.

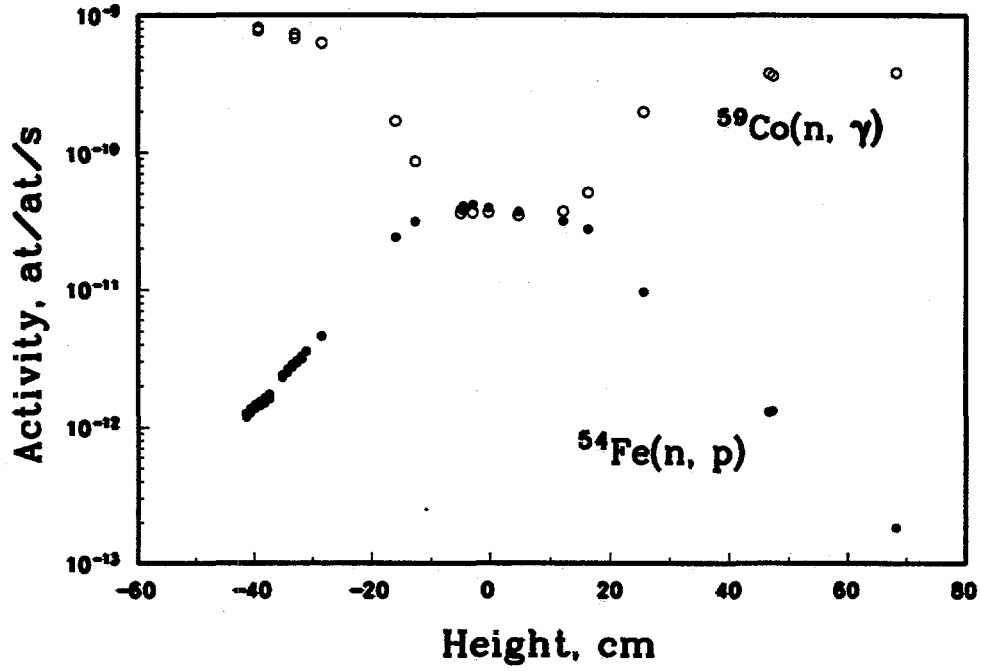

Figure 1 Activation rates as a function of height in the COBRA-1A subassembly.

Radial flux gradients can be estimated from a comparison of Fe and Co wires located in different irradiation capsules. The plots in Figure 1 show that all of the available data fall on a relatively smooth curve indicating that the radial flux gradients are rather small, as might be expected for an irradiation near core center in Row 2 of EBR II. Detailed analysis of the data show that the fast radial flux gradients average about 3-7%. Variations in the epithermal flux are less than 4%. These radial flux gradients have been neglected in subsequent analyses.

Midplane activation rates were used in the STAY'SL[2] computer code to adjust calculated neutron flux spectra for EBR II. STAY'SL performs a generalized least-squares adjustment of all measured and calculated values including the measured activities, calculated spectra, neutron cross sections, and uncertainties. Neutron cross sections and their uncertainties were generally taken from the ENDF/B-V[3] evaluation. The activation rates and the derived neutron spectra and fluences are in good agreement with the calculated neutron spectra near midplane; however, more spectral adjustment is required away from midplane.

Neutron damage calculations were performed using the SPECTER computer code[4] using the adjusted neutron spectra at the six locations of the neutron spectral dosimeters. The neutron gradient data were then used to determine neutron fluence and damage parameters for other locations, as listed in Tables 2 and 3. The total and fast (> .1 MeV) neutron fluences are listed along with the net dpa (displacements per atom) in iron and stainless steel (Fe-18Cr-8Ni).

Helium production in nickel and nickel-bearing alloys requires a more complicated non-linear calculation.[5] Helium production in stainless steel is listed in Tables 3 and 4. Near the core midplane, the extra helium produced by ^{59}Ni is negligible (0.3%). However, due to the increase in epithermal neutrons at outer locations, the nickel reactions increase helium production by 15% at -28.6 cm and by 22% at +46.7 cm. In all cases, the increased helium production due to nickel has no effect on the dpa values. Dpa and helium values for other elements and alloys are available on request.

FUTURE WORK

Additional experiments are in progress in the High Flux Isotopes Reactor.

REFERENCES

1. M. L. Hamilton, R. M. Ermi, and C. R. Eiholzer, Preparation of COBRA 1A for Insertion into EBR-II, Fusion Reactor Materials Semiannual Progress Report, DOE/ER-0313/14, pp. 3-13 (1993).

2. F. G. Perey, Least Squares Dosimetry Unfolding: The Program STAY'SL, ORNL/TM-6062 (1977).

3. Evaluated Nuclear Data File, Part B, Version V, National Nuclear Data Center, Brookhaven National Laboratory.

4. L. R. Greenwood and R. K. Smither, SPECTER: Neutron Damage Calculations for Materials Irradiations, ANL/FPP-TM-197, January 1985.

5. L. R. Greenwood, A New Calculation of Thermal Neutron Damage and Helium Production in Nickel, Journal of Nuclear Materials 116, pp. 137-142 (1983).

TABLE 1 - Activation Rates (at/at-s) - COBRA-1A

Sample Position	Ht.cm	$^{54}Fe(n,p)^{54}Mn$ (E-11)	$^{46}Ti(n,p)^{46}Sc$ (E-12)	$^{63}Cu(n,a)^{60}Co$ (E-13)	$^{58}Ni(n,p)^{58}Co$ (E-11)	$^{60}Ni(n,p)^{60}Co$ (E-13)
C08-B03	-28.6	0.463	0.508	0.241	0.642	0.930
C09-B04	-16.1	2.44	3.08	1.41	3.46	5.66
E01-E07	- 3.1	4.20	5.20	1.77	4.06	7.23
C11-B10	16.2	2.79	3.62	1.69	4.10	6.99
C12-B11	25.6	0.972	1.15	0.539	1.45	2.29
C13-B12	46.7	0.130	0.138	0.067	0.206	0.306

TABLE 1 - Activation Rates (at/at-s) - COBRA-1A, Cont.

Sample Position	Ht,cm	$^{235}U(n,f)$ (E-9)	$^{238}U(n,f)$ (E-10)	$^{237}Np(n,f)$ (E-9)	$^{93}Nb(n,g)^{94}Nb$ (E-10)	$^{55}Mn(n,2n)^{54}Mn$ (E-14)	$^{59}Co(n,g)^{60}Co$ (E-10)
C08-B03	-28.6	4.16	1.38	0.479	2.96	1.07	6.33
C09-B04	-16.1	3.66	1.71	1.09	2.77	6.09	1.72
E01-E07	- 3.1	3.21	2.20	1.43	2.26	10.79	0.368
C11-B10	16.2	3.03	1.58	1.13	2.05	7.23	0.511
C12-B11	25.6	2.55	0.775	0.549	2.30	2.38	2.00
C13-B12	46.7	2.09	0.354	0.151	1.94	0.327	3.81

TABLE 2 - Neutron Fluence and DPA - COBRA-1A1 (88.6 EFPD)

Sample Position	Ht,cm	Total Fluence (E+22 n/cm2)	Fluence >.1 MeV (E+22 n/cm2)	dpa (Iron)	dpa Fe-18Cr-8Ni	He(appm) Fe-18Cr-8Ni
C08-B03	-28.6	1.10	0:688	2.64	2.74	0.23
C09-B04	-16.1	1.75	1.30	6.16	6.37	1.31
E01-E07	- 3.1	1.97	1.56	7.70	7.95	1.89
C11-B10	16.2	1.57	1.23	5.93	6.12	1.58
C12-B11	25.6	1.04	0.701	3.00	3.10	0.51
C13-B12	46.7	0.603	0.308	1.12	1.17	0.07

TABLE 3 - Neutron Fluence and DPA - COBRA-1A2 (337.3 EFPD)

Sample Position	Ht,cm	Total Fluence (E+22 n/cm2)	Fluence >.1 MeV (E+22 n/cm2)	dpa (Iron)	dpa Fe-18Cr-8Ni	He(appm) Fe-18Cr-8Ni
C08-B03	-28.6	4.19	2.62	10.1	10.4	0.98
C09-B04	-16.1	6.66	4.95	23.5	24.2	5.02
E01-E07	- 3.1	7.50	5.94	29.3	30.3	7.20
C11-B10	16.2	5.98	4.68	22.6	23.3	6.04
C12-B11	25.6	3.96	2.67	11.4	11.8	1.99
C13-B12	46.7	2.30	1.17	4.26	4.47	0.30

NEUTRON DOSIMETRY AND DAMAGE CALCULATIONS FOR THE HFIR-JP-23 IRRADIATIONS

L. R. Greenwood and R. T. Ratner (Pacific Northwest Laboratory)

OBJECTIVE

To provide dosimetry and damage analysis for fusion materials irradiation experiments.

SUMMARY

Neutron fluence measurements and radiation damage calculations are reported for the joint U.S.-Japanese experiment JP-23, which was conducted in target position G6 of the High Flux Isotope Reactor (HFIR) at Oak Ridge National Laboratory (ORNL). The maximum neutron fluence at midplane was 4.4E+22 n/cm^2 resulting in about 9.0 dpa in type 316 stainless steel.

PROGRESS AND STATUS

The JP-23 experiments were irradiated in the G6 target position of HFIR during cycles 322 through 326, starting December 16, 1993, and ending June 3, 1994, for a net exposure of 110.2 effective full power days at 85 MW. The experiment was a collaborative effort co-sponsored by the U. S. Neutron Interactive Materials Program at PNNL and the Japanese Monbusho Program. The goal of the experiment was to irradiate TEM specimens at four temperatures of 300, 400, 500, and 600°C. A complete description of the specimen matrix and irradiation assembly has been published previously.[1]

Neutron dosimetry capsules were inserted in the bottom cavities of each TEM specimen holder, each of which measured 4.17 cm in length. The dosimetry capsules consisted of small, welded aluminum tubes measuring about 1.3 mm in diameter and 6.4 mm in length. Each tube contained small monitor wires of Fe, Ni, Ti, Nb, and 0.1% Co-Al alloy. Six capsules were irradiated with the JP-23 specimens; however, only five were recovered during disassembly. Each capsule was opened in a hot cell at PNNL and each individual monitor wire was gamma counted to determine the residual activation.

The measured activities were converted to activation rates as listed in Table 1 by correcting for nuclear burnup, gamma self-absorption, decay during and after irradiation, isotopic abundance, and atomic weight. Burnup corrections are based on an iterative procedure for the thermal/epithermal monitor reactions. The resultant estimates of the thermal/epithermal neutron fluences were then used to calculate burnup corrections for the threshold fast neutron monitor reactions. Burnup corrections averaged 20-30% for the thermal/epithermal reactions and 5-15% for the threshold reaction rates. The activation rates listed in Table 1 are normalized to full reactor power of 85 MW and have a net absolute uncertainty of about 5%.

The activation rates in Table 1 were fit to a polynomial function of form $f(x) = f(0)\,[\,1 + a\,x^2\,]$, where x is the vertical height from reactor centerline in cm. All of the data are reasonably well fit by the average polynomial (coefficient $a = -1.139 \times 10^{-3}$). Midplane activation rates were then used in the STAY'SL[2] computer code to adjust the neutron flux spectrum determined in previous spectral measurements in the target position in HFIR.[3] STAY'SL performs a generalized least-squares adjustment of all measured and calculated values including the measured activities, calculated spectra, and neutron cross sections. Neutron cross sections and their uncertainties were generally taken from

the ENDF/B-V[4] evaluation. The resultant neutron fluence values are listed in Table 2. The activation rates and the derived neutron spectra and fluences are in excellent agreement with previous measurements in the target position of HFIR.[3]

Neutron damage calculations were performed using the SPECTER computer code[5] at the midplane position of HFIR. Midplane dpa and helium (appm) values are also listed in Table 2. The fluence and damage values at other experimental positions can be calculated by the gradient equation given above. Damage parameters for other elements or compounds have been calculated and are readily available on request.

Helium production in nickel and nickel alloys requires a more complicated non-linear calculation.[6] Helium production in stainless steel is detailed in Table 3.

FUTURE WORK

Additional experiments still in progress in HFIR include MFE-200J-1 and MFE-400-J1 as well as JP9-16 and JP20-22. Activation data from the MFE-60J and -330J irradiations in HFIR and neutron flux monitors from the COBRA irradiation in EBR-II are currently being analyzed at PNNL.

REFERENCES

1. A. M. Ermi and D. S. Gelles, Preliminary Report on the Irradiation Conditions of the HFIR JP-23 Experiment, Fusion Reactor Materials Semiannual Progress Report, DOE/ER-0313/17, pp. 35-49 (1995).

2. F. G. Perey, Least Squares Dosimetry Unfolding: The Program STAY'SL, ORNL/TM-6062 (1977).

3. L. R. Greenwood, Alloy Development for Irradiation Performance Semiannual Report, DOE/ER-0045/11, pp. 30-37 (1983).

4. Evaluated Nuclear Data File, Part B, Version V, National Nuclear Data Center, Brookhaven National Laboratory.

5. L. R. Greenwood and R. K. Smither, SPECTER: Neutron Damage Calculations for Materials Irradiations, ANL/FPP-TM-197, January 1985.

6. L. R. Greenwood, A New Calculation of Thermal Neutron Damage and Helium Production in Nickel, Journal of Nuclear Materials 116, pp. 137-142 (1983).

TABLE 1 - Activation Rates (at/at-s) - HFIR JP-23

Position /Monitor	Ht,cm	$^{54}Fe(n,p)^{54}Mn$ (E-11)	$^{46}Ti(n,p)^{46}Sc$ (E-12)	$^{59}Co(n,\gamma)^{60}Co$ (E-8)	$^{93}Nb(n,\gamma)^{94}Nb$ (E-9)
3-114	13.1	5.03	7.31	5.61	2.32
6-120	0.6	5.95	8.69	6.81	2.81
7-121	-3.6	6.28	8.54	6.61	2.70
8-125	-7.7	5.84	7.97	6.15	2.58
10-129	-16.1	4.17	6.08	-	1.95

TABLE 2 - Midplane Fluence and Damage Values for HFIR JP-23

Neutron Fluence,n/cm2		Element	dpa	He,appm
Total	4.39E+22	C	8.0	18.2
Thermal (<.5 eV)	1.92E+22	Al	14.5	6.9
0.5 eV - 0.1 MeV	1.36E+22	V	10.4	0.23
> 0.1 MeV	1.12E+22	Cr	9.1	1.6
> 1 MeV	5.65E+21	Fe	8.1	2.8
		Ni Fast	8.7	37.6
		59-Ni	5.5	3139.4
		Total	14.2	3177.0
		Cu	10.5	2.5

TABLE 3 -DPA and He Values for 316 SS in HFIR JP-23
(Includes ^{59}Ni effect)

Ht (cm)	dpa	He (appm)
0	9.04	415.2
3	8.96	408.6
6	8.69	389.0
9	8.23	356.8
12	7.58	312.9
15	6.74	258.8
18	5.72	197.0

316SS = Fe(0.645), Ni(0.13), Cr(0.18), Mn(0.019), Mo(0.026) wt%

THE DEPENDENCE OF HELIUM GENERATION RATE ON NICKEL CONTENT OF Fe-Cr-Ni ALLOYS IRRADIATED AT HIGH DPA LEVELS IN FAST REACTORS -

F. A. Garner, B. M. Oliver and L. R. Greenwood (Pacific Northwest National Laboratory, Richland, WA)

To be presented at the 8th International Conference on Fusion Reactor Materials in Sendai, Japan, October 1997.

Extended Abstract

With a few exceptions in the literature, it is generally accepted that it is the nickel in Fe-Cr-Ni alloys that produces most of the transmutant helium and that the helium generation rate should scale linearly with the nickel content. Surprisingly, this assumption is based only on irradiations of pure nickel and has never been tested in an alloy series. There have also been no extensive tests of the predictions for helium production in alloys in various fast reactor spectra.

Nickel can contribute to helium production via high neutron energy (n,α) reactions with the various naturally-occurring nickel isotopes or by reactions at low-neutron energies with the radioactive isotope ^{59}Ni produced from the ^{58}Ni (n,γ) reaction, which also occurs at low neutron energies. The latter sequence is strongly dependent on neutron spectra and irradiation time, reflecting the burn-in of the ^{59}Ni.

This paper presents the results of two sets of irradiations in different fast reactors to measure directly the influence of nickel on helium production and our ability to predict such production. The first series were irradiated in a variety of in-core and out-of-core positions in FFTF over a range of dose (0.2-50 dpa) and spectral conditions, yielding different balances of helium formed by the low energy and high energy neutron reactions. The second series were irradiated simultaneously throughout the axial height of the EBR-II core to doses ranging from 76 to 131 dpa. Since the in-core spectra in EBR-II is significantly harder than that of FFTF, the helium production due to the ^{59}Ni sequence was found to be negligible in this second series, in spite of the high dose levels attained.

The alloys used in the FFTF series were Fe-15.0Cr-25.0Ni and Fe-15.0Cr-45.0Ni, while those in the EBR-II series were Fe-15.6Cr-15.7Ni, Fe-15.0Cr-45.3Ni and Fe-14.6Cr-75.1Ni. In irradiations conducted in a truly side-by-side manner, the helium generation was found to be linearly proportional to the nickel content as expected. If there existed even minor differences in position and spectra of specimens with different nickel levels, however, the proportionality is not as good, reflecting the strong spectral sensitivity of the ^{59}Ni (n,α) reaction. The latter situation sometimes occurred in the FFTF irradiation series where different alloys were placed in adjacent packets, especially in out-of-core regions where spectral variations are more pronounced.

10.0 MATERIALS ENGINEERING AND DESIGN REQUIREMENTS

IMPURITY CONTENT OF REDUCED-ACTIVATION FERRITIC STEELS AND A VANADIUM ALLOY

R. L. Klueh, M. L. Grossbeck, and E. E. Bloom (Oak Ridge National Laboratory)

OBJECTIVE

This work was conducted to obtain a benchmark for the chemical concentrations of important impurity elements in a reduced-activation ferritic steel and a vanadium alloy produced by present commercial technology and to provide a consistent set of concentration values for use in activation calculations.

SUMMARY

Inductively coupled plasma mass spectrometry was used to analyze a reduced-activation ferritic/martensitic steel and a vanadium alloy for low-level impurities that would compromise the reduced-activation characteristics of these materials. The ferritic steel was from the 5-ton IEA heat of modified F82H, and the vanadium alloy was from a 500-kg heat of V-4Cr-4Ti. To compare techniques for analysis of low concentrations of impurities, the vanadium alloy was also examined by glow discharge mass spectrometry. Two other reduced-activation steels and two commercial ferritic steels were also analyzed to determine the difference in the level of the detrimental impurities in the IEA heat and steels for which no extra effort was made to restrict some of the tramp impurities. Silver, cobalt, molybdenum, and niobium proved to be the tramp impurities of most importance. The levels observed in these two materials produced with present technology exceeded the limits for low activation for either shallow land burial or recycling. The chemical analyses provide a benchmark for the improvement in production technology required to achieve reduced activation; they also provide a set of concentrations for calculating decay characteristics for reduced-activation materials. The results indicate the progress that has been made and give an indication of what must still be done before the reduced-activation criteria can be achieved.

PROGRESS AND STATUS

Introduction

Development of low- or reduced-activation materials for fusion has focussed on the issue of radioactive waste disposal or recycle; the objective has been to eliminate or minimize alloying elements that would produce long-lived radioactive isotopes during irradiation in a fusion neutron spectrum. Emphasis in the development process has centered on eliminating Nb, Cu, Ni, Mo, and N, widely used alloying elements, with niobium often receiving much of the attention because of the very low concentrations (<1wppm) that will be required to meet criteria for shallow land burial or recycling, should those methods be chosen to handle the waste materials from a fusion power plant component after it has reached the end of its service lifetime.

Besides the elements listed above, Butterworth and his co-workers [1-3] have pointed out that there are various other elements that must be restricted to extremely low levels. Such elements could appear in the materials as tramp impurities. Table 1, which is taken from Murphy and Butterworth (M&B) [3], gives a list of elements and the limits that must be achieved to keep from compromising the reduced-activation criteria. These maxima were calculated so that "the concentrations of impurity elements were restricted to levels that would allow attainment of a surface γ dose rate not exceeding the "hands-on" dose rate limit of 25 μSvh^{-1} at a 100 y cooling time for material subjected to a first wall neutron fluence of 12 $MWym^{-2}$. This limit was suggested by M&B [3] as a "target value," and the impurity concentrations that are required to achieve this level will be used in this report for comparison with the values found in the materials analyzed. It needs to be emphasized that the M&B criteria have no "official" status relative to what might be required in the future (when fusion power plants are built or when they are decommissioned) for recycling or shallow land burial (values for recycle are expected to be lower than for shallow land burial, for which limits will probably be higher than the "hands-on" level).

Activation calculations to determine the decay characteristics of radioactive products produced during irradiation of a material in a fusion environment have often ignored some of the elements listed in Table 1. In this report, several of these elements have been determined by analytical techniques to establish a base concentration for activation calculations and also to give an indication of what elements may need to be considered when processes are developed for maximizing reduced-activation characteristics for potential structural materials.

M&B chose to apply the criterion to each element individually and disregard additive effects. However, they pointed out that additive effects could be important for real materials. Under those conditions, the concentration of the individual elements must be less than those given in Table 1. In particular, for n restricted elements, the total concentration of all such impurity elements, C, must be such that

$$C=\sum_{i=1}^{n}\frac{c_i}{c_{imax}}\leq 1$$

where c_i is the concentration of the element present in the alloy and c_{imax} is the maximum allowable concentration for that element.

Table 1. Maximum permitted concentrations of radiologically critical elements to achieve a "hands-on" dose rate limit after 100 y of cooling after a neutron fluence of 12MWy m^{-2} (after reference2)

Element	Concentration (wppm)	Element	Concentration (wppm)
Ag	0.011	U	1
Ho	0.067	Gd	4.1
Bi	0.14	Cd	5.0
Co	0.16	Ba	16
Nb	0.18	Mo	18
Sm	0.30	K	76
Lu	0.33	Al	170
Dy	0.62	Cl	8500

Experimental Procedure

A heat of ferritic/martensitic steel and a vanadium alloy were analyzed by inductively coupled plasma mass spectrometry (ICPMS). The steel specimen was taken from a 5-ton heat of modified F82H, an 8Cr-2WVTa steel that was purchased by the Japan Atomic Energy Research Institute from NKK Corporation, Kawasaki, Japan, for use in a collaborative test program by investigators in the U.S., Japan, and the European Union coordinated by the International Energy Agency (IEA) to establish the feasibility of using ferritic steels for fusion applications. Details of the melting and processing of this IEA Mod F82H steel will be published in the future. During the production of this heat, an effort was made to minimize niobium in the steel, but not any of the other elements that are not specified (i.e., Ag, Cd, Co, etc). Table 2 gives the vendor analysis of the steel. The vanadium alloy was from a 500-kg heat of V-4Cr-4Ti alloy obtained for the fusion program. This heat was specified and purchased on a "best-effort" basis from Teledyne Wah Chang, Albany, Oregon, by Argonne National Laboratory [4]; the vendor analysis is given in Table 2. Because of time considerations in delivering the 500-kg heat, Teledyne Wah

Chang used available starting materials to produce the alloy. Teledyne Wah Chang personnel believe that tramp impurities, especially molybdenum and niobium, can be lowered substantially by proper choice of starting materials. However, the niobium values of this heat seem to be typical of those obtained for vanadium alloys produced up until now. Molybdenum values are generally lower, often reported as <100 ppm. Recently, a 1200-kg ingot was produced with specification of <50 ppm for molybdenum and niobium [5]. The molybdenum specification was met (<50 ppm reported), but the niobium was measured at 140, 91, and 87 ppm at the top, middle, and bottom of the ingot [5].

To determine the variation in impurities in current fusion-program steels (reduced-activation and commercial steels), several other steels were analyzed by ICPMS. These included specimens taken from: 1) a 1-ton heat of JLF-1, a 9Cr-2WVTa steel produced in Japan by Nippon Steel Corporation; 2) an experimental 25 kg heat of a 9Cr-2WVTa steel produced by Combustion Engineering for ORNL with no effort to minimize impurities; 3) a commercial heat of modified 9Cr-1Mo (9Cr-1MoVNb) steel; and 4) a commercial heat of Sandvik HT9 (12Cr-1MoVW).

Table 2. Vendor analysis of the ingot of IEA heat of modified F82H steel and V-4Cr-4Ti alloy (wt. pct)

Element	Mod F82H	V-4Cr-4Ti	Element	Mod F82H	V-4Cr-4Ti
C	0.09	0.008	V	0.16	Balance
Si	0.11	0.078	Nb	0.0001	0.006
Mn	0.16		B	0.002	<0.0005
P	0.002	<0.003	N	0.006	0.0085
S	0.002	<0.001	Al	0.003	<0.001
Cu	0.01	<0.005	Co	0.005	
Ni	0.02		Ti	0.01	3.9
Cr	7.72	3.8	Ta	0.02	
Mo	0.003	0.031	W	1.97	
Fe	Balance	0.022	O		0.031

To examine analytical chemistry techniques for low-level concentrations, the V-4Cr-4Ti was also analyzed by glow discharge mass spectrometry (GDMS) by two different vendors. Therefore the results for the different techniques can be compared, along with the variations in the same technique when conducted by different vendors.

The metal samples for the ICPMS were dissolved in a mixture of HNO_3, HF, and H_2O_2. A reagent blank was prepared with the sample. A semiquantitative scan was conducted of the samples, and the spectra were examined for elements of interest and any other elements that were present. Before analyzing the sample, the instrument was checked for mass calibration and resolution. All elements reported were obtained by quantitative analysis using a blank, 10 ppb and 60 ppb standard for all the elements in a calibration curve. A calibration verification combined of an EPA QC standard and a multi-element SPEX standard was analyzed to validate the calibration standards. All elements in the verification standard were within 10% of the calibration standards. A ten-fold dilution was made on the dissolved sample that was analyzed, and the reagent blank was subtracted and calculated with an appropriate dilution factor applied. A portion of the diluted sample was spiked with 20 ppb of all elements reported. Spike recoveries were within 10%, which is the accuracy reported for the technique. Two readings were made and the precision for the elements for the first specimen are given in Table 3.

Table 3. Precision for elements analyzed by inductively coupled plasma mass spectrometry (wppb)

Element	Concentration (ppb)	Element	Concentration (ppb)	Element	Concentration (ppb)
Li	0.01	Cd	0.23	Ta	0.3
Zr	0.67	Co	0.43	Er	1.5
Cr	0.11	Fe	0.65	Tb	0.2
Al	0.4	Ir	0.6	Ho	0.4
Ni	1.2	Nb	0.7	Y	2.0
Ag	0.4	Mo	1.2	Hf	0.14
B	1.8	Pd	0.04	W	0.5
Bi	0.03	Sn	0.5	Eu	0.14

The GDMS analyses were conducted in two runs on the same sample on different days. Since GDMS is a sputtering process, the material for the first run was taken closer to the surface of the sample than the second run. The relative
sensitivity factor (RSF) for the elements was taken as the standard for iron, which was then normalized for vanadium. This limits the accuracy of the analysis to the accuracy of the standard iron RSF, some of which may not be correct. Thus a high accuracy could not be guaranteed, and a calibration with vanadium standards is required for high accuracy analyses.

Results

The following elemental impurities were determined by ICPMS: Ag, Bi, Cd, Co, Dy, Er, Eu, Ho, Ir, Mo, Nb, Ni, Os Tb, and U. Results for two specimens of V-4Cr-4Ti and the IEA Mod F82H are given in Table 4.

For the ferritic steel, Co (28 and 16 wppm observed vs. the 0.16 wppm limit) and Nb (3.3 wppm and 2.4 vs. 0.18 wppm) were over the B&M limit, and Mo was at the limit (21 and 19 wppm vs. 18 wppm). The limit of detection for ICPMS for the Ag and the Bi were just above the permitted limit, indicating that these two elements may or may not be above the B&M limit. A more sensitive technique is required to determine this.

The elements definitely above the B&M limits for the V-4Cr-4Ti alloy include Ag (0.86 and 0.6 wppm vs. 0.011), Co (4.2 and 0.2 wppm vs. 0.16 wppm), Mo (370 and 329 wppm vs. 18 wppm), and Nb (32 and 64 wppm vs. 0.18 wppm). The Ho and Tb may or may not be above the limit, but a more sensitive technique is required for this to be determined.

There were some discrepancies as well as agreement for the elements analyzed by the ICPMS and GDMS techniques and between the GDMS analyses of the two vendors (Table 5). The major discrepancies appeared to be between ICPMS and GDMS Vendor 1 for Ag, Bi, and Cd. The GDMS Vendor 1 found less of these elements than were found by ICPMS or by Vendor 2. The ICPMS results for the different reduced-activation and commercial steels showed a range of differences in several of the impurity elements, with the major differences being in Ag, Cd, Co, Mo, Ni, Pd, and U (Table 6).

Table 4. Chemical composition from two measurements of important impurity elements for a heat of V-4Cr-4Ti and a reduced-activation martensitic steel determined by inductively coupled plasma mass spectrometry (wppm)

Elements	V-4Cr-4Ti		IEA F82H	
Ag	0.86	0.6	<0.05	<0.1
Bi	<0.05	0.46	<0.2	<0.05
Cd	1.6	0.3*	<0.4	<0.05
Co	4.2	0.2*	28	16
Ir	<0.5	<0.05	<0.02	<0.05
Mo	370	329	21	19
Nb	32	64	3.3	2.4
Ni		11		474
Os		<0.05		<0.05
Pd		0.2		<0.05
Dy		<0.05		<0.05
Er		0.1*		<0.05
Eu	<0.2	<0.05	<0.02	<0.05
Ho	<0.2	<0.05	<0.05	<0.05
Tb	<0.2	<0.05	<0.02	
U	0.13	0.21	<0.003	<0.05

* At or near the limit of detection

Discussion

The results of the ICPMS analyses (Table 4) indicate that there are several impurities in the V-4Cr-4Ti and the IEA Mod F82H steel that are above the "hands-on" level defined by M&B [3]. These include Ag, Co, Mo, and Nb for the V-4Cr-4Ti and Co and Nb for the IEA Mod F82H steel. These results for the V-4Cr-4Ti are similar to those
of M&B, who studied the production of high-purity V, Cr, and Ti and wrote [3], "Of the three metals studied, vanadium and its compounds exhibited the highest levels of contamination. Mo, Nb, Co and Ag were frequently found near or above the concentration limits." These authors described additional purification steps that might be required to to remove these impurities.

The ICPMS results for the different steels in Table 6 provide an indication of what may be possible for reduced-activation steels without special purification. They can also serve as the starting point for determining how these steels can be processed to the levels required. That is, a detailed analysis of the materials processing techniques used for these heats could indicate reasons for the differences and how the impurities might be further reduced.

Table 5. Chemical composition of impurity elements for V-4Cr-4Ti alloy determined by ICPMS and GDMS (wppm)

Element	ICPMS		GDMS Vendor 1		GDMS Vendor 2	
Ag	0.86	0.6	0.11	0.045	<0.3	<0.6
Bi	<0.05	0.46	<0.0075	<0.0061	<2	<<134
Cd	1.6	0.3*	<0.19	≤0.13	1	1
Co	4.2	0.2*	0.31	0.28	≤0.22	≤0.21
Ir	<0.5	<0.05	<0.003	<0.003	1.5	<0.1
Mo	370	329	310	320	325	350
Nb	32	64	<59	<63	70	78
Ni		11	9.5	9.7	7	7
Os		<0.05	<0.009	<0.0072	<0.004	<0.002
Pd		0.2	<0.13	0.14	0.4	0.3
Dy		<0.05			<0.002	N/D
Er		0.1*			<0.08	<0.3
Eu	<0.2	<0.05			<0.035	<0.009
Ho	<0.2	<0.05			<0.008	<0.016
Tb	<0.2	<0.05			N/D	<0.004
U	0.13	0.21	0.085	0.082	<0.03	<0.003

N/D Not detected
* At or near the limit of detection

Special purification techniques were used by NKK Corporation to obtain the iron used to make the IEA Mod F82H, along with the selection of clean materials for the other alloying additions. This choice of materials resulted in this steel having the lowest silver content. This approach was used in the hope that it would reduce the niobium to extremely low levels, and a low level was achieved compared to the commercial HT9 (Table 6); however, the concentration of niobium for this steel was only slightly lower than that for JLF-1 and 9Cr-2WVTa, for which no such precautions were taken. The exact procedure used for choosing the melt stock for the JLF-1 is not known, but the ORNL 9Cr-2WVTa was an experimental steel made by Combustion Engineering, Chattanooga, TN, using off-the-shelf melt stock to make the small heat. The Sandvik HT9, which was a large commercial heat, probably was made with the use of scrap, and the niobium concentration was an order of magnitude higher than for the reduced-activation steels. Molybdenum was slightly lower in the IEA Mod F82H and the JLF-1 steel than the 9Cr-2WVTa, but only by a factor of 3. Most of the cobalt must come from the nickel. Even electrolytic nickel (99.95% Ni), which is also known as "pure nickel," contains 0.3-0.5% cobalt. The data in Table 6 indicate a correlation between the cobalt and nickel in the steels. Of interest is the low level of cobalt in the JLF-1 and the relatively high level in the IEA Mod F82H and 9Cr-2WVTa. Since no nickel was added to any of these steels, tracing the origin of the nickel should indicate part of the solution of what will be required to reduce cobalt in future heats.

Table 6. Chemical composition of important impurity elements for reduced activation of ferritic steels determined by inductively coupled plasma mass spectrometry (wppm)

Element	IEA Mod F82H		JLF-1	ORNL 9Cr-2WVTa	Mod 9Cr	HT9
Ag	<0.05	<0.1	0.21	0.16*	0.23	1.3
Bi	<0.2	<0.05	<0.1	<0.05	<0.1	<0.1
Cd	<0.4	<0.05	<0.05	<0.05	3.3	5.1
Co	28	16	7.6	34	58	393
Ir	<0.02	<0.05	<0.05	<0.05	<0.05	<0.05
Mo	21	19	20	70	**	**
Nb	3.3	2.4	4.3	4	**	23
Ni		474	13	402	1251**	5692**
Os		<0.05	<0.05	<0.02	<0.02	<0.05
Pd		<0.05	<0.05	0.18*	0.27	0.4
Dy		<0.05	<0.05	<0.05	<0.05	<0.05
Er		<0.05	<0.05	<0.05	<0.05	<0.05
Eu	<0.02	<0.05	<0.05	<0.05	<0.05	<0.05
Ho	<0.05	<0.05	<0.05	<0.05	<0.05	<0.05
Tb	<0.02		<0.05		<0.05	<0.05
U	<0.003	<0.05	<0.05	0.6	0.12	<0.05

* At or near the limit of detection
** Element is part of the specified composition

As stated above, it is believed that with the proper choice of starting materials the molybdenum and niobium can be reduced substantially from the values in Table 5. However, the 500-kg heat is one of the largest vanadium-alloy heats ever produced, and so the results for this heat and the information on the IEA Mod F82H provide a "starting point" for discussing the present status of potential reduced-activation materials and the steps required to reach the goal of a reduced-activation material.

Recently, calculations have been made to predict decay characteristics of fusion first wall and blanket structures after service operation [6,7]. Various assumptions were used for the concentrations of the impurities. Ehrlich et al. [6] considered the radioactivity decay after a neutron wall loading of 5 MW/m^2 for 2.5 years, which gives an integral wall loading of 12.5 $MWym^{-2}$. For the pure materials, V, Ti, and Cr had the best decay characteristics, followed by iron. Without impurities, V-Cr-Ti alloys have radioactivity decay properties superior to any other potential reduced-activation structural material, including silicon carbide, often considered the best low-activation material. When the calculations were made for the vanadium alloy with "realistic" impurity concentrations, Ehrlich et al. [6] found that, "a strong increase of long-term activation by several orders of magnitude can be caused by impurities."

Of the impurities discussed in the present report, Ehrlich et al. [6] assumed values for Ag, Co, Nb, and Mo of 0.03, 0.02, 0.01, and 0.15 wppm, respectively . These values are respectively about 30, 200, 3000, and 2500 times less than the values observed for the vanadium alloy analyzed by ICPMS (Table 4). Ehrlich et al. chose those impurity concentrations because these values were estimated by Johnson Matthey as concentrations that could be achieved in vanadium alloys by special techniques, although these limits would be difficult and expensive to reach [6].

Ehrlich et al. [6] also examined reduced-activation ferritic steels and made calculations for existing steels and for an optimized steel, where the impurity levels are assumed to be those that should be achievable under conditions where special efforts are made to reduce impurity levels. The interesting observation that came out of the comparison of the optimized ferritic steel and the V-Cr-Ti alloy with impurities at the level that should be achievable was the conclusion by Ehrlich et al. [6] that a "realistic assumption of technically achievable amounts of tramp elements leads nearly to the same level of activation [for the vanadium alloy] as for the optimized ferritic-martensitic steels."

Attaya and Smith [7] performed radioactivity decay calculations for a V-4Cr-4Ti alloy and the ORNL 9Cr-2WVTa steel after exposure to a $5MWm^{-2}$ neutron wall loading and 5 years of operation . The vanadium alloy was found superior to the 9Cr-2WVTa steel with and without the impurities. Impurity levels were assumed to be those typical for present technology. For the V-4Cr-4Ti, it was stated that [7], " impurity content is based on chemical analyses of different heats of similar alloys." Impurities had a large effect on the behavior of the vanadium alloy, but a relatively small effect on the ferritic steel. Attaya and Smith assumed that Ag, Co, Nb, and Mo were present in the V-4Cr-4Ti at levels of 0, 0, 1, and 4 wppm, respectively. These are low values for niobium and molybdenum based on the values of Table 4 and those reported for vanadium alloys produced up to the present; likewise, the values for silver and cobalt are low for those measured in the 500-kg heat. In the case of ferritic steel, Attaya and Smith [7] stated that the "impurities of the ORNL 9Cr-2WVTa ferritic steel are assumed as that of the modified HT-9" [7], which appears to be a hypothetical steel postulated for a previous calculation [8]. The concentrations for Ag, Co, Nb, and Mo were assumed to be 0.9, 50, 1.1, and 2.7 wppm, respectively. In this case, the Nb and Mo were below what was observed in the IEA Mod F82H, and the Ag and Co were substantially above what was observed in the present analyses. Since Attaya and Smith [7] found that impurities had a large effect on the decay characteristics of the vanadium alloy but much less relative effect on the ferritic steel, the additional impurities found in the results given in Table 4 would cause the vanadium alloy decay curve to approach the curve for the ferritic steel.

If it is assumed that the impurity levels measured by ICPMS (Table 4) are representative of today's processing practice for vanadium alloys and reduced-activation ferritic steels, calculations similar to those of Ehrlich et al. [6] and Attaya and Smith [7] could be used to qualitatively estimate the relative reduced-activation status of vanadium alloys and ferritic steels today and where the materials will stand once they are optimized with respect to deleterious impurities. Although the calculations need to be performed, it appears that if the Ag, Co, Nb, and Mo impurities detected in the present study (or appropriate values from other heats in the case of molybdenum, which appears extra high in the 500-kg heat) were used for the calculations, values that were not used by either Ehrlich et al. [6] or Attaya and Smith [7], the differences between the two materials would not be extremely large, based on the larger amounts of Nb, Mo, and Ag present in the vanadium alloy and the greater effect of impurities in the vanadium alloys than the ferritic/martensitic steel. Then, the question becomes: Can the optimized impurity values of Ehrlich et al. be achieved? If both can be achieved, then according to Ehrlich et al. [6], "the actual advantage of vanadium-chromium-titanium alloys in comparison to the optimized ferritic-martensitic steels diminishes to about one order of magnitude with regard to the long-term radioactivity."

Conclusions

Chemical analysis of potential reduced-activation ferritic steels and a V-4Cr-4Ti alloy produced by present technology provides an indication of the status of some of the important impurity elements in the steels and gives an indication of the precision of the analytical chemistry methods. Several detrimental impurities are present that

would compromise the reduced-activation characteristics of these materials. Nevertheless, the results for the steels indicate that progress has been made in reducing the level of these impurities for two large heats of reduced-activation steel. Likewise, information exists that processes can be employed that will lower the impurity levels of vanadium alloys. There has probably never before been a requirement for a structural material to be processed to have specified impurity levels as low as those that will be required to meet the reduced-activation criteria. Even though the materials will not be needed for some time, it would appear that an effort should be mounted in the near future to determine the means to achieve the desired purity levels. As a start, an effort should be made to determine how low the impurity levels can be reduced in a large vanadium heat by selecting the starting materials with low impurity concentrations. In the case of the ferritic/martensitic steels, a study needs to be conducted to determine the origin of the various impurities to determine what starting materials will need to be purified to reach the desired goal. Such an effort should enlist support from industrial materials processors to determine techniques used in the past and how they might be combined with the latest technology for future application. The effort should not be delayed if reduced-activation materials are to be available when fusion power production is ready to begin operation.

REFERENCES

1. G. J. Butterworth, and L. Giancarli, J. Nucl. Mater. 155-157 (1988) 575.
2. G. J. Butterworth, J. Nucl. Mater. 179-181 (1991) 135.
3. D. Murphy and G. J. Butterworth, J. Nucl. Mater. 191-194 (1992) 1444.
4. H. M. Chung, H. -C. Tsai, D. L. Smith, R. Peterson, C. Curtis, C. Wojcik, and R. Kinney, p. 178 in: Fusion Materials Semiann. Prog. Rept. For Period Ending September 30, 1994, DOE/ER-013/17.
5. W. R. Johnson, J. P. Smith, and R. D. Stambaugh, p. 3 in: Fusion Materials Semiann. Prog. Rept. for period ending June 30, 1996, DOE/ER-0313/20.
6. K. Ehrlich, S. Cierjacks, S. Kelzenberg, and A. Möslang, in: Effects of Radiation on Materials: 17th Volume, ASTM STP 1270, Eds D. S. Gelles, R. K. Nanstad, A. S. Kumar, and E. A. Little (American Society for Testing and Materials, Philadelphia, 1996) 1109.
7. H. Attaya and D. Smith, p. 107 in: Fusion Materials Semiann. Prog. Rept. For Period Ending March 31, 1995, DOE/ER-0313/18.
8. H. Attaya and D. Smith, J. Nucl. Mater. 191-194 (1992)1469.

11.0 IRRADIATION FACILITIES, TEST MATRICES, AND EXPERIMENTAL METHODS

STATUS OF DOE/JAERI COLLABORATIVE PROGRAM PHASE II AND PHASE III CAPSULES – J. P. Robertson, K. E. Lenox (Oak Ridge National Laboratory), I. Ioka and and E. Wakai (Japan Atomic Energy Research Institute)

OBJECTIVE

The objective of the High Flux Isotope Reactor (HFIR) irradiations is to determine the response of various U.S. and Japanese structural alloys with different pretreatments and alloy compositions to the combined effects of displacement damage and helium generation.

SUMMARY

Significant progress has been made during the last year in the post-irradiation examinations (PIE) of the specimens from nine DOE ORNL/JAERI collaborative capsules and in the design and fabrication of four additional capsules. JP21, JP22, CTR-62, and CTR-63 were disassembled, JP20 tensile specimens were tested, and a variety of specimens from the RB-60J-1, 200J-1, 330J-1, and 400J-1 capsules were tested. Fabrication of RB-11J and 12J was completed and progress made in the matrix finalization and design of RB-10J and JP25.

PROGRESS AND STATUS

Post-Irradiation Examination

Significant progress has been made during the last year in the post-irradiation examinations (PIE) of the specimens from nine DOE ORNL/JAERI collaborative capsules. Tables 1 and 2 summarize the progress and status of the capsules involved in the Phase II and Phase III irradiation programs. Details of the capsule design, assembly, and operation, specimen matrices and testing, and alloy compositions can be found in previous reports in this series. The locations of some of the more detailed reports are shown in the table, but this is not intended to be an exhaustive list. The dose levels shown in the table are the peak capsule values achieved at the reactor centerline. The dpa values in the HFIR target are estimated by assuming 8.73×10^{-4} dpa/MWd. The dpa values in the hafnium-shielded HFIR RB experiments are estimated by assuming 2.45×10^{-4} dpa/MWd. While a status of "testing complete" is listed for several of the capsules, it should be noted that data analyses and microscopy examinations are still in progress.

The JP series HFIR target capsules (JP9-16, JP20-22) contain primarily transmission electron microscopy disks (TEM) and SS-3 flat tensile specimens. A wide variety of alloys and thermomechanical conditions are included. Many of the TEM disks were made from isotopically tailored alloys to produce a range of He/dpa ratios (<0.1, 10, 20, 70 appm/dpa). The specimen temperatures are 300, 400, 500, and 600°C and the dose levels are 8, 18, 34, and 57 dpa.

During this reporting period, 17 of the 24 SS-3 tensile specimens from HFIR-JP20 (8 dpa peak) were tested at the respective irradiation temperatures. Four of the tensile specimens (V-5Cr-5Ti) were shipped to Argonne National Laboratory (ANL) for testing and the other three (TiAl alloys) are scheduled to be shipped to the Japan Atomic Energy Research Institute for testing. Analyses of these data are still in progress and will be discussed in future reports in this series. Three of the five TEM disk packets were opened and sorted (JP20, Position 6, 300°C; JP20, Position 7, 500°C; and JP20, Position 9, 400°C). Of these disks (approximately 120 disks per packet), 12 of the Ti-Al disks were identified to be shipped to JAERI for microscopy, 12 isotopically tailored ferritic disks were identified to be shipped to Pacific Northwest National Laboratory (PNNL) for microscopy, and 24 isotopically tailored ferritic disks were selected for microscopy at ORNL.

The HFIR-JP21 and JP22 capsules, which were irradiated to a peak damage level of 18 and 34 dpa, respectively, were disassembled in August 1996. All of the specimens and all but one of the 12 flux monitors were recovered without incident. The lost flux monitor was Monitor #48 from the topmost position in the JP21 capsule. These specimens are now in storage in the Irradiated Materials Examination and Testing (IMET) Facility and are scheduled for PIE during the next reporting period. One TEM disk

Table 1. Summary of Target Capsule Irradiation Parameters and Status

Capsule	Primary Research Objectives	Irradiation Start and End; Number of Cycles	Operating Parameters: MWd; dpa; temperature	Status	Most Pertinent Semiannual Report Numbers DOE/ER-0313/*xx*
JP10 JP11 JP13 JP16	austenitic and ferritic steels; isotopically tailored TEM disks; tensile specimens	start: 7/90 end: 9/91 11 cycles	20161 MWd 17.3 dpa 300-600°C	testing complete	Design: 0313/3 Loading: 0313/5 Operation: 0313/16 Dosimetry: 0313/19
JP14	austenitic and ferritic steels; isotopically tailored TEM disks; tensile specimens	start: 7/90 end: 9/92 21 cycles	38786 MWd 33.9 dpa* 300-600°C	testing complete	Design: 0313/3 Loading: 0313/5 Operation: 0313/16
JP9 JP12 JP15	austenitic and ferritic steels; isotopically tailored TEM disks; tensile specimens	start: 7/90 end: 4/94 35 cycles	64904 MWd 56.7 dpa* 300-600°C	disassembly complete	Design: 0313/3 Loading: 0313/5 Operation: 0313/16
JP17	austenitic and ferritic steels; fracture toughness, tensile, TEM specimens	start: 12/91 end: 2/92 2 cycles	3702 MWd 2.9 dpa 250-300 °C	testing complete	Design: 0313/12 Loading: 0313/12 Operation: 0313/19 Dosimetry: 0313/19
JP18 JP19	austenitic and ferritic steels; fracture toughness, tensile, TEM specimens	start: 8/91 end: 10/91 2 cycles	3575 MWd 2.9 dpa 60-125°C	testing complete	Design: 0313/11 Loading: 0313/11 Operation: 0313/19 Dosimetry: 0313/19
JP20	austenitic and ferritic steels; isotopically tailored TEM disks; tensile specimens	start: 12/93 end: 6/94 5 cycles	9367 MWd 8.2 dpa* 300-600°C	testing in progress	Design: 0313/12 Loading: 0313/15 Operation: 0313/18
JP21	austenitic and ferritic steels; isotopically tailored TEM disks; tensile specimens	start: 12/93 end: 4/95 11 cycles	21337 MWd 18.6 dpa* 300-600°C	disassembly complete	Design: 0313/12 Loading: 0313/15 Operation: 0313/18
JP22	austenitic and ferritic steels; isotopically tailored TEM disks; tensile specimens	start: 12/93 end: 1/96 19 cycles	38880 MWd 34 dpa* 300-600°C	disassembly complete	Design: 0313/12 Loading: 0313/15 Operation: 0313/18
CTR-62 CTR-63	ferritic steels; tensile, CVN, and TEM specimens	start: 4/95 end: 12/95 7 cycles	14 dpa* 300, 400°C	disassembly complete	Design: 0313/18 Loading: 0313/18
JP25	ferritic steels; tensile, CVN, and TEM specimens	12 cycles	20 dpa* 300, 500°C	design in progress	

*estimated

Table 2. Summary of RB Capsule Irradiation Parameters and Status

RB-60J-1	spectrally tailored (Hf-shielded); tensile, creep, TEM specimens	start: 7/90 end: 11/92 24 cycles	44450 MWd 11.6 dpa 60°C	testing in progress	Design: 0313/3, 4 Loading: 0313/4 Operation: 0313/13 Dosimetry: 0313/17
RB-200J-1	spectrally tailored (Hf-shielded); tensile, creep, TEM specimens	start: 11/92 end: 1/95 20 cycles	37450 MWd 9.2 dpa* 200°C	testing in progress	Design: 0313/3, 6 Loading: 0313/14 Operation: 0313/15, 18
RB-330J-1	spectrally tailored (Hf-shielded); tensile, creep, TEM specimens	start: 7/90 end: 11/92 24 cycles	44450 MWd 11.6 dpa 330°C	testing in progress	Design: 0313/3, 5 Loading: 0313/5 Operation: 0313/11, 13 Dosimetry: 0313/17
RB-400J-1	spectrally tailored (Hf-shielded); tensile, creep, TEM specimens	start: 11/92 end: 1/95 20 cycles	37450 MWd 9.2 dpa* 400°C	testing in progress	Design: 0313/3, 6 Loading: 0313/14 Operation: 0313/15, 18
TRIST-ER1	alumina; in-situ measurement of electrical conductivity	start: 3/96 end: 6/96 3 cycles	3 dpa* 450°C	irradiation complete	Design: 0313/19, 20 Loading: 0313/19 Operation: 0313/20
RB-10J	austenitic steels and V alloys; spectrally tailored (Eu_2O_3-shielded); tensile, fracture, TEM specimens	start: 1/98* end: 12/98* 10 cycles	5 dpa* steel: 250°C V: 400-500°C	design in progress	
RB-11J RB-12J	ferritic steels and V alloys; spectrally tailored (Eu_2O_3-shielded); tensile, fracture, TEM specimens	start: 2/97 end: 12/97* 10 cycles	5 dpa* 300, 500°C	fabrication complete	

*estimated

packet (JP22 Position 7, 34 dpa, 500°C) has been opened and the disks sorted and cleaned in preparation for density measurements.

The RB-60J-1, 200J-1, 330J-1, and 400J-1 experiments are a continuation of the Oak Ridge Research Reactor (ORR) spectrally tailored experiments The capsules operated in the RB positions of the HFIR surrounded by a hafnium shield to simulate the expected fusion helium to damage (He/dpa) ratio in steel. The doses shown in the table are in addition to the 7 dpa accumulated during the ORR irradiation, bringing the total for the two-stage irradiation to 16-19 dpa. Dosimetry and helium measurements from specimens from the 60J-1 and 330J-1 capsules indicate that this experiment was successful in producing fusion relevant helium/dpa levels (approximately 11 appm He/dpa). The irradiation temperatures in these experiments were actively controlled at 60, 200, 330, and 400°C. Pressurized creep tube measurements and analyses were completed on the specimens from the 200J and 400J capsules [e.g., 1] and the data reported along with those from 60J and 330J. In addition, several of the pressurized tubes from the 60J and 400J capsules were punctured and the released pressure measured in order to verify the creep measurements. A number of Grodzinski fatigue specimens were separated out from each of the four capsule sets and set aside for shipping to JAERI. These specimens will be used in slow strain rate tests (SSRT) as part of the investigation of irradiation assisted stress corrosion cracking. Tensile testing was also conducted on specimens from each of these four capsules. In some cases, analyses of the data and

integration into the existing databases are still in progress. Optical photographs of the fracture areas have been made on most of the tested specimens and reduction in area measurements completed. An experimental plan to complete the test matrix during the next year has been developed. Twenty-nine SS-3 tensile specimens made from low activation ferritic steels were collected for eventual shipment to PNNL for testing. Sixteen vanadium alloys specimens were collected and shipped to ANL. Sixty-two SS-1 and SS-3 specimens were tested at ORNL. Transmission electron microscopy disk packets from 200J and 400J were also identified for eventual shipment to PNNL and ANL.

The CTR-62 and 63 capsules, containing low activation ferritic steel specimens, were irradiated for 7 cycles to approximately 14 dpa. The tensile, Charpy, and TEM specimens operated at either 300 or 400°C. These capsules were successfully disassembled in August 1996 and the specimens are awaiting testing in the IMET storage facility.

Pre-Irradiation Progress

The RB-11J and 12J capsules are the first of the spectrally tailored capsules scheduled for irradiation in the Phase III program. These capsules will operate in the HFIR removable beryllium (RB) positions with a europium oxide (Eu_2O_3) thermal neutron shield in place. They will achieve approximately 5 dpa at 300 and 500°C, respectively. The capsules will contain primarily low activation ferritic steel and vanadium alloy specimens in the form of tensile, fracture, creep, and TEM specimens. Fabrication and assembly of the capsules are complete, and the Eu_2O_3 shields have been approved by the Research Reactor Division. The capsules are scheduled to begin irradiation with the start of HFIR cycle 352 (February 1997).

The RB-10J capsule will be irradiated to 5 dpa in a Eu_2O_3-shielded RB position. It will be composed of two distinct sections separated at the reactor centerline. The upper portion will contain vanadium alloy specimens tentatively operating at 420 and 480°C. Bend bars, fracture toughness specimens, tensile specimens, and TEM disks will be included at each temperature. The specimens will be surrounded by lithium in order to prevent oxygen contamination and to provide good thermal contact to the specimens. The lower portion will contain primarily austenitic stainless steels and will operate at approximately 250°C. Tensile specimens, Charpy V-notch specimens, and TEM disks will be included. Some weld and joint specimens may be included also. This capsule is scheduled to be fabricated during the next year and is to be ready for irradiation in January 1998.

The HFIR-JP25 target capsule will be the last of five capsules that compose the ORNL/JAERI Phase III Task I project on low activation ferritic steels (the other capsules are RB-11J, RB-12J, CTR-62, and CTR-63). This capsule is to be irradiated to a peak dose of 20 dpa. The specimens will operate at 300 and 500°C, the same temperatures as the RB-11J and 12J capsules. The capsule will include tensile, Charpy V-notch, pre-cracked Charpy, and TEM specimens of IEA F82H base metal, nickel-doped base metal, weld metal, and weldment.

REFERENCES

1. M. L. Grossbeck, L. T. Gibson, S. Jitsukawa, L. K. Mansur, and L. J. Turner, in Effects of Radiation on Materials: 18th International Symposium, ASTM STP 1325, R. K. Nanstad, Ed., American Society for Testing and Materials, 1997, in press.

STATUS OF ATR-A1 IRRADIATION EXPERIMENT ON VANADIUM ALLOYS AND LOW-ACTIVATION STEELS*

H. Tsai, R. V. Strain, I. Gomes, H. Chung, and D. L. Smith (Argonne National Laboratory), and H. Matsui (Tohoku University, Japan)

SUMMARY

The ATR-A1 irradiation experiment in the Advanced Test Reactor (ATR) was a collaborative U.S./Japan effort to study at low temperature the effects of neutron damage on vanadium alloys. The experiment also contained a limited quantity of low-activation ferritic steel specimens from Japan as part of the collaboration agreement. The irradiation was completed on May 5, 1996, as planned, after achieving an estimated neutron damage of 4.7 dpa in vanadium. The capsule has since been kept in the ATR water canal for the required radioactivity cool-down. Planning is underway for disassembly of the capsule and test specimen retrieval.

OBJECTIVE

The main objective of the experiment was to obtain mechanical property data, including in-reactor creep, on vanadium alloys irradiated at two low temperatures (≈200 and 300°C). The objective of the present activities is to return the capsule to ANL-E for disassembly and specimen retrieval.

SUMMARY DESCRIPTION OF EXPERIMENT

The irradiation vehicle was a drop-in capsule consisting of fifteen lithium-bonded subcapsules in four gas-filled segments, as shown in Fig. 1. The material for both the capsule and subcapsule components was Type 304 stainless steel. A gadolinium filter set, consisting of a tube, a top end disk, and a bottom end disk, was incorporated in each subcapsule to mitigate transmutations from the thermal flux. The types of specimens included in the experiment are tensile, Charpy, compact tension, tranmission electron microscopy disks, and creep (pressurized tubes). Flux dosimeters and melt-wire temperature monitors were incorporated into selected subcapsules.

STATUS OF CAPSULE DISASSEMBLY PLANNING

A dry cask from ANL-W is being used to ship the cpasule to the ANL-E hot cells for disassembly. Loading of the capsule into the cask requires the capsule to be out of the water pool, i.e., without shielding, for ≈1 min while being inserted into the cask. Because of the high induced activities in the capsule (estimated to be ≈80 R/h at 1 m in air), extensive evaluation and detailed planning were required by the ATR. At present, all requirements appear to have been met for a successful transfer. If the actual in-air activity measurement results are within the ATR allowed limits, cask loading is expected to take place in January 1997 and the shipment would follow immediately.

*Work supported by U.S. Department of Energy, Office of Fusion Energy Research, under Contract W-31-109-Eng-38.

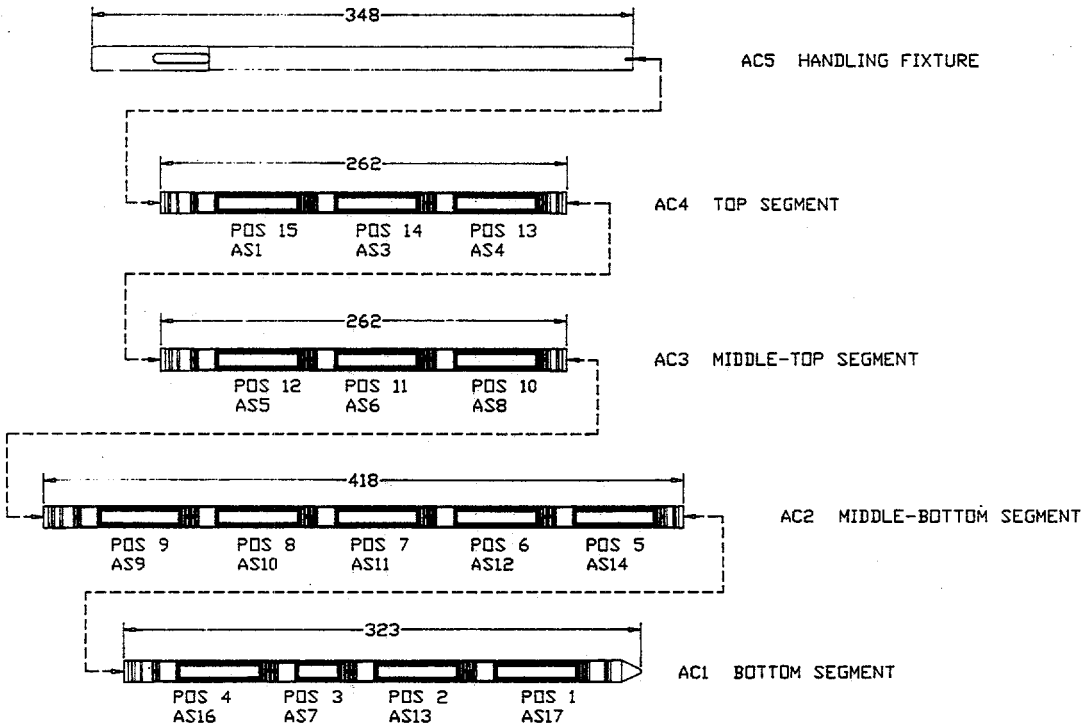

Fig. 1. Schematic diagram of ATR-A1 Showing Capsule Segments and Subcapsule (dimensions in mm)

Planning of the capsule disassembly has started. The disassembly will consist of three major tasks: removal of the subcapsules from the capsule segments; removal of the end caps of the subcapsules to expose the lithium bond; and removal of the lithium bond by dissolution with ammonia and alcohol. While the last task is expected to be routine based on earlier experience, the first two command special attention for the reasons given below.

By design, the clearances between the subcapsule and capsule tube and between the filter assembly and subcapsule tube are tight. Therefore, it is likely that force will be required to separate these components. Burrs from the tubing cutter, which will be used to sever the capsule and subcapsule tubing, and the gummy lithium bond will also increaase the pushing force necessary for disassembly. Because these forces are not readily achievable with hot cell manipulators, two special fixtures utilizing small hydraulic pumps have been designed to facilitate the removal. Construction will begin shortly after the required design and safety reviews are completed.

Eight of the subcapsules contain pressurized creep specimens. Before the disassembly of these subcapsules, their plena will be punctured to measure the internal pressures. These tests will provide a definitive indication of the integrity of the creep specimens inside.

A draft procedure delineating the above activities has been completed.

FUTURE ACTIVITIES

The capsule is expected to be shipped to the ANL-E hot cell in January 1997. Disassembly is expected to start in February and be completed in April 1997.

PROGRESS REPORT ON THE DESIGN OF A VARYING TEMPERATURE IRRADIATION EXPERIMENT FOR OPERATION IN HFIR

A. L. Qualls (Oak Ridge National Laboratory) and T. Muroga (National Institute for Fusion Science, Japan)

OBJECTIVE

The purpose of this experiment is to determine effects of temperature variation during irradiation on microstructure and mechanical properties of potential fusion reactor structural materials.

SUMMARY

A varying temperature irradiation experiment is being performed under the framework of the Japan-USA Program of Irradiation Tests for fusion Research (JUPITER) to study the effects of temperature variation on the microstructure and mechanical properties of candidate fusion reactor structural materials. An irradiation capsule has been designed for operation in the High Flux Isotope Reactor (HFIR) at Oak Ridge National Laboratory (ORNL) that will allow four sets of metallurgical test specimens to be irradiated to exposure levels ranging from 5 to 10 dpa. Two sets of specimens will be irradiated at constant temperatures of 500°C and 350°C. Matching specimen sets will be irradiated to similar exposure levels, with 10% of the exposure to occur at reduced temperatures of 300°C and 200°C. A listing of the specimens included in the experiment is given in Table 1.

Table 1. Specimen Listing for the Varying Temperature Experiment

Specimen Type	Material	Number (350/200)	Number (500/300)
JP-TEM	Ferritic	200	200
	Vanadium	320	320
	Molybdenum	90	90
	Tungsten	50	50
	Austenitic	130	150
	Copper	80	80
	Nickel	120	120
	Others	50	50
JP-CVN-F1	Ferritic	48	48
JP-TN-1	Ferritic	110	110
	Vanadium	170	120
	Austenitic	70	50
Bar-7	Molybdenum	40	40
	Tungsten	40	40

The specimens are sealed in a static helium environment inside holes drilled into four axially displaced cylindrical specimen holders, as shown in Figures 1 and 2. The low temperature holders are aluminum, and the high temperature holders are beryllium. Aluminum and beryllium sleeves surround the specimens and ensure adequate thermal contact between the specimens and the holders. Holder temperatures, and therefore the specimen temperatures, are controlled by regulating the heat from cartridge type heaters within each holder. Independently controlled temperature control gas mixtures of helium and neon (or argon if required) flow between the holders and the capsule housing tube. The relative amount of the gases in the mixtures is adjusted to control the thermal conductivity of the mixture so that the heater output required to maintain the desired operating temperatures can be minimized.

Specimen temperatures are controlled whenever the reactor power is greater than a low power limit tentatively set at 8.5 MW in order to reduce the exposure levels at improper low temperatures to below 10^{-4} dpa. Specimens in the variable temperature holders will be maintained at 200°C and 300°C for approximately the first 55 hours of each 23-day (average) reactor cycle. Their temperature will then be increased to equal that of the specimens in the corresponding constant temperature zone for the duration of the cycle. The capsule is scheduled for 10 cycles of operation in an europium shielded RB☆ position beginning in early 1998.

PROGRESS

The design of the varying temperature experiment is approaching completion having moved from the conceptual design phase to the final design stage during this reporting period. Work has focused on 1) the development of a robust heater design, 2) testing of the proposed control gas mixture separation scheme, and 3) development of heat transfer models required to set final holder dimensions. A test facility has been constructed and is being used to operate a prototype holder in order to test the heater and gas seal designs used in this experiment, to measure the time response and extent of temperature variations due to control gas mixture adjustments and to benchmark the thermal calculations used in the design of the experiment.

Gas Flow Tests

Electric heaters are used to control specimen temperatures. The required heater output is reduced by flowing less thermally conductive gas mixtures through the temperature control gas gaps during periods of reduced reactor power operation. The thermal conductivity of the gas mixture must be reduced before the reactor can be operated at full power. In order to minimize the delays associated with changing the gas mixture, the capsule is designed to allow the neon or argon to mix with helium inside the capsule at the entrance of the temperature control gas gaps. This is accomplished by utilizing the arrangement shown in Figure 3.

Helium is supplied to the inner region of all four specimen holders at a constant flow rate in order to increase the heat transfer between the heaters and holders. The helium exits the inner region of the capsule by flowing through small holes in the wall of the zone separation piece attached to the base of each specimen holder. Neon or argon (or helium if required) is supplied to this region and mixes with the helium to form the gas mixture. The mixture flows up through the gap and out of the capsule through an effluent tube. To return the control gas to pure helium, the flow of neon is terminated. Pure helium quickly sweeps the residual neon out of all four gas gaps because it is supplied to them in parallel.

The inner radius of the capsule housing tube is used as the outer edge of the four temperature control gas gaps. The outer radius of the holders defines the inner edge of the gas gaps. The four gas gap regions are separated by a grafoil seal held by the upper and lower separation pieces of adjacent specimen holders. An overhanging portion of the seal is compressed between the housing wall and the lower edge of the upper separation piece. The seals mitigate the mixing of gas mixtures from adjacent zones, however some mixing is tolerable and can be compensated for by adding either extra neon or helium to the gas mixtures of upper zones as required.

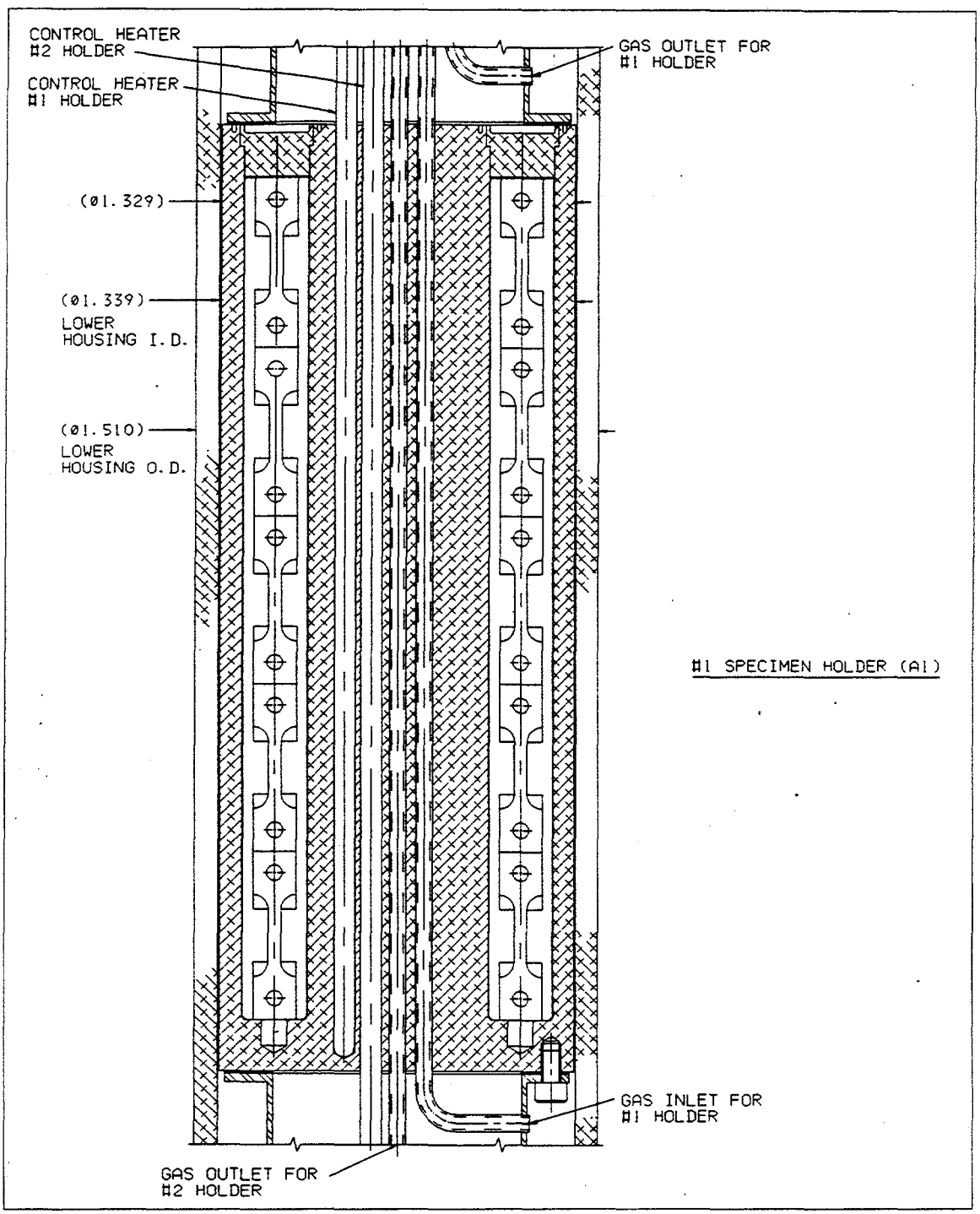

Figure 1.A specimen holder. The specimens are encased in sleeves, which are inserted into holes drilled into the face of the holder. Caps are welded at the end of the holes to seal the specimens in a static helium atmosphere. The inner radius of the housing tube and the outer radius of the holder defines the temperature control gas gap for the holder.

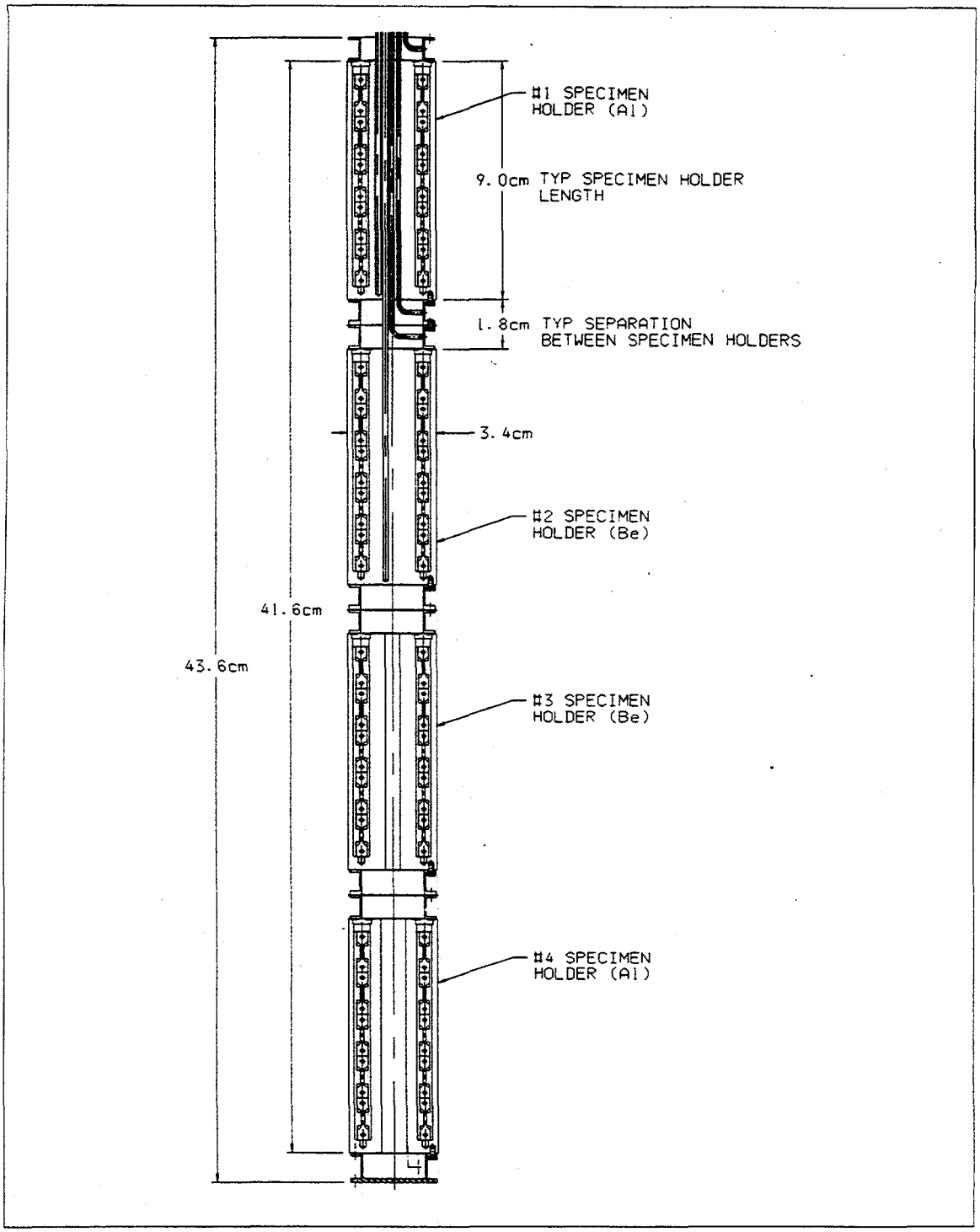

Figure 2. The arrangement of four specimen holders in the Varying Temperature Experiment. The lower two holders are varying temperature holders and the upper holders are their constant temperature counterparts. The two central, high temperature, holders are beryllium and the end, low temperature holders are aluminum.

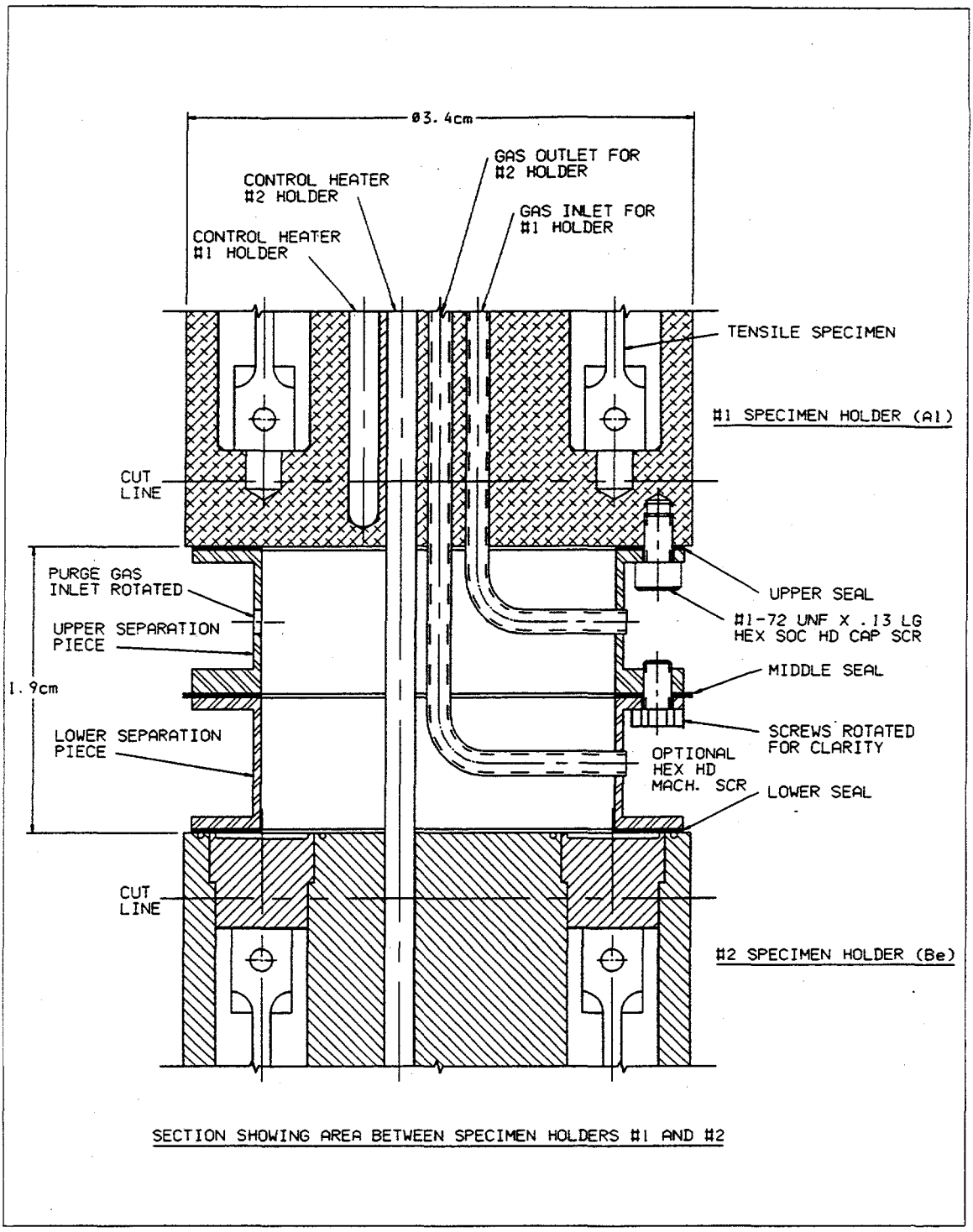

Figure 3. Arrangement of the region between two holders. The heaters and gas tubes for lower holders passes through holes in the upper holders. Stainless steel separation pieces physically and thermally separate the holders. The seal between the separation piece separates the control gas mixtures and centers the holders in the capsule housing tube.

The gas gap separation seals also center the holders within the capsule housing tube, helping to establish a symmetric gas gap, and provide insulation against heat loss from the end of the holders. The maximum range of temperature control through gas mixture adjustment is permitted when all of the heat generated within the holder is lost across the gas gap. The thin-walled, stainless steel separation pieces are designed to minimize parasitic end losses.

Time response tests have been conducted in which the temperature of a prototype holder was increased using a combination of heat input and gas mixture adjustment. The results from a typical experiment are shown in Figure 4. The temperature began to drop almost immediately after the flow of argon was terminated and was essentially eliminated within a minute of terminating the flow.

Heater Development

Two heater designs are used in this experiment. Both designs incorporate two axially displaced, nichrome elements housed in a 2.23-mm O.D. stainless steel sheath. The elements can be controlled independently, together, or with elements from other heaters to form heating zones. The heaters are inserted into axial holes in the inner region of the holders. One type of heater is used to control holder temperature. The other is used to add heat to the holder when the reactor is operating at reduced power.

The heater elements in the control heaters are slightly overlapped and together span the length of a holder. By operating either the upper or lower element, heat can be added selectively to the top or bottom of a specimen holder. This allows the heaters to compensate for the temperature gradients encountered during the operation of the experiment. There are three control heaters for each specimen holder.

The common heaters (named because they add heat to more than one holder) are similar to the control heaters except that their elements are longer (each element spans the length of a specimen holder) and the elements are displaced so that they add heat to adjacent holders. The common heaters are used in conjunction with the control gas mixtures primarily to reduce the required power output of the control heaters. They can be also used as the control heaters if necessary.

Several control heaters have been built and tested to failure in the testing facility. The greatest potential for failure occurs due to overheating in the region between the holder into which a heater is suppling heat and the holder directly above it. This is due to the nickel extension leads in this region, which produce an appreciable amount of heat when the heaters are operated at high current. A nickel transition is required between the nichrome heater element and the copper extension leads because the high temperatures expected within the elements at full power would melt copper extension leads if they were connected directly to the nichrome.

The exposed region of the heaters is a fusible link in the event of a simultaneous heater controller and fuse failure. If the controller were to inadvertently expose the heaters to the maximum voltage potential of 110 VAC and the fuse for that heater (10 amps) did not blow, the nickel wire will overheat and melt, opening the control circuit. It is possible that the current could short through the sheath to the grounded structure of the capsule, however the heat input into the capsule would be terminated. Testing has shown that heater failure can be avoided by limiting the sheath temperature in the region between holders to less than 1000°C. In the capsule, thermocouples monitor heater sheath temperatures in the exposed region between the two high temperature holders.

Three control heaters have been cycled dozens of times beyond the peak demand expected during the experiment. The current through both elements has (to date) been rapidly increased from 0 to 9 amps (a total of power output of approximately 160 watts per element) and allowed to operate at this power until temperature equilibrium was attained. Both elements in the heaters have been operated at 9 amps for extended periods to simulate reactor start-up with long delays at low power. Also, individual elements have been operated at

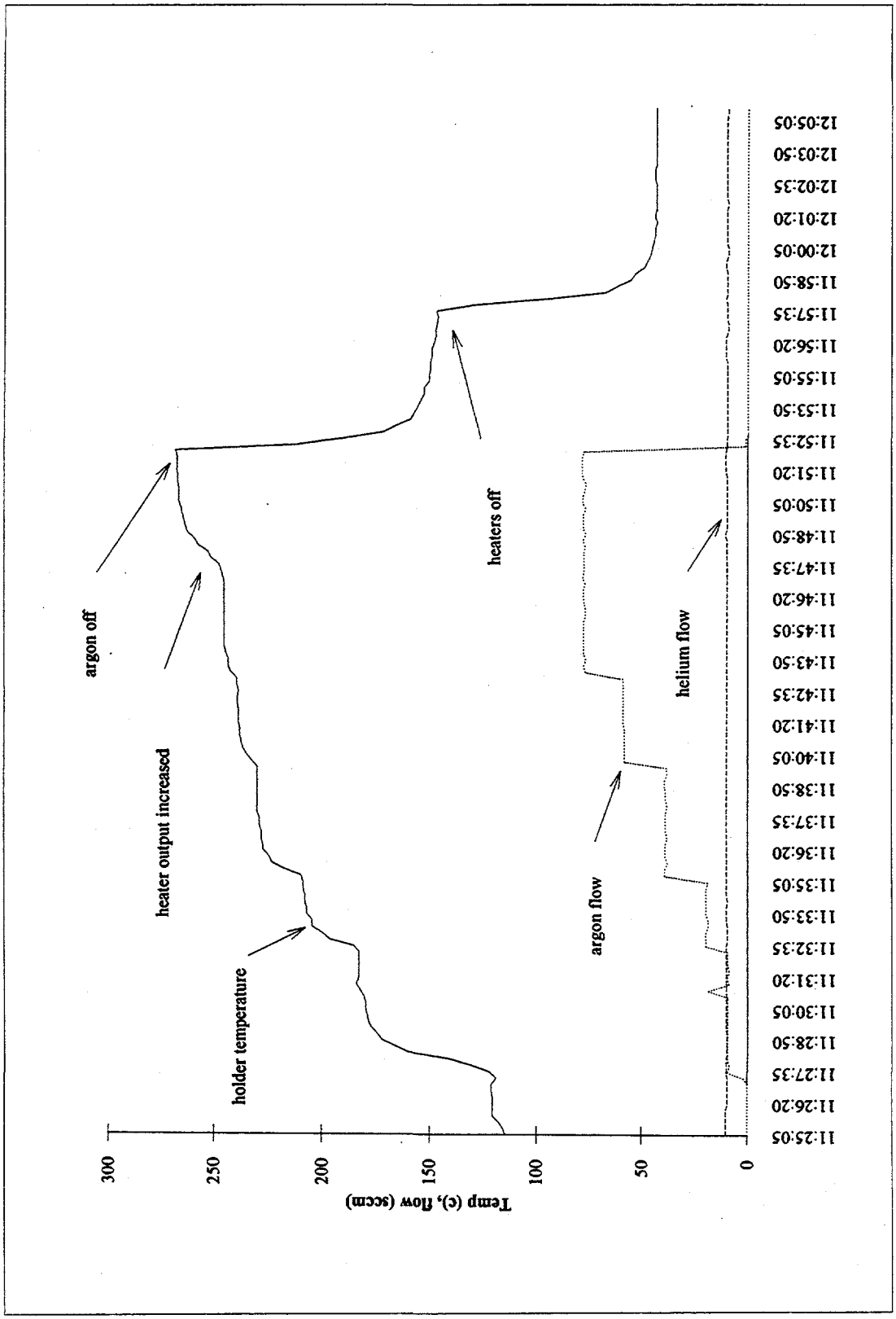

Figure 4. Plot showing the temperature response of the prototype holder to a sudden elimination of argon from the temperature control gas mixture.

currents greater than 14 amps (approximately 400 watts) for extended periods. Temperature gradients of greater than 4 °C/cm can be established across the prototype holder by operating either the upper or lower elements as a group, which is adequate to compensate for the expected temperature gradients.

FUTURE WORK

Heater power output is controlled by regulating the current passing through them. The controllers must have adequate response time to compensate for the temperature changes associated with temperature control gas mixture adjustments and reactor power changes. Avoiding specimen temperature overshoot is a principal requirement of the control system. The testing facility is presently being used to evaluate controllers and a selection is expected soon.

The engineering drawings for the experiment are nearing completion. The final aspect of the design will be to set the outer dimension of the four specimen holders in order to establish the temperature control gas gap. The setting of the holder dimensions is complicated by an unknown heat generation within the europium liners and unknown heat generation rate in beryllium. The operation of the RB-11J and RB-12J capsules is being evaluated to determine the heat generation rate of materials inside the europium liners. The neutron and gamma flux calculations used in the design of RB-11J and RB-12J are being modified to estimate heat generation rate in a beryllium holder inside the new liners as opposed to the aluminum holder material that was assumed in the RB-11J and RB-12J calculations. Heat transfer models are being benchmarked against the prototype tests so that the final holder dimensions can be set as soon as the heat generation rate is established.

Except for a few details, the design is complete. Test welds are to be performed in March 1997 to develop a procedure for sealing the specimens in the holder specimen holes. The specimens are scheduled to be delivered to ORNL in June, at which time assembly will begin. A paper on the final testing results and design is being prepared for presentation at the ICFRM-8 Conference in Japan in October 1997.

DISASSEMBLY OF THE FUSION-1 CAPSULE AFTER IRRADIATION IN THE BOR-60 REACTOR*

H. Tsai (Argonne National Laboratory), V. A. Kazakov and V. P. Chakin (Research Institute of Atomic Reactors, Russia), and A. F. Rowcliffe (Oak Ridge National Laboratory)

SUMMARY

A U.S./Russia (RF) collaborative irradiation experiment, Fusion-1, was completed in June 1996 after reaching a peak exposure of ≈17 dpa in the BOR-60 fast reactor at the Research Institute of Atomic Reactors (RIAR) in Russia. The specimens were vanadium alloys, mainly of recent heats from both countries. In this reporting period, the capsule was disassembled at the RIAR hot cells and all test specimens were successfully retrieved. For the disassembly, an innovative method of using a heated diffusion oil to melt and separate the lithium bond from the test specimens was adopted. This method proved highly successful.

OBJECTIVE

The main objective of this task was to disassemble the Fusion-1 irradiation vehicle and retrieve the specimens contained inside.

BACKGROUND

The Fusion-1 experiment utilized a single lithium-bonded stainless steel capsule 508 mm long and 36 mm in diameter. The construction of the capsule consisted of (from bottom) a bottom end plug with a pedestal, an assembly of six tiers of U.S. specimens placed on top of the pedestal, four separate tiers of RF specimens place on top of the U.S. assembly, a hold-down spring, and a top end plug. Nichrome wires were used to tie the specimens into bundles in each tier, and additional nichrome wires were used to secure the bundles to the three spacer rods connecting the tiers. A fill tube at the top of the capsule was used to charge lithium into the capsule as the last step of the assembly.

As part of the collaborative agreement, the capsule was disassembled in the RIAR hot cell facilities. The central issue of the disassembly was how to remove the bulk of the lithium bond. The conventional method used in the U.S. on capsules (usually of much smaller sizes) is to dissolve the lithium bond with liquid ammonia. But that approach was judged to be impractical due to the large size of the Fusion-1 capsule. An alternative method of using heated diffusion-pump oil to melt the bulk lithium, proposed by RIAR, was adopted for the present work. After the bulk lithium had been removed with the hot oil, acetone would be used to remove the oil film on the specimens and alcohol would be used to remove the residual lithium and clean the specimens. Because of the potential for fire from molten lithium and/or hot oil in the air atmosphere of the hot cell, provisions to preclude and extinguish fires were incorporated into the procedures.

Before disassembly, simulated oil exposure tests were conducted with unirradiated vanadium specimens. The results showed that the heated oil would not affect the surface conditions of the materials under the anticipated heating conditions for the disassembly, i.e., ≤250°C for 4 h.

---

*Work supported by U.S. Department of Energy, Office of Fusion Energy Research, under Contract W-31-109-Eng-38.

RESULTS

The disassembly work was accomplished in two RIAR Materials Science hot cells, K2 for capsule opening and bulk lithium removal and K12 for final cleaning. Prior to the disassembly work, the K2 cell, which had been used for fuel element sectioning, was decontaminated by washing and wiping to a reported surface α level of 50 dpm/cm^2. The K12 cell, a structural materials testing cell, was clean and had no reported prior α contamination.

In the K2 cell, two circumferential cuts were made with an abrasive saw to remove the top and bottom end plugs of the capsule. Although part of the lower cut was through the lithium bond, the operation was completed with no incidents because the cutting speed was kept extremely low and the region of the cut was cooled periodically with poured liquid nitrogen. The opened capsule was placed immediately in a stainless steel pan filled with VM-1 oil, a mineral-based diffusion pump oil with only a moderate flash point. An electric heater was used to gradually heat the oil to the target temperature of 220°C (lithium melts at 181°C) in approximately 2 h. Noticeable smoking of the oil occurred above ≈200°C but otherwise the heating process was uneventful. A few nodules of lithium floated to the top of oil during the heating, lithium being lighter than the oil. When 220°C was reached, the capsule was lifted out of the oil with a hoist and all contents were poured out of the capsule into a clean tray. The liquid lithium at this point had a silvery shine but solidified immediately into grayish ingots in the tray. There was no fire with the exposed lithium. Most of the recovered specimens remained fixed in bundles in the tiers; however, some were loose, apparently due to breakage of the nichrome wires during irradiation.

All contents were returned to the oil pan to minimize oxidation of the residual lithium. The oil pan was kept at a reduced temperature of 200°C for 1 h to allow more complete separation of the lithium from the specimens. The bath was then allowed to cool to room temperature. The solidified lithium ingots on the oil surface were removed and the oil was drained to recover all specimens.

Following degreasing with acetone and several rinses with alcohol, the specimen assembly was taken apart tier-by-tier. The separated tiers were cleaned with additional alcohol. Visual inspection of the cleaned specimens (loose and in bundles) showed their condition to be satisfactory, i.e., none appeared to be bent or broken. Because of the care taken by the hot cell staff, no specimens appeard to have been lost in the operation. All bundles and loose specimens, in plastic pouches, were then transferred from the K2 cell to the K12 cell for wire removal, final cleaning, and sorting.

Preliminary smear testing of partially cleaned specimens in the K12 cell showed the surface α-contamination to be ≈ 1 dpm/cm^2, which is within the handling limitations of the U.S. hot cells.

CONCLUSIONS

The Fusion-1 capsule was successfully disassembled at RIAR. There was no loss or damage of the specimens during the disassembly operation. All tasks were accomplished without incident in the hot cells. For large-size capsules, such as the Fusion-1, using a heated oil appears to be a satisfactory method to separate the lithium bond from the specimens.

SCHEDULE AND STATUS OF IRRADIATION EXPERIMENTS – A. F. Rowcliffe and M. L. Grossbeck (Oak Ridge National Laboratory)

OBJECTIVE

To provide an updated summary of the status of irradiation experiments for the neutron-interactive materials program.

SUMMARY

The current status of reactor irradiation experiments is presented in tables summarizing the experimental objectives, conditions, and schedule.

PROGRESS AND STATUS

Currently, the program has two irradiation experiments in reactor; and 8 experiments in the planning or design stages. Postirradiation examination and testing is in progress on 18 experiments.

Summary of Reactor Irradiation Experiments

Experiment	Lead Lab	Collaborators	Responsible Person	Major Objectives	Materials	Temperature °C	Dose (dpa) or fluence	Irrad. Start	Irrad. Finish	Status
EBR-II, Reactor, ANL, Idaho Falls, ID										
COBRA 1A1	PNL	ORNL, ANL, MONBUSHO	M.L. Hamilton	Tensile and fatigue prop., Charpy impact, fracture toughness, TEM	Austenitic and ferritic steels, Fe-alloys, V, Be, low act. materials, Cu alloys, Ti-Al, SiC, C-C comp.	370, 500, 600	9	Nov-92	Apr-93	
COBRA 1A2	PNL	ORNL, ANL, MONBUSHO	M.L. Hamilton	Tensile and fatigue prop., Charpy impact, fracture toughness, TEM	Austenitic and ferritic steels, Fe-alloys, V, Be, low act. materials, Cu alloys, Ti-Al, SiC, C-C comp.	370, 400, 800	33	Nov-92	Sep-94	
X530	ANL		H. Tsai, H.M. Chung	He-effects, swelling, Charpy impact, fracture toughness, tensile prop.	V alloys	370	5	Aug-94	Sep-94	
High Flux Isotope Reactor, ORNL, Oak Ridge, TN										
HFIR-CTR-60	ORNL		S.J. Zinkle	Flexure bars, TEM, indentation disks	Isotopically tailored ceramics	100-600	2.4E+26 n/m2	Dec-94	Aug-95	
HFIR-CTR-61	ORNL		S.J. Zinkle	Similar to HFIR-CTR-60			7.20E+26	Dec-94	Aug-97	
HFIR-JP-9	ORNL	JAERI	P.J. Maziasz/ J.E. Pawel	He effects by isotopic tailoring, tensile prop., TEM	Austenitic and ferritic steels	300-600	57	Jul-90	Apr-94	
HFIR-JP-10	ORNL	JAERI	P.J. Maziasz/ J.E. Pawel	He effects by isotopic tailoring, tensile prop., TEM	Austenitic and ferritic steels	300-600	17	Jul-90	Sep-91	
HFIR-JP-11	ORNL	JAERI	P.J. Maziasz/ J.E. Pawel	Similar to HFIR-JP-10			17	Jul-90	Sep-91	
HFIR-JP-12	ORNL	JAERI	P.J. Maziasz/ J.E. Pawel	Similar to HFIR-JP-9			57	Jul-90	Apr-94	
HFIR-JP-13	ORNL	JAERI	P.J. Maziasz/ J.E. Pawel	Similar to HFIR-JP-10			17	Jul-90	Sep-91	
HFIR-JP-14	ORNL	JAERI	P.J. Maziasz/ J.E. Pawel	He effects by isotopic tailoring, tensile prop., TEM	Austenitic and ferritic steels	300-600	34	Jul-90	Sep-92	

Summary of Reactor Irradiation Experiments

Experiment	Lead Lab	Collaborators	Responsible Person	Major Objectives	Materials	Temperature °C	Dose (dpa) or fluence	Irrad. Start	Irrad. Finish	Status
HFIR-JP-15	ORNL	JAERI	P.J. Maziasz/ J.E. Pawel	Similar to HFIR-JP-9			57	Jul-90	Apr-94	
HFIR-JP-16	ORNL	JAERI	P.J. Maziasz/ J.E. Pawel	Similar to HFIR-JP-10			17	Jul-90	Sep-91	
HFIR-JP-17	ORNL	JAERI	M.L. Grossbeck/ J.E. Pawel	Fracture toughness, tensile prop. TEM	Austenitic and ferritic steels	250-300	3	Dec-91	Feb-92	
HFIR-JP-18	ORNL	JAERI	M.L. Grossbeck/ J.E. Pawel	Fracture toughness, tensile prop. TEM	Austenitic and ferritic steels	60-125	3	Aug-91	Oct-91	
HFIR-JP-19	ORNL	JAERI	M.L. Grossbeck/ J.E. Pawel	Similar to HFIR-JP-18		60-125	3	Aug-91	Oct-91	
HFIR-JP-20	ORNL	JAERI	J.E. Pawel	Tensile Prop., TEM, He effects by isotopic tailoring	Austenitic and ferritic steels	300-600	8	Dec-93	Jun-94	
HFIR-JP-21	ORNL	JAERI	J.E. Pawel	Similar to HFIR-JP-20			18	Dec-93	Apr-95	
HFIR-JP-22	ORNL	JAERI	J.E. Pawel	Similar to HFIR -JP-20			34	Dec-93	Jan-96	
HFIR-JP-23	PNL	MONBUSHO	D.S. Gelles	TEM	Austenitic and ferritic steels, *Cu, Mo, V alloys,* TiAl	300-600	8	Dec-93	Jun-94	
HFIR-MFE-60J	ORNL	JAERI	J.L. Scott/ M.L. Grossbeck	Spectrally tailored for fusion He prod. Began in ORR as ORR-MFE-6J (6.9 dpa). TEM, Charpy, irrad. creep, tensile and crack growth prop.	Austenitic and ferritic steels, and Ni alloys	60	19 (total)	Jul-90	Nov-92	
HFIR-MFE-330J	ORNL	JAERI	J.L. Scott/ M.L. Grossbeck	Similar to HFIR-MFE-60J. Began in ORR as ORR-MFE-7J (7.4 dpa)		330	19 (total)	Jul-90	Nov-92	
HFIR-MFE-200J	ORNL	JAERI	M.L. Grossbeck/ J.E. Pawel	Similar to HFIR-MFE-60J. Began in ORR as ORR-MFE-6J (6.9 dpa)		200	17 (total)	Nov-92	Jan-95	
HFIR-MFE-400J	ORNL	JAERI	M.L. Grossbeck/ J.E. Pawel	Similar to HFIR-MFE-60J. Began as ORR-MFE-7J (7.4 dpa)		400	17 (total)	Nov-92	Jan-95	
HFIR-HT-S1, -S7	ORNL		L.L. Snead	Thermal conductivity	Various insulators	80-350	0.01-1.0	Jun-95	Aug-95	
HFIR-HT-F Series	ORNL		L. L. Snead	Fiber tensile	SiC	80-800	0.001-1.0	Jan-95	Mar-96	

Summary of Reactor Irradiation Experiments

Experiment	Lead Lab	Collaborators	Responsible Person	Major Objectives	Materials	Temperature °C	Dose (dpa) or fluence	Irrad. Start	Irrad. Finish	Status
HFIR-TRIST-ER1	ORNL	MONBUSHO/ JAERI	S.J. Zinkle	In-situ electrical conductivity	Al2O3	450	3E+25 n/m2	Apr-96	Jun-96	
HFIR-MFE-RB-10J	ORNL	JAERI	J.E. Pawel	Tensile, fracture	Vanadium, 316LN-1G, J316	200, 500	5	Feb-98	Feb-99	
HFIR-MFE-RB-11J	ORNL	MONBUSHO/ JAERI	M. L. Grossbeck	Tensile, fracture, TEM	Low activation ferritics, V alloys, SiC	300	5	Feb-97	Feb-98	
HFIR-MFE-RB-12J	ORNL	MONBUSHO/ JAERI	M. L. Grossbeck	Tensile, fracture, TEM	Low activation ferritics, V alloys, SiC	500	5	Feb-97	Feb-98	
HFIR-CTR-62	ORNL	JAERI	R.L. Klueh	Charpy impact and He effects	Reduced act. and conventional ferritic steels	300, 400	13	Apr-95	Dec-95	
HFIR-CTR-63	ORNL	JAERI	R.L. Klueh	Charpy impact and tensile, TEM, He effects	Reduced act. and conventional ferritic steels	300, 400	13	Apr-95	Dec-95	
HFIR-JP25	ORNL	JAERI	R.L. Klueh	Tensile, fracture, TEM	Low activation ferritics	300, 500	20	Oct-97	Dec-98	
HFIR-JP27	ORNL	JAERI	L.L. Snead	Fracture, TEM	Intermetallics, SiC	500-800	10	Oct-97	Jan-98	
HFIR-JP28	ORNL	JAERI	L.L. Snead	Fracture, TEM	SiC	500-800	10	Sep-97	Mar-98	
HFIR-P3-6	ORNL	MONBUSHO	K. R. Thoms	Varying Temperature	TBD	400-600	5	May-97	Apr-98	
High Flux Beam Reactor, Brookhaven National Laboratory										
HFBR-ISEC-3	ORNL		L.L. Snead	In-situ electrical	WESGO Al2O3	450	1.5	Jul-95	Sep-95	
HFBR-V1	ORNL		L.L. Snead	Tensile, fracture	V-4Cr-4Ti	75, 150, 225	0.4	May-95	Jun-95	
HFBR-V2	ORNL		L.L. Snead	Tensile, fracture	V-4Cr-4Ti	75, 225, 300, 375	0.4	Jul-95	Aug-95	
HFBR-V3	ORNL		L.L. Snead	Tensile, fracture	V-4Cr-4Ti	160, 265, 315, 420	0.4	Aug-96	Sep-96	
HFBR-V4	ORNL		L.L. Snead	Tensile, fracture	V-4Cr-4Ti	105-505	0.1	Aug-96	Sep-96	
Advanced Test Reactor, Idaho Falls										
ATR-A1	ANL	MONBUSHO	D.L. Smith	Tensile, fracture toughness, TEM, creep	Vanadium alloys	200, 300	5	Dec-95	May-96	

Summary of Reactor Irradiation Experiments

Experiment	Lead Lab	Collaborators	Responsible Person	Major Objectives	Materials	Temperature °C	Dose (dpa) or fluence	Irrad. Start	Irrad. Finish	Status
BOR-60 Reactor, RIAR, Dimitrovgrad, Russia										
BOR-60-Fusion-1	ORNL, ANL	RDIPE, RIAR	A.F. Rowcliffe, D.L. Smith	Mechanical and microstructural properties	V alloys	350-380	10	Jul-95	Mar-96	
SM-2 Reactor, RIAR, Dimitrovgrad, Russia										
SM-2.1	ORNL, PNL	RIAR	S.J. Zinkle	Tensile, electrical, microstructural, and creep properties	Cu alloys	100, 200, 330	1, 5	Dec-93	Feb-94	
SM-2.2	PNL	SRIAR	D.J. Edwards	Mechanical behavior of bonded materials	Cu alloys/SS, Cu/Be	120, 300	0.2	Jan-96	Mar-96	
SM-2.3	PNL	SRIAR	D.J. Edwards	Mechanical behavior of bonded materials	Cu alloys/SS, Cu/Be	100, 250	0.2	Apr-97	Jun-97	

Irradiation complete

Irradiation in progress

Irradiation planned

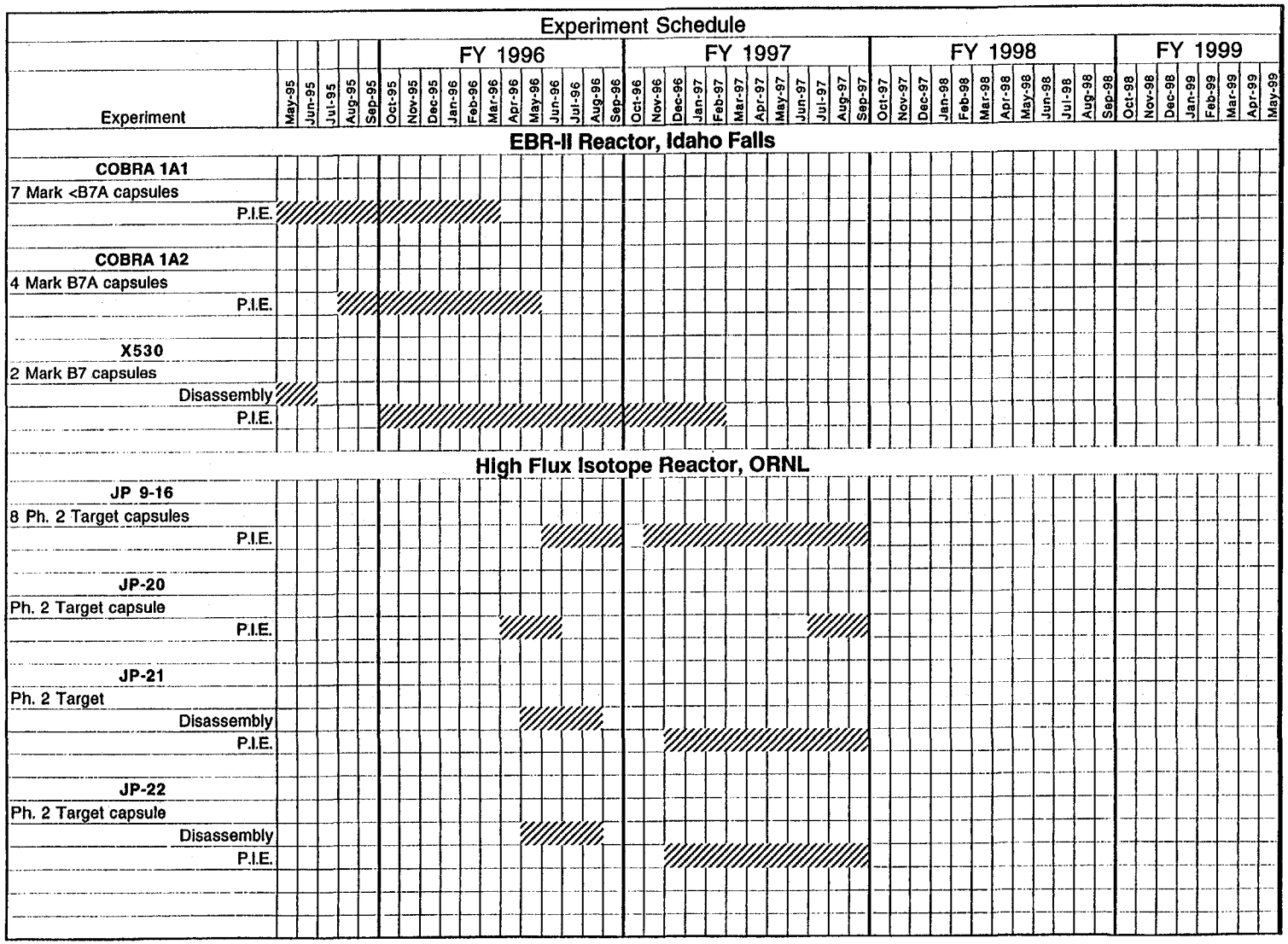
Experiment Schedule
FY 1996
FY 1997
FY 1998
FY 1999
Experiment
May-95 Jun-95 Jul-95 Aug-95 Sep-95 Oct-95 Nov-95 Dec-95 Jan-96 Feb-96 Mar-96 Apr-96 May-96 Jun-96 Jul-96 Aug-96 Sep-96 Oct-96 Nov-96 Dec-96 Jan-97 Feb-97 Mar-97 Apr-97 May-97 Jun-97 Jul-97 Aug-97 Sep-97 Oct-97 Nov-97 Dec-97 Jan-98 Feb-98 Mar-98 Apr-98 May-98 Jun-98 Jul-98 Aug-98 Sep-98 Oct-98 Nov-98 Dec-98 Jan-99 Feb-99 Mar-99 Apr-99 May-99
EBR-II Reactor, Idaho Falls
COBRA 1A1
7 Mark <B7A capsules
P.I.E.
COBRA 1A2
4 Mark B7A capsules
P.I.E.
X530
2 Mark B7 capsules
Disassembly
P.I.E.
High Flux Isotope Reactor, ORNL
JP 9-16
8 Ph. 2 Target capsules
P.I.E.
JP-20
Ph. 2 Target capsule
P.I.E.
JP-21
Ph. 2 Target
Disassembly
P.I.E.
JP-22
Ph. 2 Target capsule
Disassembly
P.I.E.

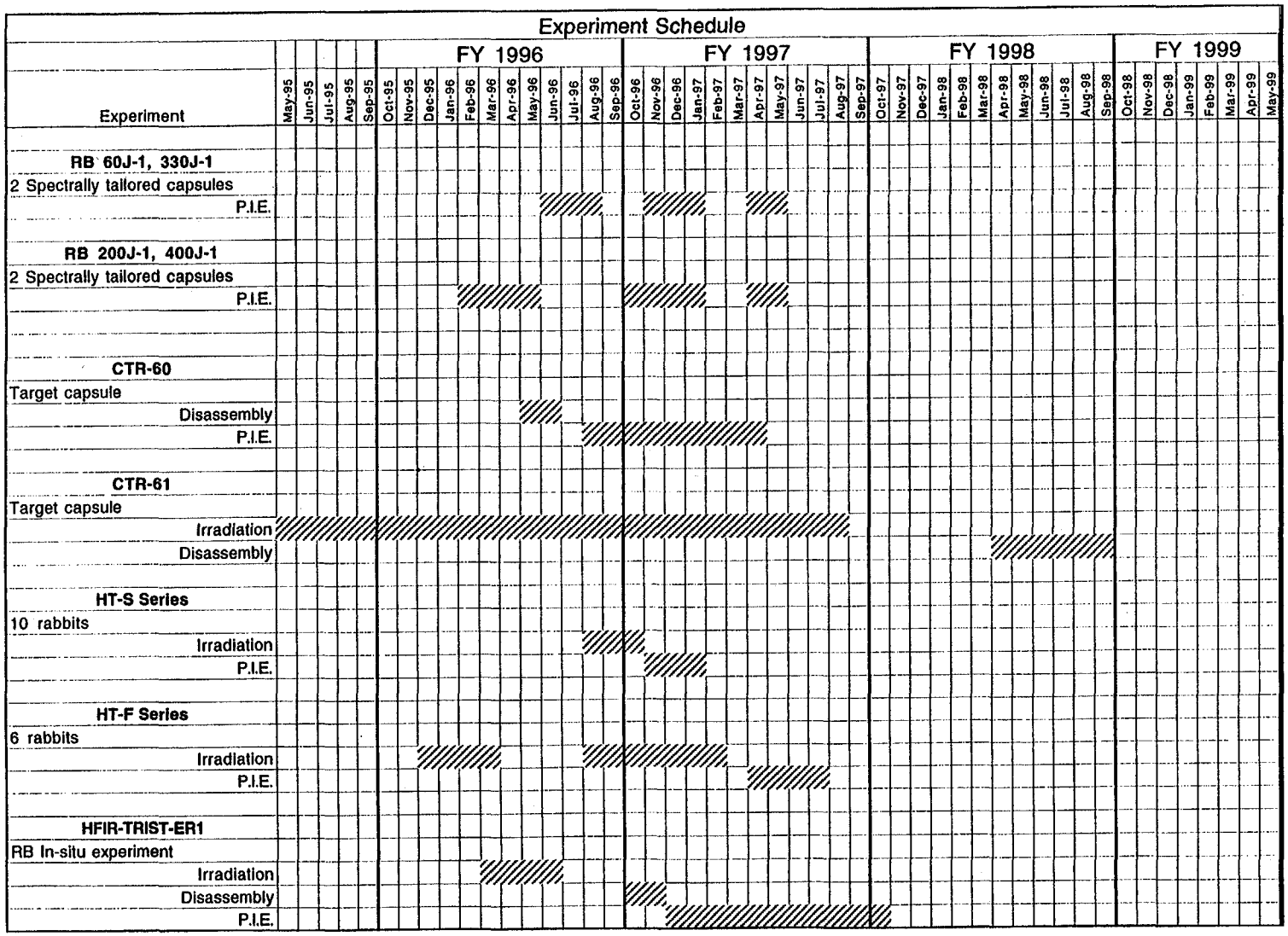
Experiment Schedule
FY 1996
FY 1997
FY 1998
FY 1999
Experiment
May-95
Jun-95
Jul-95
Aug-95
Sep-95
Oct-95
Nov-95
Dec-95
Jan-96
Feb-96
Mar-96
Apr-96
May-96
Jun-96
Jul-96
Aug-96
Sep-96
Oct-96
Nov-96
Dec-96
Jan-97
Feb-97
Mar-97
Apr-97
May-97
Jun-97
Jul-97
Aug-97
Sep-97
Oct-97
Nov-97
Dec-97
Jan-98
Feb-98
Mar-98
Apr-98
May-98
Jun-98
Jul-98
Aug-98
Sep-98
Oct-98
Nov-98
Dec-98
Jan-99
Feb-99
Mar-99
Apr-99
May-99
RB 60J-1, 330J-1
2 Spectrally tailored capsules
P.I.E.
RB 200J-1, 400J-1
2 Spectrally tailored capsules
P.I.E.
CTR-60
Target capsule
Disassembly
P.I.E.
CTR-61
Target capsule
Irradiation
Disassembly
HT-S Series
10 rabbits
Irradiation
P.I.E.
HT-F Series
6 rabbits
Irradiation
P.I.E.
HFIR-TRIST-ER1
RB In-situ experiment
Irradiation
Disassembly
P.I.E.

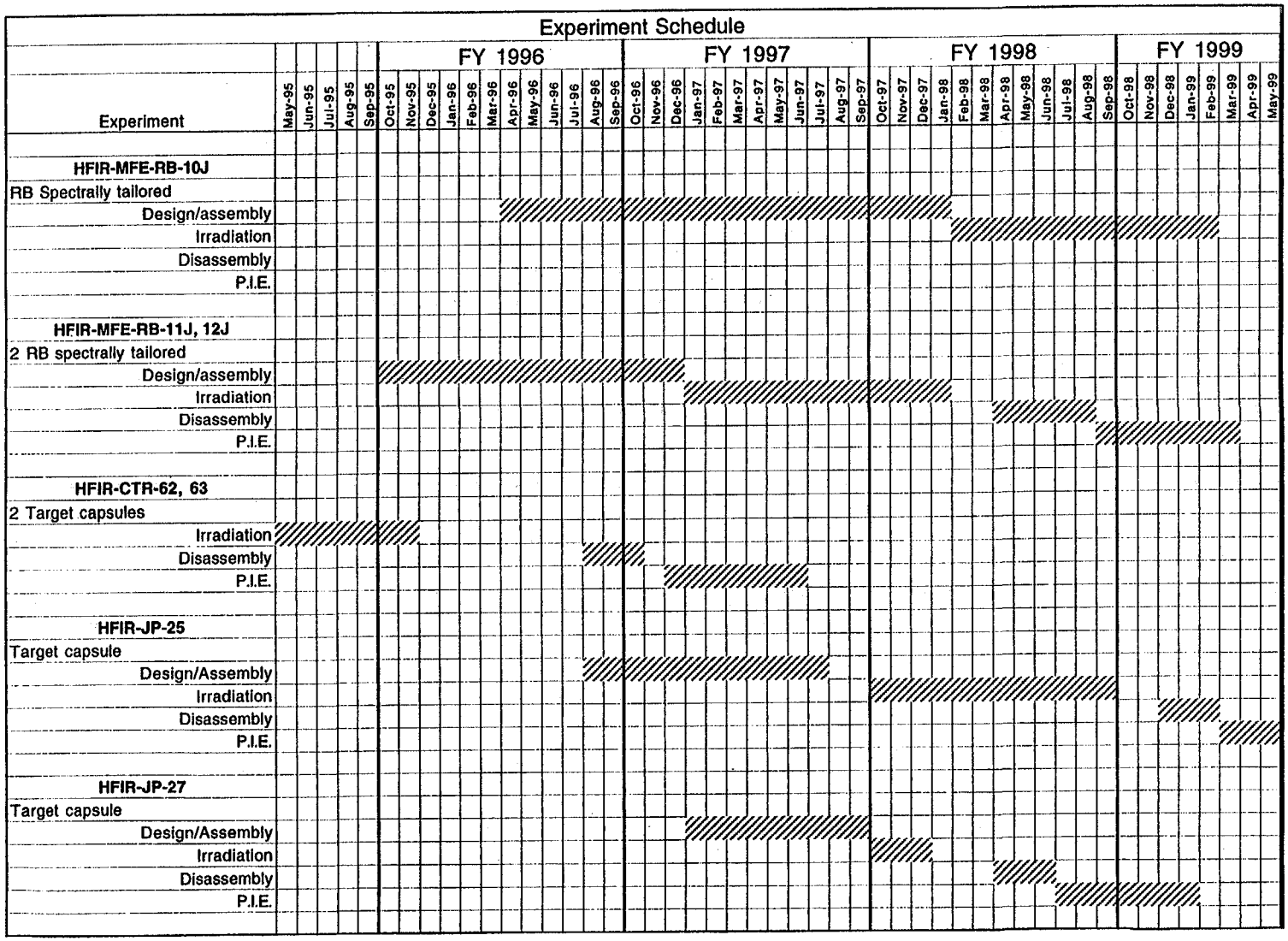
Experiment Schedule
FY 1996
FY 1997
FY 1998
FY 1999
Experiment
May-95
Jun-95
Jul-95
Aug-95
Sep-95
Oct-95
Nov-95
Dec-95
Jan-96
Feb-96
Mar-96
Apr-96
May-96
Jun-96
Jul-96
Aug-96
Sep-96
Oct-96
Nov-96
Dec-96
Jan-97
Feb-97
Mar-97
Apr-97
May-97
Jun-97
Jul-97
Aug-97
Sep-97
Oct-97
Nov-97
Dec-97
Jan-98
Feb-98
Mar-98
Apr-98
May-98
Jun-98
Jul-98
Aug-98
Sep-98
Oct-98
Nov-98
Dec-98
Jan-99
Feb-99
Mar-99
Apr-99
May-99
HFIR-MFE-RB-10J
RB Spectrally tailored
Design/assembly
Irradiation
Disassembly
P.I.E.
HFIR-MFE-RB-11J, 12J
2 RB spectrally tailored
Design/assembly
Irradiation
Disassembly
P.I.E.
HFIR-CTR-62, 63
2 Target capsules
Irradiation
Disassembly
P.I.E.
HFIR-JP-25
Target capsule
Design/Assembly
Irradiation
Disassembly
P.I.E.
HFIR-JP-27
Target capsule
Design/Assembly
Irradiation
Disassembly
P.I.E.

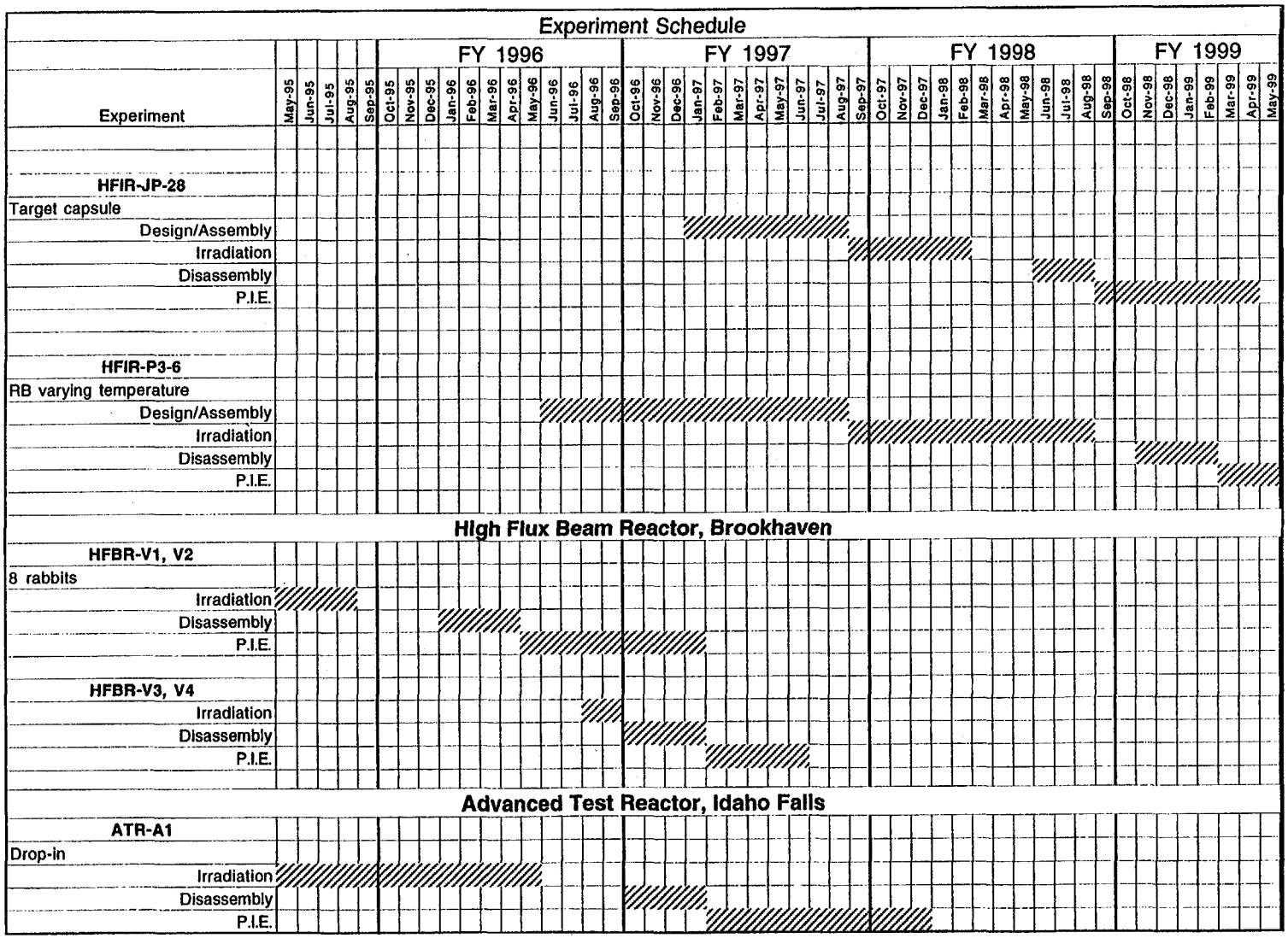
Experiment Schedule
FY 1996
FY 1997
FY 1998
FY 1999
Experiment
May-95
Jun-95
Jul-95
Aug-95
Sep-95
Oct-95
Nov-95
Dec-95
Jan-96
Feb-96
Mar-96
Apr-96
May-96
Jun-96
Jul-96
Aug-96
Sep-96
Oct-96
Nov-96
Dec-96
Jan-97
Feb-97
Mar-97
Apr-97
May-97
Jun-97
Jul-97
Aug-97
Sep-97
Oct-97
Nov-97
Dec-97
Jan-98
Feb-98
Mar-98
Apr-98
May-98
Jun-98
Jul-98
Aug-98
Sep-98
Oct-98
Nov-98
Dec-98
Jan-99
Feb-99
Mar-99
Apr-99
May-99
HFIR-JP-28
Target capsule
Design/Assembly
Irradiation
Disassembly
P.I.E.
HFIR-P3-6
RB varying temperature
Design/Assembly
Irradiation
Disassembly
P.I.E.
High Flux Beam Reactor, Brookhaven
HFBR-V1, V2
8 rabbits
Irradiation
Disassembly
P.I.E.
HFBR-V3, V4
Irradiation
Disassembly
P.I.E.
Advanced Test Reactor, Idaho Falls
ATR-A1
Drop-in
Irradiation
Disassembly
P.I.E.

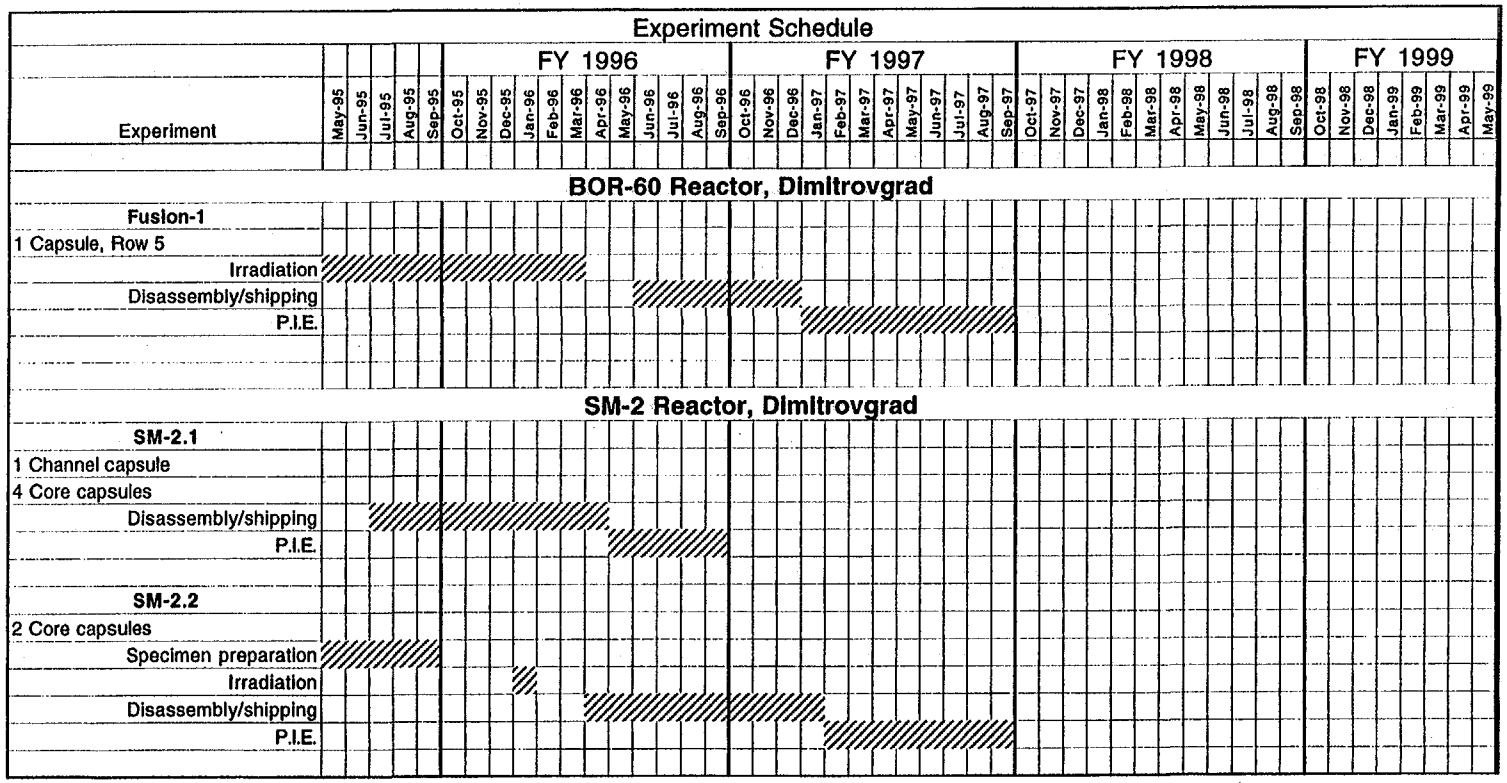
Experiment Schedule
FY 1996
FY 1997
FY 1998
FY 1999
Experiment
May-95
Jun-95
Jul-95
Aug-95
Sep-95
Oct-95
Nov-95
Dec-95
Jan-96
Feb-96
Mar-96
Apr-96
May-96
Jun-96
Jul-96
Aug-96
Sep-96
Oct-96
Nov-96
Dec-96
Jan-97
Feb-97
Mar-97
Apr-97
May-97
Jun-97
Jul-97
Aug-97
Sep-97
Oct-97
Nov-97
Dec-97
Jan-98
Feb-98
Mar-98
Apr-98
May-98
Jun-98
Jul-98
Aug-98
Sep-98
Oct-98
Nov-98
Dec-98
Jan-99
Feb-99
Mar-99
Apr-99
May-99
BOR-60 Reactor, Dimitrovgrad
Fusion-1
1 Capsule, Row 5
Irradiation
Disassembly/shipping
P.I.E.
SM-2 Reactor, Dimitrovgrad
SM-2.1
1 Channel capsule
4 Core capsules
Disassembly/shipping
P.I.E.
SM-2.2
2 Core capsules
Specimen preparation
Irradiation
Disassembly/shipping
P.I.E.

Distribution

1-16. Argonne National Laboratory, 9700 South Cass Avenue, Argonne, IL 60439

M. C. Billone	C. E. Johnson	J. H. Park
O. K. Chopra	F. Kassner	D. L. Smith
H. M. Chung	J. P. Kopasz	W. Tam
D. R. Diercks	R. F. Mattas	H. C. Tsai
J. Gazda	K. Nateson	
A. B. Hull	L. A. Niemark	

17-18. Argonne National Laboratory, EBR-II Division, P.O. Box 2528, Idaho Falls, ID 83403-2528

H. P. Planchon D. L. Porter

19. Auburn University, Department of Mechanical Engineering, 201 Ross Hall, Auburn, AL 36849

B. A. Chin

20-35. Pacific Northwest National Laboratory, P.O. Box 999, Richland, WA 99352

D. J. Edwards	L. R. Greenwood	R. H. Jones
J. L. Ethridge	M. L. Hamilton	W. W. Laity
F. A. Garner (5)	H. L. Heinisch	O. D. Slagle
D. S. Gelles	G. W. Hollenberg	J. Youngblood

36. Carnegie Institute of Technology, Carnegie-Mellon University, Schenley Park, Pittsburgh, PA 15213

W. M. Garrison, Jr.

37. Commissariat à l'Energie Atomique, Direction des Technologies Advancées, M2R1/DECM Cen-Saclay, Gif Sur Yvette, Cedex, France

F. Tavassoli

38-40. General Atomics, P.O. Box 85608, San Diego, CA 92138

W. R. Johnson K. R. Schultz C. Wong

41. Georgia Institute of Technology, Fusion Research Center, 0225, Atlanta, GA 30332

W. M. Stacey

42. Grand Canyon University, Department of Natural Science, 3300 W. Camelback Rd., Phoenix, AZ 85017

W. A. Coghlan

43-45. Idaho National Engineering Laboratory, Fusion Safety Program, P.O. Box 1625, Idaho Falls, ID 83415-3523

G. Longhurst K. McCarthy D. Petti

46. Knolls Atomic Power Laboratory, P.O. Box 1072, Schenectady, NY 12301

G. Newsome

47-48. Lawrence Livermore National Laboratory, P.O. Box 808, Livermore, CA 94550

E.C.N. Dalder J. Perkins

49-55. Los Alamos National Laboratory, P.O. Box 1663, Los Alamos, NM 87545

J. L. Anderson	H. M. Frost	W. F. Sommer
D. W. Cooke	R. E. Siemon	K. E. Sickafus
E. H. Farnum		

56-58. Massachusetts Institute of Technology, Department of Metallurgy and Materials Science, Cambridge, MA 02139
L. W. Hobbs N. J. Grant K. C. Russell

59. Massachusette Institute of Technology, Plasma Fusion Center Headquarters, Cambridge, MA 02139
D. B. Montgomery

60-61. McDonnell-Douglas Corporation, Mail Code 106 7211, McDonnell Blvd., Dock 106, Berkeley, MO 63134
J. W. Davis G. W. Wille

62. MER Corp., 7960 South Kolb Rd., Tucson, AZ 85706
W. Kowbel

63. Merrimack College, Dept. of Physics, 315 Turnpike Street, North Andover, MA 01845
D. P. White

64. M. J. Schiff & Associates, 1291 N. Indian Hill Blvd., Claremont, CA 91711-3897
G.E.C. Bell

65. NASA Lewis Research Center, MS-106-5, Cleveland, OH 44135
G. Morscher

66-68. National Institute of Standards and Technology, Boulder, CO 80302
F. R. Fickett H. I. McHenry R. P. Reed

69-70. Naval Research Laboratory, Code 6506, Washington, DC 20375
D. L. Gibson J. A. Sprague

71-113. Oak Ridge National Laboratory, P.O. Box 2008, Oak Ridge, TN 37831

Central Research Library	M. L. Grossbeck	J. P. Robertson
Document Reference Section	A. N. Gubbi	T. C. Reuther
Laboratory Records Department (2)	J. F. King	A. F. Rowcliffe (10)
Laboratory Records-RC	E. A. Kenik	M. J. Saltmarsh
Patent Section	R. L. Klueh	J. Sheffield
D. J. Alexander	E. H. Lee	L. L. Snead
J. Bentley	L. K. Mansur	R. E. Stoller
E. E. Bloom	P. J. Maziasz	K. R. Thoms
T. D. Burchell	M. C. Osborne	P. F. Tortorelli
G. M. Goodwin	L. Qualls	R. L. Wallace
R. H. Goulding	P. M. Rice	S. J. Zinkle

114. Oregon Graduate Institute, Dept. of Materials Science & Engineering, 19600 N.W. Von Neumann Drive, Beaverton, OR 97006
J. M. McCarthy

115-117. Princeton University, Princeton Plasma Physics Laboratory, P.O. Box 451, Princeton, NJ 08540
R. C. Davidson Long-Poe Ku D. M. Meade

118-120. Rensselaer Polytechnic Institute, Troy, NY 12181
S. D. Connery D. Duquette D. Steiner

121. Rockwell International Corporation, NA02, Rocketdyne Division, 6633 Canoga Avenue, Canoga Park, CA 91304
D. W. Kneff

122-124. Sandia National Laboratories, Fusion Technology Dept., Dept. No 6531, P.O. Box 5800, Albuquerque, NM 87185-5800
M. J. Davis M. Ulrickson R. D. Watson

125-127. Sandia National Laboratories, Livermore Division 8316, Livermore, CA 94550
W. Bauer K. Wilson W. G. Wolfer

128. San Diego State University, Mechanical Engineering Dept., San Diego, CA 92182-0191
L. D. Thompson

129. Texas A&M University, Box 397, Prairie View, TX 77446
D. Baker

130. TSI Research, 225 Stevens Ave., #110, Solana Beach, CA 92075
E. T. Cheng

131. Westinghouse Hanford, P.O. Box 1970, Richland, WA 99352
A. M. Ermi (L6-37)

132-133. University of California at San Diego, U.S. ITER Project Office, 9500 Gilman Drive, Bldg. 302, La Jolla, CA 92093-0035
C. C. Baker T. R. James

134-135. University of California, Dept. of Mechanical and Environmental Engineering, Engineering II, Room 2355, Santa Barbara, CA 93106-5070
G. E. Lucas G. R. Odette

136-138. University of California, Dept. of Chemical, Nuclear, and Thermal Engineering, Los Angeles, CA 90024
M. A. Abdou N. M. Ghoniem S. Sharafat

139. University of Michigan, Dept. of Nuclear Engineering, Ann Arbor, MI 48109
T. Kammash

140. University of Missouri, Department of Nuclear Engineering, Rolla, MO 65401
A. Kumar

141. University of Tennessee, Dept. of Materials Science and Engineering, 427-B Dougherty Bldg., Knoxville, TN 37996-2200
P. K. Liaw

142-143. University of Wisconsin, Nuclear Engineering Dept., 1500 Johnson Drive, Madison, WI 53706
J. B. Blanchard G. L. Kulcinski

144-146. Hokkaido University, Faculty of Engineering, Kita 13, Nishi 8, Kita-ku, Sapporo 060, Japan
Heischichiro Takahashi Somei Ohnuki Akira Okada

147-148. Japan Atomic Energy Research Institute, Tokai Research Establishment, Tokai-mura, Naka-gun, Ibaraki-ken 319-11, Japan
Akimichi Hishinuma K. Noda

149. Kyoto University, Institute of Atomic Energy, Gokasho, Uji, Kyoto 611, Japan
Akira Kohyama

150. Kyushu University, Dept. of Nuclear Engineering, Faculty of Engineering, Kyushu University 36, Hakozaki, Fukuoka 812, Japan
C. Kinoshita

151. Kyushu University, Research Institute for Applied Mechanics, Kasuga, Fukuoka 816, Japan
Naoaki Yoshida

152-153. Muroran Institute of Technology, Dept. of Metallurgical Engineering, 27-1 Mizumoto-cho, Mororan 050, Japan
Toshihei Misawa Akihiko Kimura

154-155 Nagoya University, Dept. of Nuclear Engineering, Furo-Cho, Chikusa-ku, Nagoya 464-01, Japan
Michio Kiritani Tetuo Tanabe

156-160. National Institute for Fusion Science, Furo-cho, Chikusa-ku, Nagoya 464-01, Japan
Yutai Katoh Chusei Namba
Osamu Motojima Nobuaki Noda
Takeo Muroga

161-164. National Research Institute for Metals, Tsukuba Branch, Sengen, Tsukuba-shi, Ibaraki-ken, 305, Japan
Fujio Abe Tetsuji Noda
Josei Nagakawa Haruki Shiraishi

165. PNC Oarai, 4002 Narita, Oarai, Ibaraki 311-13, Japan
Itaru Shibahari

166. Science University of Tokyo, Dept. of Materials Science & Technology, 2641 Yamazaki Noda City, Chiba Prefecture 278, Japan
Naohira Igata

167. Teikyo University, Otsuka, Hachioji, Tokyo 192-03, Japan
Akira Miyahara

168-169. Tohoku University, Institute for Materials Research, Katahira 2-2-1, Sendai 980-77, Japan
Akihiko Kimura Hideki Matsui

170-173. Tohoku University, Institute for Materials Research, Oarai Branch, Oarai, Ibaraki 311-13, Japan
Hideo Kayono Tamaki Shibayama
Hiroaki Kurishita Tatsuo Shikama

174-175. Tohoku University, Dept. of Nuclear Engineering, Aoba, Aramaki, Sendai 980-77, Japan
Katsunori Abe Akira Hasegawa

176. Tohoku University, Dept. of Machine Intelligence and Systems Engineering, Aramaki, Aoba-ku, Sendai 980-77, Japan
Tatsuo Kondo

177. Tokai University, Dept. of Nuclear Engineering, 1117 Kitakaname, Hiratsuka-shi, Kanagawa-ken 259-12, Japan
Shiori Ishino

178. University of Tokyo, Dept. of Nuclear Engineering, 3-1, Hongo 7-Chome, Bunkyo-Ku, Tokyo 113, Japan
Naoto Sekimura

179. University of Tokyo, Dept. of Materials Science, 3-1, Hongo 7-Chome, Bunkyo-ku, Tokyo 113, Japan
Yutaka Kohno

180. Commission of European Communities, Directorate-General for Research Science and Education, Fusion Programme RUE De La Loi 200, B-1049 Brussels, Belgium
F. Cozzani

181-182. Chalk River Nuclear Laboratories, Atomic Energy of Canada, Ltd., Chalk River, Ontario KOJ 1J0, Canada
I. J. Hastings D. P. Jackson

183-184. Southwestern Institute of Physics, P.O. Box 432, Chenedu 610041, Sichuan, P.R. China
J. P. Qian Zeng Yu Xu

185. Institute of Atomic Energy, Academia Sinica, P.O. Box 275-51, Beijing, P.R. China
J. Yu

186. Riso National Laboratory, Materials Dept., P.O. Box 49, DK-4000, Roskilde, Denmark
B. N. Singh

187. Centre d'Etudes Nucleaires, Saclay, DLPC/SMCM, Commissariat a l'Energie Atomique, 91191 Gif-Sur-Yvette, Cedex, France
N. Roux

188. Commission for European Communities, Joint Research Centre, I.A.M. Ispra Establishment 21020 Ispra (Varese), Italy
P. Fenici

180. EURATOM/CIEMAT Fusion Association, Avenida Complutense 22, 28040, Madrid, Spain
E. R. Hodgson

190. Paul Scherrer Institute, CH-5232 Villigen, Wuerenlingen PSI, Switzerland
M. Victoria

191. Harwell Laboratory, B393, Radiation Damage Dept., Oxfordshire, OX11 ORA, United Kingdom
C. A. English

192. Metallurgical and Nuclear Consultant, 9A Cumnor Rise Road, Cumnor Hill, Oxford OX2 9HD, United Kingdom
D. R. Harries

193. Hahn-Mietner-Institut fur Kernforschung Berlin, Postfach 390128, Glienicker Str. 100, D-14109, Germany
H. Wollenberger

194. Institut fur Festkorperforschung Forschungszentrum Jülich, Postfach 1913, D-52425 Jülich, Germany
H. Ullmaier

195-198. ITER Garching Joint Work Site, Max-Planck-Institute für Plasmaphysik, Boltzmannstrasse 2, D-85748 Garching bei München, Germany
B. Barabash G. Kalinin
Y. Gohar R. Parker

199-200. ITER Naka Joint Work Site, 801-1 Mukouyama, Naka-machi, Naka-gun, Ibaraki-Ken, 311-01, Japan
M. Huguet (2)

201-204. ITER San Diego Joint Work Site, 11025 N. Torrey Pines Road, La Jolla, CA 92037
V. Chuyanov F. Puhn
S. J. Piet P. Smith

205-206. Kernforschungszentrum Karlsruhe, Postfach 3640, 75 Karlsruhe 1, Germany
M. Dalle-Donne (INR) K. Ehrlich (IMF-II)

207. Max-Planck-Institut für Plasmaphysik, Boltzmannstrasse 2, D-85748 Garching bei München, Germany
Patrick Lorenzetto

208. A. A. Baikov Institute of Metallurgy, USSR Academy of Sciences, Leninsky Prospect 49, Moscow, Russia
L. I. Ivanov

209. CRISM "Prometey," Naberezhnava r. Monastyrick 1, 193167, St. Petersburg, Russia
V. V. Rybin

210. D. V. Efremov Institute of Electro-Physical Apparatus, 189631, St. Petersburg, Russia
S. A. Fabritsiev

211. Kharkov Institute of Physics & Technology, Radiation Damage and Materials Dept., Akademicheskaya 1, 310108 Kharkov, Ukraine
I. M. Neckludov

212-214. V. I. Lenin Research Institute of Atomic Reactors, 433510 Dimitrovgrad-10, Ulyanovsk Region, Russia
V. Kazakov A. S. Pokrovsky V. K. Shamardin

215. Korea Advanced Institute of Science and Technology, Department of Nuclear Engineering, DaeDukDanji, Taejon, 305-701, Korea
I-S. Kim

216-217. Korean Atomic Energy Research Institute, P.O. Box 105, Yusung, Taejon, 305-600, Korea
Thak-Sang Byun Jun Hwa Hong

218. Seoul National University, Dept. of Nuclear Engineering, 56-1 Shinrim-Dong, Kwanak-Ku Seoul, 151-742, Korea
K. H. Chung

219. Sung Kyun Kwan University, Dept. of Metallurgical Engineering, 300 Chunchun-dong, Jangan-gu, Suwon, 440-746, Korea
J. G. Han

220. Department of Energy, DOE Oak Ridge Field Office, P.O. Box 2008, Oak Ridge, TN 37831-6269
Assistant Manager for Energy Research and Development

221. Department of Energy, DOE Oak Ridge Field Office, P.O. Box 2008, Oak Ridge, TN 37831-6269
S. D. Frey

222. Department of Energy, Office of Basic Energy Sciences, Washington, D.C. 20585
R. J. Gottschall

223-228. Department of Energy, Office of Fusion Energy, Germantown, MD 20874

S. E. Berk	W. F. Dove	W. Marton
N. A. Davies	R. McKnight	F. W. Wiffen

229. Department of Energy, Richland Operations Office, P.O. Box 550, MS-K850, Richland, WA 99352
J. Turner

230-231. Department of Energy, Office of Scientific and Technical Information, Office of Information Services, P.O. Box 62, Oak Ridge, TN 37831
For distribution by microfiche as shown in DOE/OSTI-4500-R75, Distribution Categories UC-423 (Magnetic Fusion Reactor Materials) and UC-424 (Magnetic Fusion Energy Systems)